Gas membrane characterization via the time-lag method for neat and mixed-matrix membranes

Haoyu Wu

Thesis submitted to the University of Ottawa
in partial Fulfillment of the requirements for the
Doctorate in Philosophy in Chemical Engineering

Department of Chemical and Biological Engineering

Faculty of Engineering

University of Ottawa

Abstract

Separation technologies with polymeric membranes are widely studied and have a wide range of applications. The membrane's heart is a dense selective layer whose permeability should strongly depend on the permeating species' properties. In turn, permeability depends on the diffusivity and solubility of the permeating species in the selective layer, which are considered intrinsic properties of the polymer forming the selective layer. When developing new membrane materials, the ultimate objective is to exceed the famous "upper bound" limit by achieving simultaneously higher selectivity and higher permeability. This objective is impossible without a reliable and accurate characterization method to determine the selective layer's intrinsic transport properties. The time-lag method is the most common membrane characterization technique, initially developed for polymeric membranes. However, as the membrane technology and material science advance, the selective layer structure becomes more complex and not limited to organic polymers. As a result, the time-lag method needs to be reviewed and adapted to these more complicated cases, which was the main objective of this thesis.

Numerical simulation of dynamic gas permeation experiments is a powerful tool to examine different aspects of the time-lag method. Therefore, we have established a comprehensive variable-mesh finite-difference scheme, which was used throughout the thesis. It allowed us to investigate the effect of different random and resolution errors and an extrapolation error on the resulting time lag of an ideal membrane. We then considered more complex systems, particularly those of glassy polymers and mixed matrix membranes, to investigate the effect of different transport mechanisms on the results of dynamic and steady-state gas permeation experiments. In parallel, we also focused on developing a novel gas permeation system that would monitor dynamic gas permeation experiments based on pressure decay at the feed side. All the existing constant-volume gas permeation systems rely on monitoring pressure to rise at the membrane's permeate side. Although this work is still ongoing, we have made considerable progress.

Among the numerous contributions made through this thesis, there are three of particular significance. We have developed an analytical model to predict mixed matrix membranes' relative permeability with the uniformly dispersed non-permeable fillers of

different shapes. The model requires three structural parameters arising from the filler's shape and size, and it is superior to all existing analytical models, including the famous Maxwell model. We have also demonstrated that the diffusivity of mixed matrix membranes determined by the time-lag method depends on the number of layers of dispersed particles. In the limiting case of a single layer of uniformly impermeable fillers, it is possible for the diffusivity determined by the time-lag method to be greater than that of the host polymer, which might appear as counterintuitive in the absence of defects at the polymer-particle interface. In the case of glassy polymers, it is possible to observe an upward deviation from the steady-state flux, resulting from a non-instantaneous equilibrium between permeating species in Henry's and Langmuir adsorption sites.

Résumé

Les technologies de séparation utilisant des membranes en polymère sont largement étudiées et ont un large éventail d'applications. Le cœur de la membrane est une couche sélective dense dont la perméabilité dépend fortement des propriétés de l'espèce pénétrante. À son tour, la perméabilité dépend de la diffusivité et de la solubilité de l'espèce pénétrante dans la couche sélective, qui sont considérées comme des propriétés intrinsèques du polymère formant la couche sélective. Lors du développement de nouveaux matériaux pour la fabrication des membranes, l'objectif ultime est de dépasser la fameuse "limite supérieure" en atteignant simultanément une sélectivité plus élevée et une perméabilité plus élevée. Cet objectif est impossible sans une méthode de caractérisation fiable et précise pour déterminer les propriétés de transport intrinsèques de la couche sélective. La méthode du décalage dans le temps est la technique de caractérisation des membranes la plus courante, initialement développée pour les membranes en polymère. Cependant, à mesure que la technologie des membranes et la science des matériaux progressent, la structure de la couche sélective devient plus complexe et ne se limite pas aux polymères organiques. Par conséquent, la méthode du décalage dans le temps doit être revue et adaptée à ces cas plus complexes, ce qui était l'objectif principal de cette thèse.

La simulation numérique des expériences de perméation dynamique de gaz est un outil puissant pour examiner différents aspects de la méthode du décalage temporel. Par conséquent, nous avons établi un schéma complet de différences finies à maillage variable, qui a été utilisé tout au long de la thèse. Cela nous a permis d'étudier l'effet de différentes erreurs aléatoires et de résolution et une erreur d'extrapolation sur le décalage temporel résultant d'une membrane idéale. Nous avons ensuite examiné des systèmes plus complexes, en particulier ceux des polymères vitreux et des membranes à matrice mixte, pour étudier l'effet de différents mécanismes de transport sur les résultats d'expériences de perméation de gaz dynamiques et en régime permanent. En parallèle, nous nous sommes également concentrés sur le développement d'un nouveau système de perméation de gaz qui est utiliserait les expériences de perméation de gaz dynamique basées sur la décroissance de la pression du côté l'alimentation. Tous les systèmes de perméation de

gaz à volume constant existants reposent sur la surveillance de la pression pour augmenter du côté du perméat de la membrane. Bien que ce travail soit toujours en cours, nous avons fait des progrès considérables.

Parmi les nombreuses contributions apportées à travers cette thèse, il y en a trois d'une importance particulière. Nous avons développé un modèle analytique pour prédire la perméabilité relative des membranes à matrice mixte avec des particules non perméables et de différentes formes qui sont uniformément dispersées à l'intérieur de la membrane. Le modèle nécessite trois paramètres structurels découlant de la forme et de la taille des particules, et ce modèle est supérieur à tous les modèles analytiques existants, y compris le célèbre modèle de Maxwell. Nous avons également démontré que la diffusivité des membranes à matrice mixte déterminée par la méthode du décalage temporel dépend du nombre de couches de particules dispersées. Dans le cas limite d'une seule couche de particules imperméables uniformément dispersées, il est possible que la diffusivité déterminée par la méthode du retard soit supérieure à celle du polymère hôte, ce qui pourrait apparaître comme contre-intuitif en l'absence de défauts au niveau de l'interface polymère- particules. Dans le cas des polymères vitreux, il est possible d'observer une déviation vers le haut par rapport au flux stationnaire, résultant d'un équilibre non instantané entre les espèces pénétrantes dans les sites d'adsorption de Henry et Langmuir.

Acknowledgments

As a famous old Chinese saying goes, “One minute of performance on stage requires ten years of hard practicing off stage.” My thesis is a work of six and a half years, including a semester of an undergraduate project, a semester of MEng project, and 17 semesters of my Ph.D. (MASc. included). This thesis could finally come out thanks to the behind-the-scene contributions from many people. I would like to take this opportunity to express my appreciation for all these wonderful people.

I would like first to thank my dearest supervisors, Drs. Jules Thibault and Boguslaw Kruczek, who brought me into the door of membrane characterization, believed in my potentials and allowed me to fast-track from MASc to Ph.D. to dig deep on the topic. Without their professional guidance and generous encouragement, this thesis would have never been possible. By working with them; I understand what professionalism is and how passionate they can be to their areas of interest. I will always remember things and merits I learnt from them for the rest of my life.

I would like to thank Drs. Takeshi Matsuura, David Taylor, and Handan Tezel for participating as committee members for my comprehensive exam and reviewing my final thesis. Your comments and questions made this thesis more precise and understandable to a broader audience.

Special thanks to the department technicians' technical support and advice, namely Gérard, Franco, Louis, and James. Especially, I would like to thank Gerard for helping me install the electronic devices and set up the temperature box and the software LabView and Franco for his mechanical work, which put my design into a real system.

Thanks are also given to Dr. Cao for letting me use the DSC (Differential Scanning Calorimetry) and the spin coater, Dr. Tezel, for letting me use the GC (Gas Chromatography), and my colleagues who helped me with testing some samples, Dean and Yujie.

I would like also to thank the graduate and undergraduate students involved in this project, Neveen, Chris, Nneka, Samir, Ramzi, Maryam, and Peter. Working with them was a bonus beyond my anticipation.

I would like to thank the National Science and Engineering Research (NSERC) for the financial support for this project, the University of Ottawa for the International Doctoral Scholarship, and the Department of Chemical and Biological Engineering for the Wilfrid Brisson Graduate scholarship. These financial supports made my life easier and enabled me to be more focused on my graduate studies.

Last but not least, I am grateful for the unconditional love from my family and social support from my friends. They made my pursuit of knowledge more meaningful.

The biggest treasure I found is never taking knowledge for granted but exploring both the unknowns and the knowns. This thesis is not the end of my exploration but only a humble beginning.

Statement of contributions of collaborators

I hereby declare that I, Haoyu Wu, am the sole author and the principal researcher of this thesis and that no parts of this work have been submitted or accepted for any other degree.

Drs. Boguslaw Kruczek and Jules Thibault supervised this thesis. Both provided continued guidance during the work carried out and editorial comments to the final version of this thesis. Dr. Naveen Al-Qasas, the former doctoral student, has co-authored the paper in **Chapter 2**. Dr. Al-Qasas guided the paper as the work was also a part of her Ph.D. thesis. Mr. Peter Leszczynski has co-authored the paper in **Chapter 4**. Mr. Peter Leszczynski helped with developing the final membrane characterization system. Dr. Maryam Zamanian, who was a visiting doctoral student from Iran for 10 months, has co-authored the paper in **Chapter 6**. She provided the original real-life context of the mixed-matrix membranes for barrier materials. The original computer code in this thesis was written by Dr. Jules Thibault (**Chapter 2**), which I modified and added features suitable for the studies in **Chapters 3 and 5**. Dr. Jules Thibault coded the first version of the computer program to perform numerical simulations in Chapters 6, 7, and 8. I planned all simulations, analyzed all the results and developed the models.

The responsibilities of the author, Haoyu Wu, to fulfill the requirements of this thesis were as follows:

1. Investigate the reliability of a numericalfinite-difference tool used to simulate a membrane permeation process and determine the optimal numerical scheme.
2. Perform an accuracy analysis on a membrane permeation system and use the numerical finite-difference tool to determine the optimum system parameters and experimental conditions. Add noise function in the numerical tool.
3. Develop a new gas membrane characterization system that is based on the upstream pressure measurements.
4. Investigate the complex solution-diffusion model both numerically and experimentally and improve the current time-lag method. Add the feature of the

non-instantaneous equilibrium model and partial immobilization model into the numerical tool.

5. Design all numerical experiments. Develop analytical models for the gas permeation across mixed-matrix membranes and validate the applicability of the time-lag method.
6. Prepare a thesis in partial fulfillment of the requirement for obtaining a Ph.D. degree in Chemical Engineering.

Table of contents

List of Figures

List of Tables

Chapter 1

Introduction

1.1 Introduction

Separation technologies with polymeric membranes are widely studied and have a wide range of applications, such as biotechnology, water treatment, pharmaceutical manufacturing, food processing, petroleum, and gas separation [1-3]. It has attracted significant attention in the industry for many years due to its multiple advantages: small space footprint and energy cost, easy operation and clean process [4]. A membrane mainly consists of a permeable layer that is usually used for its selective permeation of different species due to the permeability difference of permeates [5]. Membranes are usually thin to favour higher permeation fluxes while preserving the selectivity. Sometimes, a membrane serves as a barrier material to reduce mass transfer rates in the coating, drug release, and packaging applications [6-7]. Polymeric membranes, such as Polyvinyl alcohol (PVA), poly(sulfone) (Psf), poly(di-methyl-siloxane) (PDMS), and poly(phenylene) oxide (PPO), are popular membranes in separation applications and are extensively studied in laboratories [1,5,6,8]. The focus of research in membrane laboratories is on developing new membrane materials to improve membranes' performance in terms of permeation rate and selectivity. The ultimate objective is to break the famous “upper bound” limit [9-11] by achieving high selectivity and high permeability. Different approaches to improve performance were proposed, including discovering or synthesizing new membrane materials such as mixed-matrix membranes [12,13], reducing membranes’ thickness while keeping the mechanical strength, and improving the process design [13]. To accelerate the development of better membranes, it is essential to understand the transport phenomena underlying the membrane permeation process and have a robust method to characterize membranes that provide a reliable and accurate estimation of membrane transport properties [14].

Dense polymeric membranes are formed with rubbery polymers or glassy polymers. Above the glass transition temperature (T_g), segments of polymeric chains have sufficient energy to freely rotate along their axis, thus creating short gaps and a transient opening between these gaps through which gas molecules can diffuse. This type of polymers is referred to as rubbery polymers. Rubbery polymer films are less effective than glassy polymer films in gas separation due to a weaker relation between molecule size and diffusivity [15]. The significant difference in the structures of glassy and rubbery polymers is the so-called excess free volume caused by restricted polymer chain movements below the glass transition temperature T_g [15]. In addition to rubbery and glassy membranes, mixed-matrix membranes are also considered for gas separation applications. A mixed-matrix membrane (MMM) typically refers to embedding a homogenously-dispersed inorganic or organic filler into the continuous phase of a polymeric matrix [16-18]. A critical application of MMMs is to create barrier materials. More specifically, impermeable nanoparticles are added as fillers into the polymeric matrix, thereby creating torturous diffusion pathways to prevent or delay the permeation of water or gas molecules [16]. The shape, volume fraction, and dimensions of the particles are essential factors determining the effective gas permeability of a mixed-matrix membrane [17-18].

The transport of a species across a membrane requires applying a driving force, which is a partial pressure gradient in the case of gas separation membranes. The transport mechanism in polymeric membranes is described by the solution-diffusion model [15,19]. In this mechanism, the permeation process is comprised of three steps: (1) sorption of gas molecules at the feed-membrane interface; (2) diffusion of sorbed gas molecules in the direction of decreasing chemical potential (concentration); and (3) desorption of gas molecules at the membrane-permeate interface [15,19]. The separation of permeating species is achieved by the differences of their solubility and diffusivity coefficients in the membrane. The solubility coefficient (S) represents the equilibrium concentration of gas molecules dissolved in the membrane at a given pressure. Apart from operating conditions (temperature, pressure, composition), the solubility coefficient is directly related to the condensability of the permeating gases and polymer-gas interactions [14]. Diffusivity (D) is the ability of dissolved gas molecules to move through the membrane. The diffusivity coefficient usually increases with a decrease in the size of the molecules. Gas sorption and

desorption are assumed to be instantaneous processes that follow Henry's law (Eq. (1)). The permeation in polymeric membranes is controlled by the diffusion rate, which is proportional to the concentration gradient and is assumed to obey Fick's second law of diffusion (Eq. (2)). The solubility coefficient (S) and diffusivity coefficient (D) are two intrinsic transport properties of the membrane. Their product, the permeability coefficient (P) (Eq. (3)), which is also an intrinsic membrane property, signifies the overall ability of gas molecules to permeate through the membrane [20].

$$C = Sp \tag{1}$$

$$\frac{\partial C}{\partial t} = D\frac{\partial^2 C}{\partial x^2} \tag{2}$$

$$P = SD \tag{3}$$

where C is the concentration of the permeating gas species within the membrane, p is the gas pressure in contact with the membrane. Henry's law constant (S) corresponds to the solubility coefficient, P is the permeability coefficient. The ideal selectivity (α) of a binary gas system is simply the ratio of the two gases' permeability. A mathematical representation of permeability and ideal selectivity is presented in Eqs. (4)-(5).

$$P = J \cdot L / \left(p_u - p_d \right) \tag{4}$$

$$\alpha_{1/2} = P_1 / P_2 \tag{5}$$

where J is the flux of gas molecules across the membrane, L is the membrane thickness and (p_u - p_d) is the pressure difference between the upstream and the downstream sides of the membrane, and 1 and 2 indicate two different gas species.

Commonly, the dual-mode sorption model [21-23], which explains a non-linear relationship between gas pressure and gas concentration in glassy polymers, is used to interpret the permeation behaviour of glassy membranes. In this model, two mechanisms prevail Henry's sorption mechanism and Langmuir's "hole-filling" mechanism. In addition to P, D and S, the complete characterization of the membrane, in this case, also requires the determination of the hole saturation constant (C_L'), and the affinity constant (b) (Eq. (6)). Several assumptions [20] prevail for the "dual-mode sorption" model: (1) complete

immobilization in the Langmuir's sorption sites, and (2) instantaneous equilibrium between the Langmuir's and Henry's sites.

$$C = Sp + \frac{C'_L bp}{1 + bp} \tag{6}$$

The transport phenomena across an MMM also follow Henry's law and Fick's first and second diffusion laws. However, adding impermeable fillers into neat membrane forces permeates to circumvent filler particles, thereby causing a decrease in the permeability and a change in its overall diffusivity. The transport properties of a neat membrane are represented by P, S, and D. The MMM's transport properties are, instead, represented by the effective permeability (P_{eff}), effective solubility (S_{eff}), and effective diffusivity (D_{eff}). The relationship between the three coefficients are in Eq. (7). A more detailed discussion will be given in later chapters.

$$P_{eff} = S_{eff} D_{eff} \tag{7}$$

For materials used extensively in the packaging industry, the barrier properties such as water permeation, oxygen, nitrogen, and carbon dioxide are essential indexes. Transient-state transport behaviour is often more critical than the steady-state permeation rate. A similar concern prevails in cyclic transient membrane gas separation processes [24]. In these cases, the simple solution-diffusion model and dual-mode sorption model are not subtle enough to estimate the variable transient permeation behaviours in the actual processes under different conditions. For example, a different feed pressure of a membrane may result in different molecule transfer rates between Henry's sites and Langmuir's sites. This relationship is not accounted for in the solution-diffusion and the dual-mode sorption models because the former assumes the sorption rates are zero. The latter assumes they are infinity, regardless of the concentration in the membrane. The transfer rate controls the number of mobile gas molecules in Langmuir sites and affects the overall diffusivity. When the Langmuir sites are partially mobile, the diffusivity is contributed by both diffusion processes in Henry's sites and mobile Langmuir sites. The introduction of partial immobilization and non-instantaneous models allow representing this relationship and therefore providing a better estimation of the time-dependent permeation rate. This will benefit the control of the packaging thickness design and the selection of packaging

materials. For membranes used in gas separation processes, such as air separation, hydrogen recovery, carbon dioxide capture, biogas purification, and membrane design modules may affect separation effectiveness. Different species of gas molecules have different transport properties within a membrane under different conditions. Therefore, a more versatile model would assist in providing more accurate predictions of various transport behaviours. The information will greatly benefit in the design of membrane modules for a specific application.

Among all the available membrane characterization techniques, the transport properties are usually determined by permeation experiments in constant-volume systems [25], where gas permeation is measured based on the pressure accumulation as a function time, as illustrated in Fig. 1.1. Using the downstream time-lag method [26,27], the tested membrane's permeability coefficient and diffusivity coefficient are easily obtained from the slope and the time-axis intercept of the quasi-steady state downstream pressure accumulation plot (pressure versus time), respectively. The solubility coefficient is simply the permeability coefficient divided by the diffusivity coefficient. The technique is popular mostly due to its simplicity. Theoretically, one could also obtain the upstream time lag similarly from the upstream pressure decay curve shown in Fig. 1.1. The time lags and slopes' representations are shown in Eqs. (8)-(11). Details of a permeation experiment are described in the following chapters.

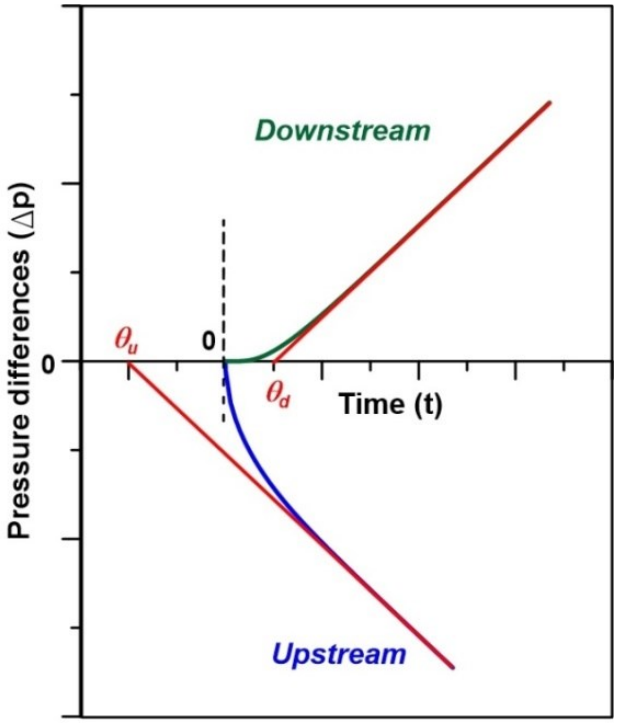

Figure 1.1 Schematic diagram illustrating the upstream and downstream time-lag method. The green and the blue lines are the pressure changes in the downstream and upstream sides of the membrane.

$$\theta_u = -\frac{L^2}{3D} \tag{8}$$

$$\theta_d = \frac{L^2}{6D} \tag{9}$$

$$Slope_u = -\frac{p_0 ARTP}{V_u L} \tag{10}$$

$$Slope_d = \frac{p_0 ARTP}{V_d L} \tag{11}$$

where A is the area of the membrane, and p_0 is the feed pressure, T is the membrane temperature, R is the gas constant. V_u and V_d are the upstream and downstream volumes, θ_u is the upstream time lag, and θ_d is the downstream time lag. The time-lag method initially developed based on the solution-diffusion mechanism is the oldest and most common membrane characterization method. However, as the membrane technology and material science, advance and membranes are becoming more complex. As a result, the time-lag

method needs to be reviewed and adapted to more complex cases to remain suitable and valuable.

1.2 Objectives

The thesis's main objective is to introduce several feasible improvements regarding the accuracy of the determination of membrane transport properties and discuss the applicability of the time-lag method to several special cases of membrane characterization. Inadequate estimation of the transport properties mainly results from complex characterization systems, improper application of transport models and the characterization method. A comprehensive numerical model is instrumental in predicting and assessing the experimental results and developing methods to estimate the membrane's transport properties. Therefore, the thesis's first objective is to establish a stable and comprehensive numerical tool to represent the permeation process and run accurately simulated experiments. The second objective is to provide some insights into the current constant-volume system's effectiveness by analyzing multiple potential sources of errors that could affect the analysis. The third objective is to re-design the current membrane characterization system with the explicit goal of improving the accuracy of the system and meeting the need of a practical upstream pressure change measurements, which is not available in conventional constant volume systems. The fourth objective is to study the transport phenomena and the applicability of the time-lag method in glassy polymers with the dual-mode sorption, non-instantaneous equilibrium and partial immobilization. The final objective is to study the transport properties within the MMMs with impermeable fillers and the time-lag method's applicability to characterize mixed-matrix membranes.

1.3 Thesis structure

The thesis is comprised of nine chapters, including Chapter 1 for the introduction and Chapter 9 for the conclusions. Chapters 2-8 are the main chapters of the thesis, each covering a specific topic. Chapters 2, 3 and 8 are scientific articles published in peer-

reviewed journals. Chapters 4-7 are articles that were submitted or are to be submitted to reviewed journals.

Chapter 2, “Simulation of time-lag permeation experiments using finite differences,” discusses a proper numerical scheme to perform simulated permeation experiments under different boundary conditions with two finite difference methods and two numerical mesh schemes. A benchmark analytical solution is used to evaluate the accuracy of each case studied. This chapter provides the basic numerical program used for generating data in most other chapters.

Chapter 3, “Impact of Measuring Devices and Data Analysis on the Determination of Gas Membrane Properties,” is a comprehensive error analysis for a gas permeation system. Based on this analysis, the chapter provides useful information on the characteristic of the experimental setup design, the electronic device selection, and the optimum operating conditions to run membrane permeation experiments.

Chapter 4, “Design considerations for a novel polymeric membrane characterization system based on upstream pressure decay,” is a detailed design of an experimental membrane system combining the measurements of the downstream pressure rise and the upstream pressure decay. It discusses some of the main challenges in designing an upstream time-lag measurement system and overcoming these challenges.

Chapter 5, “Instantaneous time lag: new insight on gas transport in membranes,” introduces the concept of “instantaneous time lag” to analyze data from experiments with a non-instantaneous equilibrium between the Langmuir’s and Henry’s sites in dual-mode sorption membranes.

Chapter 6, “Gas permeation model of mixed-matrix membranes with embedded impermeable cuboid particles,” proposed a simple and effective new model to represent the relative permeability of MMMs with impermeable cuboid particles.

Chapter 7, “Generalized model for the prediction of the permeability of mixed-matrix using impermeable fillers of diverse geometry,” extends the model developed in Chapter 6 to various filler geometries in MMMs. It is shown that the simple model remains effective for most cases, and only minor modifications are required for some geometries.

Chapter 8, "Validity of the time-lag method for the characterization of mixed-matrix membranes," examines the applicability of the conventional time-lag method to MMMs. Various filler geometries and orientations were analyzed and explained in detail. The effect of the number of layers of dispersed particles on the apparent diffusivity is discussed.

1.4 References

[1] Asad Asad, Dan Sameoto, Mohtada Sadrzadeh, Chapter 1 - Overview of membrane technology, Editor(s): Mohtada Sadrzadeh, Toraj Mohammadi, In Micro and Nano Technologies, Nanocomposite Membranes for Water and Gas Separation, Elsevier, 2020, Pages 1-28,

[2] K. C. Chong, S. O. Lai, H. S. Thaim, H. C. Teoh and S. L. Heng, "Recent progress of oxygen/nitrogen separation using membrane technology," J. Eng. Sci. Tech.., vol. 11, no. 7, pp. 1016-1030, 2016.

[3] Charcosset, Catherine. "Membrane Processes in Biotechnology: An Overview." Biotechnology Advances, vol. 24, no. 5, Elsevier Inc, 2006, pp. 482–92, doi:10.1016/j.biotechadv.2006.03.002.

[4] A. F. Ismail, T. D. Kusworo, A. Mustafa and H. Hasbullah, "Understanding the solution-diffusion mechanism in gas separation membrane for engineering students," Regional Conf. Eng. Educ., Johor, Malaysia, pp. 155-159, 2005.

[5] Z.W. Abdullah, Y. Dong, I.J. Davies, S. Barbhuiya, PVA, PVA Blends, and Their Nanocomposites for Biodegradable Packaging Application, Polymer-Plastics Tech. & Eng., 56 (2017) 1307-1344. http://dx.doi.org/10.1080/03602559.2016.1275684

[6] W. J. Koros and G. K. Fleming, "Membrane-Based Gas Separation," J. Memb. Sci., vol. 83, no. 1, pp. 1–80, 1993.

[7] S.E.M. Selke, J.D. Culter, Plastics Packaging: Properties, Processing, Applications, and Regulations, Third Edit, Carl Hanser Verlag, Munich, 2016. https://doi.org/10.1016/B978-3-446-40790-9.50001-9.

[8] B. Kruczek, & T. Matsuura. “Development and Characterization of Homogeneous Membranes de from High Molecular Weight Sulfonated Polyphenylene Oxide.” J. Memb. Sci., vol. 146, no. 2, pp. 263–75, 1998. doi:10.1016/S0376-7388(98)00120-3.

[9] L. M. Robeson, “Correlation of separation factor versus permeability for polymeric membranes,” J. Memb. Sci, vol. 62, no. 2, pp. 165–185, 1991.

[10] L. M. Robeson, “The upper bound revisited,” J. Memb. Sci, vol. 320, no. 1-2, pp. 390–400, 2008.

[11] B. D. Freeman, “Basis of Permeability/Selectivity Trade-off Relations in Polymeric Gas Separation Membranes,” Macromolecules, vol. 32, no. 2, pp. 375–380, 1999.

[12] Atikah Mohd Nasir, Pei Sean Goh, Ahmad Fauzi Ismail, Chapter 3 - Synthesis route for the fabrication of nanocomposite membranes, Editor(s): Mohtada Sadrzadeh, Toraj Mohammadi, In Micro and Nano Technologies, Nanocomposite Membranes for Water and Gas Separation, Elsevier, 2020, Pages 69-89.

[13] Oindrila Gupta, Sagar Roy, Chapter 2 - Recent progress in the development of nanocomposite membranes, Editor(s): Mohtada Sadrzadeh, Toraj Mohammadi, In Micro and Nano Technologies,Nanocomposite Membranes for Water and Gas Separation, Elsevier, 2020, Pages 29-67.

[14] F. Vašák and Z. Brož, “A method for determination of gas diffusion and solubility coefficients in poly(vinyltrimethylsilane) using a personal computer,” J. Memb. Sci., vol. 82, no. 3, pp. 265–276, 1993

[15] K. Ghosal and B. D. Freeman, “Gas separation using polymer membranes: an overview” Polym. Adv. Tech., vol. 5, no. 11, pp. 673–697, 1994.

[16] S. Zid, M. Zinet, E. Espuche, Modeling diffusion mass transport in multiphase polymer systems for gas barrier applications: A review, J. Polym. Sci. Part B Polym. Phys. 56 (2018) 621–639. https://doi.org/10.1002/polb.24574.

[17] H.A. Silvério, W. Pires, F. Neto, D. Pasquini, Effect of Incorporating Cellulose Nanocrystals from Corncob on the Tensile , Thermal and Barrier Properties of Poly (Vinyl Alcohol) Nanocomposites, J. Nanomater. 2013 (2013). https://doi.org/http://dx.doi.org/10.1155/2013/289641.

[18] C. Wolf, H. Angellier-Coussy, N. Gontard, F. Doghieri, V. Guillard. How the shape of fillers affects the barrier properties of polymer/non-porous particles nanocomposites: A review. J. Memb. Sci., 556 (2018) 393-418. https://doi.org/10.1016/j.memsci.2018.03.085

[19] J. Wijmans and R. Baker, "The solution-diffusion model: a review" J. Memb. Sci, vol. 107, no. 1-2, pp. 1–21, 1995.

[20] J. A. Tshudy and C. Von Frankenberg, "A model incorporating reversible immobilization for sorption and diffusion in glassy polymers," J. Polym. Sci. Polym. Phys. Ed., vol. 11, no. 10, pp. 2027–2037, 1973.

[21] R. M. Barrer, J. A. Barrie, and J. Slater, "Sorption and diffusion in ethyl cellulose. Part III. Comparison between ethyl cellulose and rubber," J. Polym. Sci., vol. 27, no. 115, pp. 177–197, 1958.

[22] D. R. Paul and W. J. Koros, "Effect of partially immobilizing sorption on permeability and the diffusion time lag," J. Polym. Sci. Polym. Phys. Ed., vol. 14, no. 4, pp. 675–685, 1976.

[23] W. R. Vieth, J. M. Howell, and J. H. Hsieh, "Dual sorption theory," J. Memb. Sci., vol. 1, pp. 177–220, 1976.

[24] R. T. Yang, "Cyclic Gas Separation Processes," Gas Separation by Adsorption Processes, pp. 201–235, 1987.

[25] S. Lashkari and B. Kruczek, "Effect of resistance to gas accumulation in multi-tank receivers on membrane characterization by the time lag method. Analytical approach for optimization of the receiver," J. Memb. Sci, vol. 360, no. 1-2, pp. 442–453, 2010.

[26] H. A. Daynes, "The Process of Diffusion through a Rubber Membrane," Proc. Roy. Soc. A: Math., Phys. Eng. Sci., vol. 97, no. 685, pp. 286–307, Jan. 1920.

[27] R. M. Barrer and E. K. Rideal, "Permeation, diffusion and solution of gases in organic polymers," Trans. Faraday Soc., vol. 35, p. 628, 1939.

Chapter 2

Simulation of Time-lag Permeation Experiments Using Finite Differences

Haoyu Wu, Neveen Al-Qasas, Boguslaw Kruczek, Jules Thibault*

Abstract

Membrane-based pressure-driven processes are used in an increasing number of applications. To properly design membrane applications, it is necessary to have a good estimate of membrane properties. To characterize membrane permeation properties, the time-lag method is commonly used. A study has been undertaken to gain a deeper understanding of the time-lag method's accuracy under realistic boundary conditions using numerical methods. Numerical simulations offer the opportunity to obtain a solution to Fick's diffusion equation under various boundary conditions and for nonlinear sorption behaviour for which analytical solutions are difficult or impossible to obtain. This paper is mainly concerned with the selection of the optimal finite difference scheme for solving the Fick's diffusion equation that leads to the accurate determination of the membrane time lag. Pressure responses in the upstream and downstream reservoirs at both membrane interfaces are determined from the concentration gradients. The concentration gradient at the upstream side of the membrane is initially steep, and to accurately extract membrane properties, it is essential to predict it accurately. Simulation results for predicting concentration profiles and gradients at both interfaces are compared with known benchmark analytical equations to assess the precision of numerous numerical schemes where the effect of mesh size and the time step is quantified. Results show that a variable mesh size is required to predict the concentration gradient accurately at the upstream

interface. The choice of a variable mesh size scheme is vital as a compromise must be struck between the smallest mesh size and the time step as it greatly impacts on the computation time. Results also showed that both the implicit and explicit finite difference schemes gave similar results.

Keywords: Membrane characterization, finite differences, time lag, upstream pressure decay, variable mesh scheme

Publication status: Journal of Fluid Flow, Heat and Mass Transfer, 2(2015) 14-25

***Corresponding author**

2.1 Introduction

Membrane-based pressure driven processes are used in an increasing number of applications, and are the subject of intensive research and development [1]. To characterize simple permeation processes as well as more complex processes involving diffusion with simultaneous adsorption, the time-lag method initially proposed by Daynes [2] and then modified by Barrer [3] is the method that is currently being used by most researchers. The determination of the time lag allows finding the membrane diffusion coefficient for a target solute. The downstream time lag is based on the downstream pressure increase, while the upstream time lag is based on the detection of the pressure decay in the upstream chamber. Our research group has undertaken an experimental research program to devise new and improved methods to rapidly and accurately determine membrane properties. To complement the experimental program, numerical simulations are also performed to gain a deeper understanding on the flow of molecules across the membrane. Numerical simulations offer the opportunity to obtain solutions for the Fick's diffusion equation under various boundary conditions at which analytical solutions are difficult or impossible to obtain, in addition to consider diffusion within membranes that is characterized with nonlinear sorption behaviours.

This paper is mainly concerned with the selection of the optimal finite difference scheme for solving the Fick's diffusion equation that leads to the accurate determination of the upstream and downstream membrane time lags. For the experimental determination of the time lag, the system usually consists of a thin membrane separated by two fixed-volume chambers, which are initially maintained under high vacuum (see Fig. 2.1 and 2.2). The experiment starts when the upstream chamber is rapidly filled with a high pressure gas. The gas then progressively permeates through the membrane leading to a decrease in the pressure in the upstream chamber and an increase in the pressure of the downstream chamber. Based on the plots of the upstream and downstream pressure differences as a function of time, it is possible to determine the upstream and downstream time lags, respectively. The time lags are obtained by evaluating the intercept of the linear portion of the pressure difference curves with the time axis as schematically shown in Fig. 2.3. The time lag θ is directly proportional to the reciprocal of the membrane diffusion coefficient D [2] Eqs. (1) and (2) give, respectively, the relationships that exist between the upstream and downstream time lags with the membrane diffusion coefficient and thickness.

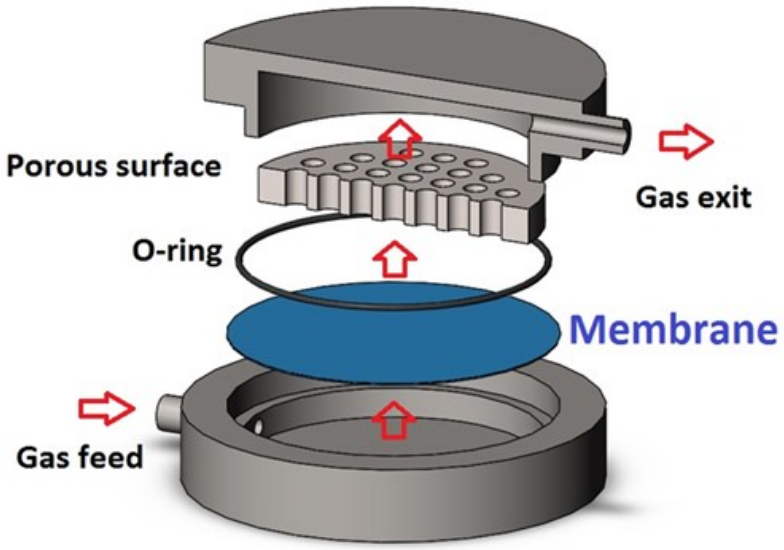

Figure 2.1 Schematic diagram of a typical membrane testing module.

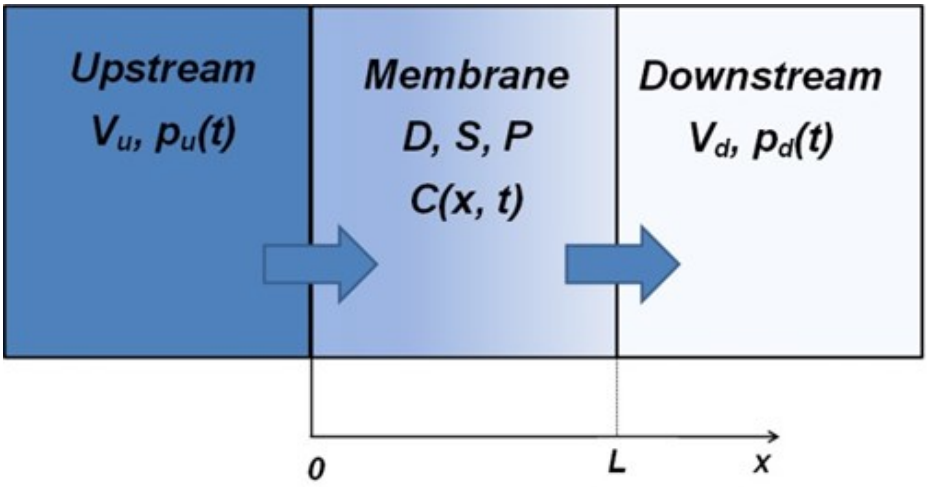

Figure 2.2 Schematic model of the membrane-based pressure driven processes in a constant volume (CV) system.

At time $t = 0^-$, the system is maintained under high vacuum and at $t = 0^+$ the system is suddenly exposed to high pressure gas that rapidly fills the upstream chamber. V_u and V_d are the upstream and downstream volumes, $p_u(t)$ and $p_d(t)$ are the upstream and downstream pressure changes as a function of time, $C(x,t)$ is the concentration profile within the membrane as a function of permeation distance x and time t and D, S and P are the membrane properties: diffusion coefficient, solubility and permeability, respectively.

$$\theta_u = -\frac{L^2}{3D} \tag{1}$$

$$\theta_d = \frac{L^2}{6D} \tag{2}$$

where L is the membrane thickness, D is the diffusion coefficient, and θ_u and θ_d are the upstream and downstream time lags, respectively.

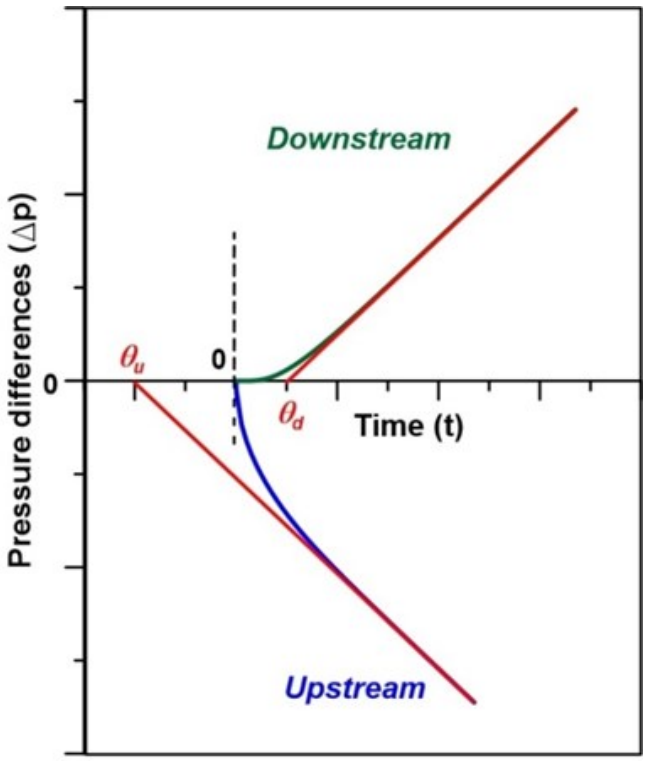

Figure 2.3 Schematic representation of the time lag determination from the upstream and downstream pressure difference curves.

The change in gas pressure in both chambers as a function of time is determined from the concentration gradients at their respective gas-membrane interfaces. Because the upstream interface of the membrane is subjected to a step change in the gas pressure, the concentration gradient at the upstream side of the membrane is initially steep compared to the concentration gradient observed at the downstream side of the membrane. To accurately extract membrane properties from the upstream pressure difference curve, it is important to predict as accurately as possible the concentration gradient at that interface. A numerical model was developed to simulate the gas permeation process and predict the concentration profile as a function of time. The derivative of the concentration profile at the interfaces leads to the calculation of the interface gradients, which in turn allows calculating the pressure change in the upstream and downstream chambers of known volumes as a function of time. The time lag can then be obtained. In this investigation, the finite difference method (FDM) is used to discretize the one-dimensional Fick's second law of diffusion

over the membrane into a number of finite thin slices and to solve numerically the partial differential equation to obtain the concentration profile of the gas permeating within the membrane.

In this paper, to support the experimental and numerical research program undertaken to determine the conditions under which the evaluation of the upstream and downstream time lags leads to better accuracy, numerical permeation experiments are performed to assess this precision. For quantifying this precision, simulation results for the prediction of concentration profiles, the concentration gradients at the two gas-membrane interfaces, the upstream and downstream pressure profiles and the time lag as a function of time were compared with benchmark analytical solutions. The paper is divided as follows. The benchmark analytical solutions for conventional boundary conditions are first presented, followed by a description of the various numerical schemes that have been investigated. Results of the various numerical studies are presented and discussed before concluding.

2.2 Analytical Solutions

A series of benchmark analytical solutions for the concentration profiles, the gradients at both interfaces, and the changes in pressures in the upstream and downstream volumes have been used to compare the different numerical schemes. These analytical solutions are presented in this section.

For the simplest case, the gas permeation via diffusion through the membrane follows Fick's second law of diffusion which allows representing the concentration $C(x, t)$ of the permeating species as a function of time (t) and position (x) via Eq. (3) where the diffusion coefficient (D) of the permeating gas within the membrane is assumed to be constant.

$$\frac{\partial C}{\partial t} = D \frac{\partial^2 C}{\partial x^2} \tag{3}$$

For deriving one of the benchmark solutions, the two chambers separating the membranes are initially under high vacuum such that the initial concentration throughout the membrane is equal to zero. The experiment starts when the upstream chamber is rapidly filled with the permeating species to reach a relatively high pressure which is maintained constant during the experiment. The permeating gas molecules start diffusing through the membrane and eventually emerge into the downstream chamber. The amount of the gas that accumulates in the downstream chamber is considered to be negligible so that the concentration of the gas at the permeate interface of the membrane is assumed to be zero during the experiment. Based on these assumptions, the initial condition (IC) and the two boundary conditions (BC1 and BC2) used to derive the analytical solution are given in Eq. (4).

$$\begin{aligned} &\text{IC: } C(x,0) = 0 && \text{(a)} \\ &\text{BC1: } C(0,t) = p_0 \cdot S && \text{(b)} \\ &\text{BC2: } C(L,t) = 0 && \text{(c)} \end{aligned} \qquad (4)$$

where C is the concentration of the permeating gas, p_0 is the constant pressure in the upstream chamber, S is the solubility of the membrane and L is the thickness of the membrane. The two boundary conditions are ideal boundary conditions for which it is possible to derive an analytical solution. The solution of Eq. (3) subjected to the initial and ideal boundary conditions of Eq. (4) can be obtained using the method of separation of variables and is given in Eq. (5) [4]. This equation gives the concentration profile as a function of time t and permeation distance x.

$$C(x,t) = p_0 S\left(1 - \frac{x}{L}\right) - \frac{2p_0 S}{\pi} \times \sum_{n=1}^{\infty} \frac{1}{n} \sin\left(\frac{n\pi x}{L}\right) \exp\left(-\frac{Dn^2\pi^2 t}{L^2}\right) \qquad (5)$$

The concentration profiles inside the membrane at five different times following a step change in the upstream pressure are presented in Fig. 2.4. Fig. 2.4 shows a steep variation in the concentration profile at the upstream boundary condition at small times. On the other hand, a smooth variation in concentration at the downstream boundary condition is observed. As the steady state is progressively established, the concentration

profile will assume a straight-line relationship as observed for the concentration profile at 80 s.

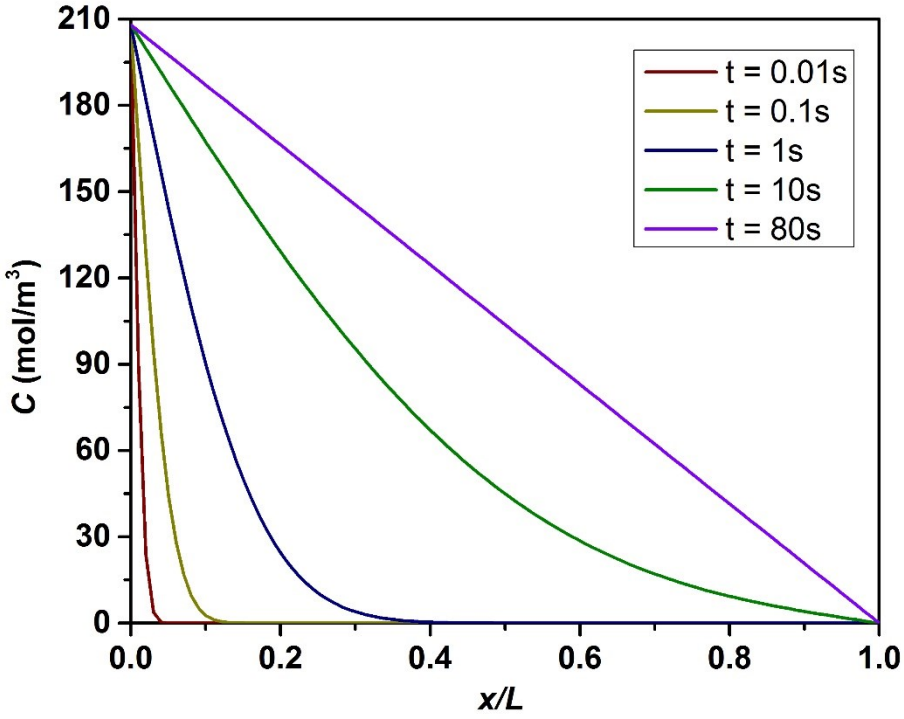

Figure 2.4 Concentration profiles inside the membrane for five different times following a step change in the upstream pressure. These concentration profiles were obtained using Eq. (5).

To determine the concentration gradients at both interfaces, the Fick's first law can be used where, as expressed by Eq. (6), the flux J is the negative of the product of the diffusivity and the gradient.

$$J = -D\frac{\partial C}{\partial x} \tag{6}$$

The benchmark analytical solutions for the gas fluxes at the upstream side ($x = 0$) and downstream side ($x = L$) of the membrane are evaluated using Eqs. (7) and (8), respectively:

$$J_u = J(0,t) = \frac{Dp_0S}{L} + \frac{2Dp_0S}{L} \times \sum_{n=1}^{\infty} \exp\left(\frac{-n^2\pi^2Dt}{L^2}\right) \tag{7}$$

$$J_d = J(L,t) = \frac{Dp_0S}{L} + \frac{2Dp_0S}{L} \times \sum_{n=1}^{\infty} \cos(n\pi) \exp\left(\frac{-n^2\pi^2 Dt}{L^2}\right) \quad (8)$$

To develop the analytical solutions for the concentration profile (Eq. (5)) and the mass fluxes at the interfaces (Eqs. (7) and (8)), it was necessary to use the boundary conditions given in Eq. (4). To determine the time lag, a pressure difference needs to be recorded in the upstream and/or downstream chambers such that the two boundary conditions of Eq. (4) are not perfectly satisfied. However, the pressure changes in both chambers are relatively small such that the deviations from the theoretical boundary conditions are relatively small and do not have a major impact on the determination of the time lag. As a result, the mass flux at the two interfaces are calculated with the prevalence of the two boundary conditions of Eq. (4) even if the two gradients at the interfaces would be in reality slightly different than the ones calculated with the assumptions of Eq. (4).

The pressures in the upstream and downstream chambers can be calculated by performing a simple mass balance in each chamber while integrating Eqs. (7) and (8) with time. The following expressions were derived for the upstream and downstream pressures as a function of time:

$$p(0,t) - p_0 = -\frac{ART}{V_u} \int_0^t J(0,t)\, dt \quad (9)$$

$$\Delta p_u = p(0,t) - p_0 = -\frac{p_0 ARTDS}{V_u L}\left[t + \frac{L^2}{3D} + \frac{2L^2}{\pi^2 D} \times \sum_{n=1}^{\infty}\left(\frac{-1}{n^2}\right) \exp\left(-\frac{Dn^2\pi^2 t}{L^2}\right)\right] \quad (10)$$

$$p(L,t) - 0 = \frac{ART}{V_d} \int_0^t J(L,t)\, dt \quad (11)$$

$$\Delta p_d = p(L,t) - 0 = \frac{p_0 ARTDS}{V_d L}\left[t - \frac{L^2}{6D} + \frac{2L^2}{\pi^2 D} \times \sum_{n=1}^{\infty} \frac{(-1)^{n+1}}{n^2} \exp\left(-\frac{Dn^2\pi^2 t}{L^2}\right)\right] \quad (12)$$

where $p(0, t)$ and $p(L, t)$ are the respective pressure at the upstream and downstream interfaces, p_u and p_d are the pressure decrease at the upstream interface and pressure

increase at the downstream interface, A is the area of the membrane and R is the gas constant.

At long permeation time ($t \cdot D/L^2 > 1$), the transient terms in Eqs. (10) and (12) become negligible and these equations reduce to the following two linear equations:

$$\lim_{t\to\infty} \Delta p_u = -\frac{p_0 ARTDS}{V_u L}\left(t + \frac{L^2}{3D}\right) \tag{13}$$

$$\lim_{t\to\infty} \Delta p_d = \frac{p_0 ARTDS}{V_d L}\left(t - \frac{L^2}{6D}\right) \tag{14}$$

The intercept of the linear portion of the pressure difference curves with the time axis (see Fig.2.3), obtained after a long permeation time, gives the upstream and downstream time lags. The time lags, evaluated from the pressure changes on both sides of the membrane, are directly proportional to the reciprocal of the membrane diffusion coefficient, as shown in Eqs. (1) and (2).

2.3 Numerical Solutions

2.3.1 Numerical solutions

The benchmark analytical solutions derived in the previous section under ideal boundary conditions can be used to evaluate the accuracy of the numerical solutions. The evaluation was performed for the following variables: concentration profiles, gradients at the interfaces, changes in the upstream and downstream pressures, and time lag. Eq. (3), subject to the initial and boundary conditions of Eq. (4), was solved numerically using finite differences [5]. The continuous domain of the membrane was discretized into a number of grid points and the Fick's second law of diffusion was approximated by finite differences for each of these grid points. For each point of the grid, it is therefore possible to write an algebraic equation to approximate the differential equation using Taylor's series expansion with respect to a change in time, Δt. For all grid points in the solution domain, Eq. (3) can be approximated as follows.

$$\frac{\partial C}{\partial t} = D\frac{\partial^2 C}{\partial x^2} \rightarrow \frac{C_x^{t+\Delta t} - C_x^t}{\Delta t} = D\frac{\partial}{\partial x}\left(\frac{\partial C}{\partial x}\right) = D\frac{\left(\frac{\partial C}{\partial x}\right)_{x+\frac{\Delta x_2}{2}} - \left(\frac{\partial C}{\partial x}\right)_{x-\frac{\Delta x_1}{2}}}{\frac{\Delta x_1}{2} + \frac{\Delta x_2}{2}} \qquad (15)$$

where Δx_1 and Δx_2 are the grid sizes upstream and downstream of the grid point located at x, respectively. For a uniform grid size, Δx_1 would be equal to Δx_2. The concentration profile can be obtained numerically via Eqs. (16) and (17) respectively, using an explicit or implicit numerical scheme. For the explicit scheme, the concentration can be calculated directly at time $t+\Delta t$ at every grid point whereas for the implicit scheme the concentration profile at time $t+\Delta t$ is obtained by solving a tridiagonal matrix [5]. For the explicit scheme, the Courant number [6] or dimensionless time increment $(D\Delta t / \Delta x_s^2)$ must be smaller than or equal to 0.5 to ensure numerical stability. Δx_s is smallest mesh size (in this investigation it corresponds to the first mesh size) for both the variable and uniform mesh schemes. The implicit scheme is unconditionally stable but in this investigation we have used the same criterion to select the integration time step. In addition, the Crank-Nicolson algorithm [5], which is a combination of explicit and implicit algorithms, was also implemented.

$$C_x^{t+\Delta t} = C_x^t + 2D\Delta t\left(\frac{C_{x+\Delta x_2}^t - C_x^t}{\Delta x_2\left(\Delta x_1 + \Delta x_2\right)} - \frac{C_x^t - C_{x-\Delta x_1}^t}{\Delta x_1\left(\Delta x_1 + \Delta x_2\right)}\right) \qquad (16)$$

$$\left(-\frac{2D\Delta t}{\Delta x_1\left(\Delta x_1 + \Delta x_2\right)}\right)C_{x-\Delta x_1}^{t+\Delta t} + \left[1 + \frac{2D\Delta t}{\Delta x_1 \Delta x_2}\right]C_x^{t+\Delta t} + \left(-\frac{2D\Delta t}{\Delta x_2\left(\Delta x_1 + \Delta x_2\right)}\right)C_{x+\Delta x_2}^{t+\Delta t} = C_x^t \qquad (17)$$

Eqs. (16) and (17) are valid for all interior grid points. To satisfy the two boundary conditions, Eqs. (18) (a) and (b) are used for the first and last grid points, respectively.

$$\begin{array}{lll} (x=0) & C_0^t = p_0 S & \text{(a)} \\ (x=L) & C_L^t = 0 & \text{(b)} \end{array} \qquad (18)$$

The concentration gradients at both surfaces of the membranes are calculated from the concentration profile using Eqs. (19) and (20).

$$G_u = \frac{C(\Delta x_1, t) - C(0,t)}{\Delta x_1} \tag{19}$$

$$G_d = \frac{C(L,t) - C(L - \Delta x_{N-1}, t)}{\Delta x_{N-1}} \tag{20}$$

where N is the number of grid points in the solution domain. The pressure differences are calculated from the gradient on both sides of the membrane via Eqs. (21) and (22) where T is the absolute temperature, G_u and G_d are the upstream and downstream concentration gradients, V_u and V_d are the upstream and downstream volumes of the chambers and n is the number of time increments Δt for which the simulation was run.

$$\Delta p_u = \sum_{i=1}^{n} \frac{DART\Delta t}{V_u} G_{ui} \tag{21}$$

$$\Delta p_d = \sum_{i=1}^{n} \frac{DART\Delta t}{V_d} G_{di} \tag{22}$$

2.3.2 Numerical schemes for variable mesh sizes

Since the gradient at upstream interface of the membrane is steep, especially at a short permeation time, it is desired to resort to a relatively small mesh size at this interface to predict accurately the concentration gradient. In this investigation, both uniform and variable mesh sizes were used. For the scheme with variable mesh size, a number of uniform grid sizes at the two membrane boundaries were transformed into a number of progressively increasing mesh sizes starting with a small mesh size at the surface. Fig. 2.5 shows one of the variable mesh schemes that were used in this study where 3 uniform mesh sizes were converted into 10 variable mesh sizes.

To obtain an exponentially increasing mesh size, a multiplication factor was defined for each variable mesh scheme such that the smallest mesh point at the boundary is progressively increased until the uniform central mesh size is obtained. The uniform mesh size is then used for all the other interior points. For the variable mesh scheme illustrated in Fig. 2.5, the factor to convert the 3 uniform mesh sizes into 10 variables mesh is 1.311129915. The size of the first mesh is calculated using Eq. (23) where the uniform

mesh size (=$L/(N_0 - 1)$) is divided by the factor to the 10th power. N_0 is the number of grid points used with a uniform mesh size.

$$\Delta x_1 = \frac{L}{(N_0 - 1) \times Factor^{10}} \tag{23}$$

The sizes of the subsequent variable meshes are calculated using Eqs. (24) and (25) for the upstream and downstream boundaries, respectively.

$$\Delta x_i = \Delta x_{i-1} \times Factor \qquad (2 \le i \le 10) \tag{24}$$

$$\Delta x_i = \frac{\Delta x_{i-1}}{Factor} \quad (i \ge (N_0 - 1) + 2(N_2 - N_1) - 10) \tag{25}$$

Three different factors were tested in this investigation and their values are given in Table 2.1 In Eqs. (23) and (25), N_0 represents the original number of mesh points in a uniform grid. N_1 represents the number of uniform mesh sizes that were converted into N_2 variable mesh sizes. The number of grid points will therefore increase from N_0 to N_0+2(N_2 - N_1) when a variable grid scheme is used. For both mesh schemes, the total number of mesh points will be denoted N.

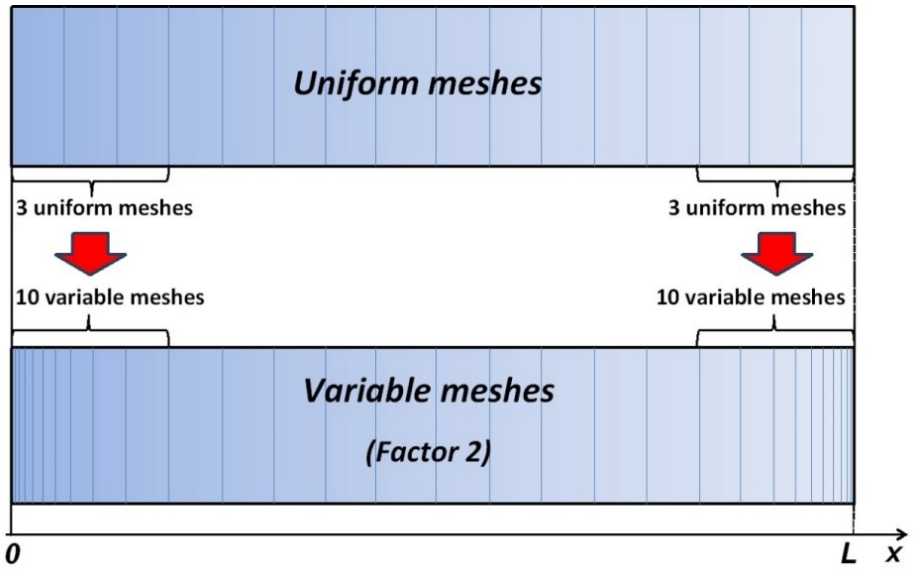

Figure 2.5 Schematic illustration of the transformation of a uniform mesh into a variable mesh with Factor 2.

It is important to reiterate that in practice, the upstream and downstream pressure changes cannot be observed under ideal boundary conditions (Eq. (4)) and analytical solutions are only available under these ideal conditions. However, in this investigation, these ideal boundary conditions were used to estimate the pressure changes that would occur in the upstream and downstream chambers. Since the changes in pressures for real boundary conditions are usually small, errors associated with these ideal boundary conditions are also small. The concentration profiles, concentration gradients, pressure differences and time lags calculated numerically were compared with the analytical benchmark solutions and average percentage errors were calculated to determine the accuracy of various numerical schemes. The numerical scheme was then used to gain a deeper understanding of the time lag method.

Table 2.1 Factors used in variable mesh schemes. N_1 is the number of uniform mesh sizes converted into N_2 variable mesh sizes.

Factor	**Factor 1**	**Factor 2**	**Factor 3**
Factor	1.490777275	1.311129915	1.150984101
N_1	2	3	5
N_2	10	10	10

2.4 Results and Discussion

In this investigation, analytical calculations and numerical simulations were performed under typical laboratory operating conditions that were used in actual experimental membrane tests. The typical experimental parameters are listed in Table 2.2

Table 2.2 Simulation conditions and membrane system parameters.

Parameter		Value	Units
Operating conditions	Temperature T	273.15	K
	Operating pressure p_0	689 (100)	kPa (psi)
Membrane properties	Membrane solubility S	2.74×10^{-4}	mol/(m^3 Pa)
	Membrane diffusivity D	4.52×10^{-12}	m^2/s
	Membrane thickness L	$23.5x10^{-6}$	m
	Membrane area A	0.00125	m^2
Membrane system parameters	Upstream volume V_u	9.68×10^{-5}	m^3
	Downstream Volume V_d	9.68×10^{-5}	m^3

2.4.1 Concentration profiles

Fig. 2.6 presents the dimensionless average percentage error for the prediction of the concentration profiles as a function of the number of mesh points. In Fig. 2.6, results are presented for both uniform and variable (Factor 2) schemes using both explicit and implicit finite difference methods. The dimensionless concentration percentage average error $\varepsilon(C)$, calculated using Eq. (26), corresponds to the average error for the prediction of the concentration profiles for all mesh points (N) and m different times. In the present investigation, m was equal to 8 which corresponds to the times the numerical and analytical solutions were compared which, in this investigation, the comparison was performed each 10 s up to 80 s. Superscript A in Eq. (26) designates the evaluation with the analytical solution (Eq. (5)).

$$\varepsilon(C) = \frac{\sum_{i=1}^{N}\sum_{j=1}^{m}\left|C_{ij} - C_{ij}^{A}\right|^2}{N\times m}\times\frac{100\%}{S\cdot p_0} \tag{26}$$

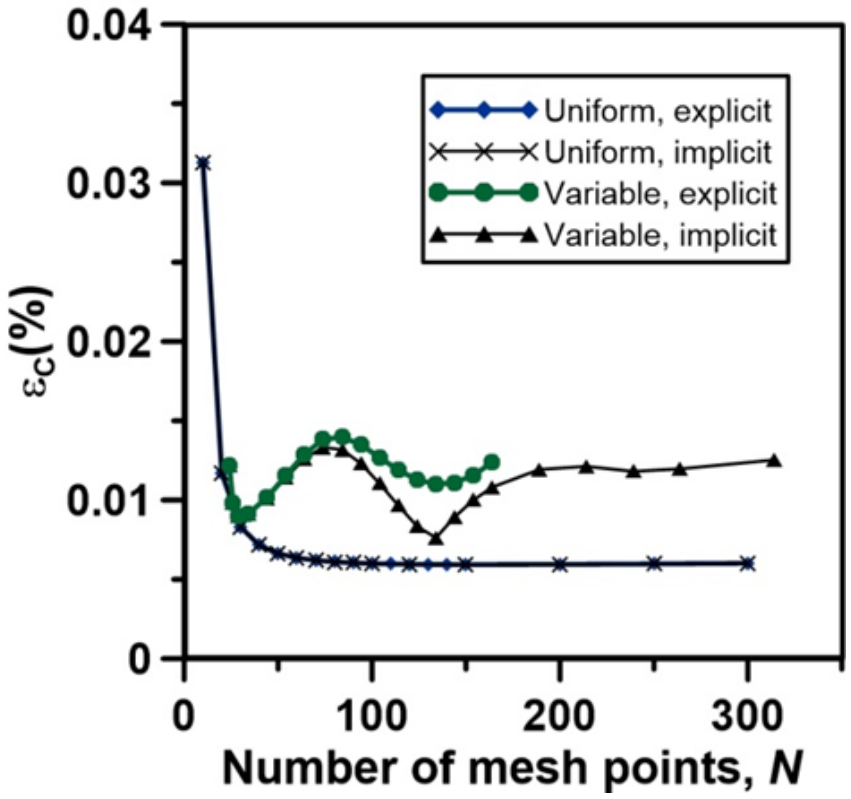

Figure 2.6 Dimensionless percentage average error $\varepsilon(C)$ of the concentration profiles versus the number of mesh points (N). An integration time step of 0.00001 s was used for both explicit and implicit methods and for uniform and variable mesh (Factor 2) schemes.

Results of Fig. 2.6 clearly show that the concentration profiles are obtained accurately with an average percentage error of less than 0.015% when the number of mesh points is larger than about 25. For the prediction of the concentration profiles, both the explicit and implicit finite difference schemes lead to small errors with slightly better predictions obtained with the implicit scheme. Similar results were obtained with the Crank-Nicolson algorithm where the error was always between the explicit and implicit methods. Since no benefits using the Crank-Nicolson algorithm were observed, only the explicit and implicit methods were considered in this investigation. In addition, results were identical for the uniform and variable mesh size. It can be safely stated that the numerical scheme used in this investigation led to accurate concentration profile

predictions and that it can be used with confidence for other problems for which analytical solutions do not exist or were not yet derived.

2.4.2 Concentration gradients

Fig. 2.7 and Fig. 2.8 present the plots of the upstream and downstream gradient percentage errors evaluated at three different times: 2, 4 and 10 s. The gradients were computed numerically (Eqs. (19) and (20)) and compared with the analytical gradients in order to determine the error in its prediction as defined by Eqs. (27) and (28)

$$\varepsilon\left(G_u\right)=\frac{G_u^A-G_u}{G_u^A}\times 100\% \tag{27}$$

$$\varepsilon\left(G_d\right)=\frac{G_d^A-G_d}{G_\infty^A}\times 100\% \tag{28}$$

where G_u and G_d are the upstream and downstream gradients, respectively. Superscript A designates the analytical solution. Since the downstream gradient is initially zero, the steady-state analytical gradient was used in Eq. (28) to avoid dividing by zero or by an extremely small number.

Results for the upstream gradient (Fig. 2.7) obtained with a uniform mesh size show a progressively decreasing percentage error starting with 10 grid points with relatively high percentage error values of 4.915%, 2.395% and 0.953% at 2, 4 and 10 s, respectively. As the number of grid points increases, the percentage error becomes small and reaches a value below 0.013% when the number of mesh points is 300. The percentage error in the case of the variable mesh size starts with relatively small negative values of -0.437%, -0.402% and -0.067% evaluated at 2, 4 and 10 s, respectively. The percentage errors then decrease to cross the zero-error line and to assume small positive percentage errors before progressively decreasing to small percentage errors as the number of mesh points is increased. For a number of mesh points greater than 100, both uniform and variable mesh schemes lead to small percentage errors. The insert in Fig. 2.7 shows that the percentage

errors are slightly smaller for a uniform mesh size when a higher number of mesh points is used and times larger than 2 s.

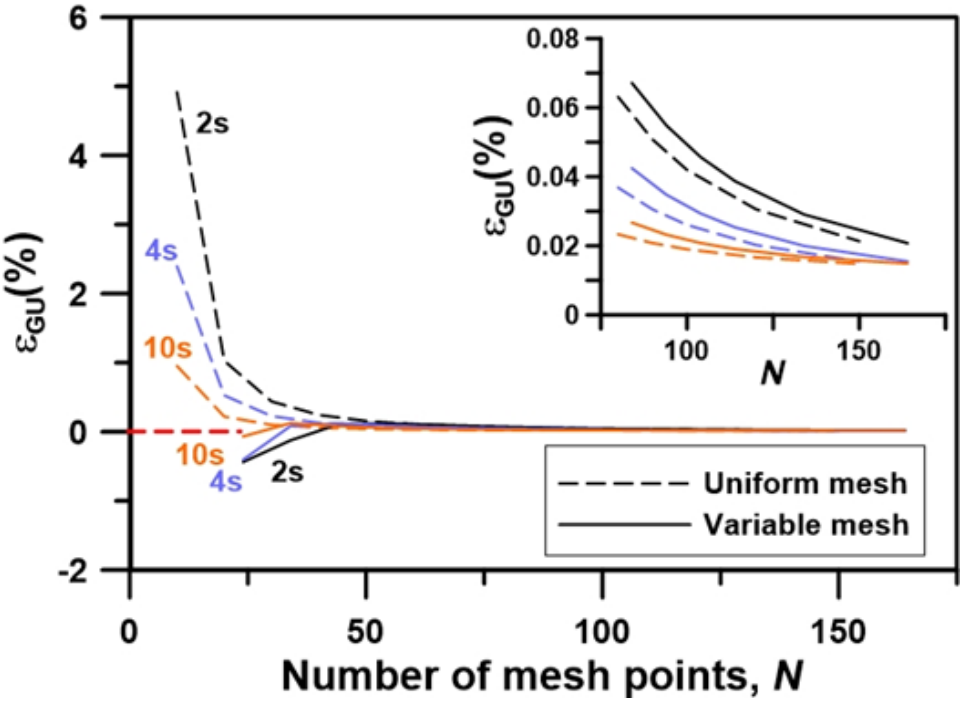

Figure 2.7 Upstream gradient percentage error $\varepsilon(G_u)$ versus the number of mesh points (N) with an integration time step of 0.00001 s and at 2, 4 and 10 s for uniform and variable mesh schemes.

Results for the downstream gradient (Fig. 2.8) obtained with a uniform and a variable mesh size show a progressively decreasing percentage error as the number of mesh points is increased. For the downstream gradient, the percentage error for the variable mesh size is slightly higher than for the uniform mesh size. The use of a variable mesh size for the downstream side of the membrane is therefore not required. The percentage prediction error for the downstream gradient is extremely low for small simulation times because the permeating gas has not yet emerged from the membrane. At higher times, the downstream gradient becomes more pronounced and approaches the steady-state analytical gradient (G_∞^A). For all simulation times, the percentage errors were always below 0.02% for a number of mesh points of 150 or more.

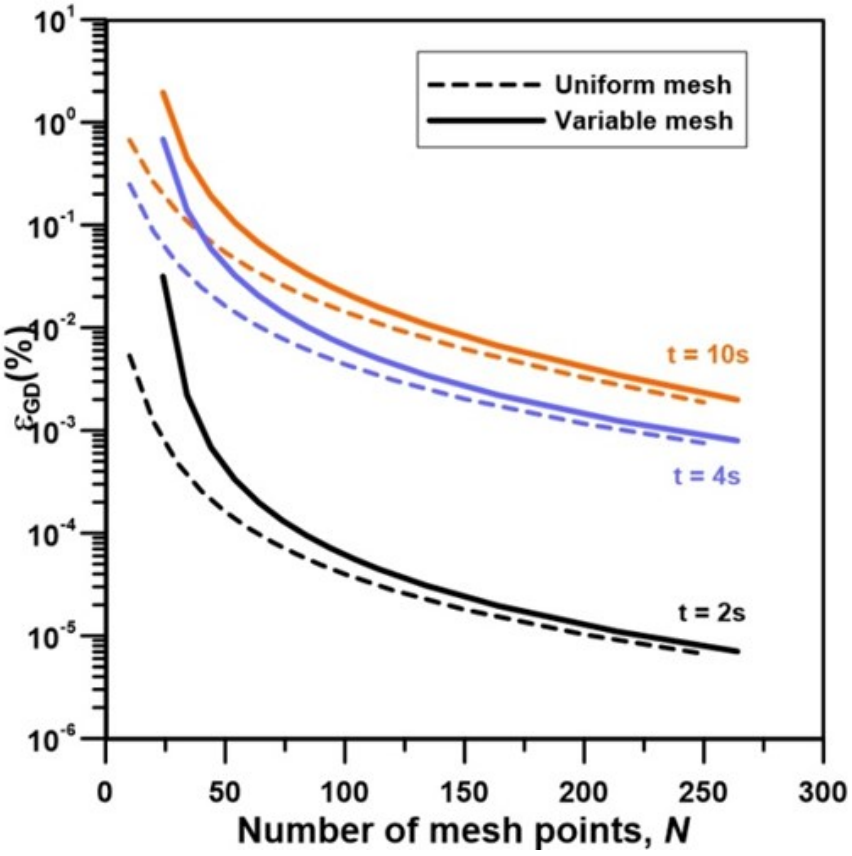

Figure 2.8 Downstream gradient percentage error ($\varepsilon(G_d)$) versus the number of mesh points (N) with an integration time step of 0.00001 s and at 2, 4 and 10 s for uniform and variable mesh schemes.

2.4.3 Pressure changes

With the instantaneous values of the gradients being calculated at the membrane boundaries, it is possible to determine the pressure changes in the upstream and downstream chambers using Eqs. (21) and (22). Fig. 2.9 presents the plots of the upstream pressure decay percentage error at 10 and 80 s. The pressure decay is computed with the results of the implicit finite difference method and the pressure decay relative percentage error equation is calculated by comparing the analytical and numerical values using Eq. (29).

$$\varepsilon\left(\Delta p\right)=\frac{\Delta p^{A}-\Delta p}{\Delta p^{A}}\times 100\% \tag{29}$$

Results show that the upstream pressure decay percentage error for both uniform and variable meshes decreases steadily with an increase in the number of mesh points. For a given number of mesh points, the percentage error is smaller by an order of magnitude when a variable mesh size is used. Since the change in pressure is the integration of the permeating gas flux at the interface, any error in the determination of the gradient will progressively accumulate as a function of time. The insert of Fig. 2.7 shows that for a sufficiently large number of mesh points, smaller positive percentage prediction errors were observed for a uniform mesh point for simulation time greater than 2 s. To better explain the significant difference observed between the uniform and variable mesh sizes of Fig. 2.9, it is important to examine the percentage errors of the upstream gradient at short permeation time where the upstream gradient is the steepest (Fig. 2.4). Fig. 2.10 presents the variation of the percentage error of the upstream gradient for short permeation times. It is clear from this graph that the gradient percentage error for the variable mesh size is much smaller at short permeation time and decreases by two orders of magnitude in the first 0.5 s. The difference observed in Fig. 2.9 between the uniform and variable mesh sizes is mainly due to the integration performed at early time and this difference persists for larger time. This is certainly for the upstream pressure change that the use of variable mesh points takes all its importance.

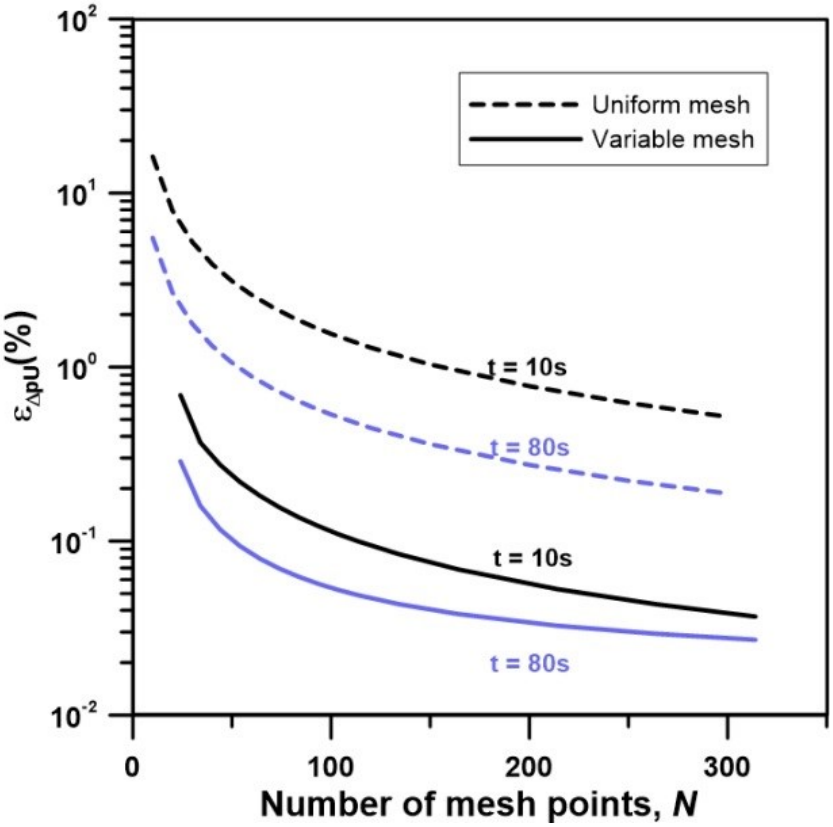

Figure 2.9 Upstream pressure decay percentage error ($\varepsilon(\Delta P_u)$)versus the number of mesh points (N) with an integration time step of 0.00001 s and at 10 s and 80 s for uniform and variable mesh schemes.

The percentage error for the downstream pressure change as a function of the number of mesh points is presented in Fig. 2.11. In general, regardless of the number of mesh points and the permeation time, the percentage error for the downstream pressure change is similar for the uniform and variable mesh schemes. For a number of mesh points greater than 120 and a shorter permeation time (10 s), the pressure change is over-predicted by approximately 0.09% and the error decreases with an increase in the number of mesh points. On the other hand, at a longer permeation time (80 s) and N = 120, the pressure change is under-predicted by roughly 0.01%. For both upstream and downstream pressure differences, the errors are relative percentage errors.

However, if the absolute errors were considered instead of the relative errors, results would show that the error accumulates with time. For instance, for a variable scheme with 150 mesh points, the absolute error at 10 s is 0.525 Pa while the error at 80 s is 0.548 Pa whereas for a uniform scheme with 164 mesh points, the absolute error at 10 s is 0.035Pa while the error at 80 s is 0.058 Pa. These results clearly show the importance of using a variable mesh scheme to capture adequately the concentration gradient at the upstream interface and that the absolute error strongly depends on the prediction error occurring at a short time where the concentration gradient is steep.

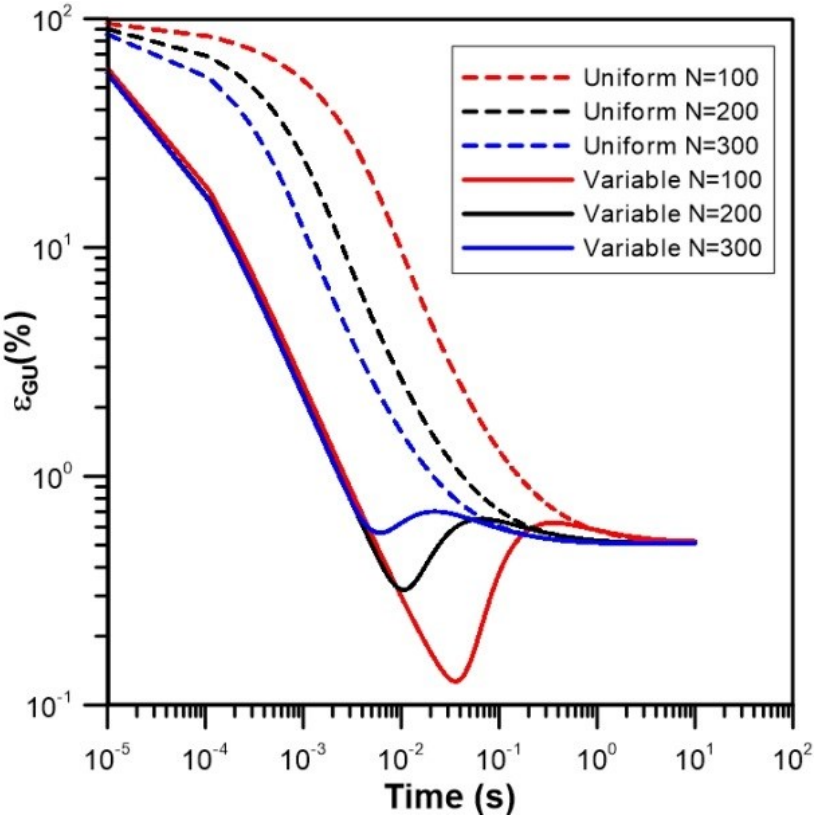

Figure 2.10 Upstream gradient percentage error $\varepsilon(\Delta G_u)$ versus time (s) at the first 10 seconds with an integration time step of 0.000001 *s* and the number of mesh points (*N*) of 100, 200 and 300 for uniform and variable mesh schemes.

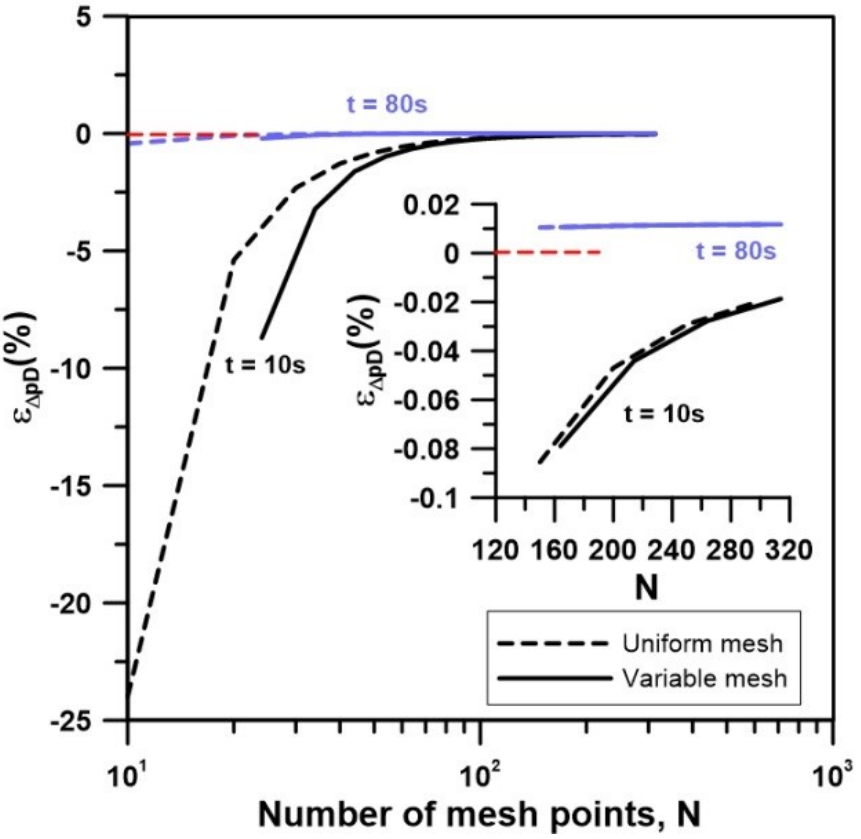

Figure 2.11 Modified downstream pressure decay percentage error $\varepsilon(\Delta P_d)$ versus the number of mesh points (N) with an integration time step of 0.00001 s and at 10 and 80 s for uniform and variable mesh schemes.

2.4.4 Time lags

Fig. 2.12 and 2.13 show the plots of the upstream and downstream time lag percentage errors as a function of the number of mesh points, respectively. The evaluation of the time lag, that is the extrapolation of the linear portion of the pressure curve as a function of time, was performed at a permeation time of 190 s. The time lag is computed with the implicit finite difference method and the percentage time lag prediction error is calculated via Eq. (30).

$$\varepsilon(\theta) = \frac{\theta^A - \theta}{\theta^A} \times 100\% \qquad (30)$$

Fig. 2.12 shows that the percentage error of the upstream time lag is strongly influenced by the mesh scheme used to solve the problem. For a greater accuracy in the determination of the time lag, it is important to use a variable mesh scheme to capture the steep gradient at early permeation times because the determination of the time lag relies strongly on total upstream pressure change which results from the integration of the permeation flux at the upstream interface. Variable mesh schemes V1, V2 and V3 correspond to variable mesh scheme using Factors 1, 2 and 3, respectively. It appears that the variable mesh size with Factors 1 or 2 lead to good results. Simulations presented in Fig. 2.12 with Factor 2 for short permeation times, were also performed for Factors 1 and 3. Results (not shown) were nearly identical for Factors 1 and 2 but significantly better that those for Factor 3 and uniform mesh. Since the smallest mesh size for Factor 1 is significantly smaller than for Factor 2, the time step needs also to be smaller which leads to higher computation time. Factor 2 was therefore used for most results presented in this investigation.

For the downstream time lag, results of Fig. 2.13 show that the percentage time lag prediction error is a function of the number of mesh points, but unlike the upstream time lag, the uniform mesh size is slightly better than the variable mesh size, but the difference is rather insignificant. The reason for the insignificant difference is the smooth concentration profile for the downstream interface. The accuracy of the time lag stabilizes to a percentage error of less than 0.015% for a number of mesh points greater than 150.

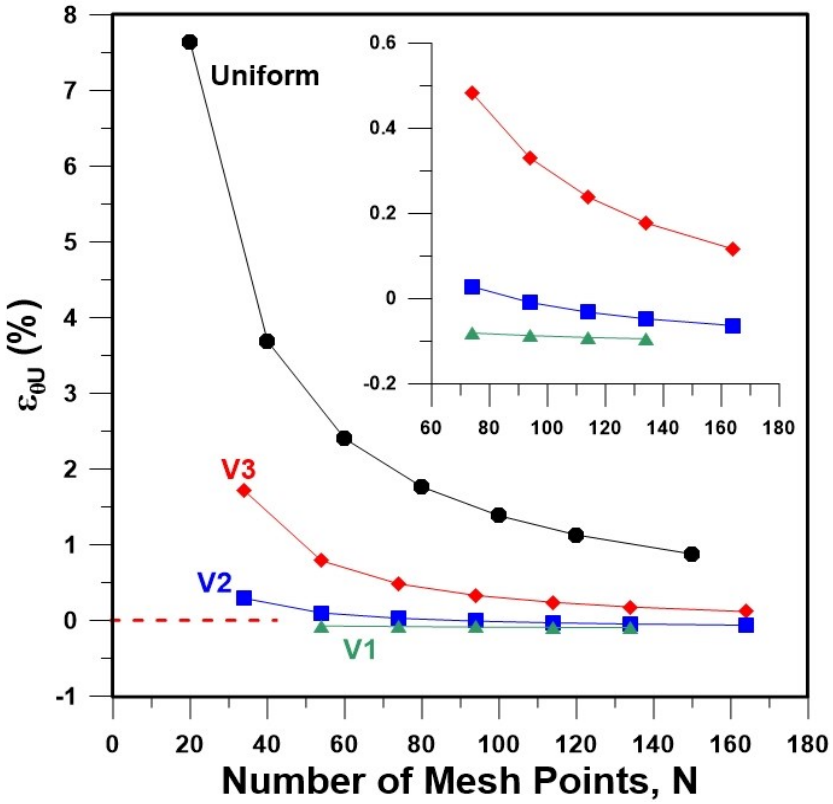

Figure 2.12 Upstream time lag prediction error ($\varepsilon(\theta_u)$) versus the number of mesh points (N) with an integration time step of 0.00001 s for uniform and variable mesh (with different factors) schemes. Time lag was evaluated at 190 s.

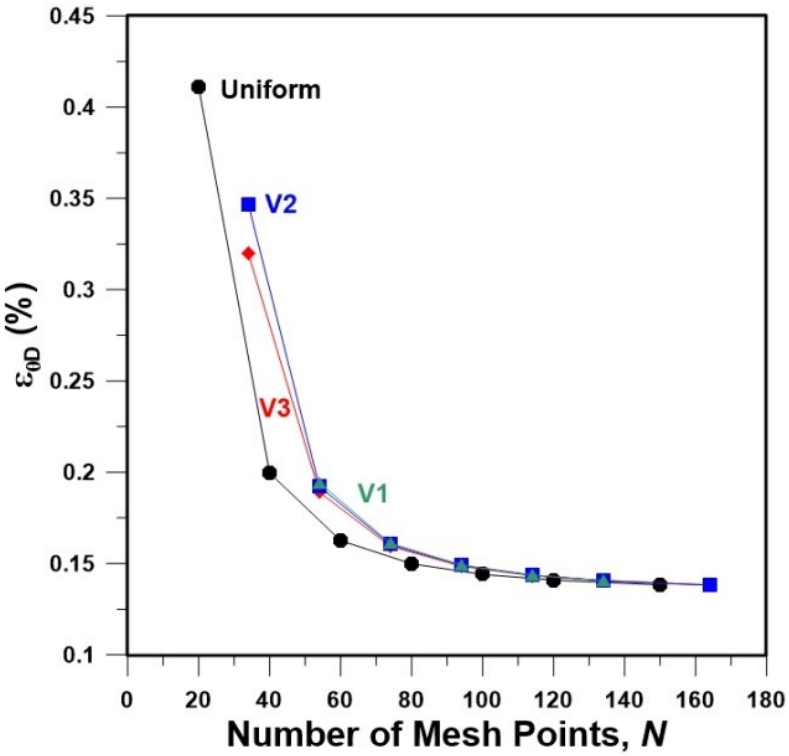

Figure 2.13 Downstream time lag error $\varepsilon(\theta_d)$ versus the number of mesh points (N) with an integration time step of 0.00001 s for uniform and variable mesh (with different factors) schemes. Time lag was evaluated at 190 s.

2.4.5 Computation time

Fig. 2.14 presents the magnitude of dimensionless percentage average error $\varepsilon(C)$ for the concentration profile within the membrane as a function of the integration time step to study the accuracy of the numerical method with respect to the time step. Results clearly show that for the range of time steps that was investigated, the percentage error is small in all cases. However, for a greater accuracy, a time step of 0.00005 s could be chosen as an optimal value and a compromise between accuracy and computation. Indeed, using a smaller time step would only lead to greater computation time and not to a greater accuracy.

Fig. 2.15 presents an analysis to determine the computation time as a function of the number of mesh points. The computation time increases linearly with the number of mesh points. Comparing the two numerical methods, the implicit method with the same

time step required a larger computation time than the explicit method because it is required to solve at each time step the resulting tridiagonal matrix. Since the explicit finite difference led most of the time to a similar accuracy and it requires much less computation time, it is recommended to use explicit finite differences to solve the type of problems encountered in this investigation.

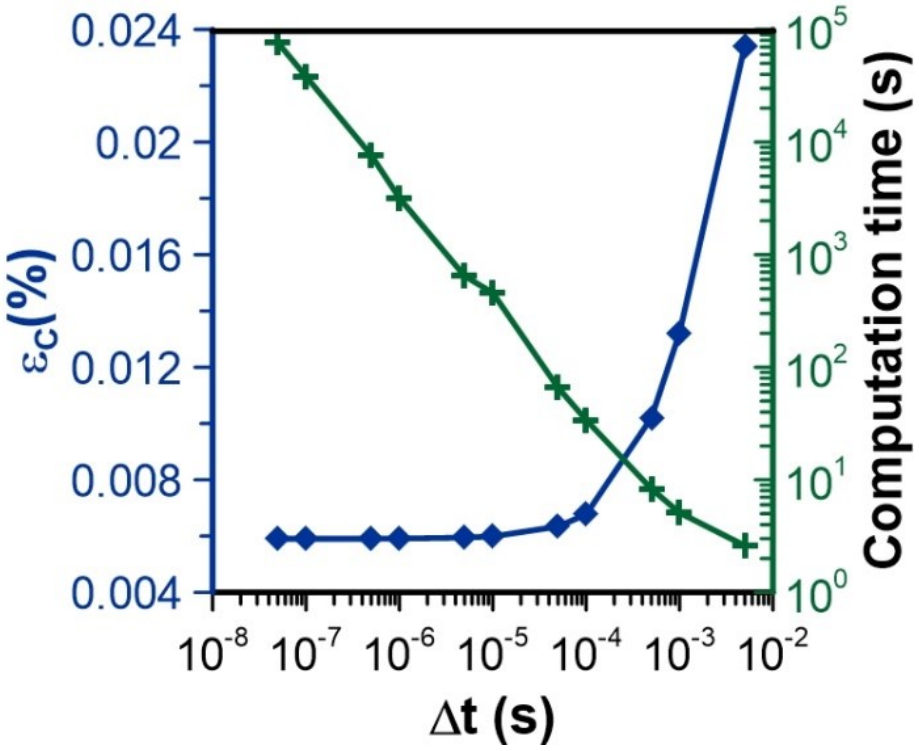

Figure 2.14 The average percentage error $\varepsilon(C)$ of the concentration profiles versus the size of the integration time step with a uniform mesh scheme and a number of mesh points $N = 100$ and the corresponding computation time for each experiment.

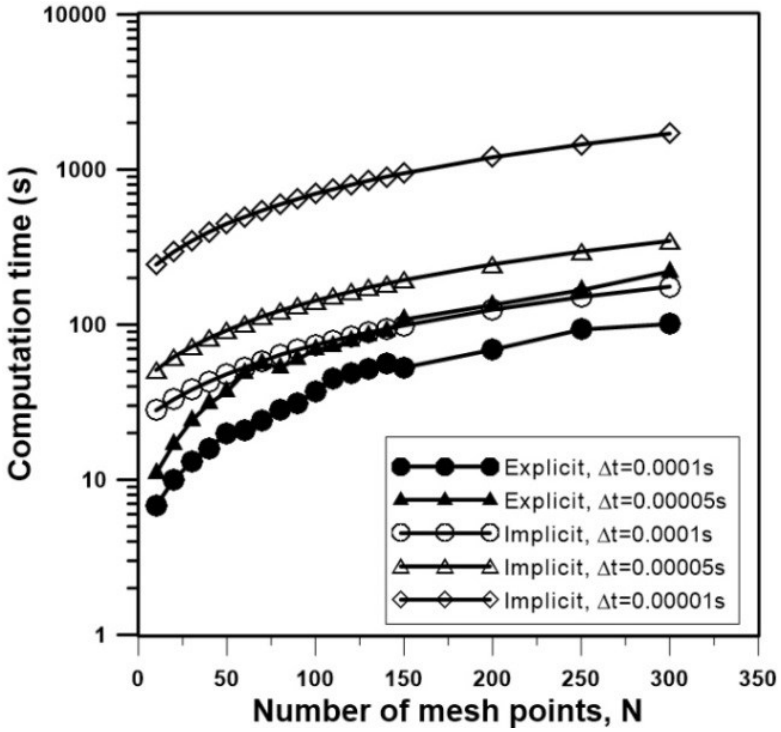

Figure 2.15 Computation times for different mesh points and for explicit and explicit schemes with uniform mesh size and simulation time of 80 s. Computer and processor used are Dell OptiPlex 780 and Intel Core 2 Duo E8400 (3.00 GHz), respectively.

2.5 Conclusion

Results have shown that the concentration profiles can be solved accurately regardless of the finite difference scheme used to solve the Fick's second law of diffusion. The concentration gradients obtained with a uniform mesh scheme can predict the downstream time lag with a good accuracy. However, to predict the upstream time lag, using a variable mesh size to have a small mesh size at the interface is required. Results have shown that the gradient percentage errors obtained with a variable mesh size are significantly smaller that the gradients percentage errors obtained with a uniform mesh size, especially at earlier permeation time when the gradient is steep. Since the pressure change is the time-integration of the flux at the interface, the prediction errors on the gradients have a major impact on the upstream pressure difference curve from which the time lag is

evaluated. Results have shown that a variable mesh scheme where the first three uniform mesh sizes are transformed into 10 variable meshes (Factor 2) is a good compromise between accuracy and computation time.

This investigation has also allowed showing that both explicit and implicit finite difference schemes led to similar results. It is recommended to use an explicit scheme because of lower computation time for the same accuracy. However, the implicit scheme would be advantageous over the explicit method when 1) the time interval is too large for the explicit method to remain stable; 2) solving "stiff" initial value/boundary value problems and 3) solving nonlinear problems where stability criteria are sensitive to nonlinearity. Crank-Nicolson algorithm [5] was also tested and the accuracy was found to be between the explicit and implicit schemes.

It is concluded that the numerical scheme used in this investigation can be used with confidence to solve problems with various boundary conditions and for systems where nonlinear diffusive behaviour is observed.

2.6 Nomenclature

A	Membrane area, m^2
C	Permeating gas concentration, mol/m^3
D	Diffusion coefficient, m^2/s
G_A	Analytical concentration gradient, $mol/(m \cdot m^3)$
	Steady-state analytical concentration gradient, $mol/(m \cdot m^3)$
G_u	Upstream concentration gradient, $mol/(m \cdot m^3)$
G_d	Downstream concentration gradient, $mol/(m \cdot m^3)$
J	Flux, $mol/(m^2 \cdot s)$
L	Membrane thickness, m
n	Number of time increments

N	Total number of mesh points for both uniform and variable mesh schemes
N_0	Number of original uniform mesh sizes before conversion to variable mesh
N_1	Number of uniform mesh sizes converted to variable mesh sizes
N_2	Number of converted variable mesh sizes from uniform mesh sizes
p_A	Analytical pressure change, kPa
p_0	Constant pressure in the upstream chamber, kPa
p_u	Upstream pressure, kPa
p_d	Downstream pressure, kPa
P	Permeability, mol·m/(m^2·Pa·s)
R	Universal gas constant, J/(K·mol)
S	Solubility, mol/(m^3 Pa)
t	Simulation time, s
T	Absolute temperature, K
V_u	Upstream volume, m^3
V_d	Downstream volume, m^3
x	Permeation distance, m
ε	Error between analytical results and numerical results
Δt	Simulation time step, s
Δx_1	Grid size upstream of the grid point located at x, m
Δx_2	Grid size downstream of the grid point located at x, m

Δx_s First and smallest mesh size for both the variable and uniform mesh schemes.

Δp_u Upstream pressure decrease, kPa

Δp_d Downstream pressure increase, kPa

θ_A Analytical time lag, s

θ_u Upstream time lag, s

θ_d Downstream time lag, s

2.7 References

[1] P. Bernardo, and G. Clarizia, "30 Years of Membrane Technology for Gas Separation," Chemical Engineering Transactions, vol. 32, pp. 1999-2004, 2013.

[2] H.A. Daynes, "The process of diffusion through a rubber membrane", Proceedings of the Royal Society of London., vol. 97A, pp. 286-307, 1920.

[3] R. Barrer, and E. Rideal, "Permeation, diffusion and solution of gases in organic polymers," Transactions of the Faraday Society, vol. 35, pp. 628-643, 1939.

[4] S.W. Rutherford, and D.D. Do, "Review of time lag permeation technique as a method for characterisation of porous media and membranes", Adsorption, vol. 3, pp. 283-312, 1997

[5] B. Carnahan, H.A. Luther, and J. O. Wilkes, Applied numerical methods, New York, USA: Wiley, 1969.

[6] A. Iserles, A first course in the numerical analysis of differential equations. No. 44. Cambridge University Press, 2009.

Chapter 3

Impact of Measuring Devices and Data Analysis on the Determination of Gas Membrane Properties

Haoyu Wu, Boguslaw Kruczek and Jules Thibault*

Abstract

The time-lag method, using a gas permeation experiment, is the currently the most popular method for determining the membrane properties: diffusivity coefficient and permeability coefficient and from which the solubility coefficient can be calculated. In this investigation, the impact of systematic, random (noise), resolution and extrapolation errors associated with gas permeation experiments on the determination of the membrane properties using the time-lag method is investigated. A comprehensive error analysis for each type of errors and their combination is presented. Random and resolution errors have a greater impact on the determination of the time lag for low rates of downstream pressure accumulation which can be alleviated by increasing the capacity parameter. Increasing the feed pressure lowers the resolution errors, but has no effect on random errors. Extrapolation errors associated with the time-lag method, which increase with time, can be reduced by increasing the number of evaluation points and the length of the evaluation window. Because of their strong correlation, it is difficult to decouple solubility and diffusivity coefficients accurately without using the time-lag. A judicious balance between data precision, the drop in the driving force and the duration of an experiment must be considered in the design of a constant-volume membrane system and in the selection of experimental operating conditions to minimize the impact of pressure variability. The necessity of a small capacity parameter for the accurate determination of membrane properties needs to be reconsidered in the presence of experimental noise.

Keywords: Gas Membrane Characterization; Time-lag; Pressure Transducer; Data Variability; Nonlinear Least Squares

Publication status: Journal of Membrane Science and Research, 4(2018) 4-14

***Corresponding author**

3.1 Introduction

Although significant progress has been made to extend the "upper bound" of membrane performance, i.e. the well-known permeability-selectivity trade-off, the main obstacle for a wider implementation of membrane technology is the lack of high-performance membrane materials [1-3]. To delve the causes and to overcome this challenge, studies on the relationships between the dynamics of penetrant transportation inside a membrane and their transport properties are of primary importance. The time-lag method, developed by Daynes [4] and Barrer [5], is commonly used in membrane characterization as an integral approach [6]. However, measurement errors by time-lag method was reported from literature [7]; the graphical determination of the time lag from experimental pressure data lacks accuracy and repeatability [8-10]. The use of personal computers in data acquisition and analysis [10-12] has significantly improved the methods of analysis and relative accuracy [13,14]. Personal computers allow researchers to plot the whole set of pressure data during the span of an experiments instead of relying only on a small portion of the data points at steady state. Nevertheless, a detailed discussion on errors caused by digital devices and computer software as well as the impact of experimental conditions and experimental data analysis on the level of errors is rarely found in the literature. The objective of this investigation is to bring greater awareness to researchers and practitioners in the field of membranes that the disagreement reported for some homogeneous membrane properties [15-18] could be the result of noise affecting the membrane characterization method. In existing literature [16, 19-21], noise affecting experiments or data analysis was either ignored or only mentioned qualitatively. This paper attempts to provide a comprehensive and quantitative analysis on the effect of noise and other experimental errors in the determination of membrane properties. Another objective was to assess the many sources of potential errors in automated constant-volume membrane permeation

systems and to discuss the impact of experimental conditions and experimental data analysis on these errors and their implication on the determination of the membrane time lag and membrane properties.

Gas permeation experiments are typically conducted in a constant volume (CV) membrane system [20, 22] which consists of two fixed-volume compartments separated by a membrane cell module. The system is normally evacuated prior to each experiment. The permeation process is initiated by performing a step change in the gas pressure at the upstream side of the membrane. The progressive permeation of the gas through the membrane leads to a pressure accumulation at the downstream side of the membrane which is recorded via a high precision absolute pressure transducer. The volume of the upstream compartment is typically large to ensure a constant feed pressure during the experiment, whereas the volume of the downstream compartment, which is generally smaller than that of the upstream compartment, represents a compromise between maintaining a relatively constant downstream pressure during the experiment and the sensitivity of the pressure transducer. Fig. 3.1 illustrates a typical downstream pressure rise curve plotted versus time and how the downstream time lag (θ_d) is estimated by extrapolating a linear portion of the pressure rise curve to the time axis. The extrapolation requires selecting a proper length of an evaluation time window (W) and a number of evaluation points (NP). Typically, the evaluation should be performed at least after 3-4 times the actual time lag to ensure that the permeation process has come to quasi steady-state [23-27]. However, in this investigation, the extrapolations are performed using a personal computer throughout an experiment to access the propagation magnitude and trend of the errors.

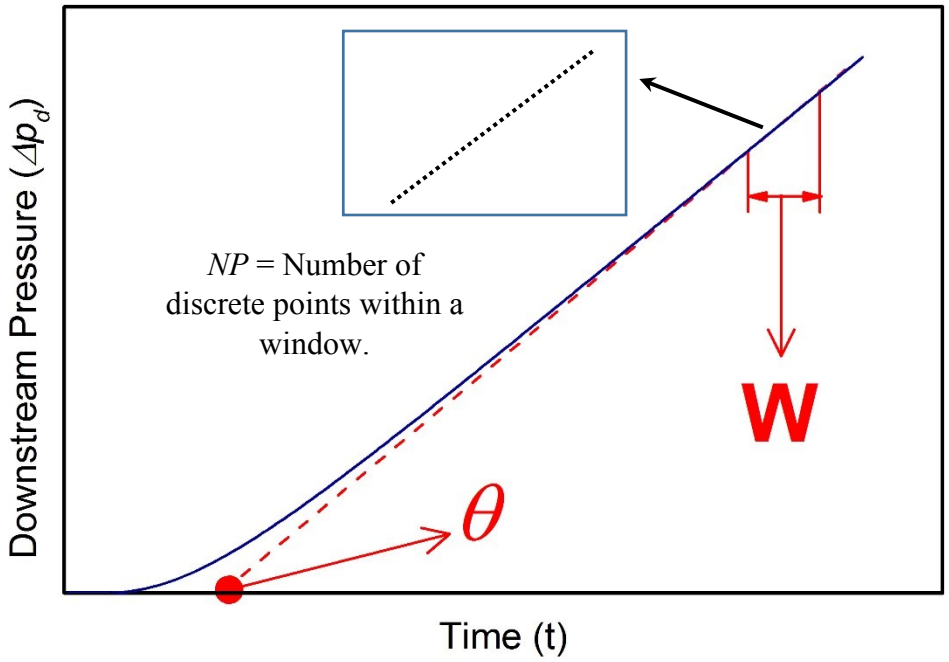

Figure 3.1 Progress of a typical time-lag gas permeation experiment showing the downstream pressure rise curve plotted versus time and illustration of the extrapolation necessary to determine the time lag.

In the conventional time-lag analysis, the time lag is inversely proportional to the membrane diffusivity coefficient (D):

$$\theta_d = \frac{L^2}{6D} \tag{1}$$

where L is the membrane thickness.

One of the important assumptions of the conventional time-lag method is that the amount of permeate gas accumulating in the downstream receiver is small enough to have a negligible effect on the driving force across the membrane and the permeation process can be approximated under ideal boundary conditions (Eq. 2) for which analytical solutions are available. Ideal boundary conditions are specified under the assumptions that: (a) prior to starting the experiment, the system is under complete vacuum such that the concentration is zero throughout the membrane; (b) the permeation experiment starts by subjecting the membrane to a step change in the upstream pressure of gas and the pressure is maintained

constant throughout the experiment; and (c) the marginal accumulation of gas at the downstream side of the membrane is negligible.

$$\begin{aligned} &\text{IC: } C(x,0)=0 && \text{(a)} \\ &\text{BC1: } C(0,t)=p_0 S && \text{(b)} \\ &\text{BC2: } C(L,t)=0 && \text{(c)} \end{aligned} \tag{2}$$

where C is the concentration of the permeating gas in the membrane and p_0 is the constant pressure in the upstream chamber. However, in real experiments, these conditions can only be approximated as the time-lag method requires their violation and, as a result, gas permeation in a CV system follows more realistic boundary conditions (Eq. 3) where the accumulation of permeated gas molecules in the downstream reservoir leads to a decrease of the driving force. It can be shown that a finite downstream volume with downstream pressure rise can affect the time-lag determination [23, 28-30].

$$\begin{aligned} &\text{IC: } C(x,0)=0 && \text{(a)} \\ &\text{BC1: } C(0,t)=p_0 S && \text{(b)} \\ &\text{BC2: } C(L,t)=p_d(t) S && \text{(c)} \end{aligned} \tag{3}$$

where $p_d(t)$ is the time-dependent pressure accumulation in the downstream chamber. The boundary condition 3(b) still assumes here that the upstream pressure remains constant throughout the permeation process, which is reasonable when using a large upstream reservoir. The magnitude of the impact of the downstream pressure increase on the time lag is proportional to the capacity parameter (η) [11,12,23,28]:

$$\eta = \frac{ALS\mathrm{R}T}{V_d} \tag{4}$$

where A is the area of the membrane, R is the universal gas constant, T is the temperature and V_d is the volume of the downstream reservoir.

Some researchers [8,9,13,14,20,24] have attempted to develop analytical solutions for membranes subjected to real boundary conditions to embed the effect of the decrease in the driving force. However, the available solutions are semi-analytical and cumbersome. To gain a better understanding of the gas permeation process and the impact of the boundary conditions, in the absence of effective analytical solutions, numerical methods

were used to simulate the real experimental process and to predict the behaviour of gas membranes with linear sorption under various boundary conditions [31,32].

Taveira et al. [23] studied the effect of the capacity parameter on the determination of the diffusivity coefficient and concluded that η (inversely proportional to V_d) should be small to reduce the effect of the decrease in the driving force. However, this conclusion might only be applicable to a noise-free environment and should not be used in the design of membrane systems without a careful analysis because the existence of experimental variability can have a major impact on the determination of the membrane properties. In other words, the necessity of a small capacity parameter for the accurate determination of these properties needs to be tested in the presence of experimental noise.

In this investigation, the impact of the accuracy of measuring devices and data analysis on the determination of the membrane properties is analyzed. The analyses are limited to the simplest case of a membrane in which gas sorption follows Henry's law and the diffusivity coefficient is independent of concentration. The sources of variability in the experimental data are classified into four types of errors: systematic, random, resolution and extrapolation errors. The effect of the capacity parameter (η), the length of the evaluation window (W) and the number of points (NP) used to extrapolate to the time-axis on the accuracy of the estimated time lag is carefully analyzed. Results obtained by the traditional time-lag method, where only a subset of experimental points is used, are compared with those obtained with a nonlinear regression method which uses the complete range of data of the downstream pressure.

3.2 Theoretical Background

The transport of a gas through a membrane, in which the diffusion coefficient of the permeating gas is constant, is described via Fick's second law of diffusion:

$$\frac{\partial C}{\partial t} = D\frac{\partial^2 C}{\partial x^2} \tag{5}$$

where x is the distance from the upstream interface of the membrane and t is the permeation time.

The solution of Eq. (5) subjected to the ideal initial and boundary conditions (Eq. 2) can be obtained using the method of separation of variables [33]. The analytical expression for the downstream pressure build-up (Δp_d) due to gas molecules permeating through the membrane is given by:

$$\Delta p_d = \frac{p_0 ARTDS}{V_d L}\left[t - \frac{L^2}{6D} + \frac{2L^2}{\pi^2 D} \times \sum_{n=1}^{\infty} \frac{(-1)^{n+1}}{n^2} \exp\left(-\frac{Dn^2\pi^2 t}{L^2}\right)\right] \tag{6}$$

At a long permeation time ($tD/L^2 > 1$), the summation term vanishes resulting in a linear equation (Eq. (7)) which directly highlights the basis of the time-lag method. Indeed, the time lag, extrapolated from the pressure change on the downstream side of the membrane to intercept the time axis, is directly proportional to the reciprocal of the membrane diffusion coefficient, as shown in Eq. (1).

$$\lim_{t\to\infty} \Delta p_d = \frac{p_0 ARTDS}{V_d L}\left(t - \frac{L^2}{6D}\right) \tag{7}$$

When the initial and boundary conditions are given by Eq. (3), the governing partial differential equation cannot be solved analytically; a numerical solution using finite differences can be used. This approach can be used for any set of the initial and boundary conditions [32,34]. The accuracy of the numerical scheme was thoroughly evaluated using benchmark analytical solutions in a previous investigation [32]. A summary of the main discretized equations (Eq. (8)-(11)) using a uniform mesh size is as follows:

$$\frac{\partial C}{\partial t} = D\frac{\partial^2 C}{\partial x^2} \rightarrow \frac{C_x^{t+\Delta t} - C_x^t}{\Delta t} = D\frac{\partial}{\partial x}\left(\frac{\partial C}{\partial x}\right) = D\frac{\left(\frac{\partial C}{\partial x}\right)_{x+\frac{\Delta x}{2}} - \left(\frac{\partial C}{\partial x}\right)_{x-\frac{\Delta x}{2}}}{\Delta x} \tag{8}$$

where Δx is the grid size used to discretize the membrane thickness. For an explicit numerical scheme and constant grid size, Eq. (9) is obtained for all interior mesh points within the membrane.

$$C_x^{t+\Delta t} = C_x^t + D\Delta t\left(\frac{C_{x+\Delta x}^t - 2C_x^t + C_{x-\Delta x}^t}{\Delta x^2}\right) \tag{9}$$

Eq. (8) could also be expressed using an implicit discretization numerical scheme for both variable and uniform mesh sizes. It was shown that all numerical schemes lead to accurate results provided the number of discretization points is sufficiently large [32]. Eqs. (10a)

and (10b) are used for the first and last grid points, respectively, to represent the two Dirichlet boundary conditions.

$$\begin{array}{lll} (x=0) & C_0^t = p_0 S & \forall \mathrm{t} \quad \text{(a)} \\ (x=L) & C_L^t = p_d\left(t\right) S & \forall \mathrm{t} \quad \text{(b)} \end{array} \tag{10}$$

The pressure increase at the downstream side of the membrane is calculated by numerically integrating the concentration gradient via Eq. (11). If the initial boundary condition at the downstream side of the membrane is zero, Eq. (11) considers the accumulation of the permeating gas entering the downstream reservoir. The total downstream pressure build-up is therefore the summation of the instantaneous downstream pressure increases in the downstream reservoir.

$$\Delta p_d = \sum_{i=1}^{n} \left[\frac{DART\Delta t}{V_d} \left(\frac{C(L, i\Delta t) - C\left(L - \Delta x_{N-1}, i\Delta t\right)}{\Delta x_{N-1}} \right) \right] \tag{11}$$

where N is the number of grid points in the solution domain and n is the number of time increments Δt for which the simulation is performed.

3.2.1 Error analysis and noise simulation

In this investigation, potential sources of errors associated with a gas permeation experiment are investigated for their impact on the determination of the membrane properties. These errors can be classified into systematic errors, random errors (noise), resolution errors and extrapolation errors. The list of potential sources for the first three errors is presented in Table 3.1.

Systematic errors are those having a nonzero mean that is caused by an inaccuracy of an observation or a measurement. A systematic error affects the experimental data independently of individual experiments, or may change from experiment to experiment, but is normally fixed during a given experiment. In this study, the systematic errors are comprised of the uncertainties in measuring the membrane thickness, the membrane area, the volumes of upstream and downstream reservoirs, the leak rate, the temperature and the downstream pressure transducer calibration error. These measurements are usually performed prior to performing an experiment.

Random errors (random noise) have been considered in previous research [8,35] as an observation variation. In computer-based experiments, most of these errors result from an instrument inherent accuracy and the unpredictable environment by which the experimental results are affected in an irregular and inconsistent way. Random errors can be influenced by some experimental parameters. These parameters are all parts of the capacity parameter (Eq. (4)).

Resolution errors are due to the resolution limit of the analogue-to-digital converter (ADC), i.e. the finest information unit a data acquisition system with a given number of bits can provide. Both random errors and resolution errors can be significant when the accumulation rate of the permeating gas is low.

At the end of a permeation experiment, the time lag is determined by extrapolating the pressure-time curve to intercept the time axis. Inaccuracy in the determination of the time lag may result during this process, so the error associated with this extrapolation is referred to as extrapolation error. The extrapolation error is not only affected by the level of random errors and ADC resolution errors, but it is also affected by the length of the evaluation time window, the number of evaluation points in the evaluation window and the time at which the extrapolation is performed.

All in all, the accuracy of the obtained time lag is influenced by the combination of the systematic errors, the random errors, the resolution errors and the extrapolation errors. Systematic errors are impossible to detect. Nevertheless, they can be estimated and analysed statistically. On the other hand, random errors do not bias the downstream pressure difference, but reduce the overall confidence in an individual reported value. To measure the impact of the variability induced by random errors and resolution errors, artificial noise was added to the simulation data to better represent actual experimental data. The advantage of performing this analysis numerically is that the real values of the downstream pressure and time lag are known and can be used to assess the error in various simulations.

Table 3.1 Error sources

Classification	Affected Parameters	Measurement/Measuring Device
Systematic errors	Membrane thickness	Micrometer with an accuracy of 1 μm
	Membrane area	Caliper ruler with an accuracy of 10 μm
	Upstream volume	Calibrated volume and pressure transducers with accuracy of 0.12%
	Downstream volume	
	Leak rate	Leak test
	Temperature	Thermocouple calibration
Random errors	Downstream pressure	Pressure transducer accuracy
	Temperature	Thermocouple accuracy
Resolution errors	Downstream pressure	Pressure transducer and data acquisition system

3.2.1.1 Random noise generation

Random errors are normally assumed to follow a Gaussian distribution characterized by a mean value (μ) and a standard deviation (σ). In this investigation, numerical simulations were performed to investigate the impact of random errors in the determination of the time lag. The variability in measured data due to random errors was simulated numerically by Gaussian noise as given by Eqs. (12) and (13).

$$\Delta p'_d = \Delta p_d + \delta(z) \tag{12}$$

$$\delta(z) = \frac{1}{\sigma\sqrt{2\pi}} e^{-\frac{(z-\mu)^2}{2\sigma^2}} \tag{13}$$

where $\Delta p'_d$ is the simulated downstream pressure build-up with a random noise, $\delta(z)$ is the centred probability density function of a Gaussian random variable z. In this case, the mean value μ was set to 0 and the standard deviation σ was constant for a given numerical experiment.

3.2.1.2 Resolution error generation

The pressure in the downstream reservoir is measured with a pressure transducer and the recorded signal has an inherent variability resulting in $\Delta p'_d$ as given by Eq. (12). The available noisy pressure measurement is then processed through an analogue-to-digital converter (ADC) to provide the corresponding number to the computer. The number output from the ADC can only be a multiple of the minimum resolution of the ADC. The pressure recorded by the computer is proportional to the number read by the computer and the calibration factor as shown in Eq. (14).

$$\Delta p''_d = \frac{N_{\Delta p_d}}{2^a - 1} \Delta p_{d,\max} \tag{14}$$

where $\Delta p''_d$ is the recorded downstream pressure accumulation that contains the random Gaussian noise and ADC resolution errors. This is the pressure signal that is available to the data processing software. $N_{\Delta p_d}$ is the number provided by the ADC corresponding to the noisy downstream pressure data $\Delta p'_d$, a is an integer value corresponding to the number of bits of the ADC (16 in this investigation) and $\Delta p_{d,\max}$ is the maximum pressure that the pressure transducer can measure and, if properly calibrated, corresponds to the maximum number that the ADC can provide.

In this investigation, the resolution error of the ADC was also simulated to accurately represent all the steps involved in the data acquisition process and in the determination of the time-lag.

3.2.2 Nonlinear regression

The traditional method for the determination of the time lag resorts to a limited portion of the downstream pressure rise curve to perform the required extrapolation to the time axis. When a numerical model is available, an alternative method to obtain the membrane properties is to fit the variation of the pressure change in the downstream reservoir as a function of time using a nonlinear least squares method [36]. By minimizing the sum of squares of the differences between the experimental data and the numerical model, the optimal combination of *S* and *D* can be obtained. The nonlinear regression method has three advantages in diminishing the noise effect: 1) it uses the whole range of pressure data instead of only the quasi-steady state data; 2) many powerful algorithms are available to find an optimal solution; and 3) it overcomes extrapolation error by obtaining

the diffusivity coefficient directly without extrapolating the time lag. However, although this alternative can reduce the effect of the experimental noise, an accurate recovery of the membrane properties from the original pressure data may still be challenging given the strong correlation that exists between *S* and *D*. The mean relative sum of squares is calculated and serves as a metrics for assessing the performance of the nonlinear regression:

$$\overline{\varepsilon} = \frac{\sqrt{\sum_{i=1}^{n}\left(\frac{\hat{p}_{di} - p_{di}}{p_0}\right)^2}}{n} \tag{15}$$

where $\bar{\varepsilon}$ is the mean relative error (*MSRE)* between the predicted downstream pressure $\hat{p}_d$ and the experimental downstream pressure p_d, n is the number of data points used in the regression.

3.3 Experiments

The main purpose of gas permeation experiments in this work was to access the resolution error of the downstream pressure transducer in the actual experiment and to compare it with the value simulated based on the specifications provided by the transducer's manufacturer and to justify the applicability of the numerically generated noise. If the simulations can reproduce with a high fidelity the experimental gas permeation experiments, including the different types of noise, then it becomes possible to use the numerical gas permeation experiments to assess with confidence the impact of measuring devices and data analysis in the determination of gas membrane properties.

The details of the CV system used in this work are described elsewhere [20,22]. The design of the downstream compartment allows varying the volume for gas accumulation from 77.6×10^{-6} m^3 to 1009.7×10^{-6} m^3; at the same time, the effects of resistance to gas accumulation reported in ref. [37-38] are minimized. The absolute pressure transducer (MKS model 627B11TBC1B) to monitor gas accumulation operates in a range of 0 to 1333 Pa (10 torr), with an accuracy of 0.0133 Pa (0.0001 torr) and a maximum error of 0.12% of the pressure reading. This level of precision is typical of the best precision from pressure transducers currently available on the market. Prior to each experiment, the system is

evacuated using a rotary vacuum pump (Edwards model RV3) for at least 48 h, and just before the experiment, leak tests for both upstream and downstream sides of the membrane are performed. During the leak tests, the vacuum pump is disconnected from the system and gas accumulation (if any) in the downstream reservoir is monitored for a period of time (from 20 minutes to 1 hour depending on the duration of the experiment).

The membrane used in the tests was a solution-cast, high molecular polyphenylene oxide (PPO) film prepared by a spin-coating technique. The details of membrane preparation are described elsewhere [15]. Other relevant experimental parameters are summarized in Table 3.2.

3.4 Results and Discussion

3.4.1 Systematic errors

The potential sources of the systematic errors have been inventoried for the constant volume system used in this work. These systematic errors are presented in Table 3.2 along with their estimations considering the precision of the measuring devices and actual measurements. To assess the respective impact of these systematic errors, the relative percentage standard deviations of the calculated time lag from the real time lag under quasi-steady state was evaluated. To perform this evaluation via a simulated permeation experiment, all measured variables were kept constant at their nominal values except for one variable that was varied at a time upward and downward of its nominal value by the degree of uncertainty as given in Table 3.2. From the simulated downstream pressure rise curve, the time lag was estimated using the traditional time-lag method at a time corresponding to 5 times the nominal (actual) value of the time lag θ_d (considered as quasi-steady state) with a time window of 50 s with 100 pressure data points.

Table 3.2 shows that realistically-estimated systematic errors for most of the variables of Table 3.2 have a minor impact on the resulting time lag. The systematic error having the largest impact on the determination of the time lag with a potential variation of 17.5% results from the measurement of the membrane thickness using a micrometre calliper having a measurement accuracy of 1 μm. The accuracy could vary if a different membrane fabrication technique is used or a different method for measuring the membrane

thickness is used. A more precise but also more expensive technique is the spectroscopic ellipsometer which measures the thickness and uniformity of a polymeric film at the nano-level by investigating the optical properties of thin films [39].

Table 3.2 Systematic error analysis

Parameters	**Equations**	**Best estimate and uncertainty**	**Time-lag error (%) (t = 5 θ_d)**	**Measurement**
Membrane thickness	$\delta L = \frac{2.365\sigma_L}{\sqrt{N}} \quad (N = 9)$	$\bar{L} = 30\times10^{-6}\,\text{m}$ $\delta L = 2\times10^{-6}\,m$ (6.67%)	17.50	Micrometer with accuracy of 1 μm
Membrane area	$\delta L = \frac{2.770\sigma_D}{\sqrt{N}} \quad (N = 5)$ $\delta A = A\left(\frac{\pi}{4}\times 2\times\frac{\delta D}{D}\right)$	$\bar{A} = 0.00125\text{m}^2$ $\delta A = 2\times10^{-6}\,\text{m}^2$ (0.16%)	0.0008	Caliper ruler with accuracy of 0.00001m
Upstream volume	$\frac{\delta V_2}{V_2} = \sqrt{\left(\frac{\delta V_1}{V_1}\right)^2 + \left(\frac{\delta P_2}{P_2}\right)^2 + 2\left(\frac{\delta P_1}{\Delta P_1}\right)^2}$	$V_u = 5.00\times10^{-5}\,\text{m}^3$ $\frac{\delta V}{V} = 0.2078\%$	0.00076	Calibrated volume and pressure transducers with accuracy of 0.12%
Downstream volume		$V_d = 9.68\times10^{-5}\,\text{m}^3$ $\frac{\delta V}{V} = 0.2078\%$	0.00095	
Leak rate	$\delta p = \Delta t \times LR$	$LR_u = 2.67\times10^{-4}\,\text{Pa/s}$ $LR_d = 6.67\times10^{-5}\,\text{Pa/s}$	8.75×10^{-6}	Leak test
Temperature	--	$T = 298K \quad \delta T = 1\,\text{K}$	2×10^{-9}	Thermocouple

3.4.2 Random errors

The variability of the temperature and the downstream pressure measurements is considered as sources of random errors while the digital discrete output of the analogue-to-digital (ADC) converter, part of the data acquisition system, gives rise to the resolution error. Random errors are inevitable and the accuracy of measuring instruments is usually provided in the instrument manufacturer specifications.

3.4.2.1 Temperature-drift error

An experimental gas membrane permeation experiment can take anywhere from a few minutes to several hours. During the course of an experiment, even if the system is well insulated, the recorded temperature may still vary slightly with time in addition to be subjected to inherent random errors. In this investigation, the temperature did not vary significantly and an average temperature was used in performing calculations. To evaluate the error that is caused with a potential change in temperature, Eq. (16) was used. This equation states that for a constant volume of the permeating gas with a fixed number of moles, a variation of temperature will simply be perceived as a change in the gas permeation rate.

$$q = \frac{d}{dt}\left(\frac{pV}{RT}\right) = \frac{V}{RT}\frac{dp}{dt} - \frac{pV}{RT^2}\frac{dT}{dt} \tag{16}$$

where q (mol/s) is the molar permeation rate of the tested gas. The permeation rate is measured indirectly based on the pressure increase rate on the permeated side. The second term of the right-hand side of Eq. (16), referred here as the temperature-drift error in q, is directly proportional to the downstream pressure p. When the pressure on the permeated side is low, the error is negligible compared to the first term of the right-hand equation, the original molar permeation rate. For this reason, most constant-volume time-lag experiments are ideally conducted in an initially highly evacuated system as it is the case in this investigation where perfect vacuum is assumed.

3.4.2.2 Downstream pressure transducer random error

A series of numerical experiments was performed to assess the impact of the magnitude of the random noise on the determination of the time lag. Resolution noise from the ADC will be considered in the next section. Simulations are performed under realistic boundary conditions where the driving force is decreasing due to the downstream pressure accumulation. The instantaneous downstream time lag was estimated continuously by extrapolating the pressure rise curve to the time axis using a 50 s moving window containing 100 uniformly distributed pressure data points. The results are presented in Fig. 3.2 for three noise levels, having respectively pressure standard deviations σ of 0.0001,

0.001 and 0.01 Pa. In Fig. 3.2, the estimated instantaneous downstream time lag is plotted as a function of the dimensionless time (t/θ_d). Results show that for a noise standard deviation of 0.001 Pa or less, the time lag is estimated accurately and the variation in its determination is small even at relatively large time. The current instrument used in our laboratory has an accuracy corresponding to a standard deviation σ of 0.0012 Pa and therefore has sufficient accuracy to estimate with sufficient confidence the time lag. For a standard deviation of 0.01 Pa in the pressure noise level, a much greater variability in the estimation of the time lag is observed and this variability grows with time mainly due to the extrapolation error of noisy data to the time axis. Typically, it is recommended to perform the experiments for at least 3-4 actual time lags to ensure a quasi-steady-state permeation process [23-27]

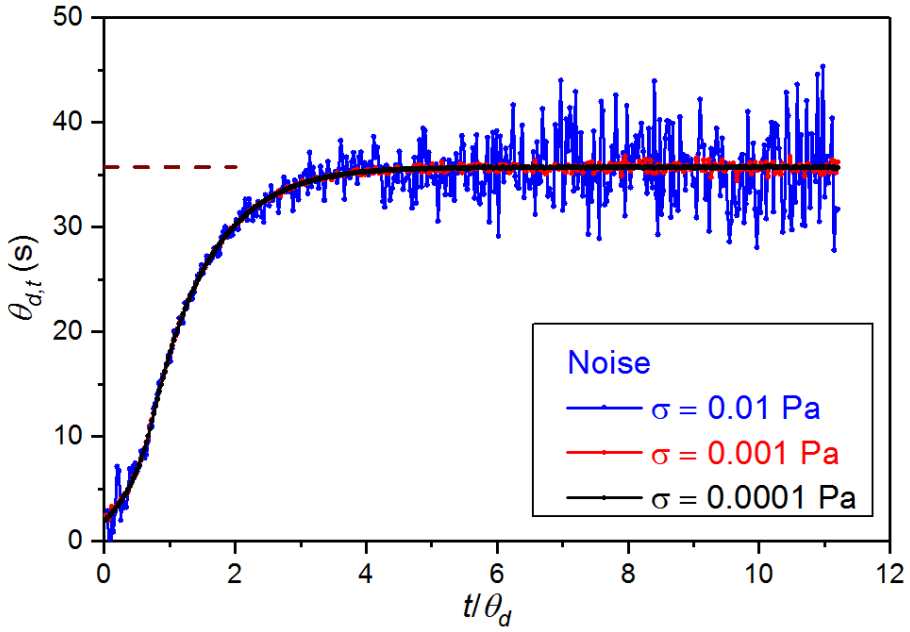

Figure 3.2 Estimation of the instantaneous downstream time lag $\theta_{d,t}$ as a function of dimensionless time (t/θ_d) for three different levels of Gaussian random noise corresponding to the accuracy of the pressure transducer. Evaluations were performed over a time window of 50 s containing 100 data points. θ_d is the actual time lag value. Experimental conditions are shown in Table 3.A.1.

To gain a better understanding of the impact of the different noise levels, a total of 100 simulations under the same conditions with random noise were performed and the

standard deviations of the estimated instantaneous downstream time lag were calculated as a function of the dimensionless time (t/θ_d) for each of the three noise levels (σ = 0.0001, 0.001 and 0.01 Pa). Results for all levels of noise, presented in Fig. 3.3, show that the standard deviation of the estimated time lag follows the same trend. The standard deviation of the estimation error of the time lag initially decreases with time and plateau at a minimum prior to increase continuously with time. The minimum corresponds to the rapid increase in the estimated time lag (Fig. 3.2). For the lowest noise level (σ = 0.0001 Pa), the standard deviation of the error of the estimated time lag evaluated at $5\theta_d$ is 2.1%. If the level of noise is increased, the accuracy in the estimation of the time lag greatly deteriorates. For noise levels with a standard deviation of 0.001 and 0.01 Pa, the percentages of the estimation error of the time lag evaluated at $5\theta_d$ are 23% and 218%, respectively. For the three noise levels, the expected accuracy in the estimated time lag is magnified with respect to the standard deviation of the measuring instrument. This magnification in the estimation of the time lag, due mainly to extrapolation errors (discussed in Section 4.5) of noisy data, increases with time. Fig. 3.2 and 3.3 clearly show that the evaluation of the time lag at a large experimental time becomes more difficult and less accurate with a higher level of the pressure random noise. It is obviously important to ensure working with a high accuracy pressure transducer.

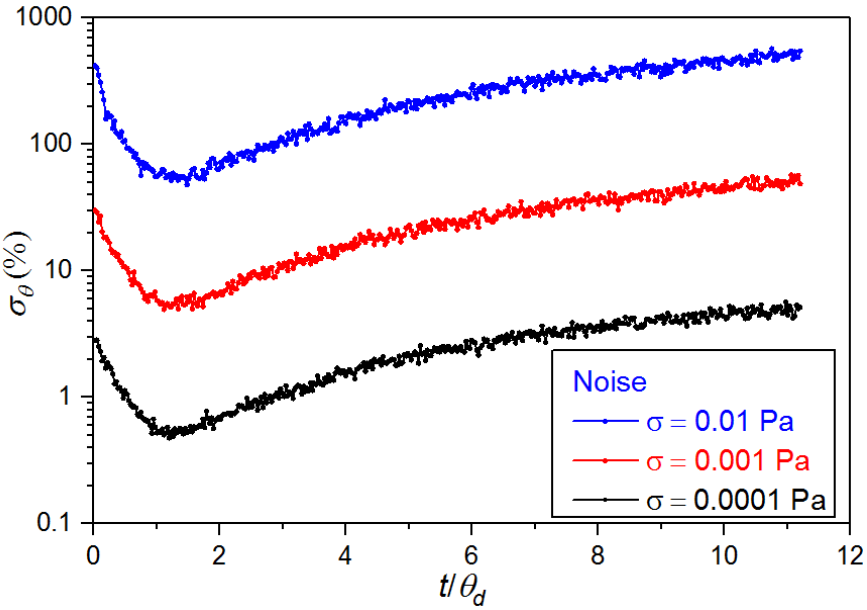

Figure 3.3 Variation of the standard deviations in the estimation of the instantaneous downstream time lag as a function of dimensionless time (t/θ_A) due to pressure

transducer accuracy for different Gaussian random noise levels (σ = 0.0001, 0.001 and 0.01 Pa) based on 100 simulations for each noise level. Evaluations were performed over a time window of 50 s containing 100 uniformly-distributed data points. Experimental conditions are shown in Table 3.A.1.

3.4.3 Resolution error

In the previous section, the estimation of the time lag was performed assuming that the noisy pressure signal could be available directly. It was assumed that no errors were caused by the resolution of the analogue-to-digital converter. In this section, the impact of the resolution errors caused by the discrete nature of a digital-to-analogue converter (ADC) output signal is analyzed.

The sampled pressure signal that is recorded by the computer is the output of the pressure transducer that is affected by inherent random noise and the error resulting from the data acquisition and conversion through an ADC. The latter one leads to a resolution error due to the digital limit of the ADC of the data acquisition system. In this investigation, the range of the pressure transducer is 1333 Pa (10 torr) and its output voltage range is 0 - 10V. For the current laboratory system, the input voltage range of the 16-bit ADC was set to 0-1 V range such that the effective ADC resolution (Eq. (14)) is 1.53×10^{-5} torr or 2.03×10^{-3} Pa. This high accuracy can only be obtained if the recording system upon converting the ADC digit to the corresponding pressure provides the proper number of significant digits to retain this high accuracy. It turns out that for the current experimental system; only four decimals can be reported such that the smallest recorded pressure unit is 0.013 Pa (0.0001 torr). For this system, the ADC resolution error is thereby compounded with a truncation error. The observation of this additional truncation error points to the importance of carefully analyzing the data acquisition system to ensure the pressure signal is recorded with the highest possible precision. The resulting resolution error in the current experimental system is therefore 0.0001 torr or 0.013 Pa, which can be clearly observed in Fig. 3.4a showing a segment of the actual permeation experiment.

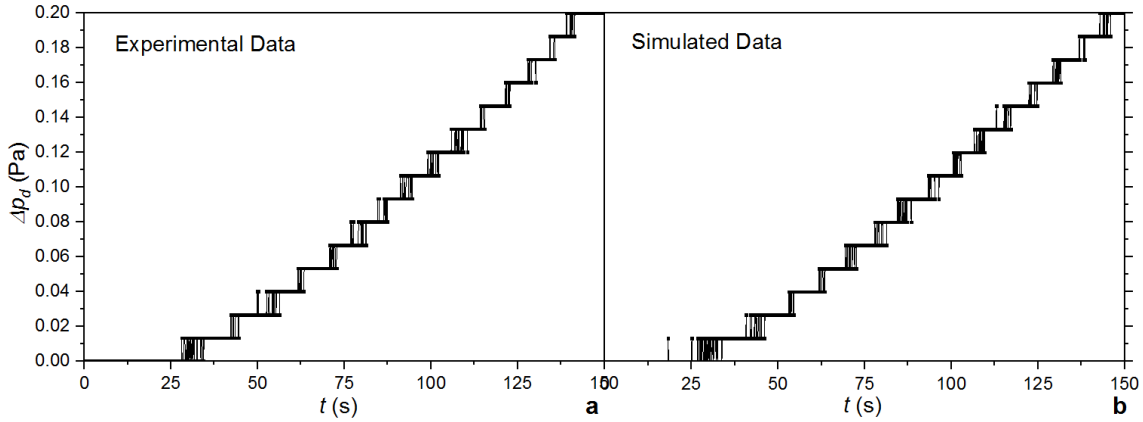

Figure 3.4 Downstream experimental pressure data (a) and simulated data (b) as recorded by the 16-bit ADC. The input of the ADC is the output voltage of the pressure transducer corresponding to the pressure signal affected by random errors (σ = 0.002 Pa).

To perform representative simulated permeation experiments that are able to represent realistic error scenarios, the observed resolution was programmed for the downstream pressure accumulation curves. A simulated permeation experiment with ADC resolution errors, presented in Fig. 3.4b, is a good representation of the actual permeation experiment. The pressure accumulation is recorded in a stepwise fashion and because random errors affect the pressure signal preceding the ADC, the recorded signal frequently jumps between two adjacent stages.

To illustrate the impact of resolution errors, simulated permeation experiments were performed in the absence of random errors. The results of three simulated permeation experiments, performed at three different feed pressures (10, 100 and 1000 kPa) are presented in Fig. 3.5 in terms of the estimated time lag. It is observed that the resolution errors lead to a significant variation of the estimated time lag at a lower feed pressure (10 kPa). A low feed pressure gives rise to a lower rate of increase of the downstream pressure and the pressure signal spends a longer time at each pressure step and, if the estimation of the time lag is performed over a fixed time window, the extrapolation to the time-axis will be greatly affected. On the other hand, a higher feed pressure leads to a higher rate of increase of the downstream pressure and therefore lower resolution errors. In addition, as shown in Fig. 3.5, a periodical behaviour on the estimation of the time-lag curves is observed. This cyclic effect is created by the extrapolations of the pressure curve data

changing in a discrete fashion from one level to another caused by the resolution and truncation errors. This effect becomes significant for small pressure increase rates associated with lower feed pressure. In the case of a feed pressure of 10 kPa, this effect is important and increases with time.

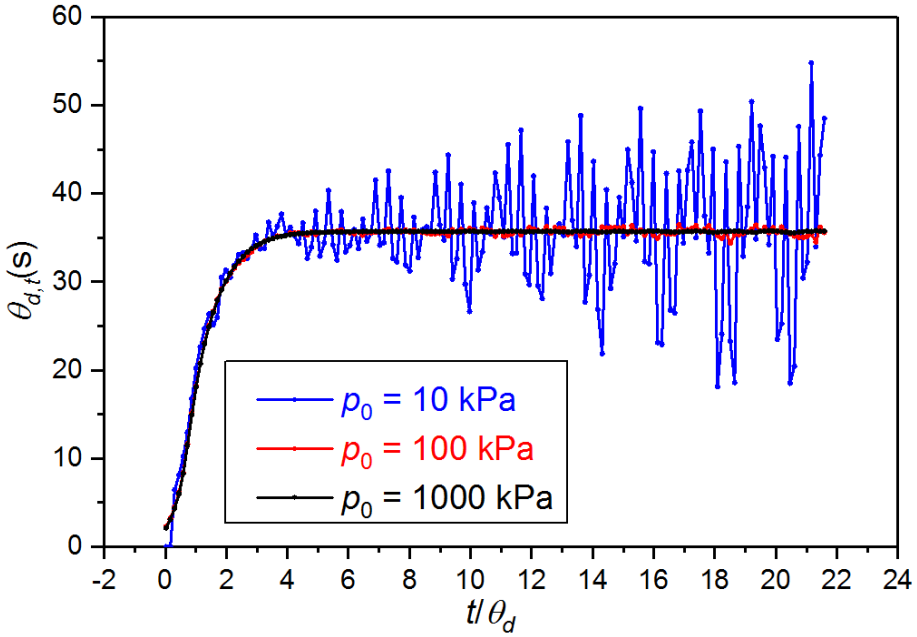

Figure 3.5 The variation in the estimation of the time lag as a function of the dimensionless time due to data acquisition error only in a single simulation. The data evaluation time sliding window is 50 s; 100 equidistant pressure data points are used for each evaluation. Estimated time lag is presented for three initial feed pressures: 10 kPa, 100 kPa and 1000 kPa. Experimental conditions are shown in Table 3.A.1.

3.4.4 Impact of experimental conditions on random and resolution errors

Previous research [23,24,27] suggested using a small capacity parameter (η) in designing permeation experiments in order to obtain a more accurate estimation of the time lag by minimizing the effect of the decrease in the driving force across the membrane. However, as it will be discussed in this section, the capacity parameter does not only impact the driving force, but also the noise level. In the definition of η given by Eq. (4), the membrane area (A), membrane thickness (L), temperature (T) and downstream volume (V_d) are factors that influence the overall noise level. Therefore, when the accuracy of

instruments is fixed, the noise level in the estimation of the time lag can be controlled by carefully selecting the operating conditions under which permeation experiments are conducted. Of all the parameters in Eq. (4), the membrane area and the membrane thickness are considered fixed when a system is set up. The temperature is usually well within control and it is selected to correspond to the intended application temperature, which is often the ambient temperature as it was the case in this investigation. Therefore, the effect of the capacity parameter on the noise level of the estimated time lag is mainly affected by the downstream volume.

To illustrate the impact of the capacity parameter on the estimated time lag, permeation experiment simulations were performed for three different capacity parameters η: 10^{-4}, 10^{-5} and 10^{-6}. For each capacity parameter, 100 simulations were carried out at three different random noise levels (0.01, 0.001 and 0.0001 Pa) in order to observe the resulting variability in the estimation of the time lag. This variability is reported in Fig. 3.6 in terms of the standard deviations of the estimated time lag. For this series of simulations, the resolution error was identical to the one described in the previous section for a feed pressure of 100 kPa. Results clearly show that for a low noise level (σ = 0.0001 Pa) (Fig 3.6a), the larger value of the capacity parameter ($\eta = 10^{-4}$) leads to a small standard deviation, $\sigma_\theta \approx 1\%$ at $5\theta_A$ from the actual time lag. On the other hand, smaller capacity parameters (η = 0.00001 and 0.000001) lead to conspicuous variability in the estimated time lag with σ_θ equal approximately to 30% and 160%, respectively. In Fig. 3.6a, the rugged plots are the result of the resolution errors, which induce a periodical effect on the estimation of the time lag. This effect is reduced when the capacity parameter is increased ($\eta = 10^{-4}$ and 10^{-5}) because larger rates of increase in the downstream pressure are prevailing. In addition, Fig. 3.6b and 6c show that, when the input random noise level is increased, the errors in the estimated time lag are increased for all capacity parameters. The differences in σ_θ between the highest and the lowest capacity parameter also increase with the level of random noise. The difference in σ_θ between $\eta = 10^{-4}$ and $\eta = 10^{-6}$ at $5\theta_d$ is approximately 130% when the random noise level is 0.0001 Pa, 500% when the random noise level is 0.001 Pa, 2650% when the random noise level is 0.01 Pa.

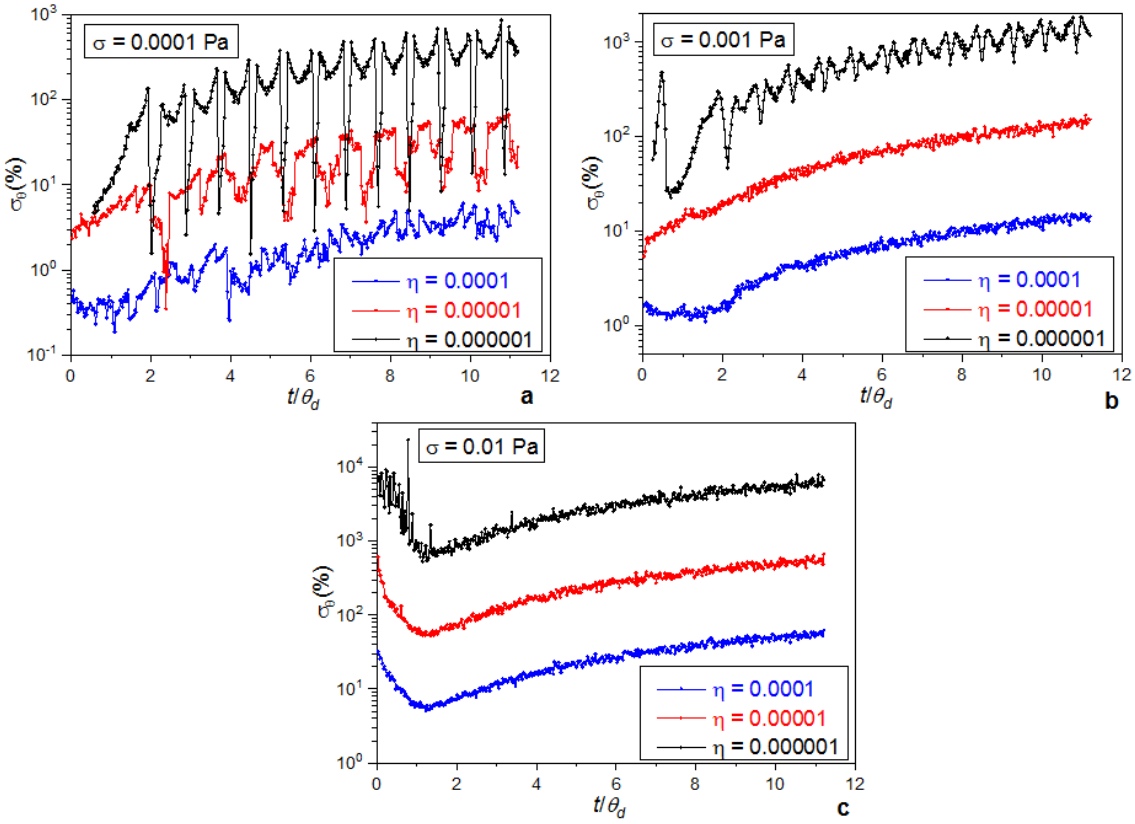

Figure 3.6 Variation of the standard deviations in the estimation of the time lag as a function of time based on the downstream pressure signal for three capacity parameters ($\eta = 10^{-4}$, 10^{-5} and 10^{-6}) and three levels of random noise (0.0001, 0.001 and 0.01 Pa). The standard deviations were calculated based on 100 simulations performed under real BC over a time window of 50 s containing 100 data points. The feed pressure was 100 kPa and a recording resolution of 0.013 Pa (0.0001 torr) prevailed. Experimental conditions are shown in Table 3.A.1.

3.4.5 Extrapolation errors

Results presented in the preceding sections considered the two major sources of experimental errors: random errors and resolution errors. These two errors are associated with the physical instrumentation: pressure sensor and the data acquisition system. A range, referred in this investigation as a time window (W), of the noisy pressure data is used to find the straight line that best fits these experimental data. This linear best fit is then

extrapolated to the time-axis to estimate the time lag. The factors that can lead to more or less extrapolation error in the estimation of the time lag are the level of random and resolution errors, the length of the time window, the number of points contained in the time window, the time at which the time-lag evaluation is made, the feed pressure, and the capacity parameter. In the limiting case where the pressure data are not affected by the noise and ideal boundary conditions prevail, the estimation of the time lag can be performed accurately after a time corresponding to three time lags or more. Under this ideal case, the length of the time window, the number of data inside the time window and time of evaluation do not impact on the time-lag estimation and no significant extrapolation error would be observed. However, in permeation experiments where real boundary conditions prevail, extrapolation errors are inevitably presented due to random and resolution errors. In addition, for real boundary conditions, the pseudo-steady-state pressure curve will never become perfectly linear such that, even in the absence of noise, extrapolation error would exist.

In this investigation, to study the effect of extrapolation errors, three factors that are specific to extrapolation errors were considered: the length of the time window, the number of data points within the evaluation window, and the time at which the estimation of the time lag is performed. 100 permeation experiment simulations were performed with a random noise level of 0.001 Pa for three different time window lengths W (25, 50 and 100 s) and three different numbers of data points within the time window NP (50, 100 and 200). For each simulation, the time lag was estimated by extrapolating the downstream pressure rise curve to the time-axis and the standard deviation of the estimated time lag was calculated and used to assess the effect of each factor. Results of this series of simulations are presented in Fig. 3.7-3.9, where it is clearly shown that the most significant factor contributing to the extrapolation error is the time at which the estimation of the time lag is performed. Indeed, the further in time the extrapolation is performed, the larger the variability in the estimated time lag will be. For example, for 100 points in a 50 s time evaluation window (Fig. 3.7), the standard deviation of the estimated time lag is approximately 30% at $3\theta_A$, 52% at $5\theta_A$, and 130% at $10\theta_A$. In Fig. 3.7, for a length of the time window of 50 s, a larger number of data points used in the time window lead to a decrease in the variability of the estimated time lag at the same evaluation time. A larger

number of points in a fixed window length have a filtering effect on the estimation of the time lag and its estimation variability is reduced.

It is observed that using 200 evaluation data points in a 50 s time window leads to a time lag standard deviation at $5\theta_d$ of approximately 40% while a standard deviation of around 77% was observed for a number of evaluation points of 50. However, there is a limit at which rate pressure data can be acquired, such that extrapolation errors will always be present.

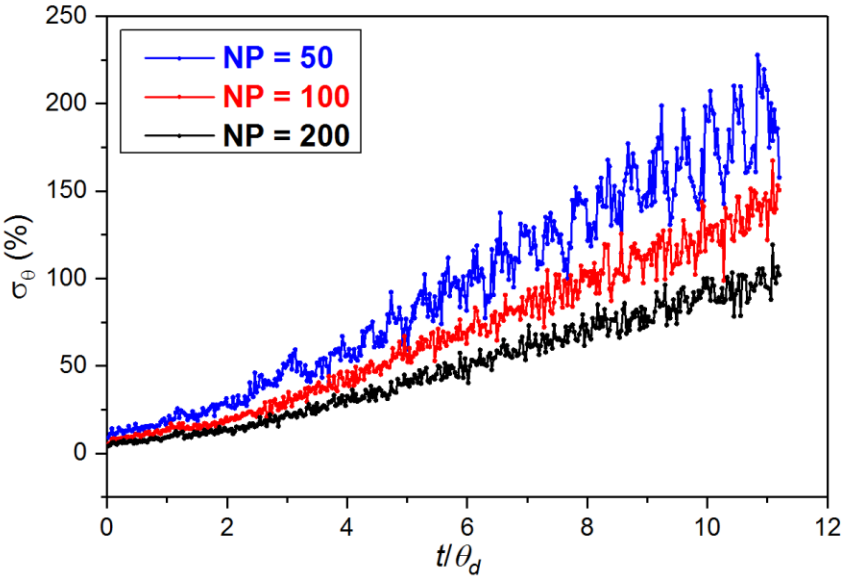

Figure 3.7 Variation of the standard deviation in the estimation of the time lag as a function of time based on the downstream pressure signal. The estimation was performed for three different numbers of evaluation data points NP (50, 100 and 200) per window and standard deviation is calculated based on 100 simulations. Evaluations were performed under real BC over a time window of 50 s, a noise level of 0.001 Pa and a capacity parameter η = 0.00001. Experimental conditions are shown in Table 3.A.1.

Fig. 3.8 presents the standard deviation in the estimation of the time lag for three different lengths of the time window: 25, 50 and 100 s. Results clearly show that a larger time window gives an estimation of the time lag with less variability. At a time corresponding to $5\theta_A$, the time lag standard deviations are approximately 110%, 52% and 27% with an evaluation window of 25, 50 and 100 s, respectively. However, it is not

suggested to use an evaluation time window as large as possible to minimize the variability in the estimation of the time lag. Without noise, small evaluation windows are always preferred because they provide the least distortion. With noise, a proper window length has to be selected considering the trade-off between minimizing the noise effect and minimizing the distortion. Fig. 3.9 shows the errors in the estimation of the time lag at $3\theta_d$ and $5\theta_d$ as a function of the length of the evaluation window with two different noise levels based on 100 simulated permeation experiments. The experiments were performed under real BC with the evaluation window containing 100 data points. Results clearly show the distortion effect as the window length is increased and starts to encompass the initial region where the downstream pressure curve rise rapidly and to a much lesser extent the higher part of the curve where the pressure rise curve deviates from a straight line due to real boundary conditions. This distortion effect is obviously observed earlier when the midpoint of the evaluation window is located at $3\theta_d$ as shown in Fig. 3.9. At $5\theta_d$, the distortion effect is delayed and the drop in the estimation of the time lag becomes only obvious at a window length of 150 s.

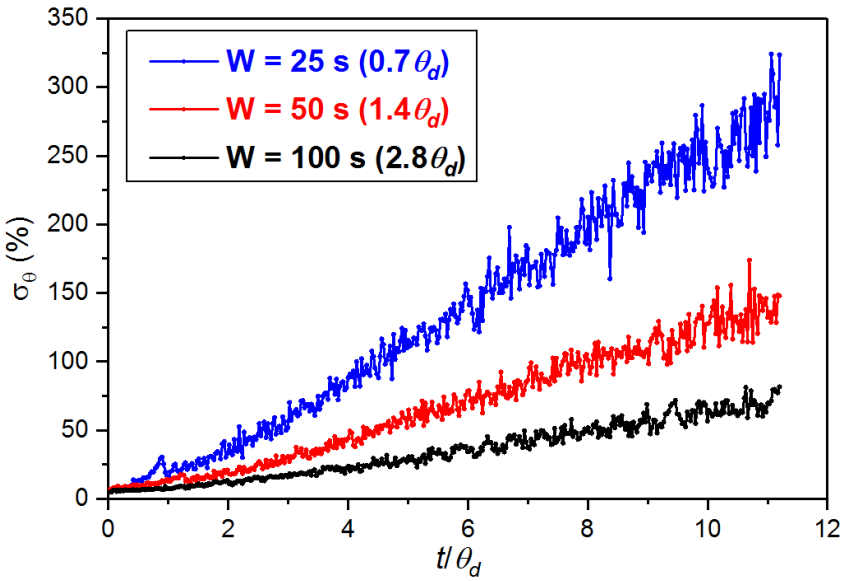

Figure 3.8 Variation of the standard deviations in the estimation of the time lag as a function of time using the downstream pressure signal for three different evaluation windows W (25, 50 and 100 s). 100 evaluations were performed under real BCs with 100 data points within the window and a noise level of 0.001 Pa. Experimental conditions are shown in Table 3.A.1.

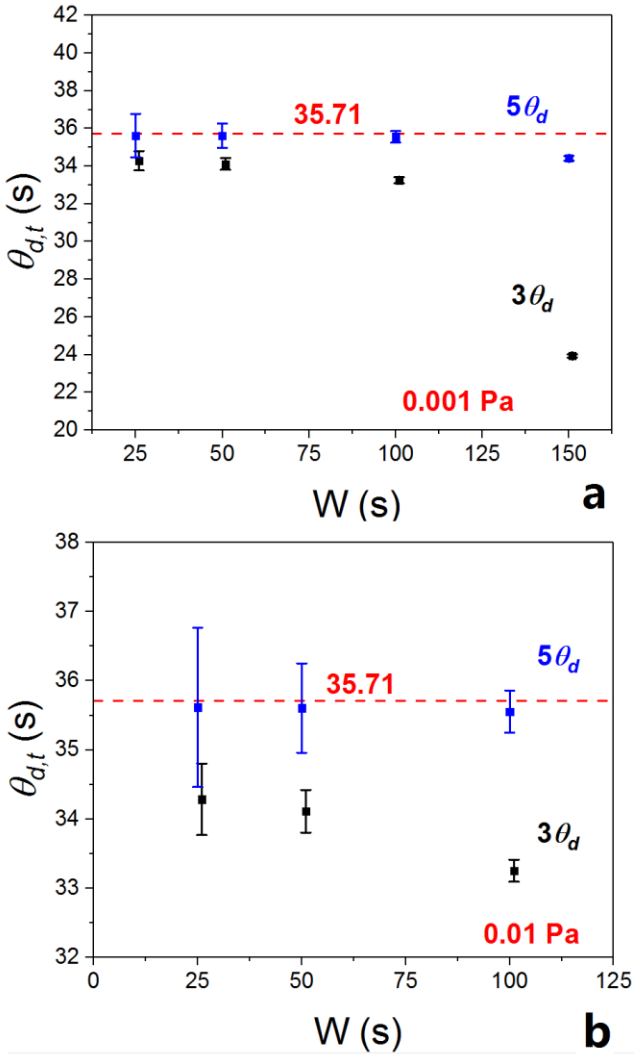

Figure 3.9 Estimation of the time lag at $3\theta_d$ and $5\theta_d$ as a function of the length of the evaluation window with a noise level of 0.001 and 0.01 Pa. 100 evaluations were performed under real BC with 100 data points and a noise level of 0.001 Pa. Experimental conditions are shown in Table 3.A.1.

3.4.6 Nonlinear regression

An alternative way to determine the solubility and diffusivity coefficients of the membrane is to use nonlinear regression where, instead of using a subset of downstream pressure data points in a certain evaluation time window to determine the time lag and thus diffusivity coefficient, the complete data set of the downstream pressure-time curve is used. By minimizing the mean square relative error (*MSRE*), which will be denoted as $\bar{\varepsilon}$ (Eq. (15)) between the experimental data and the simulated data, the values of the solubility and diffusivity coefficients can in principle be estimated.

To determine the sensitivity for the determination of solubility and diffusivity coefficients with respect to the downstream pressure rise curve, a large number of simulations were performed with different combinations of *S* and *D* to cover a relatively narrow range (± 5%) around their nominal values. The *MSRE* was calculated between the pressure data obtained with the nominal values of *D* and *S* ($S = 3\times10^{-4} mol/m^3\ Pa$, $D = 4.2\times10^{-12} m^2/s$) and the pressure data obtained with the different combinations of *S* and *D*. The results of these simulations are presented in terms of contour plots without noise in Fig. 3.10a and with noise (noise level is 0.01 Pa) in Fig. 3.10b. The strong correlation existing between parameters *D* and *S* is clearly illustrated in Fig. 3.10 where a combination of the two parameters located on the diagonal leads to relatively lower values of the *MSRE*. As the set of parameters *D* and *S* moves away from the diagonal line, the *MSRE* increases rapidly. Fig. 3.10b present similar contour plots of the MSRE when the noise level is 0.01 Pa. In this figure, not only the impact of the strong *S*-*D* correlation still exists giving elliptical contour lines, but the noise also increases significantly the MSRE values along the diagonal line. It can be concluded that with noise recovering real values of *S* and *D* becomes even more difficult.

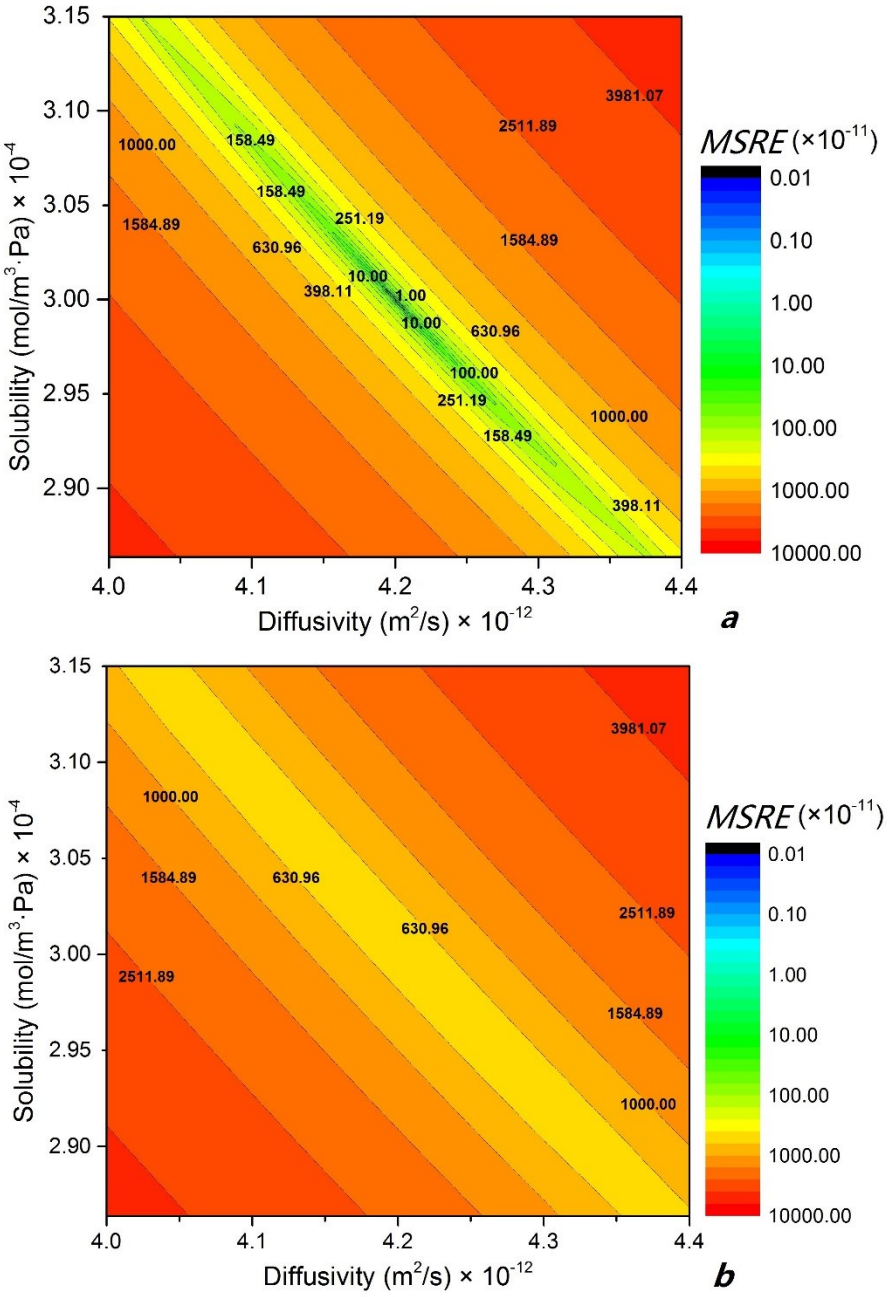

Figure 3.10 Contour maps of the MSRE between the downstream pressure curve for the nominal *S* and *D* values and for a wide set of *S* and *D* in the vicinity (± 5%) of the nominal *D*-*S* set: (a) noise free and (b) 0.01 Pa. Nominal values are $S = 3\times10^{-4}$ mol/m^{3}Pa, $D = 4.2\times10^{-12}$ m^2/s. Experimental conditions are shown in Table 3.A.1.

As it is already known, it is the membrane permeability coefficient that dictates the rate of ascent of the downstream pressure curve and in solution-diffusion model, it is the product of solubility and diffusivity coefficients. As a result, it is difficult to decouple solubility and diffusivity coefficients accurately without using the time lag. If a nonlinear regression is used with noisy data, the recovery of membrane properties becomes even more difficult in addition to the correlation between S and D. However, the nonlinear regression may have some advantages over the time-lag method in complex transport models such as partial immobilization model and non-instantaneous equilibrium model since the x-axis extrapolation from pressure accumulation curve may have multi-plateaus and it does not directly indicate the time lags. Therefore, a combined usage of the two methods in membrane characterization is suggested in studying those models.

3.5 Conclusion

In a noise-free theoretical design of an experiment, a small capacity parameter is desirable to minimize the decrease in the permeation driving force. However, choosing a small capacity parameter is limited in actual experiments considering the presence of noise which causes significant data variability. Data variability is an inherent part of any measurement and impacts on the accurate determination of membrane properties. Therefore, in the design of time-lag experiments, researchers need to reconsider the recommendation of using a small capacity parameter in constant-volume membrane characterization experiments to obtain more accurate estimation of the time lag. In this investigation, four main types of errors were discussed: systematic errors from the experimental setup, random errors from the downstream pressure transducer, resolution errors from analogue-to-digital converter and extrapolation errors in the time-lag method. A comprehensive error analysis was presented in this paper to examine the impact of data variability on the determination of membrane properties using the time-lag method and nonlinear regression.

Systematic errors are usually inherited in an experimental setup and do not change during an experiment. Careful calibration and accurate observation are the only ways to avoid systematic errors. Resolution errors are generated by the analogue-to-digital

converter which converts the downstream pressure into a discrete signal. It is therefore important to resort to a high-resolution ADC and to ensure the recording system is able to read to such resolution. Random errors mainly come from the accuracy of the pressure transducer. Improving instrument accuracy is the best way to reduce uncertainty. Nevertheless, the availability of such accurate instrument might be limited. In this case, manipulating the capacity parameter and operational conditions need to be carefully considered to reduce uncertainties. Results showed that random and resolution errors are more significant for small pressure accumulation rates, which can be alleviated by increasing the feed pressure p_0 or the capacity parameter η (i.e. decrease in the downstream volume V_d). Increasing p_0 lowers the resolution error but has no effect on the random error. A judicious balance must exist between data precision, the drop in the pressure driving force and the duration of an experiment when choosing V_d and p_0. Rarely discussed in the literature, the extrapolation error associated with the time-lag method using the pressure data that is affected by the other types of errors and noise. It increases with time and can be reduced by increasing the number of evaluation points *NP* and the length of the evaluation window *W*. However, a larger evaluation window may cause a distortion in the extrapolated time lag.

Apart from the convenience and simplicity of the time lag method, it predicts the diffusivity coefficient without any correlation with the solubility coefficient. However, it uses only a subset of the downstream pressure data points to determine the time lag, neglecting the information outside the evaluation window. In comparison, the nonlinear regression can be used to determine membrane properties by minimizing the *MSRE* between the complete data set of experimental and predicted downstream pressure accumulation curves. However, it turns out that the strong correlation between *S* and *D* impedes their accurate determination. It is suggested to use a combination of the time-lag method and nonlinear regression to accurately determine the individual membrane transport properties. In addition, the nonlinear regression method may be instrumental in the determination of more complex diffusion mechanisms such as partial immobilization model and non-instantaneous equilibrium model since the time-axis extrapolation from the pressure accumulation curve may have multi-plateaus and it does not directly indicate the time lag.

Studies in this investigation were conducted assuming a constant diffusivity coefficient. However, this is not always the case, especially for glassy polymers. It is important to emphasize that even in the simplest case – membranes with constant diffusivity coefficient – all the four types of errors affecting the system will impact on the determination of the time lag which may lead to the misinterpretation of the underlying model. Moreover, a careful selection of experimental conditions and proper data analysis will benefit not only the determination of the constant diffusivity coefficient but all time lag determination cases. Future studies may address the issue with a concentration-dependent diffusivity coefficient.

3.6 Acknowledgement

The authors gratefully acknowledge the financial support for this project provided by the Natural Science and Engineering Research Council of Canada.

3.7 Nomenclature

a	Integer number of bits of the ADC (16 in this investigation).
A	Membrane area, m^2.
C	Gas concentration, mol/m^3.
D	Diffusion coefficient, m^2/s.
L	Membrane thickness, μm.
LR	Leak rate, Pa/s.
n	Number of time increments.
NP	Number of evaluation points in a selected window.
$N_{\Delta pd}$	Number provided by the ADC corresponding to the noisy downstream pressure data.
p_0	Constant pressure in the upstream chamber, Pa.
p_u	Upstream pressure change, Pa.
p_d	Downstream pressure change, Pa.
$\hat{p}_d$	Predicted downstream pressure.
P	Permeability coefficient, $mol \cdot m/(m^2 \cdot Pa \cdot s)$.

q	Molar permeation rate, mol/s.
R	Gas constant, J/(K·mol).
S	Solubility coefficient, mol/(m^3 ·Pa).
t	Simulation time, s.
T	Absolute temperature, K.
V_u	Upstream volume, m^3.
V_d	Downstream volume, m^3.
W	Evaluation time window, s.
x	Permeation distance, μm.
Δp_d	Downstream pressure build up, Pa.
$\Delta p'_d$	Simulated downstream pressure build up with random noise, Pa.
$\Delta p''_d$	Simulated downstream pressure build up with random and resolution noise, Pa.
Δt	Simulation step, s.
σ	Standard deviation.
μ	Mean.
$\delta(z)$	Centred probability density function of a Gaussian random variable z.
ε	Error between analytical results and numerical results.
η	Capacity parameter.
$\theta_{d,t}$	Downstream time lag, s.
θ_d	Actual downstream time lag, s.

3.8 References

[1] L.M. Robeson, The upper bound revisited, J. Memb. Sci. 320 (2008) 390–400. doi:10.1016/j.memsci.2008.04.030.

[2] L.M. Robeson, Correlation of separation factor versus permeability for polymeric membranes, J. Memb. Sci. 62 (1991) 165–185. doi:10.1016/0376-7388(91)80060-J.

[3] B.D. Freeman, Basis of Permeability/Selectivity Tradeoff Relations in Polymeric Gas Separation Membranes, Macromolecules. 32 (1999) 375–380. doi:10.1021/ma9814548.

[4] H.A. Daynes, S.W.J. Smith, The Process of diffusion through a rubber membrane, Proc. R. Soc. A Math. Phys. Eng. Sci. 97 (1920) 286–307. doi:10.1098/rspa.1983.0054.

[5] R.M. Barrer, E.K. Rideal, Permeation, diffusion and solution of gases in organic polymers, Trans. Faraday Soc. 35 (1939) 628–643.

[6] R.M. Felder, Estimation of gas transport coefficients from differential permeation, integral permeation, and sorption rate data, J. Memb. Sci. 3 (1978) 15–27. doi:10.1016/S0376-7388(00)80408-1.

[7] Y. Chen, Y. Zhang, X. Feng, An improved approach for determining permeability and diffusivity relevant to controlled release, Chem. Eng. Sci., 65 (2010) 5921-5928. https://doi.org/10.1016/j.ces.2010.08.028

[8] R.D. Siegel, R.W. Coughlin, Errors in diffusivity as deduced from permeation experiments using the time-lag technique, J. Appl. Polym. Sci. 14 (1970) 3145–3149. doi:10.1002/app.1970.070141218.

[9] L. Bao, J.R. Dorgan, D. Knauss, S. Hait, N.S. Oliveira, I.M. Maruccho, Gas permeation properties of poly(lactic acid) revisited, J. Memb. Sci. 285 (2006) 166–172. doi:10.1016/j.memsci.2006.08.021.

[10] F. Vasak, Z. Broz, A method for determination of gas diffusion and solubility coefficients in poly (vinyltrimethylsilane) using a personal computer, J. Memb. Sci. 82 (1993) 265–276. doi:10.1016/0376-7388(93)85191-X.

[11] K. Toi, T. Ito, T. Shirakawa, H. Ichimura, I. Ikemoto, Use of a microcomputer with a gas permeation apparatus, J. Appl. Polym. Sci. 29 (1984) 2413–2419. doi:10.1002/app.1984.070290715.

[12] S.S. Dhingra, E. Marand, Mixed gas transport study through polymeric membranes, J. Memb. Sci. 141 (1998) 45–63. doi:10.1016/S0376-7388(97)00285-8.

[13] J.P.G. Villaluenga, B. Seoane, Experimental estimation of gas-transport properties of linear low-density polyethylene membranes by an integral permeation method, J. Appl. Polym. Sci. 82 (2001) 3013–3021. doi:10.1002/app.2156.

[14] K. Mizoguchi, K. Terada, Y. Naito, T. Hirose, Y. Kamiya, Experimental estimation of gas-transport properties of linear low-density polyethylene membranes by an integral permeation method, Sen-I Gakkaishi. 46 (1990) 568–574.

[15] S. Lashkari, B. Kruczek, Effect of resistance to gas accumulation in multi-tank receivers on membrane characterization by the time lag method. Analytical approach for optimization of the receiver, J. Memb. Sci. 360 (2010) 442–453. doi:10.1016/j.memsci.2010.05.043.

[16] E. Favre, N. Morliere, and D. Roizard, "Experimental evidence and implications of an imperfect upstream pressure step for the time-lag technique," , J. Memb. Sci, vol. 207, no. 1, pp. 59–72, 2002.

[17] A. Alsari, B. Kruczek, and T. Matsuura, "Effect of Pressure and Membrane Thickness on the Permeability of Gases in Dense Polyphenylene Oxide (PPO) Membranes: Thermodynamic Interpretation," Separation Science and Technology, vol. 42, no. 10, pp. 2143–2155, 2007.

[18] Y. Maeda and D. Paul, "Selective gas transport in miscible PPO-PS blends," Polymer, vol. 26, no. 13, pp. 2055–2063, 1985.

[19] R. Chapanian, F. Shemshaki, and B. Kruczek, "Flow rate measurement errors in vacuum tubes: Effect of gas resistance to accumulation," The Canadian Journal of Chemical Engineering, vol. 86, no. 4, pp. 711–718, 2008.

[20] S. Lashkari, B. Kruczek, Reconciliation of membrane properties from the data influenced by resistance to accumulation of gasses in constant volume systems, Desalination. 287 (2012) 178–189. doi:10.1016/j.desal.2011.01.071.

[21] B. Kruczek, F. Shemshaki, S. Lashkari, R. Chapanian, H.L. Frisch, Effect of a resistance-free tank on the resistance to gas transport in high vacuum tube, J. Memb. Sci. 280 (2006) 29–36. doi:10.1016/j.memsci.2006.01.001.

[22] M. Al-Ismaily, J.G. Wijmans, B. Kruczek, A shortcut method for faster determination of permeability coefficient from time lag experiments, J. Memb. Sci. 423–424 (2012) 165–174. doi:10.1016/j.memsci.2012.08.009.

[23] P. Taveira, A. Mendes, C. Costa, On the determination of diffusivity and sorption coefficients using different time-lag models, J. Memb. Sci. 221 (2003) 123–133. doi:10.1016/S0376-7388(03)00252-7.

[24] R.C.L. Jenkins, P.M. Nelson, L. Spirer, Calculation of the transient diffusion of a gas through a solid membrane into a finite outflow volume, Trans. Faraday Soc. 66 (1969) 1391–1401.

[25] C.E. Rogers, Permeation of Gases and Vapours in Polymers, in: J. Comyn (Ed.), Polym. Permeability, Springer Netherlands, Dordrecht, 1985: pp. 11–73. doi:10.1007/978-94-009-4858-7_2.

[26] J. Crank, The mathematics of diffusion, Oxford Univ. Press. (1975) 414. doi:10.1016/0306-4549(77)90072-X.

[27] J.C. Shah, Analysis of permeation data: evaluation of the lag time method, Int. J. Pharm. 90 (1993) 161–169. doi:10.1016/0378-5173(93)90152-6.

[28] D.R. Paul, A.T. Dibenedetto, Diffusion in amorphous polymers, J. Appl. Polym. Sci. 39 (1966) 1496–1512. doi:10.1002/app.1960.070041025.

[29] J.A. Barrie, H.G. Spencer, A. Quig, Transient diffusion through a membrane separating finite and semi-infinite volumes, J. Chem. Soc. Faraday Trans. 1 Phys. Chem. Condens. Phases. 71 (1975) 2459. doi:10.1039/f19757102459.

[30] X.Q. Nguyen, Z. Brož, F. Vašák, Q.T. Nguyen, Manometric techniques for determination of gas transport parameters in membranes. Application to the study of dense and asymmetric poly (vinyltrimethylsilane) membranes, J. Memb. Sci. 91 (1994) 65–76. doi:10.1016/0376-7388(94)00019-0.

[31] N. Al-Qasas, J. Thibault, B. Kruczek, The effect of the downstream pressure accumulation on the time-lag accuracy for membranes with non-linear isotherms, J. Memb. Sci. 511 (2016) 119–129. doi:10.1016/j.memsci.2016.03.047.

[32] H. Wu, N. Al-Qasas, B. Kruczek, J. Thibault, Simulation of Time-Lag Permeation Experiments Using Finite Differences, J. Fluid Flow, Heat Mass Transf. 2 (2015) 1–17. doi:10.11159/jffhmt.2015.003.

[33] S.W. Rutherford, D.D. Do, Review of time lag permeation technique as a method for characterisation of porous media and membranes, Adsorption. 3 (1997) 283–312. doi:10.1007/BF01653631.

[34] B. Carnahan, H. A. Luther, and J. O. Wilkes, Applied numerical methods. Malabar, FL: R.E. Krieger Pub. Co., 1990.

[35] J.H. Petropoulos, C. Myrat, Error analysis and optimum design of permeation time-lag experiments, J. Memb. Sci. 2 (1977) 3–22. doi:10.1016/S0376-7388(00)83229-9.

[36] D.M. Himmelblau, Process analysis by statistical methods, New York : Wiley, 1970.

[37] B. Kruczek, H.L. Frisch, R. Chapanian, Analytical solution for the effective time lag of a membrane in a permeate tube collector in which Knudsen flow regime exists, J. Memb. Sci. 256 (2005) 57–63. doi:10.1016/j.memsci.2005.02.006.

[38] S. Lashkari, B. Kruczek, H.L. Frisch, General solution for the time lag of a single-tank receiver in the Knudsen flow regime and its implications for the receiver's configuration, J. Memb. Sci. 283 (2006) 88–101. doi:10.1016/j.memsci.2006.06.015.

[39] W. Ogieglo, H. Wormeester , K. J. Eichhorn, M. Wessling, & N. E. Benes, In situ ellipsometry studies on swelling of thin polymer films: A review. Progress. Pol. Sci, 42, (2015) 42-78.

3.9 Appendix

Table 3.A.1 Simulation conditions and analysis parameters for Fig. 3.2-3.3 and 3.5-3.10.

Fig.	W (s)	NP	p_0 (atm)	η ($\times 10^{-6}$)	V_d (m^3)	σ (Pa)
3.2 3.3	50	100	1	10	0.00279	0.0001, 0.001, 0.01
3.5	50	100	0.1, 1, 10	10	0.00279	-
3.6	50	100	1	1, 10, 100	0.0279, 0.00279 0.000279	0.0001, 0.001, 0.01
3.7	50	50,100,200	1	10	0.00279	0.001
3.8	25, 50, 100	100	1	10	0.00279	0.001
3.9	25, 50, 100, 150	100	1	10	0.00279	0.001
3.10	-	-	1	10	0.00279	-
Membrane thickness L: 0.00003 m; Membrane area A: 0.00125m^2; Upstream volume V_u: 8×10^{-5} m^3; Temperature T: 293.15K; Diffusivity coefficient D: 4.2×10^{-12} m^2/s; Solubility coefficient S: 3×10^{-4} mol/m^3 Pa.						

Chapter 4

Design considerations for a novel polymeric membrane characterization system based on upstream pressure decay

H. Wu, Peter Leszczynski, J. Thibault, B. Kruczek*

Abstract

Dynamic gas permeation experiments, which provide the basis for the time-lag measurements, are a well-known method for determining permeability, diffusion and solubility coefficients of gases in polymer films. These dynamic permeation experiments are typically performed in a constant volume (CV) system, in which time-dependent gas permeation across the membrane is obtained from the rate of pressure increase in a receiving volume downstream from the membrane. In principle, one could monitor time-dependent gas permeation into the membrane based on the pressure decay rate in a fixed upstream volume. However, since the resolution of an absolute pressure transducer is inversely related to the pressure transducer's upper limit, the latter is not used in practical dynamic permeation experiments. On the other hand, dynamic permeation experiments have potential advantages relying on the upstream pressure decay.

In this paper, we present the progress in developing a constant-volume system capable of monitoring the rate of pressure decay. The latter is measured based on a pressure difference between a working part of the upstream volume, in which the pressure decreases because of gas permeation into the membrane, and the reference volume in which the pressure is constant. This approach allows overcoming the resolution limit of high-pressure absolute pressure transducers.

Determining the membrane permeation and diffusion properties with the time-lag method from the downstream pressure rise curve in a constant-volume permeation system is a commonly used method in membrane characterization research. Despite its simplicity and popularity, the nature of the downstream pressure measurement stops it from having a

broader application, such as permeation through thick barrier materials and having gas mixtures as feed gases. In comparison, the upstream time-lag method is inviting because of the shortened measurement time for barrier materials and the downstream apparatus's flexibility. The challenge of the upstream measurement comes from the measurement accuracy and the measurement range, which is usually sacrificed in a system due to an excessive dead volume, the existence of compression/expansion effect, and the temperature effect on the upstream pressure.

Keywords: Gas membrane characterization; Permeation experiment; Constant-volume system; Upstream pressure decay

Publication status: Results presented at NAMS 2019 and CCEC 2019.

***Corresponding author**

4.1 Introduction

When applied a driving force, such as gas pressure difference, to a dense membrane, transport phenomena happen. Gas molecules start to permeate across the membrane from the high-pressure side to the low-pressure side. An essential part of membrane characterization is determining its transport properties during permeation. These properties are a membrane's permeability (P), solubility (S), and diffusivity (D) to the gas molecules. When in contact with the dense membrane, the transport phenomena of gases can be represented by the famous solution-diffusion model [1,2]. The permeation follows 3 steps: (1) gas molecules dissolve into the upstream surface of the membrane; (2) dissolved gas molecules diffuse through the membrane; and (3) gas molecules emerge from the downstream surface of the membrane by desorption. Gas permeation experiments are a well-known method to measure a membrane's transport properties. Ongoing researches are done to improve the reliability of the measurement techniques [3-5]. Two primary techniques are the integral permeation method and the differential permeation method. The integral permeation method is typically done with a constant volume system or a constant

pressure system, where the membrane is initially degassed to a high vacuum before initiating the experiment. The measurement finishes when the system reaches a steady-state or a quasi-steady state. In a constant volume system, the volumes of the feed chamber and the receiving chamber are constant where the membrane permeation causes pressure at the feed side to decrease and the pressure at the permeate side to increase. Theoretically, the transport properties could be determined from the recorded pressure rise at the permeate side, or the pressure decrease at the feed side with Eq.(1). In a constant pressure system, the feed pressure is kept constant. The transport properties are obtained by measuring the permeate gas's flow rate while maintaining a constant permeate pressure (usually to the atmosphere pressure) with Eq.(2). Although techniques are widely used, the constant volume technique is favoured when the permeation rate is low because it is usually more sensitive than the constant pressure technique. [6]

$$P = \frac{VL}{p_0 ART}\frac{dp}{dt} \tag{1}$$

where A is the area of the membrane and p_0 is the feed pressure, T is the membrane temperature, R is the gas constant. V is the volume of the feed or the receiving chamber, dp/dt is the corresponding rate of pressure change in the chamber.

$$P = \frac{Lp_d}{\left(p_u - p_d\right) ART}\frac{dV}{dt} \tag{2}$$

where p_u is the pressure of the feed (upstream) chamber, and p_d is the receiving (downstream) chamber.

In a differential permeation method, an inert sweep gas is used at the downstream side of the membrane. The measurement is done under a dynamic state of the composition of the permeate. Measurements are performed continuously before reaching a steady state. [6]

The paper focuses on a constant-volume system. The Constant-volume system (Fig. 4.1) consists of 3 main sections: an upstream chamber, a downstream chamber, and a membrane. The membrane is usually held by a device called a membrane cell that provides support to the membrane and, in the meantime, cut off the contact between the interior and

exterior environment. Fig. 4.2 shows the membrane cell's interior configuration, consisting of an inlet port, a membrane, an O-ring (optional), porous support and an outlet port. The upstream and downstream chambers are closed volumes. The system is evacuated for 2 days to ensure the membrane and both sides are free of any gas before any experiment. Experiments start by performing a step change of the upstream pressure. The gas enters the membrane cell from the upstream chamber, permeates through the membrane and then exits to the downstream chamber. The upstream and downstream chambers are closed volumes so that the upstream pressure gradually decreases while the downstream pressure gradually increases during the experiment. The pressure changes can be recorded by a differential pressure transducer and an absolute pressure transducer for the upstream and downstream reservoirs.

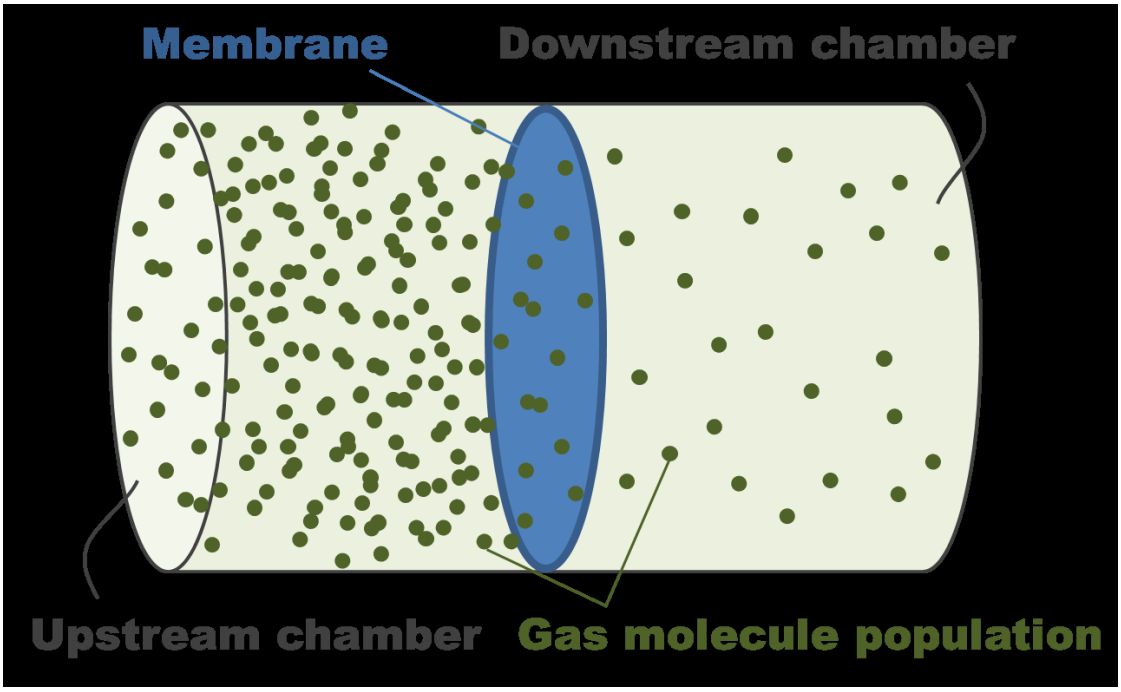

Figure 4.1 Illustration of the membrane-based pressure driven processes in a constant volume (CV) system.

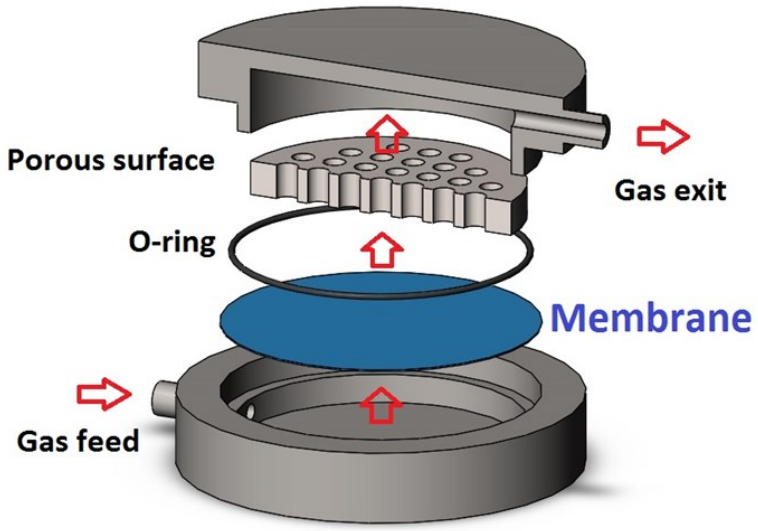

Figure 4.2 Schematic interior configuration of a membrane cell. [7]

Transport properties of a membrane are determined by the time lag method [8,9] analysis of the recorded pressure curves. Typical upstream pressure decay and downstream pressure accumulation profiles are plotted in Fig. 4.3. The time-axis intercepts of the linear portion of the curves are taken as the upstream (θ_u) and the downstream (θ_d) time lags. As shown by Eqs. (8) and (9) in Chapter 1, they are proportional to the reciprocal of the membrane diffusivity coefficient. Knowing the membrane thickness L, the diffusivity coefficient D is obtained by Eq. (3) or Eq.(4). The slopes (Eq. (10) and (11) in Chapter 1) of the linear portion depend on numerous system parameters (A, V_d, V_u and L), experimental conditions (p_0 and T), and membrane transport property (P, i.e. the permeability coefficient). Knowing the slope of one of the pressure curves, the system parameters and the experimental conditions, permeability coefficient P is obtained by Eq.(5) or Eq.(6). Known from Eq. (3) in Chapter 1, solubility coefficient S is the quotient of permeability coefficient P and diffusivity coefficient D. If the measurements and analysis are for the downstream pressure rise, the method is the downstream time-lag method. Instead, if the measurements and analysis are for the upstream pressure decay, the method is the upstream time-lag method.

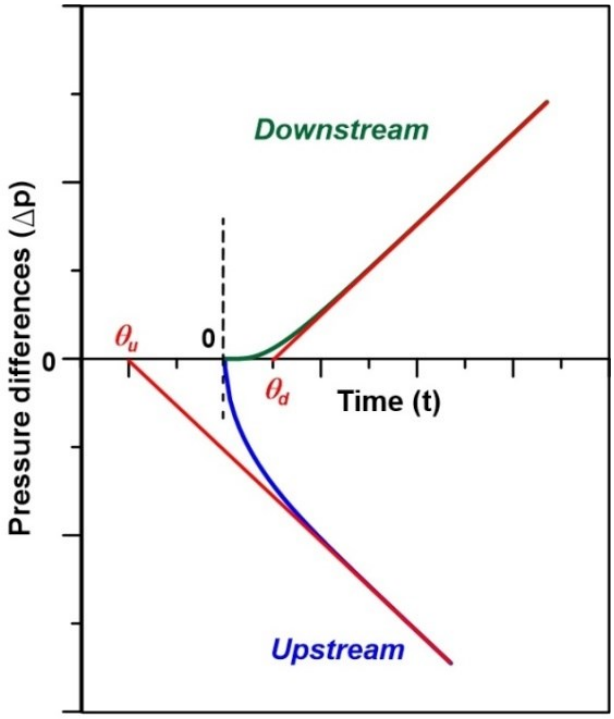

Figure 4.3 Schematic representation of the time lag determination from the upstream and downstream pressure difference curves. [7]

$$D = -\frac{L^2}{3\theta_u} \tag{3}$$

$$D = \frac{L^2}{6\theta_d} \tag{4}$$

$$P = -\frac{V_u LSlope_u}{p_0 ART} \tag{5}$$

$$P = \frac{V_d LSlope_d}{p_0 ART} \tag{6}$$

where V_u and V_d are the upstream and downstream volumes, θ_u is the upstream time lag, and θ_d is the downstream time lag.

Although the downstream time-lag method is commonly used and simple to conduct, there are potential advantages of dynamic permeation experiments relying on the upstream pressure decay. For example, when testing barrier films, it may take hours or

even days before any gas molecules appear at the membrane's permeate side. When no pressure rise data could be taken at the downstream side, the upstream pressure decay's maximum rate could be recorded and analyzed right after the initiation of a dynamic permeation experiment. Moreover, combining the capability to monitor the upstream pressure decay with monitoring of the downstream pressure-rise could provide invaluable information for the mechanism of gas transport in membranes, such as helping identify membranes with dual-mode sorption with non-instantaneous equilibrium and the partial immobilization transport mechanisms. Also, having the ability to follow the progress of gas permeation based on the membrane's upstream pressure decay will monitor the gas composition permeating through the membrane in real-time with a Gas Chromatograph. Consequently, one will carry out meaningful time-lag experiments with gas mixtures rather than just with single gases. Again, this will allow expanding the current state-of-the-art in membrane characterization to a new level.

4.2 Diagnosis of a current constant-volume system

The current CV membrane characterization system, schematically represented in Fig. 4.4, already contains a novel feature that allows the monitoring of the pressure decay at the membrane's feed side using a differential pressure transducer (DPT) [10,11]. However, due to an unavoidable expansion in the dead volume before the membrane (V_{dead}), which happens when opening of Valve 4 upon pressurization of the membrane, Valve 3, which separates the working and reference volumes, has to stay open when Valve 4 is being opened. Valve 3 can only be closed a few seconds after opening Valve 4. Consequently, the pressure decay during these few seconds cannot be recorded. Moreover, once Valve 3 is closed, the reference volume's pressure might not be equalized instantaneously, as reported by Al-Ismaily et al. [11]. Any pressure variation within the reference volume after closing Valve 4 affects the differential pressure transducer readings and thus the recorded gas permeation into the membrane. The maximum pressure range of the current differential pressure transducer (DPT) is between -0.2 torr to 0.2 torrs. Once the pressure difference between the reference and working volumes exceeds this range, the permeation experiment's progress can no longer be monitored. The useful range for monitoring the

pressure decay in the current system is further limited by a “compression effect” described by Al-Ismaily et al. [11]. Closing Valve 3 removes some finite volumes from the working and the reference sides of the system, i.e. instantaneous compression at both sides of Valve 3. However, since the compression at the reference side is more significant than that at the working side, the DPT records rapid expansion upon closing of Valve 3, which removes a portion of the useful range for recording the pressure decay due to gas permeation. The loss of the pressure range is proportional to the feed pressure. To record the pressure decay in the current CV system, gas permeation experiments had to be carried at feed pressures less than 21 × 103 Pa (3 psia) [11].

Consequently, the preliminary experiments reported in Chapter 5 were monitored exclusively based on the pressure accumulation at the membrane's permeate side. Moreover, based on the detailed accuracy analysis in Chapter 3 and sample experimental results shown in Chapter 5, it was realized that the current absolute pressure transducer at the permeate side does not satisfy the need for high accuracy experiments. The main issues with the current system are summarized in Table 4.1.

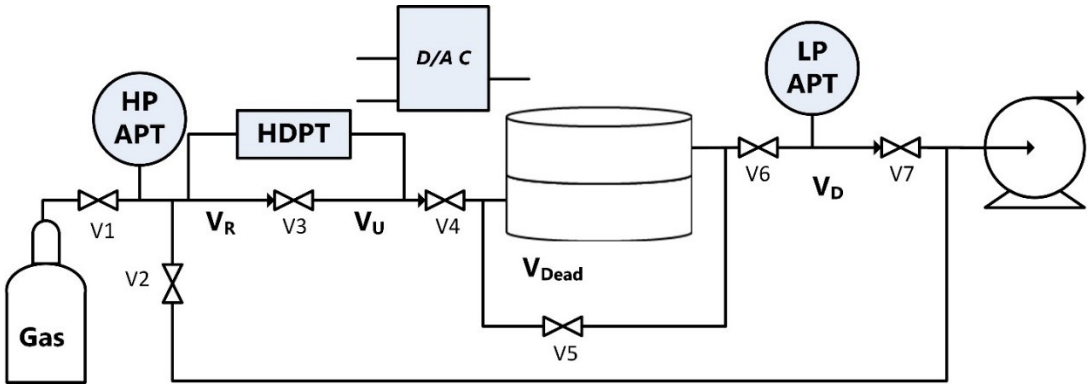

Figure 4.4 Schematic diagram of the current CV system.

Table 4.1 Main issues with the current CV system and dependent variables.

#	Main issues	Dependent variables
1	Pressure transducer	Downstream measurement accuracy and range
2	Experimental protocol	Feed pressure and measurement range
3	Valve compression	Upstream measurement range
4	Dead volume	Upstream measurement range
5	Upstream volume	Upstream measurement range

Other than known problems, potential problems include temperature effects from the upstream chamber due to its high pressure. Therefore, the existing constant-volume system will be modified to solve the above problems and ensure both reliable pressure-rise and pressure-decay measurements.

4.3 A new design of the constant-volume system

Fig. 4.5 presents the configuration of the proposed CV membrane characterization system, which addresses the problems associated with the current CV system shown in Fig. 4.4. The first improvement is a new arrangement. The reference chamber and the upstream chamber are now arranged to shorten the configuration length, minimize the tube bends, and save space. V5 is relocated before V4 to minimize dead volume. The dead volume between the valve connecting the upstream chamber and the membrane cell and the upper surface of the membrane is unavoidable. However, the greater the dead volume, the greater the initial expansion upon opening Valve 3, the lower the actual feed pressure. Therefore, reducing the dead volume allows increasing the range of the feed pressure at which gas permeation experiments can be performed. V8 is installed between the upstream chamber and V4 and before the branch to V8 to avoid evacuating the whole upstream volume at the evacuation stage before experiments. The majority of the system is welded to minimize potential leaks.

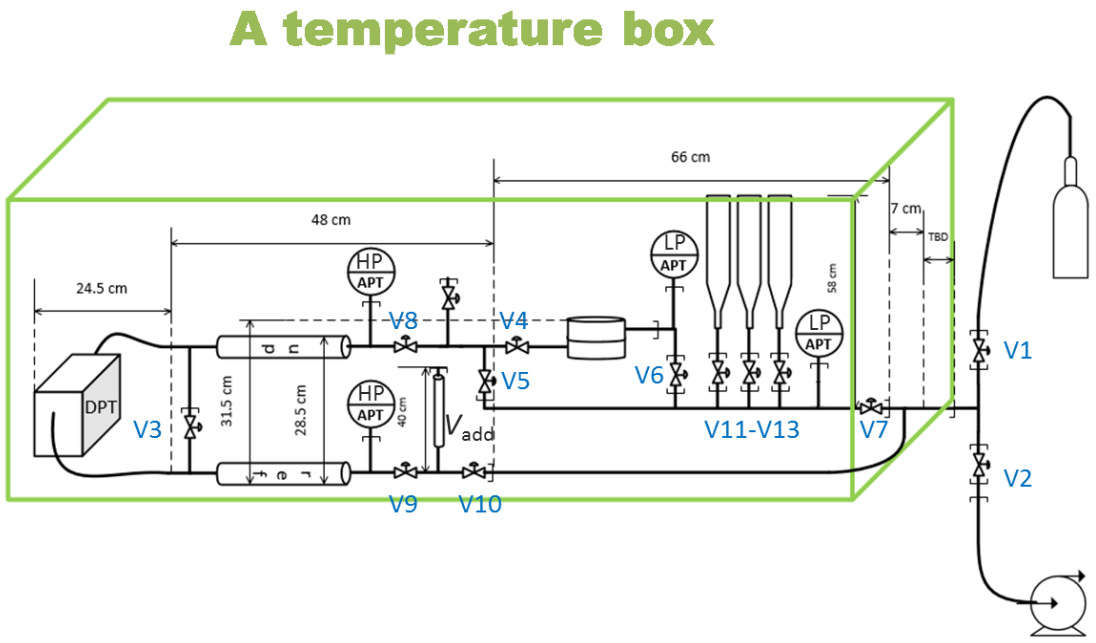

Figure 4.5 Schematic configuration of the proposed modifications of the CV system.

The second improvement is resizing the upstream volume and the reference volume and the addition of the V_{add}. As the working volume increases, the resolution of the pressure decay measurements will decrease. In addition, it results in additional time for the pressure variation caused by the gas movement to settle down. It is desired to exclude any variation that is not caused by membrane permeation during an experiment. Therefore the upstream volume has been resized to a smaller volume. The reference volume is resized as close as possible to the upstream volume. Apart from resizing, an additional volume was added to the end of the reference volume. The additional volume can be adjusted to the same size as the dead volume, so part of the reference pressure could be pre-released to match the feed pressure drop while opening V4 to start the experiment. This way, the measuring range of DPT could be saved.

The third improvement pertains to measuring instruments and the pump. The new instruments include a digital-analogue converter (DAC), a differential pressure transducer (DPT), two high-pressure absolute pressure transducers (HPAPT), and one low-pressure absolute pressure transduce beside the existing one. An analogue-to-digital converter (NI 9209, National Instrument, 24 bits, 500Sample/s) was upgraded to convert voltage signals to digital signals with enough recording resolution and frequency. A differential pressure

transducer (DPT) (CCR Process MKS range: -1 to 1 torr, resolution: 10^{-6} of full scale, accuracy: 0.05% of reading) was upgraded to a range enough to detect a meaningful upstream pressure decay without sacrificing the measuring accuracy. Two high-pressure absolute pressure transducers (HPAPT) (627F13TBC1B, CCR Process MKS, range: 0 to 2000 torr, resolution: 10^{-5} of full scale, accuracy: 0.12% of reading.) with one installed at the upstream side right before V8 to replace the existing one with high accuracy and the other symmetrically installed at the reference side. One additional low-pressure absolute pressure transducer (LPAPT) (627F11TBC1B, CCR Process MKS, range: 0 to 10 torr, resolution: 10^{-5} of full scale, accuracy: 0.12% of reading) installed right after the membrane cell to access the downstream pressure as close as possible the exit of the permeate side. With two downstream pressure transducers, studies could be done to measure the tank resistance [12]. The pump was upgraded to a two-stage turbo-diaphragm pump (Edwards T Station 75) to achieve better vacuuming and reduce evacuation time before experiments.

The fourth improvement is to change the experimental protocol to monitor the gas permeation experiment immediately after its initiation. This requires opening Valve 4 in Fig.4.5 when the Valve 3 between the reference and the working volumes is closed. Knowing the dead volume, i.e. the volume between Valves 4 and the membrane cell, the pressure in the working volume before the initiation of the experiment and the pressure in the reference volume can be adjusted accordingly beforehand to match the anticipated expansion in the working volume after the initiation of the experiments. The pressure in the reference volume can be adjusted by V_{add} or manually using the vacuum pump designated for this purpose and the new HPAPT if necessary. Suppose the pressure is decreased below the desired level. In that case, it can be adjusted using a new metering valve on the line connecting the reference volume with a high-pressure gas cylinder.

Similarly to the dead volume, this V_{add} chamber would be evacuated before the experiment. Opening the valve connecting it with the reference volume would create a similar expansion to the one in the working volume upon the membrane's pressurization. Consequently, a full range of the new DPT could be used to monitor the gas permeation experiment's progress using the pressure decay. Moreover, since the reference and the working volumes are proposed to be separated before starting the experiments, the problem

with possible non-instantaneous equalization of the pressure in the reference volume will be solved.

In addition to the main system prototype, two additional modifications of the system are shown in Fig. 4.6 (a) and (b). Adding a tee structure (joining V8, V10, and another tee connecting V4 and V5) with a small volume of upstream volume right before V4, the system provides access to two modules: the volume measuring module (Fig. 4.6 (a)) and a valve expansion dynamic module (Fig. 4.6 (b)). The volume measuring module is designed to measure the upstream volume, the reference volume, or the system's dead volume by attaching to the system a comparable known volume V_C at the free side of V10 and a high-pressure absolute pressure transducer. A simple calculation can be done with the ideal gas law to estimate any unknown volume. The valve expansion dynamic module uses a similar configuration but without the pressure transducer. Volume V_C is replaced with V_E which is designed to have the same volume as the dead volume V_{dead}. The module mimics the process of gas entering the dead volume after opening V4 before permeating through the membrane in an actual experiment.

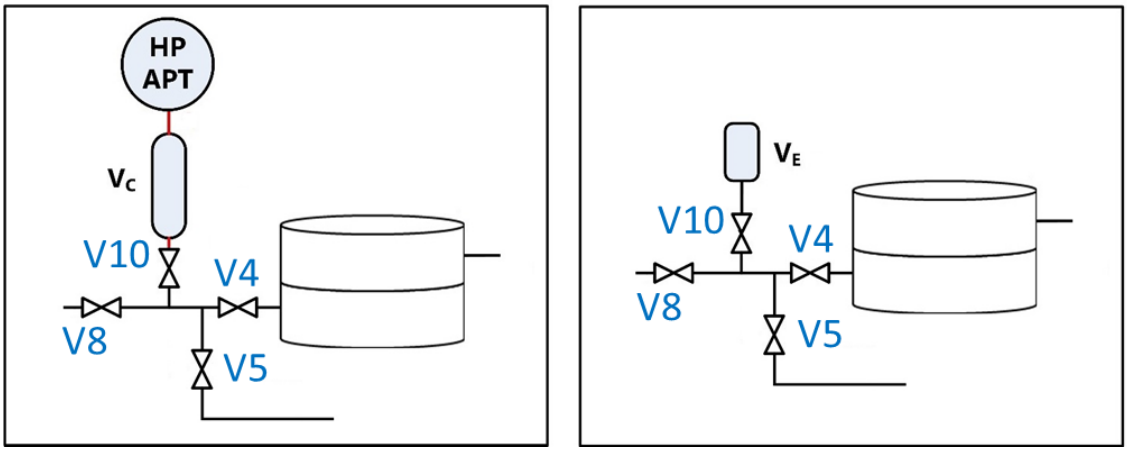

Figure 4.6 Schematic diagram showing the additional modules of the CV system.

To finalize the system, a temperature box as showed in Fig.4.5 needs to be installed to enclose the operating parts of the system. It is a necessary step as the reader will see from the section 4.4 example results that the upstream chamber is the high pressure side. Therefore the pressure decay is sensitive to any temperature variation in the lab environment. A temperature box with a temperature control system allow maintain the

temperature inside the box to further help with an accurate upstream pressure measurement. Fig. 4.7 shows a picture of the modified new CV system.

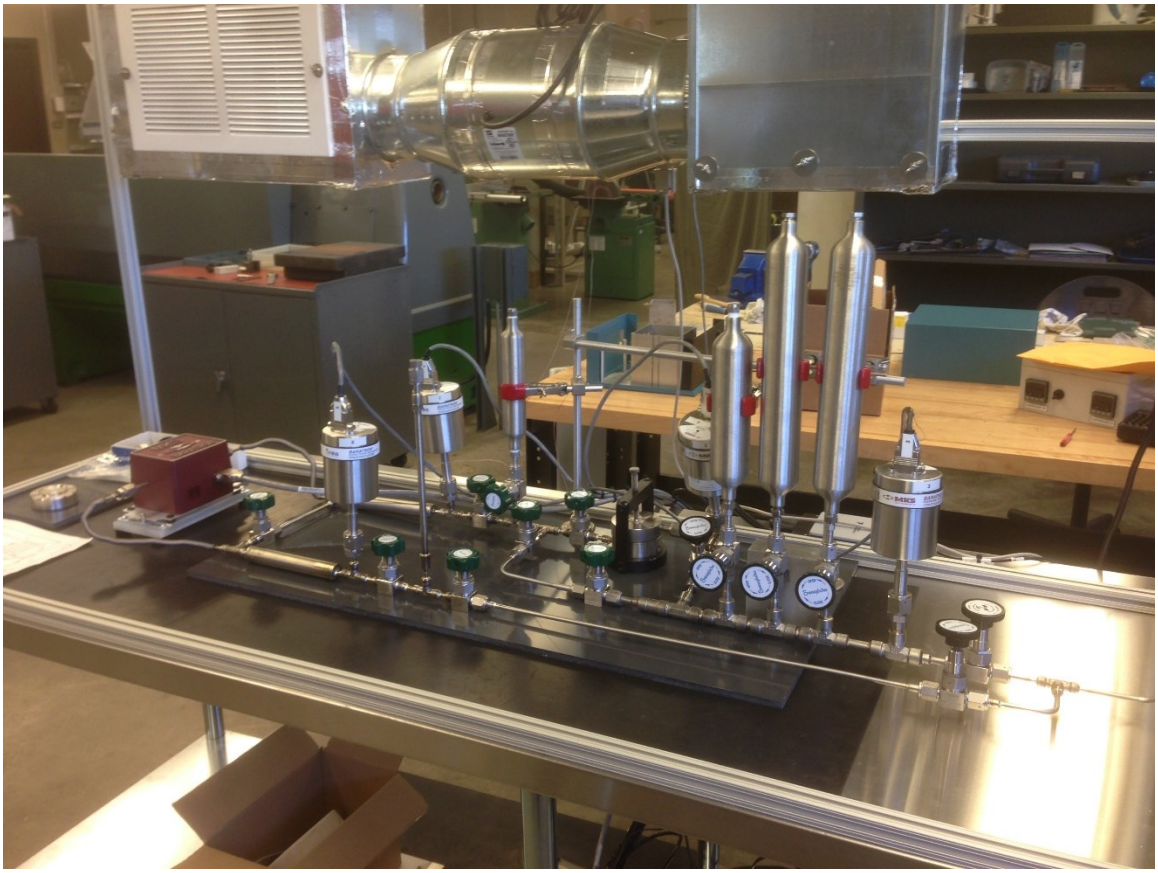

Figure 4.7 A picture of the modified new CV system.

4.4 Conclusion

Similarly to the downstream time-lag measurement, the upstream time lag can be used to estimate the membrane's transport properties. It has multiple advantages, such as allowing the measurement of properties of barrier materials much quicker. The addition of GC for the measurement in real-time gas mixture compositions permeating through the membrane would greatly benefit the upstream and the downstream time lags.

The challenges of the upstream measurement come from both the measurement accuracy and the measurement range. In this paper, five improvements were made to the

system to improve its capability of monitoring the rate of pressure decay. Firstly, the system was redesigned into a new configuration to minimize the dead volume and tube bends. Secondly, the upstream volumes were optimized to exclude unnecessary pressure variations during experiments. Thirdly, the electronic devices were upgraded to improve measurement accuracy. The fourth improvement is the new experimental protocol to allow monitoring the gas permeation experiment immediately after its initiation. The fifth improvement is adding a temperature control chamber, which is crucial for measuring the pressure decay accurately.

4.5 Acknowledgement

The authors gratefully acknowledge the financial support for this project provided by the Natural Science and Engineering Research Council of Canada.

4.6 Nomenclature

A	Membrane area, m^2.
D	Diffusion coefficient, m^2/s.
L	Membrane thickness, μm.
p_0	Constant pressure in the upstream chamber, Pa.
p_u	Upstream pressure change, Pa.
p_d	Downstream pressure change, Pa.
P	Permeability coefficient, $mol \cdot m/(m^2 \cdot Pa \cdot s)$.
R	Gas constant, $J/(K \cdot mol)$.
S	Solubility coefficient, $mol/(m^3 \cdot Pa)$.
t	Simulation time, s.
T	Absolute temperature, K.
$V_{\#}$	Valve with a number #.
V_d	Downstream volume, m^3.
V_{dead}	Dead volume, m^3.
V_R	Reference volume, m^3.

V_u	Upstream volume, m^3.
Δp_d	Downstream pressure build up, Pa.
Δp_u	Upstream pressure decay, Pa.
$\theta_{d,t}$	Downstream time lag, s.
θ_d	Actual downstream time lag, s.

4.7 References

[1] M. Al-Ismaily, J. G. Wijmans, and B. Kruczek, "A shortcut method for faster determination of permeability coefficient from time lag experiments," J. Memb. Sci., vol. 423–424, pp. 165–174. 2012.

[2] N. Al-Qasas, J. Thibault, and B. Kruczek, "A New Characterization Method of Membranes with Nonlinear Sorption Isotherm Systems Based on Continuous Upstream and Downstream Time-Lag Measurements," J. Memb. Sci., vol. 542, pp. 91-101, 2017.

[3] S. Lashkari, A. Tran, B. Kruczek, "Effect of back diffusion and back permeation of air on membrane characterization in constant pressure system", J. Memb. Sci., vol. 324, 2008, pp. 162-172. https://doi.org/10.1016/j.memsci.2008.07.006.

[4] S. Lashkari, B. Kruczek, "Reconciliation of membrane properties from the data influenced by resistance to accumulation of gasses in constant volume systems", Desalination, vol. 287, 2012, pp. 178-189. https://doi.org/10.1016/j.desal.2011.01.071.

[5] S.C. Fraga, M. Monteleone, M. Lanč, E. Esposito, A. Fuoco, L. Giorno, K. Pilnáček, K. Friess, M. Carta, N.B. McKeown, P. Izák, Z. Petrusová, J.G. Crespo, C. Brazinha, J.C. Jansen, "A novel time lag method for the analysis of mixed gas diffusion in polymeric membranes by on-line mass spectrometry: Method development and validation", J. Memb. Sci., vol. 561, 2018, pp. 39-58. https://doi.org/10.1016/j.memsci.2018.04.029.

[6] M. Sadrzadeh, M. Rezakazemi, T.Mohammadi, "Chapter 19: Fundamentals and Measurement Techniques for Gas Transport in Polymers", in: S. Thomas, R. Wilson, A. Kumar S., S.C. George (Eds), Transport Properties of Polymeric Membranes, Elsevier, 2018, pp. 391-423. https://doi.org/10.1016/B978-0-12-809884-4.00019-7.

[7] H. Wu, N. Alqasas, B. Kruczek, J. Thibault, Simulation of Time-Lag Permeation Experiments Using Finite Differences, J. Fluid Flow, Heat & Mass Transfer. vol. 2, 2015, pp. 14-25. https://doi.org/10.11159/jffhmt.2015.003

[8] H. A. Daynes, “The Process of Diffusion through a Rubber Membrane,” Proc. Roy. Soc. A: Math., Phys. Eng. Sci., vol. 97, no. 685, pp. 286–307, 1920.

[9] R. M. Barrer and E. K. Rideal, “Permeation, diffusion and solution of gases in organic polymers,” Trans. Faraday Soc., vol. 35, pp. 628, 1939.

[10] H. Wu, B. Kruczek, and J. Thibault, “Impact of Measuring Devices and Data Analysis on the Determination of Gas Membrane Properties” J. Memb Sci Research, vol. 4, pp. 4-14, 2018.

[11] M. Al-ismaily, “A Novel Method of Characterizing Polymer Membranes Using Upstream Gas Permeation Tests,” M.S. thesis, Dept. Chem. Bio. Eng., Univ. Ottawa, Ottawa, Canada, 2011.

[12] S. Lashkari and B. Kruczek, “Effect of resistance to gas accumulation in multi-tank receivers on membrane characterization by the time lag method. Analytical approach for optimization of the receiver,” J. Memb. Sci, vol. 360, no. 1-2, pp. 442–453, 2010.

Chapter 5

Instantaneous time lag: new insight on gas transport in membranes

Haoyu Wu, Jules Thibault and Boguslaw Kruczek*

Abstract

The time-lag method is the most common way to characterize gas transport properties in homogenous polymer membranes. It relies on the visual determination of a linear pressure response, which is then extrapolated to the time axis to obtain the time lag. This paper has systematically analyzed seemingly linear pressure responses at quasi-steady-state observed in conventional gas permeation experiments of nitrogen through high molecular weight homogeneous PPO membranes. Extrapolating the computer-fitted straight line, from a fixed and moving range of the experimental data to the time axis, allowed generating the plots of an instantaneous time lag as a function of time. It then became apparent that after reaching a plateau, the instantaneous time lag showed an apparent upward deviation. Numerical simulations of gas permeation experiments, in which different types of dual-mode sorption gas transport models were considered, suggest that the instantaneous time-lag curve's observed upward deviation is due to the non-instantaneous equilibrium between the penetrant molecules in the Langmuir's and Henry's sites. The observed plateau in the instantaneous time-lag does not indicate a quasi-steady-state, which occurs much later and is associated with a considerably more significant time lag.

This is the first time the concept of the instantaneous time lag to analyze the data obtained from a conventional time-lag gas permeation experiment is demonstrated to our

best knowledge. Moreover, although many researchers postulated non-instantaneous equilibrium between the Langmuir's and Henry's sites in dual-mode sorption membranes, the application of the instantaneous time lag presented in this paper provides an undeniable proof that this is the actual case, at least for the transport of nitrogen in high molecular weight PPO membranes.

Keywords: Gas membrane characterization; Permeation experiment; Instantaneous time lag; Dual-mode sorption; Non-instantaneous equilibrium

Publication status: To be submitted.

***Corresponding author**

5.1 Introduction

The use of membranes in gas separation relies on the differences in the permeability coefficients of individual gases in the membrane. Gas permeation in polymeric membranes is controlled by the diffusion of gas molecules, driven by the concentration gradient, preceded by instantaneous sorption from the feed gas phase. This is followed by rapid desorption into the permeate gas phase.

Above the glass transition temperature (T_g), segments of polymeric chains have sufficient energy to freely rotate along their axis, thus creating transient gaps and the transient opening between these gaps through which gas molecules can diffuse. This type of polymers is referred to as rubbery polymers; the rubbery membranes' transport mechanism is described by the solution-diffusion model [1]. Sorption in rubbery polymers follows Henry's law, and rubbery membranes are fully characterized by the determination of the permeability (P), diffusivity (D), and solubility (S) coefficients, where:

$$P = SD \tag{1}$$

Below T_g (i.e. in a glassy state), polymeric chains have insufficient energy to rotate freely, which leads to the formation of an excess free volume even though the total free

volume decreases with temperature. The excess free volume can be interpreted as a summation of gaps between segments of polymeric chains in which diffusing gas molecules are partly or entirely immobilized. Therefore, gas molecules diffusing through a glassy polymer membrane form two populations, present in normally densified sites between flexible segments of polymeric chains (Henry's sites), and those present in excess free volume between inflexible segments of polymer chains (Langmuir sites). Gas sorption in glassy polymers follows so-called dual-mode sorption. In the simplest case, gas molecules in Langmuir sites are assumed to be completely immobilized, yet the two populations of gas molecules are assumed to be in instantaneous equilibrium. The resulting solution-diffusion model, now referred to as the dual-mode sorption model, was described by Barrer *et al*. [2-4]. In addition to P, D and S, the complete characterization of the membrane, in this case, requires the determination of Langmuir's sites (C_L') and the affinity constant (b).

The basic solution-diffusion model with dual-mode sorption can be generalized by relaxing the two assumptions mentioned above [5-10]. Suppose there is no instantaneous equilibrium between the two populations of gas molecules. In that case, the transport model requires an additional parameter, which by the analogy with adsorption processes, can be referred to as the adsorption rate constant (k_{ad}). Furthermore, suppose gas molecules in the Langmuir's sites are not completely immobilized (i.e. partial immobilization). In that case, they are characterized by the diffusion coefficient, which is a fraction (F) of the diffusion coefficient in normally densified regions, such that: $0 < F < 1$. Some researchers also suggested the presence of two different types of Langmuir's sites with different affinities [11] and even a continuous distribution of Langmuir's sites [12]. Putting aside these suggestions, the solution-diffusion model with dual-mode sorption, partial immobilization in Langmuir sites and non-instantaneous equilibrium between Henry's and Langmuir's sites populations is complex. The complete characterization of the membrane in which this model governs gas transfer requires the determination of 7 parameters: P, D, S, C_L', b, k_{ad}, and F. It is important to emphasize that for any variation of the solution-diffusion model, the relationship between P, D and S given by Eq. (1) remains valid.

Regardless of the actual solution-diffusion model, the three main transport properties (P, D and S) are commonly determined from a dynamic gas permeation experiment. In this experiment, an utterly degassed membrane is exposed to a steep increase in feed pressure, which then is maintained constant. At the same time, time-dependent gas permeation across the membrane is determined from the rate of pressure increase in a fixed downstream volume on the other side of the membrane. The linear portion of the pressure versus time curve is extrapolated to the time axis to determine a time lag of the membrane (θ) [13]. Knowing the membrane thickness (L), D is calculated from Eq. (2):

$$\theta = \frac{L^2}{6D} \tag{2}$$

The slope of the linear portion of the pressure versus time graph is directly proportional to P. Then, knowing P and D, Eq. (1) can be used to calculate S. Thus, the time-lag method allows determining P, D and S from a single gas permeation experiment.

It is important to emphasize that Eq. (2) is valid only for rubbery membranes, in which gas sorption follows Henry's law. Moreover, the derivation of Eq. (2), among others, also assumes that the gas concentration at the membrane-permeate side interface is zero during the gas permeation experiment, which at best is only a good approximation. More complex expressions equivalent to Eq. (2) for the solution-diffusion membranes with dual-mode sorption are available in the literature [3,4,14]. Still, these expressions also rely on the assumption of zero concentration at the membrane-permeate side interface. Without this assumption, there is no analytical solution of the governing partial differential equation (PDE). The expression relating θ with D is derived, even for the simplest case of the solution-diffusion model.

In our recent paper [15], we reviewed how the oversimplified boundary condition at the membrane-permeate interface affects membrane characterization by the time-lag method. More specifically, using numerical simulations, we considered the simplest case of the dual-mode sorption, solution-diffusion model with complete immobilization in Langmuir's sites and instantaneous equilibrium between the Langmuir's and Henry's sites,

to assess the effect of gas accumulation at the permeate side of the membrane on the accuracy the time-lag method. When gas accumulation at the permeate side is taken into consideration, there is no longer a unique time lag; instead, it is more appropriate to consider an instantaneous time lag (a time-dependent quantity). On the other hand, there is a maximum instantaneous time lag, which is always smaller than the time lag corresponding to the zero concentration at the membrane-permeate interface (theoretical time lag). Nevertheless, the difference between the theoretical time lag and the maximum instantaneous time lag never exceeds 1%, and consequently, the latter can be used for the membrane characterization. In the follow-up theoretical paper [16], we have proposed a method to characterize dual-mode sorption fully, solution-diffusion membranes with complete immobilization in Langmuir's sites instantaneous equilibrium between the Langmuir's and Henry's sites in just two gas permeation experiments at different pressures. The minimization of the number of gas permeation experiments is allowed by simultaneous monitoring of the pressure rise at the permeate side of the membrane and the pressure decay at the feed side of the membrane, which is subsequently used to determine the corresponding instantaneous downstream and upstream time lags as well as their ratio as a function of time.

In this paper, the concept of time-dependent instantaneous time lag is tested in practice for the characterization of high molecular weight polyphenylene oxide (PPO) membranes. Gas permeation tests were carried out at different feed pressures and in different downstream volumes for gas accumulation. The experimental downstream pressure response data is analyzed using a "moving window" approach to produce plots of the instantaneous time lag as a function of time, which are then compared to theoretical plots generated for different types of dual-mode sorption solution-diffusion models. The new way of data analysis proposed in this paper proves the existence of a non-instantaneous equilibrium between gas molecules in Henry's and Langmuir's sorption sites during their diffusion through a PPO membrane.

5.2 Theoretical background

In the following, we review the partial differential equations (PDE) governing the transport in different types of solution-diffusion membranes in so-called time-lag gas permeation experiment. The membrane is initially degassed, and the transport process is initiated by a step change in the feed pressure from 0 to p_0; p_0 is then maintained constant. The equilibrium between gas phase and the membrane surface is assumed to be established instantaneously. In the ideal case, gas concentration at the membrane-permeate side interface is zero during the entire experiment. The above describes a transient diffusion problem, which requires using the following continuity equation:

$$\frac{\partial C}{\partial t} = -\frac{\partial J}{\partial x} \tag{3}$$

The following are the corresponding initial and boundary conditions:

$$\begin{aligned} &\text{IC: } C\left(x,0\right) = 0 && \text{(a)} \\ &\text{BC1: } C\left(0,t\right) = Sp_0 && \text{(b)} \\ &\text{BC2: } C\left(L,t\right) = 0 && \text{(c)} \end{aligned} \tag{4}$$

where C is the concentration of the permeating gas in the membrane, and x is a distance within the membrane from the feed side-membrane interface (x = 0); at the membrane-permeate interface, $x = L$; and J is the diffusive flux of the gas, which is given by Fick's first law:

$$J = -D\frac{\partial C}{\partial x} \tag{5}$$

It is important to emphasize that a conventional time-lag method relies on monitoring the pressure rise, $p_d(t)$, in a fixed volume downstream from the membrane. Consequently, the more appropriate representation is the second boundary condition is given by:

$$\text{BC2: } C\left(x = L\right) = S \cdot p_d\left(t\right) \tag{6}$$

In all cases considered below, the transport process is assumed to be isothermal. Moreover, the solubility (S) and diffusivity (D) coefficients in normally densified regions of the polymer matrix are assumed constant, which imply that P is also constant.

5.2.1 Linear sorption – applicability of Henry's law

In the case of rubbery polymers, assuming that there is no plasticization, gas sorption is governed by Henry's law:

$$C = Sp \tag{7}$$

In rubbery membranes, the entire polymer matrix is normally densified, and consequently, the governing PDE is obtained by substituting Eq. (5) into Eq. (3), which leads to Fick's second law of diffusion:

$$\frac{\partial C}{\partial t} = D\frac{\partial^2 C}{\partial x^2} \tag{8}$$

In this base case, the complete characterization of a membrane requires the determination of D and S.

5.2.2 Nonlinear dual-mode sorption

It is generally accepted that below T_g, the gas sorption in polymers follows the so-called dual-mode sorption model [4,18,19]:

$$C = C_H + C_L \tag{9}$$

where C_H and C_L refer to the concentration of gas molecules in normally densified polymer matrix (Henry's sites) and those in the Langmuir sites, respectively. Substituting expressions for C_H and C_L in Eq. (9) leads to:

$$C = Sp + \frac{C_L' bp}{1 + bp} \tag{10}$$

where C'_L and b are the capacity and the affinity factors of the Langmuir's sites, respectively. Recognizing that the pressure can be expressed by $p = C_H / S$, Eq. (9) can also be written in the following form:

$$C = C_H + \frac{C_H C'_L [b/S]}{(1 + [b/S] C_H)} \tag{11}$$

In the simplest case of dual-mode sorption, it is assumed that gas molecules in the Langmuir's sites are completely immobilized, thus Fick's first law becomes:

$$J = -D_H \frac{\partial C_H}{\partial x} \tag{12}$$

where: D_H is the diffusivity of gas molecules within the membrane considering that only the molecules in Henry's sites are mobile; D_H and C_H are equivalent to D and C in Eq. (8). Substituting Eqs. (11) & (12) into Eq. (3) and multiplying by unity, $\partial C_H / \partial C_H$, leads after rearrangement to:

$$\frac{\partial}{\partial C_H}\left[C_H + \frac{C_H C'_L [b/S]}{(1 + [b/S] C_H)} \right] \frac{\partial C_H}{\partial t} = D_H \frac{\partial^2 C_H}{\partial x^2} \tag{13}$$

Differentiating the term in the square brackets leads to the final PDE [14,17]:

$$\left[1 + \frac{C'_L [b/S]}{(1 + [b/S] C_H)^2} \right] \frac{\partial C_H}{\partial t} = D_H \frac{\partial^2 C_H}{\partial x^2} \tag{14}$$

Compared to the base case given by Eq. (8), the complete characterization of a membrane in which the transport is governed by Eq. (14) requires determination of b and C'_L, in addition to D and S.

5.2.2.1 Partial immobilization

If gas molecules in Langmuir sites are not completely immobilized, the corresponding model is referred to as a partial immobilization model [3,4]. In this case, the Fick's first law is given by:

$$J = -D_H \frac{\partial C_H}{\partial x} - D_L \frac{\partial C_L}{\partial x} \tag{15}$$

where: D_L is the diffusivity of in the Langmuir's sites, which is commonly expressed in terms of a fraction F ($0 < F < 1$) of the diffusivity in Henry's sites [20]:

$$D_L = FD_H \tag{16}$$

Alternatively, F can be interpreted as a fraction of penetrant molecules in the Langmuir's sites with the same diffusivity as the penetrant molecules in Henry's sites. In contrast, the remaining penetrant molecules in the Langmuir's sites, represented by $1 - F$, are entirely immobilized. In the latter approach, the concentration of the mobile gas molecules (C_m) and Fick's first law become:

$$C_m = C_H + FC_L \tag{17}$$

$$J = -D_H \frac{\partial C_m}{\partial x} \tag{18}$$

This allows writing the governing PDE in a form similar to Eq. (14):

$$\left[1 + \frac{C'_L [b/S]}{\left(1 + [b/S] C_H\right)^2}\right] \frac{\partial C_H}{\partial t} = D_H \frac{\partial^2 C_H}{\partial x^2} + FD_H \frac{\partial^2 C_L}{\partial x^2} = D_H \frac{\partial^2 C_m}{\partial x^2} \tag{19}$$

Compared to the case described by Eq. (14), the complete characterization of a membrane in which the transport is described by Eq. (19) requires determination of F, in addition to D, S, b and C'_L.

5.2.2.2 Non-instantaneous equilibrium

The previous governing PDE, given by Eq. (8), Eq. (14) and Eq. (19), relied on the assumption of instantaneous equilibrium between the penetrant's molecules in the Henry's and Langmuir's sites. By relaxing this assumption, the mass transfer between the two populations of molecules must be considered. This mass transfer is analogous to a reversible adsorption process:

$$E + G \underset{k_d}{\overset{k_{ad}}{\rightleftharpoons}} EG \tag{20}$$

where: E are the empty Langmuir's sites, which correspond to $C'_L - C_L$, G are the adsorbable gas molecules, which correspond to C_H, and EG are the occupied Langmuir's sites, which correspond to C_L; $k_{ad}\left[m^3 \cdot mol^{-1}s^{-1}\right]$ and $k_d\left[s^{-1}\right]$ are the adsorption and the desorption rate constants, respectively. In addition, it is essential to note that [4]:

$$\frac{k_{ad}}{k_d} = \frac{b}{S} \tag{21}$$

The corresponding adsorption rate, $r_{ad}\left[mol \cdot m^{-3}s^{-1}\right]$, and the desorption rate, $r_d\left[mol \cdot m^{-3}s^{-1}\right]$, are given by:

$$r_{ad} = k_{ad} C_H \left(C'_L - C_L\right) \tag{22}$$

$$r_d = k_{ad} \frac{S}{b} C_L \tag{23}$$

At equilibrium, the rates of adsorption and desorption are equal, but before the equilibrium is established, the mass transfer between the two populations must be taken into consideration. In the case of partial immobilization, since the two populations are not at instantaneous equilibrium, the governing PDE has to be split into a system of two equations, one describing the transport in the Henry's sites and the other in the Langmuir's sites. The term, $r_{ad} - r_d$, must have the opposite sign in the respective equations to satisfy the mass balance. Thus:

$$\frac{\partial C_H}{\partial t} = D_H \frac{\partial^2 C_H}{\partial x^2} - k_{ad}\left[C_H\left(C'_L - C_L\right) - \frac{S}{b}C_L\right] \tag{24}$$

$$\frac{\partial C_L}{\partial t} = D_L \frac{\partial^2 C_L}{\partial x^2} + k_{ad}\left[C_H\left(C'_L - C_L\right) - \frac{S}{b}C_L\right] \tag{25}$$

Therefore, in this most general case, the complete characterization of the membrane, in which the transport is governed by the set of the PDE given by Eqs. (24-25), requires the determination of D, S, b, C'_L, F and k_{ad}.

5.3 Methodology

5.3.1 Membranes and permeation experiments

The membrane was a solution-cast high molecular polyphenylene oxide (PPO) film of a thickness of 30 μm prepared by a spin-coating technique. The details of membrane preparation are described elsewhere [21]. Gas permeation experiments were carried out in a constant-volume system described elsewhere [22,23]. Before the experiment, the system was evacuated for two days to ensure the membrane was completely degassed. The experiments were started by performing a step change of the upstream pressure. The experiments were carried out at the following feed pressures (p_0): 29 314 Pa, 58 627 Pa, 117 255 Pa, 175 881 Pa, 234 508 Pa, 293 135 Pa and 351 762 Pa. The progress of gas permeation was monitored by a pressure transducer (MKS model 627B11TBC1B) having a linear range from 0 to 1333 Pa with a 0.0267 Pa reading accuracy and the maximum error corresponding to 0.12% of the read pressure. The pressure transducer was installed in the downstream volume, which could be varied. The experiments were carried out using the following downstream volumes (V_d): 1.15×10^{-5} m^3, 6.15×10^{-5} m^3 and 1.42×10^{-4} m^3. The purpose of performing experiments at different feed pressures and different downstream volumes was two-fold. On the one hand, the experiments at a low p_0 and a large V_d allowed to mimic more closely the second boundary condition given by Eq. (4c) and to increase the time the permeation data could be recorded. On the other hand, the

experiments at high p_0 and small V_d allowed minimizing the noise in recording the downstream pressure data [24].

5.3.2 Analysis of the permeation data

Regardless of the actual gas transport mechanism in the membrane, it takes time for gas molecules to emerge from the membrane following a step change of gas pressure on the feed side. This is illustrated in Fig. 5.1, which shows the progress of a typical gas permeation experiment. The rate of downstream pressure increase, which is directly proportional to the gas's permeation rate, gradually increases with time until quasi-steady-state conditions are reached, at which the rate of downstream pressure increases and hence the permeation rate becomes constant. Extrapolation of the linear portion of the downstream pressure response to the time axis gives the downstream time lag (θ), which in the simplest case of the solution-diffusion model for the gas transport in rubbery membranes, subject to the initial and boundary conditions given by Eq. (4), is defined by Eq. (2). Consequently, θ is considered to be a constant value**.**

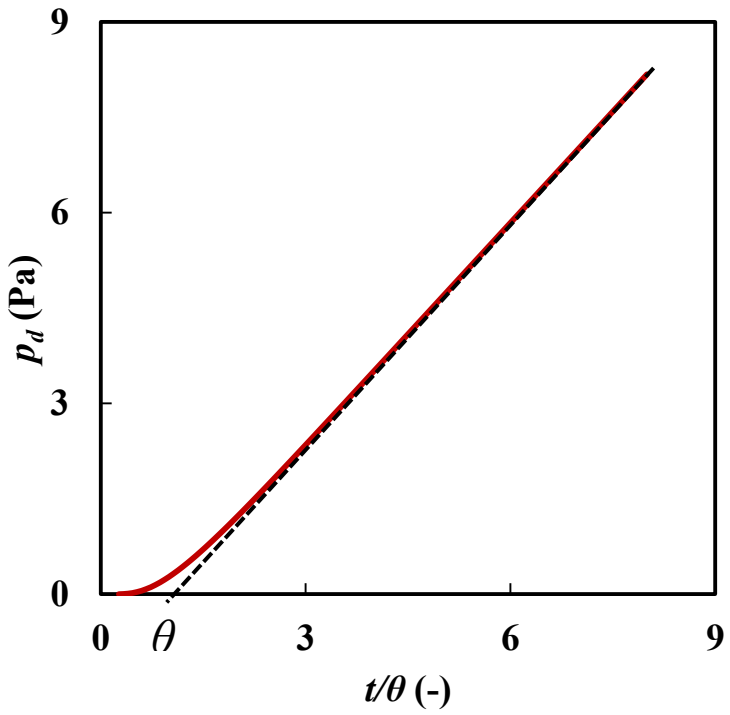

Figure 5.1 Typical result of a time-lag gas permeation experiment; the time lag is determined by extrapolation of the linear portion of the downstream pressure response curve to the time axis. Quasi-steady-state is reached approximately at a time corresponding to 3θ.

Measurement of the downstream pressure response implies that the boundary condition given by Eq. (4c) can only be approximated. In reality, the boundary condition at the membrane's permeate interface is given by Eq. (6). To solve the governing PDE analytically, even in the simplest case defined by Eq. (8), requires a guessed function $p_d(t)$. Thus, the outcome is only an approximate analytical solution. Recently, using numerical simulations, Al-Qasas et al. examined how the problem of the oversimplified boundary condition at the membrane-permeate interface affects the determination of the time lag in the simplest case of dual-mode sorption membranes described by Eq. (14) [15]. They introduced an instantaneous time lag, which is a time-dependent quantity, unlike the regular time lag. More specifically, for a given time t, the pressure response data generated in a window Δt ($t - \Delta t/2$, $t + \Delta t/2$) was used to obtain a linear trend line, which was

extrapolated to the time axis. The resulting time-axis intercepts represent the instantaneous time lag at time t, denoted as θ_t.

We have used the instantaneous time lag concept to analyze the experimental data from permeation experiments described in Section 3.1. In addition to the method described above, which we refer to as a "moving window (MW) approach", we also determined θ_t using an "expanding window (EW) approach". The two approaches are schematically shown in Fig. 5.2. In the MW approach Δt is constant, and one can analyze the data starting $t = \Delta t/2$. Eventually, at quasi-steady state θ_t should approach a constant value corresponding to θ. In the expanding window approach, the window starts from a point where the permeation is deemed to have reached a quasi-steady-state, and the window size increases until the experiment finishes.

Similarly to the MW approach, the instantaneous time lag corresponds to the time from the middle of the window. However, since the window size increases, the time axis in the EW approach does not correspond to the time axis in the MW approach. It is also important to emphasize that one cannot start the analysis at small-time values in the EW approach because it would include a transient period.

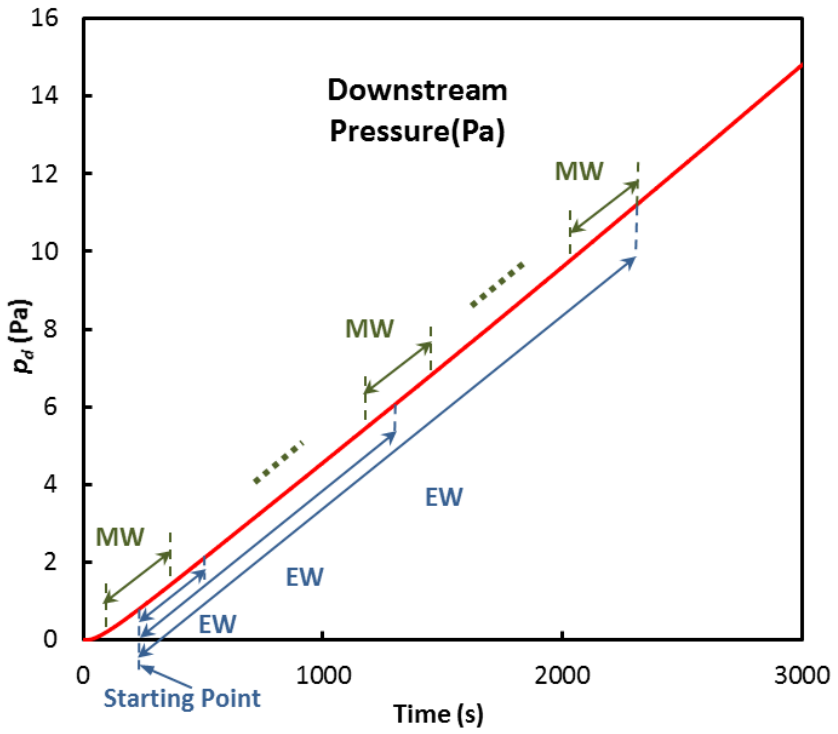

Figure 5.2 A schematic representation of the downstream pressure data analysis with the moving window (MW) and the expanding window (EW) approaches.

5.3.3 Numerical simulation

The numerical simulations' objective was to generate theoretical plots of instantaneous time lag as a function of time for different types of dual-mode sorption solution-diffusion models. The case with partial immobilization and non-instantaneous equilibrium between the Henry's and Langmuir's sites represents the most general model, which can be reduced to other models considered in this study, including the simple solution-diffusion models described by Eq. (8). The details of the numerical method for solving Eq. (8) using the finite differences with variable mesh size, which is adopted in this study, is described elsewhere [24,25]. Smaller mesh sizes at the upstream interface are paramount to accurately capture the variation of concentration in the interface's vicinity immediately after the membrane is subjected to a pressure step change.

Fig. 5.3 shows a discretized representation of the gas transport in dual-mode sorption membranes with partial immobilization and non-instantaneous equilibrium between the Henry's and Langmuir's sites. The Langmuir's sites are subdivided into mobile and immobile sites; the mobile sites have the same diffusivity as Henry's sites. In addition to the transport across the membrane and the Henry's and the mobile Langmuir's sites (denoted by the vertical arrows), there is also a lateral transport between the Henry's and Langmuir' sites (denoted by the horizontal arrows). The equilibrium between Henry's and Langmuir's sites is reached when the net transfer rate between the two types of sites over the entire membrane is zero. Penetrant molecules enter and leave the membrane exclusively via Henry's sites, and there is instantaneous equilibrium between the gas phase and the membrane interfaces on both sides, represented by the nodes 1 and N. There are a total of N-1 meshes, which can have different thicknesses ($\Delta x_n \neq \Delta x_{n+1}$). On the other hand, the time increment was kept constant, i.e., $\Delta t_i = \Delta t_{i+1}$.

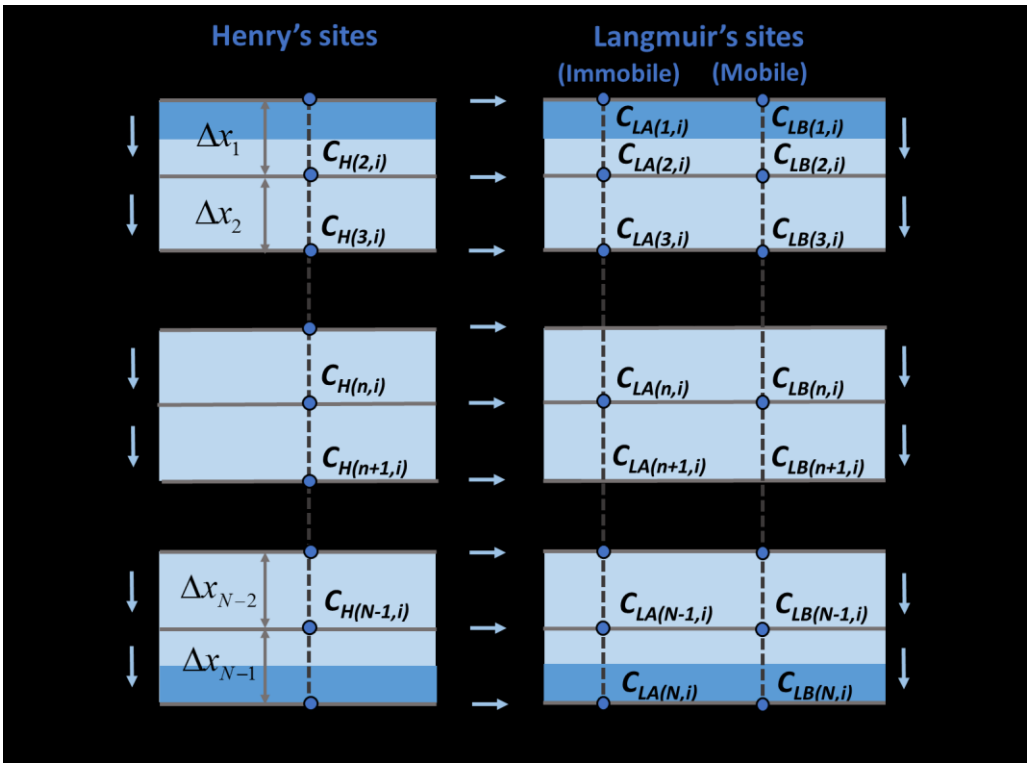

Figure 5.3 Schematic representation of dual-mode sorption model, with non-instantaneous equilibrium and partial immobilization.

$C_{H(n,i)}$ and $C_{L(n,i)}$ are the respective penetrant concentrations in the Henry's and Langmuir's sites corresponding to the node n and the i^{th} time interval. $R_{H\,(n,i)}$ and $R_{L\,(n,i)}$ are the mass diffusion rates of penetrant molecules along with Henry's sites and the mobile Langmuir's sites, respectively, from the $(n\text{-}1)^{th}$ mesh to the n^{th} mesh at the i^{th} time interval. $R_{T(n,i)}$ is the lateral net mass transfer rate of the penetrant molecules from the Henry's to the Langmuir's sites at the n^{th} node and the i^{th} time interval, which can be positive, negative or zero. Although not shown in Fig. 5.3, the penetrant molecules can accumulate in both the Henry's and Langmuir's portions of each mesh. Therefore, for the n^{th} node at the i^{th} time increment Eqs. (24-25) are discretized explicitly to calculate the concentrations in both the Henry's and Langmuir's sites at all interior nodes within the membrane:

$$\frac{C_{H(n,i)}-C_{H(n,i-1)}}{\Delta t}=D_H\left[\frac{\dfrac{C_{H(n+1,i-1)}-C_{H(n,i-1)}}{\Delta x_n}-\dfrac{C_{H(n,i-1)}-C_{H(n-1,i-1)}}{\Delta x_{n-1}}}{\left(\Delta x_{n-1}+\Delta x_n\right)/2}\right] \qquad (26)$$
$$-k_{ad}\left[C_{H(n,i-1)}\times\left(C'_L-C_{L(n,i-1)}\right)-\frac{S}{b}C_{L(n,i-1)}\right]$$

$$\frac{C_{L(n,i)}-C_{L(n,i-1)}}{\Delta t}=FD_H\left[\frac{\dfrac{C_{L(n+1,i-1)}-C_{L(n,i-1)}}{\Delta x_n}-\dfrac{C_{L(n,i-1)}-C_{L(n-1,i-1)}}{\Delta x_{n-1}}}{\left(\Delta x_{n-1}+\Delta x_n\right)/2}\right] \qquad (27)$$
$$+k_{ad}\left[C_{H(n,i-1)}\times\left(C'_L-C_{L(n,i-1)}\right)-\frac{S}{b}C_{L(n,i-1)}\right]$$

Eqs. (26) and (27) allow calculating the concentrations explicitly at the time i based on the concentrations at time i-1. The concentrations at surface nodes 1 and N are in equilibrium with the interface gas pressure, and it is assumed that the gas enters and leaves the membrane via Henry's portion of these surface nodes. The mass flux $J_{(1,i)}$ entering at node 1 at the time i is therefore equal to the sum of the mass diffusion from node 1 to node 2 and the lateral mass flux from Henry's sites to Langmuir's sites:

$$J_{(1,i)} = D_H \left(\frac{C_{H(1,i-1)} - C_{H(2,i-1)}}{\Delta x_1} \right) + k_{ad} \left[C_{H(1,i-1)} \times \left(C'_L - C_{L(1,i-1)} \right) - \frac{S}{b} C_{L(1,i-1)} \right] \times \left(\frac{\Delta x_1}{2} \right) \quad (28)$$

where $C_{H(1,i-1)}$ is given by:

$$C_{H(1,i-1)} = S \times p_{u(i-1)} \quad (29)$$

Eq. (28) implies that, unless the upstream volume is large, $p_{u(i-1)}$ and hence $C_{H(i-1)}$ are not constant, but decrease with time. However, in this investigation, we assume both $p_{u(i-1)}$ and $C_{H(i-1)}$ to be constant and thus Eq. (29) is equivalent to Eq. (4b). On the other hand, it is possible to have accumulation in the Langmuir's portion of the half of the 1st mesh adjacent to the surface; therefore, Eq. (27) becomes:

$$\frac{C_{L(1,i)} - C_{L(1,i-1)}}{\Delta t} = k_{ad} \left[C_{L(1,i-1)} \times \left(C'_L - C_{L(1,i-1)} \right) - \frac{S}{b} C_{L(1,i-1)} \right] + FD_H \frac{\left(C_{L(1,i-1)} - C_{L(2,i-1)} \right)}{\Delta x_1^{\,2} / 2} \quad (31)$$

At the permeate interface of the membrane, i.e. at the N^{th} node, Eqs. (26-27) become:

$$J_{(N,i)} = D_H \left(\frac{C_{H(N-1,i-1)} - C_{H(N,i-1)}}{\Delta x_{N-1}} \right) - k_{ad} \left[C_{H(N,i-1)} \times \left(C'_L - C_{L(N,i-1)} \right) - \frac{S}{b} C_{L(N,i-1)} \right] \times \left(\frac{\Delta x_{N-1}}{2} \right) \quad (32)$$

$$\frac{C_{L(N,i)} - C_{L(N,i-1)}}{\Delta t} = k_{ad} \left[C_{H(N,i-1)} \times \left(C'_L - C_{L(N,i-1)} \right) - \frac{S}{b} C_{L(N,i-1)} \right] + FD_H \frac{\left(C_{L(N-1,i-1)} - C_{L(N,i-1)} \right)}{\Delta x_{N-1}^{2} / 2} \quad (33)$$

where $J_{(N,i)}$ is the gas flux leaving the membrane at the i^{th} time interval, and $C_{H(N,i-1)}$ is given by:

$$C_{H(N,i-1)} = S \times p_{d(i-1)} \tag{33}$$

In the special case, which is referred to as the ideal boundary condition, $p_{d(i\text{-}1)} = 0$ and the above equation is equivalent to Eq. (4c). In a more general and realistic case, $p_{d(i\text{-}1)} = f(t)$ and the above equation is equivalent to Eq. (6). Knowing $J_{(N,i)}$, the pressure response downstream from the membrane at the i^{th} time interval can be evaluated using a simple mass balance on the downstream volume:

$$p_{d(i)} = p_{d(i-1)} + \frac{ART}{V} J_{(N,i)} \Delta t_i \tag{34}$$

5.4 Results and discussion

5.4.1 Sample of experimental results

Fig. 5.4 presents a sample of the experimental results from the PPO membrane tested with N_2 under a feed pressure of 58.6 kPa with a downstream volume of 6.2×10^{-5} m^3. The figure's central part shows the downstream pressure as a function of time for the first 500 s of the experiment, while the inset shows the pressure curve for the entire 3000 s experiment. Focusing on the first 500 s, it appears that quasi-steady-state is reached after approximately 300 s. The corresponding single time-lag value determined using a ruler is approximately 75 s. Focusing on the entire 3000 s experiment, it appears that following a transient part right after the initiation of the experiment, the pressure response forms a perfectly straight line. There is nothing visually “suspicious” in Fig. 5.4 to indicate that a time-lag experiment's typical progress was not obtained.

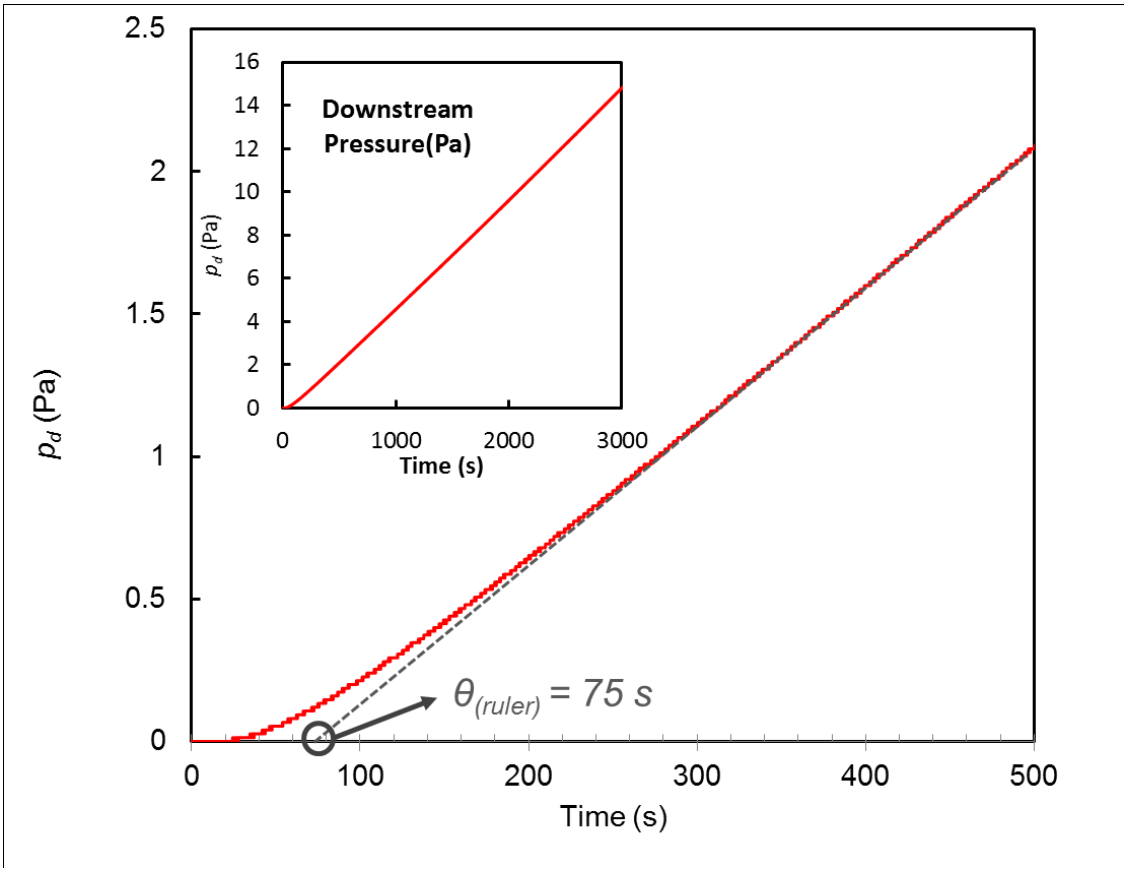

Figure 5.4 Progress of an N_2 permeation experiment with PPO membrane performed at p_0 = 58.6 kPa and T = 25°C; the permeating gas accumulates in $V_d = 6.2 \times 10^{-5}$ m^3.

The situation changes drastically when the data, shown in Fig. 5.4, is analyzed using the MW and EW approaches to obtain the instantaneous time lag θ_t. The results of these analyses are presented in Fig. 5.5. For the MW approach, the selected Δt in Fig. 5.5 is 100 s. It is important to emphasize that 100 s is an arbitrary value. A shorter window length Δt leads to a better representation of the dynamics of the experiment; however, the level of noise in the estimation of θ_t, in particular at larger experimental time, increases [24]. In Fig. 5.5, the experimental noise is mainly due to the pressure measuring system's resolution, which is a staircase increase in pressure. As already stated, by visual inspection of Fig. 5.4, we concluded that at 300 s that quasi-steady-state permeation was attained. Consequently, the EW approach was used, starting at 300 s. It can be noticed that the θ_t curves generated by the MW and EW generally coincide, but the latter is much smoother than the former. This is expected since the length of the window Δt increases with time in the EW approach,

thereby containing a larger number of experimental points for better data filtering. It is also important to note that the instantaneous time lag corresponds to the midpoint of the analysis window for both approaches. For the MW approach, the time in Figs. 5.4 and 5.5 are identical, whereas, for the EW approach, the time reported in Fig. 5.5 is delayed relative to the time in Fig. 5.4. For instance, the instantaneous time lag for the EW approach at t = 500 s in Fig. 5.3 corresponds to t = 300 + (500 – 300)/2 = 400 s in Fig. 5.5. For this reason, the last θ_t by the EW approach in Fig. 5.4 appears at t = 1,650 s, which corresponds to t = 3,000 s in Fig. 5.3 (300 + (3000 – 300)/2 = 1,650 s).

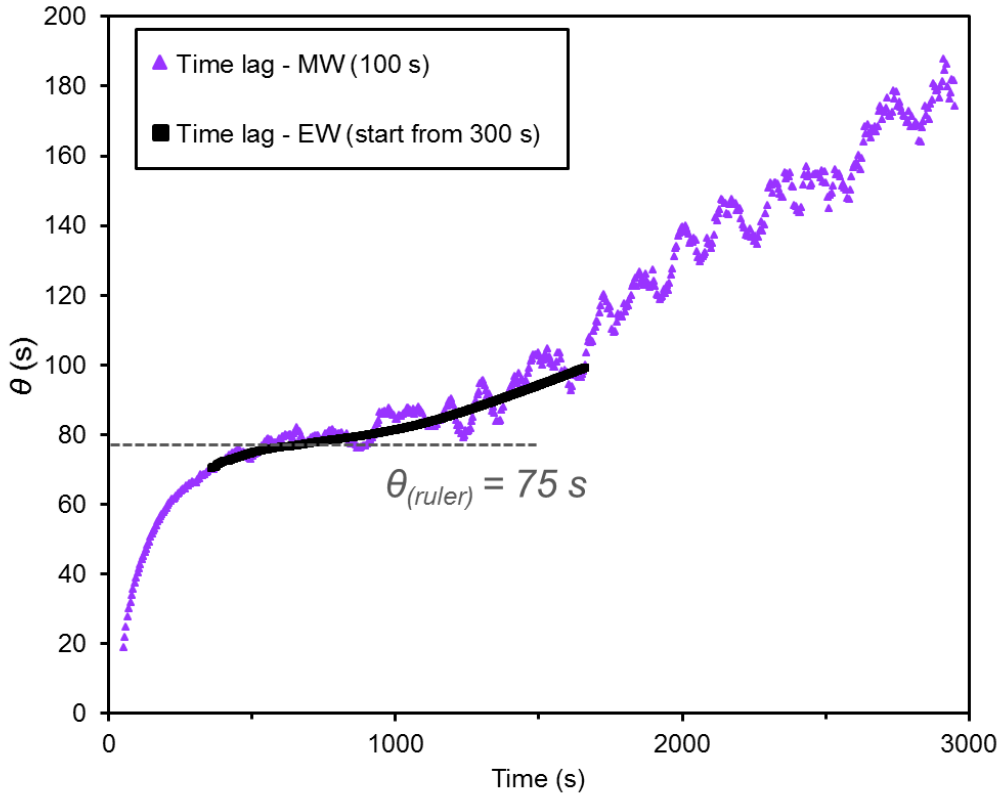

Figure 5.5 Comparison between time lags obtained from experimental data of PPO membrane of unknown properties with the conventional time-lag approach, moving-window approach (MW), and expanding-window approach (EM). A fixed window length of 100 s was used in moving-window data analysis. The expanding-window data analysis started at 300 s.

Regardless of which approach is used, Fig. 5.5 shows how subjective and misleading the conventional "ruler" approach to analyzing the results of a time-lag

permeation experiment might be. The most interesting feature in Fig. 5.5 is that the instantaneous time-lag plots do not stabilize at constant values as expected at quasi-steady-state; however, after reaching a temporary plateau, they continue to increase with time significantly above the ruler-determined θ. Despite the presence of more noise, this effect is more apparent in the MW approach. It should be noted that in the previously referenced numerical investigation [15], Al-Qasas et al. concluded that under the real boundary condition described by Eq. (6), the instantaneous time lag reaches a maximum value, which is always less than the actual time lag of the membrane. This is because as the experiment continues and the pressure downstream from the membrane increases, the driving force for gas permeation decreases, leading to a slight decrease in the slope of the pressure response curve. However, because of an increase in the extrapolation distance with time, this tiny decrease in the pressure response curve slope translates into a considerable decrease in θ_t with time. This behaviour is not observed in Fig. 5.5. It is essential to emphasize in their study, Al-Qasas et al. assumed that gas transport in their hypothetical membranes followed dual-mode sorption with complete immobilization of penetrant in the Langmuir's sites and instantaneous equilibrium between the penetrants in the Henry's and Langmuir's sites, i.e., the case described by Eq. (14). Therefore, based on the analysis presented in Fig. 5.5, one can conclude that gas transport in the PPO membrane considered in this work does not follow the model assumed by Al-Qasas et al. in their numerical studies [15]. A question arises; can any of the transport models discussed in the Theory Section predict an instantaneous time lag's upward deviation after reaching an ephemeral plateau as observed in Fig. 5.5? It is important to emphasize that the same behaviour was also observed for tests at other feed pressures and with different downstream volumes.

5.4.2 Numerical simulations of different dual-mode sorption models

The purpose of the following analysis is to investigate which of dual-mode gas sorption models (if any) would lead to an upward deviation of the instantaneous time lag. The actual determination of the gas transport parameters is beyond the scope of this study.

There is an infinite number of possible combinations of membrane properties. However, in the recent comprehensive study by Al-Qasas et al., dual-mode sorption membranes with complete immobilization in Langmuir's sites and instantaneous equilibrium between the Langmuir's and Henry's sites were investigated, and no upstream deviation of the simulated instantaneous time-lag was observed [16]. In that paper, different combinations of S, b, C'_L and p_0, covering a wide range for each of the respective parameters was considered. Consequently, the current investigation focuses on two additional parameters, F and k_{ad}, not considered by Al-Qasas et al. [16]. Fig. 5.6 shows a schematic design of numerical simulations undertaken in this study, a 3 x 3 matrix to consider three different levels for the values of F and k_{ad}. More specifically, the selected F values were: 0 (complete immobilization), 0.5 (partial immobilization), and 1 (no immobilization in Langmuir's sites). As for k_{ad}, the three selected values were: 0 (no transfer between the Henry's and Langmuir's sites), 0.0005 (non-instantaneous equilibrium), and infinity (instantaneous equilibrium). Although there are 9 different combinations, the 3 cases in which $k_{ad} = 0$, regardless of the value of F and regardless of the values of S, b, C'_L and p_u, are equivalent to a simple solution-diffusion model with a linear isotherm governed by Eq. (8). This is because, as shown in Fig. 5.4, gas molecules are sorbed by the membrane and desorbed from the membrane exclusively via Henry's sites. Table 5.2 summarizes all parameters used in all simulations.

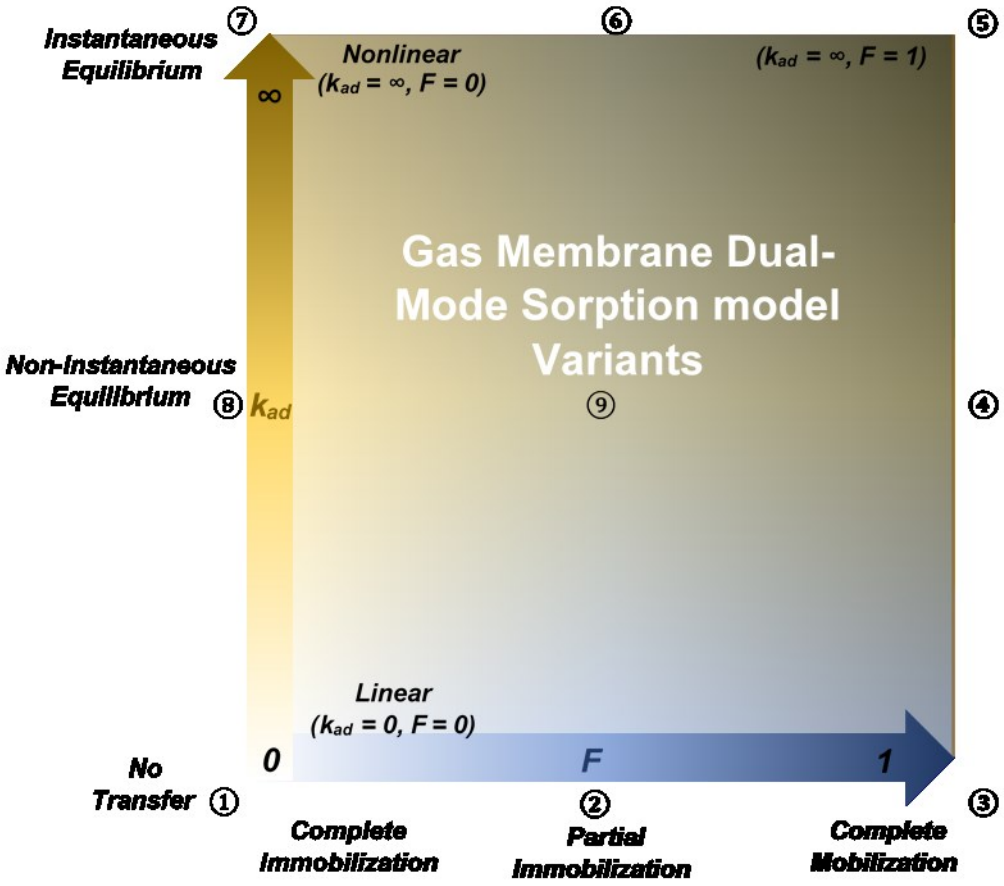

Figure 5.6 Schematic representation of the design of numerical simulations performed for a dual-mode sorption membrane with three levels of F and k_{ad} values. All input values for all simulations are summarized in Table 5.1. Circled numbers refer to different models.

Table 5.1 Values of transport properties and model parameters used in simulations with different models and simulated experimental conditions.

Model	b Pa^{-1}	C'_L mol/m^3	k_{ad} $m^3/mol\ s$	F [-]
①-③	-	-	0	-
④	6×10^{-5}	67.4	0.0005	1
⑤	6×10^{-5}	67.4	∞	1
⑥	6×10^{-5}	67.4	∞	0.5
⑦	6×10^{-5}	67.4	∞	0
⑧	6×10^{-5}	67.4	0.0005	0
⑨	6×10^{-5}	67.4	0.0005	0.5
Basic transport properties	Diffusivity $D = 4 \times 10^{-12}$ m^2/s, solubility $S = 7.44 \times 10^{-5}$ mol/m^3 Pa.			
Experimental conditions	Membrane thickness $L = 3 \times 10^{-5}$ m, membrane area $A = 1.25 \times 10^{-3}$ m^2, downstream volume $V_d = 1 \times 10^{-4}$ m^3, feed pressure $p_0 = 101\ 325$ Pa, temperature $T = 298.15$ K.			

Fig. 5.7 summarizes the simulated instantaneous time lag as a function of time for all cases listed in Table 5.1. In all cases, the instantaneous time lags eventually reach steady-state plateaus. This is because the simulations in Fig. 5.7 were carried out under ideal boundary conditions given by Eqs. (4b & c), which implies reaching steady-state, not just quasi-steady-state. This includes the instantaneous time lag for case ⑧, which eventually reaches the same steady-state time lag as for case ⑦. However, the path each membrane goes through to reach the steady state and the corresponding time lag varies considerably from case to case. It is important to emphasize that the diffusivity in all simulations was same.

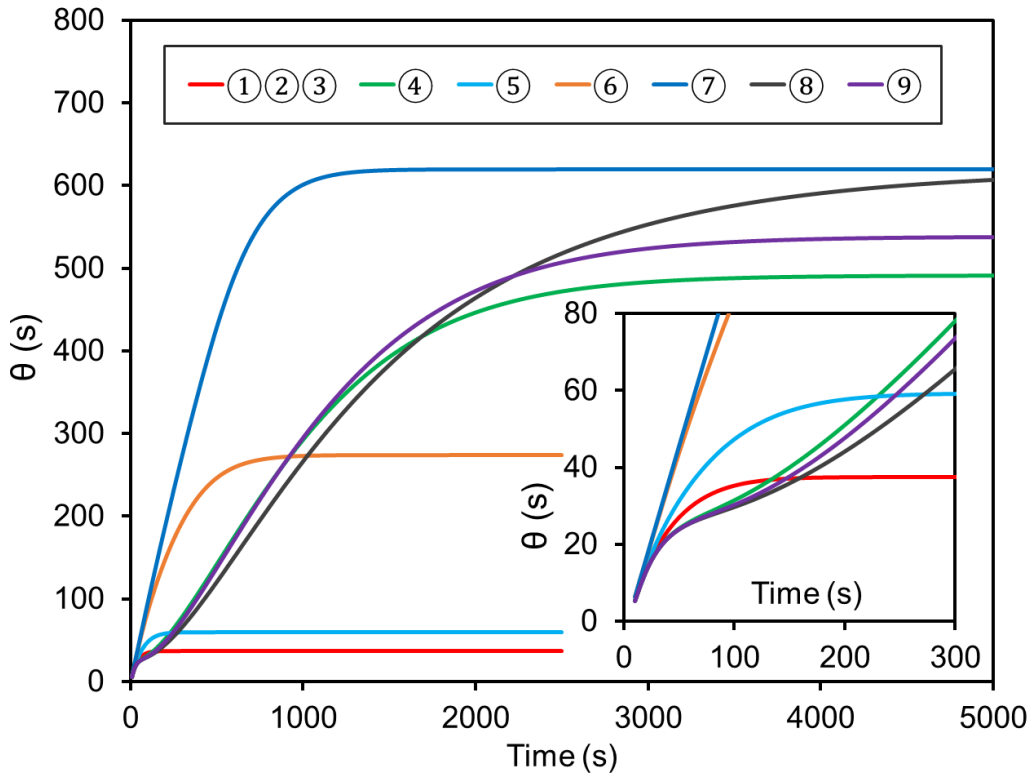

Figure 5.7 Simulated instantaneous time-lag curves for different gas transport models defined in Table 5.1. All simulations were performed under the ideal boundary conditions given by Eqs. (4b & c).

In Fig. 5.7, the instantaneous time lag for membranes represented by models ①-③ falls on a single line and reaches steady state in the fastest manner and its value is the smallest among all membranes. As already mentioned, since $k_{ad} = 0$, there is no transfer between the Langmuir's and Henry's sites; thus the resulting time lag depends only on D and L, and is given by Eq. (2). Regardless of the values of S, b, C'_L, F and p_0, there is no immobilization in the Langmuir's sites and thus there is no delay in reaching the steady state. At the other extreme, when $k_{ad} \rightarrow \infty$, i.e. for membranes characterized by instantaneous equilibrium, which are represented by sorption models ⑤-⑦, the time lag and the time required to reach steady state strongly depend on parameter F. The membrane with complete immobilization ($F = 0$) requires the longest time to reach the steady state and the corresponding time lag is largest among this group of membranes. In general, as F increases, the time lag and the time required to reach steady state decrease. When $F = 1$,

i.e. no immobilization in the Langmuir's sites represented by membrane model ⑤, the time lag and the time required to reach steady state are only slightly greater than the respective values for membranes models ①-③. With $F = 1$ ($D_H = D_L$) one might think there should be identical behaviour as for the case with $k_{ad} = 0$. However, since gas molecules are sorbed by the membrane and desorbed from the membrane exclusively via the Henry's sites, the effective path traveled by penetrants in the dual-mode sorption membrane with $F = 1$ must be somewhat greater than that in the membrane in which penetrant diffuses only through the Henry's sites ($k_{ad} = 0$), which is reflected by the difference between membrane ⑤ and membranes ①-③ in Fig. 5.7. It is important to note that changing the value of F while $k_{ad} \rightarrow \infty$ does not change the shape of the resulting instantaneous time lag curves, and there is no upward deviation as seen in Fig. 5.5.

Considering non-instantaneous equilibrium between the Langmuir's and Henry's sites (membranes ④, ⑧, and ⑨), one can make some interesting observations. First, non-instantaneous equilibrium leads to a further delay in reaching steady state and an increase, in most cases, of the time lag. In the case of complete immobilization, the time lags for the instantaneous equilibrium (membrane ⑦) and the non-instantaneous equilibrium (membrane ⑧) are the same. However, the most interesting feature is the existence of an inflection point in curves ④, ⑧, and ⑨. This inflection point occurs at $t < 100$, which better seen in the inset of Fig. 5.7, which shows the instantaneous time lag in the first 300 s. Moreover, comparing the curves of membranes ④, ⑧, and ⑨ in the inset in Fig. 5.7 with the experimental instantaneous time lag shown in Fig. 5.5, a resemblance of shapes is quite apparent. It can therefore be concluded that an upward deviation in the experimental instantaneous time lag arises from non-instantaneous equilibrium between the Langmuir's and Henry's sites.

The effect of k_{ad} on the shape of the instantaneous time lag was further investigated by performing additional simulations, in which k_{ad} was varied from 0.00001 to 0.01 m^3/mol s, while all other inputs were identical to that of membrane ⑧ in Fig. 5.7. The results of these simulations are shown in Fig. 5.8. The inset in Fig. 5.8 focuses on the first 450 s. Since $F = 0$, the steady state time lag for all membranes in Fig. 5.8 should be the same. Although not evident within the first 5000 s, the membranes with k_{ad} of 0.0001 and 0.00001

m^3/mol s reach the same time lag as the membranes with k_{ad} of 0.01 and 0.001 m^3/mol s; however, after much longer time. For the case of k_{ad} = 0.01 m^3/mol s there is no inflection point and the shape of the instantaneous time-lag curve resembles that of model ⑦ in Fig. 5.7. Therefore, k_{ad} = 0.01 m^3/mol s for all practical purposes is equivalent to instantaneous equilibrium between the Langmuir's and Henry's sites. In other words, k_{ad} = 0.01 m^3/mol is equivalent to $k_{ad} \rightarrow \infty$. It is important to emphasize that the numerical value of k_{ad} equivalent to instantaneous equilibrium might be affected by other membrane properties and operating conditions, but this aspect is beyond the scope of the current paper. On the other hand, for the smallest k_{ad} = 0.00001 m^3/mol s, the resulting instantaneous time-lag curve resembles that of membranes ①-③ in Fig. 5.7. However, a closer look at curve for the smallest k_{ad} reveals that the instantaneous time lag slightly increases after reaching a plateau at approximately 100 s. This plateau could easily be confused with steady state. The length of the plateau strongly depends on k_{ad}. As k_{ad} increases to 0.0001 m^3/mol s, there is a much shorter plateau, which however is still evident. As k_{ad} increases beyond 0.0001 m^3/mol s, the plateau is first transformed into an inflection point, but eventually disappears when k_{ad} is sufficiently large (in this case 0.01 m^3/mol s).

The simulations in Fig. 5.8 allow quantifying small and large k_{ad}, thus providing a range (from 0.00001 to 0.01 m^3/mol s, or three orders of magnitude) within which a variation of k_{ad} affects the shape of the instantaneous time-lag curves. The actual numerical values of the limiting k_{ad} probably depend on other membrane properties, in particular membrane diffusivity.

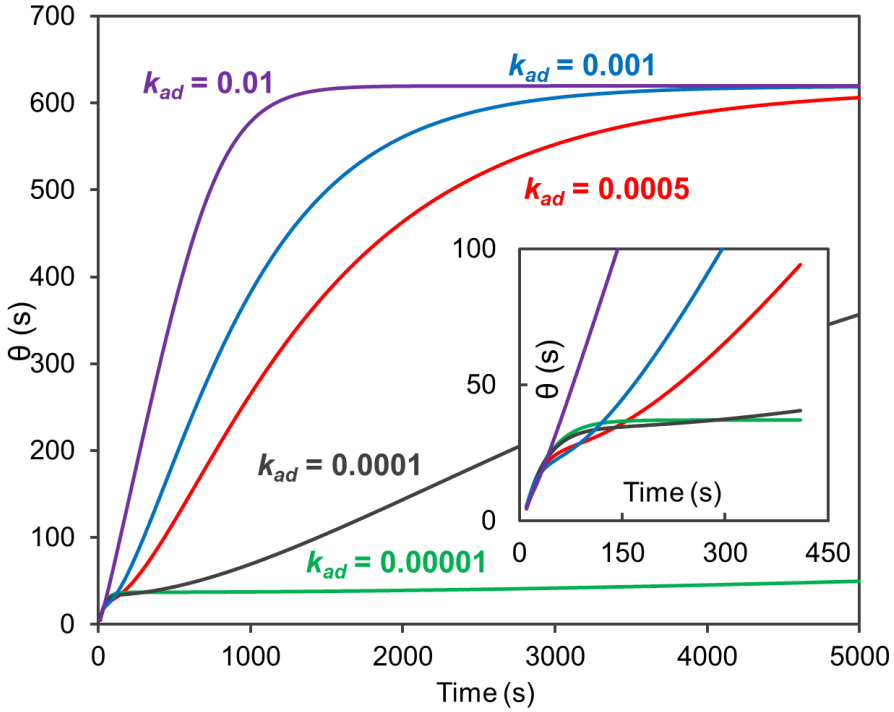

Figure 5.8 The effect of k_{ad} on the shape of instantaneous time-lag curves. All other input corresponds to membrane ⑧ in Fig. 5.7. All simulations were performed under ideal boundary conditions given by Eqs. (4b & c).

All simulations in Figs. 5.7 & 5.8 were carried out, assuming ideal boundary conditions. While it is reasonable to assume the validity of Eq. (4b), because the upstream volume can be large, the downstream volume (V_d) has to be such that the gas accumulation downstream from the membrane is detectable. This means that in reality, the 2nd boundary condition given by Eq. (4c) should be replaced by Eq. (6). Fig. 5.9 shows the simulated instantaneous-time lag of the membranes ①-③, ④, ⑦, ⑧, and ⑨ under the boundary conditions given by Eq. (4b) and Eq. (6). The downstream volume in which the permeating gas accumulates was assumed to be $V_d = 1 \times 10^{-4}$ m^3. The timeframe in Fig. 5.9 is 10,000 s compared to 5000 s in Figs. 5.7, and 5.8. Membranes ⑤ and ⑥ are not included in Fig. 5.9 for the sake of clarity. The dashed horizontal lines, denoted as SST, represent the respective steady-state time lags of the membranes.

Using Eq. (6) instead of Eq. (4c) as the 2nd boundary condition only leads to a minute change of the shape of the instantaneous time-lag curves. The inflection

point/temporary plateaus seen in Fig. 5.7 are still evident in Fig. 5.9, particularly in the inset in Fig. 5.9 showing the first 300 s of the simulations. Consequently, as expected, the real boundary condition at the membrane's permeate interface has nothing to do with the observed upward deviation in the instantaneous time-lag curves. On the contrary, after approaching the steady-state value, the instantaneous time lag starts to decrease, i.e. shows a downward deviation. In other words, the instantaneous-time lag reaches a maximum value, which, although not seen in Fig. 5.9, is lower than the steady-state time lag, which is consistent with previous findings of Al-Qasas et al. [16]. It is important to note that the maximum instantaneous time lag and a downward deviation occur longer than the upward deviation due to non-instantaneous equilibrium between the Langmuir's and Henry's sites. Consequently, for the simulation input values used in this investigation, the permeate interface's real boundary condition has a smaller effect on the temporary plateau/inflection point than on the steady-steady state time lag.

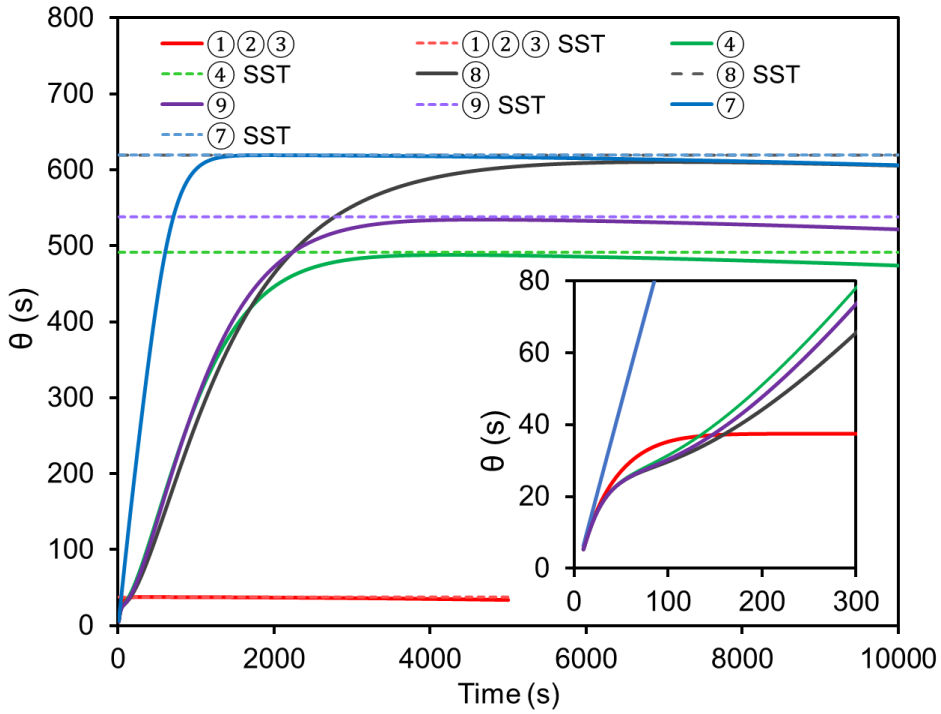

Figure 5.9 Simulated instantaneous time-lag curves for membranes ①-③, ④, ⑦, ⑧, and ⑨ defined in Table 5.1. All simulations were performed under the boundary conditions given by Eqs. (4b & 6). Dashed lines indicate the respective steady-state time lags.

5.5 Conclusion

The conventional way of measuring the time lag, which relies on the visual determination of the linear pressure response, can be misleading. The systematic analysis of a seemingly linear slope of the pressure response curve at quasi-steady-state indicates changes with time, both using a fixed number of experimental data points (moving window approach) and an increasing number of the experimental data points (expanding window approach). Although the slope changes are minute, when the resulting straight line is extrapolated to the time axis, the variation in the corresponding instantaneous time lag with time becomes evident. The moving window approach results in a considerable noise in the instantaneous time lag, which increases with time. On the other hand, the expanding window approach leads to a much smoother instantaneous time-lag curve. In both cases, when analyzing the experimental nitrogen permeation data obtained with high molecular weight PPO membranes, after reaching a plateau, there is an apparent upward deviation of the instantaneous time-lag curves. Such an upward deviation was not expected, because as time increases, the driving force for gas permeation decreases due to gas accumulation at the permeate side of the membrane.

Based on extensive simulations, in which we considered different types of dual-mode sorption gas transport models, it became apparent that the observed upward deviation of the instantaneous time-lag curve is due to the non-instantaneous equilibrium between the penetrant molecules in the Langmuir's and Henry's sites. The observed plateau in the instantaneous time lag does not indicate the actual steady-state, which occurs much later and is associated with a considerably more significant time lag. Further analysis of the effect of the adsorption constant governing the transfer of penetrant molecules from Henry's to Langmuir's sites allowed to establish a range of the values of the adsorption constant which influence the shape of the instantaneous time-lag curve. For small values (< 0.00001 m^3/mol s), the plateau is prominent and can easily be confused with steady-state. As the adsorption's constant increases, the apparent plateau's length decreases and becomes an inflection point. Eventually, for large values of the adsorption constant (> 0.01 m^3/mol s), the inflection point disappears, indicating that in practice, the instantaneous

equilibrium between penetrant molecules in the Langmuir's and Henry's sites can be assumed.

To our best knowledge, this paper presents for the first time the application of the concept of the instantaneous time lag to analyze the data obtained from a conventional time-lag gas permeation experiment. Moreover, although many researchers postulated non-instantaneous equilibrium between the Langmuir's and Henry's sites in dual-mode sorption membranes, the application of the instantaneous time lag presented in this paper provides an undeniable proof that this is the actual case, at least for the transport of nitrogen in high molecular weight PPO membranes.

5.6 Acknowledgement

The authors gratefully acknowledge the financial support for this project provided by the Natural Science and Engineering Research Council of Canada.

5.7 Nomenclature

A	**[m^2]**	Membrane area
b	**[Pa^{-1}]**	Hole affinity constant
C	**[mol/m^3]**	Gas concentration
C_H	**[mol/m^3]**	Gas concentration in Henry's sites
$C_{H\rightarrow L}$	**[mol/m^3]**	Gas concentration transferred from Henry sites to Langmuir sites
C_L	**[mol/m^3]**	Gas concentration in Langmuir's sites
C'_L	**[mol/m^3]**	Saturation capacity parameter of Langmuir's sites
C_m	**[mol/m^3]**	Concentration of mobile gas molecules in a membrane
C_T	**[mol/m^3]**	Total gas concentration within the membrane

D	$[m^2/s]$	Diffusivity coefficient
D_H	$[m^2/s]$	Diffusivity of gas molecules in Henry's sites
D_L	$[m^2/s]$	Diffusivity of gas molecules in Langmuir's sites
E	[-]	Empty Langmuir sites
EG	[-]	Gas-site complex or site-captured gas molecules
EW	[s]	Expanding (time) window
F	[-]	Partial immobilization coefficient
J	$[mol/(m^2 \cdot s)]$	Flux of gas molecules across a membrane
J_T	$[mol/(m^2 \cdot s)]$	Total flux of mobile gas molecules across a membrane
k_{ad}	$[m^3/(mol \cdot s)]$	Adsorption rate constant
k_d	$[s^{-1}]$	Desorption rate constant
L	[m]	Membrane thickness
$\dot{m}_{H\ L}$	$[mol/(m^3 \cdot s)]$	Transfer rate of gas molecules from Henry's sites to Langmuir's sites
MW	[s]	Moving (time) window
n	[-]	Number of time increments
p	[Pa]	Pressure
p_0	[Pa]	Feed pressure in the upstream chamber in a CV system
p_u	[Pa]	Pressure in the upstream chamber in a CV system
p_d	[Pa]	Pressure in the downstream chamber in a CV system
P	$[mol \cdot m/(m^2 \cdot Pa \cdot s)]$	Permeability coefficient
r_{ad}	$[mol/(m^3 \cdot s)]$	Adsorption rate

r_d	**[mol/(m^3·s)]**	Desorption rate
R	**[J/(K·mol)]**	Gas constant.
S	**[mol/(m^3 ·Pa)]**	Solubility coefficient.
t	**[s]**	Time
T	**[K]**	Absolute temperature
V_d	**[m^3]**	Downstream volume
V_u	**[m^3]**	Upstream volume
x	**[m]**	Permeation distance.
Δp_d	**[Pa]**	Downstream pressure build up
Δp_u	**[Pa]**	Upstream pressure decay
Δt	**[s]**	Size of a simulation time step
Δx	**[m]**	Grid size of the grid point located at x
θ	**[s]**	Time lag
θ_d	**[s]**	Actual downstream time lag

5.8 References

[1] J. Wijmans and R. Baker, "The solution-diffusion model: a review," J. Memb. Sci, vol. 107, no. 1-2, pp. 1–21, 1995.

[2] R. M. Barrer, J. A. Barrie, and J. Slater, "Sorption and diffusion in ethyl cellulose. Part III. Comparison between ethyl cellulose and rubber," J. Polym. Sci., vol. 27, no. 115, pp. 177–197, 1958.

[3] D. R. Paul and W. J. Koros, "Effect of partially immobilizing sorption on permeability and the diffusion time lag," J. Polym. Sci. Polym. Phys. Ed., vol. 14, no. 4, pp. 675–685, 1976.

[4] W. R. Vieth, J. M. Howell, and J. H. Hsieh, “Dual sorption theory,” J. Memb. Sci., vol. 1, pp. 177–220, 1976.

[5] J. Guo and T. A. Barbari, “A dual mode, local equilibrium relaxation model for small molecule diffusion in a glassy polymer,” Macromolecules, vol. 41, no. 1, pp. 238–245, 2008.

[6] W. J. Koros, D. R. Paul, and A. A. Rocha, “Carbon dioxide sorption and transport in polycarbonate,” J. Polym. Sci. Polym. Phys. Ed., vol. 14, no. 4, pp. 687–702, 1976.

[7] L. Wang, J. P. Corriou, C. Castel, and E. Favre, “Transport of gases in glassy polymers under transient conditions: Limit-behavior investigations of dual-mode sorption theory,” Ind. Eng. Chem. Res., vol. 52, no. 3, pp. 1089–1101, 2013.

[8] C. J. Patton, R. M. Felder, and W. J. Koros, “Sorption and transport of benzene in poly(ethylene terephthalate),” J. Appl. Polym. Sci., vol. 29, no. 4, pp. 1095–1110, 1984.

[9] G. S. Huvard, V. T. Stannett, W. J. Koros, and H. B. Hopfenberg, “The pressure dependence of CO2 sorption and permeation in poly(acrylonitrile),” J. Memb. Sci., vol. 6, pp. 185–201, 1980.

[10] J. S. Lee, J. Leisen, R. P. Choudhury, R. M. Kriegel, H. W. Beckham, and W. J. Koros, “Antiplasticization-based enhancement of poly(ethylene terephthalate) barrier properties,” Polym., vol. 53, no. 1, pp. 213–222, 2012.

[11] S. Deveci, Y. Oksuz, T. Birtane, M. Oner, “Application of constant volume – variable pressure (time-lag) method to measure oxygen gas diffusion through polypropylene pipes,” Polym Testing., vol 55, pp. 287–296, 2016.

[12] P. Meares, “The diffusion of gases through polyvinyl acetate,” J. Am. Soc. Vol 76, pp. 3415–3422, 1954.

[13] S.W. Rutherford, and D.D. Do, “Review of time lag permeation technique as a method for characterisation of porous media and membranes”, Adsorption, vol. 3, pp. 283-312, 1997.

[14] J. A. Tshudy and C. Von Frankenberg, “A model incorporating reversible immobilization for sorption and diffusion in glassy polymers,” J. Polym. Sci. Polym. Phys. Ed., vol. 11, no. 10, pp. 2027–2037, 1973.

[15] N. Al-Qasas, J. Thibault, and B. Kruczek, “The effect of the downstream pressure accumulation on the time-lag accuracy for membranes with non-linear isotherms,” J. Memb. Sci., vol 511, pp. 119-129, 2016.

[16] N. Al-Qasas, J. Thibault, and B. Kruczek, “A new characterization method of membranes with nonlinear sorption isotherm systems based on continuous upstream and downstream time-lag measurements,” J. Memb. Sci., vol 542, pp. 91-101, 2017.

[17] R. T. Yang, “Cyclic Gas Separation Processes,” Gas Separation by Adsorption Processes, pp. 201–235, 1987.

[18] W. Vieth and K. Sladek, “A model for diffusion in a glassy polymer,” J. Colloid Sci., vol. 20, no. 9, pp. 1014–1033, 1965.

[19] D. R. Paul and A. T. Dibenedetto, “Diffusion in Amorphous Polymers,” Rubber Chem. Tech., vol. 39, no. 5, pp. 1496–1512, 1966.

[20] R. T. Chern, W. J. Koros, H. B. Hopfenberg, and V. T. Stannett, “Material Selection for Membrane-Based Gas Separations,” Materials Science of Synthetic Membranes, ACS Symposium Series, vol. 269, pp. 25–46, 1985.

[21] G. Bissadi and B. Kruczek, “Thermal properties of silica/poly(2,6-dimethyl-1,4-phenylene oxide) films prepared by emulsion polymerization,” J. Therm. Anal. Calorim. vol. 117, pp. 73–83, 2014.

[22] S. Lashkari, B. Kruczek, “Effect of resistance to gas accumulation in multi-tank receivers on membrane characterization by the time lag method. Analytical approach for optimization of the receiver”, J. Memb. Sci. vol. 360, pp.442–453, 2010.

[23] S. Lashkari, B. Kruczek, “Reconciliation of membrane properties from the data influenced by resistance to accumulation of gasses in constant volume systems,” Desalination., vol 287, pp. 178-189, 2012.

[24] H. Wu, B. Kruczek, and J. Thibault, "Impact of Measuring Devices and Data Analysis on the Determination of Gas Membrane Properties," J. Memb Sci Research., vol. 4, no. 1, pp. 4-14, 2018.

[25] H. Wu, N. Al-Qasas, B. Kruczek, and J. Thibault, "Simulation of time-lag permeation experiments using finite differences," J. Fluid Flow, Heat Mass Transf., vol. 2, no. 181, pp. 1–17, 2015.

5.9 Appendices

5.9.1 Appendix I -Derivation of governing equation of the basic dual-mode sorption model

The derivation starts from equation (5.A1.1), i.e Eq. (5.13) in the main body of the paper.

$$\frac{\partial}{\partial C_H}\left[C_H+\frac{C_H C_L'\left[b/S\right]}{\left(1+\left[b/S\right]C_H\right)}\right]\frac{\partial C_H}{\partial t}=D_H\frac{\partial^2 C_H}{\partial x^2} \tag{5.A1.1}$$

The partial derivative of the second term in the left hand side bracket is represented as a partial derivative of a multiplication of u and v in Eq. (5.A1.2).

$$\frac{\partial}{\partial C_H}\left[\frac{C_H C_L'\left[b/S\right]}{\left(1+\left[b/S\right]C_H\right)}\right]=\frac{\partial}{\partial C_H}\left(u\times v\right)=v\frac{\partial u}{\partial C_H}+u\frac{\partial v}{\partial C_H} \tag{5.A1.2}$$

Where u and v are functions of C_H and are shown in Eq. (5.A1.3 (a) and (b)):

$$\begin{cases} u=\dfrac{1}{\left(1+\left[b/S\right]C_H\right)} & (a) \\ v=C_H C_L'\left[b/S\right] & (b) \end{cases} \tag{5.A1.3}$$

The partial derivatives of u and v in terms of C_H are shown in Eq. Eq. (5.A1.4 (a) and (b)):

$$\begin{cases} \dfrac{\partial u}{\partial C_H}=-\dfrac{\left[b/S\right]}{\left(1+\left[b/S\right]C_H\right)^2} & (a) \\ \dfrac{\partial v}{\partial C_H}=C_L'\left[b/S\right] & (b) \end{cases} \tag{5.A1.4}$$

Therefore, the expanded form of Eq. (5.A1.2) is obtained in Eq. (5.A1.5) which is simplified to Eq. (5.A1.6).

$$\frac{\partial}{\partial C_H}\left[\frac{C_H C_L'[b/S]}{\left(1+[b/S]C_H\right)}\right]=-\frac{C_H C_L'[b/S]^2}{\left(1+[b/S]C_H\right)^2}+\frac{C_L'[b/S]}{\left(1+[b/S]C_H\right)} \tag{5.A1.5}$$

$$\frac{\partial}{\partial C_H}\left[\frac{C_H C_L'[b/S]}{\left(1+[b/S]C_H\right)}\right]=\frac{C_L'[b/S]}{\left(1+[b/S]C_H\right)^2} \tag{5.A1.6}$$

Substitute Eq. (5.A1.6) back into Eq. (5.A1.1), the final governing equation is obtained in Eq. (5.A1.7), which is Eq. (5.14) in the main body of the paper.

$$\left[1+\frac{C_L'[b/S]}{\left(1+[b/S]C_H\right)^2}\right]\frac{\partial C_H}{\partial t}=D_H\frac{\partial^2 C_H}{\partial x^2} \tag{5.A1.7}$$

5.9.2 Appendix II - Details for the interpretation of the reversible adsorption process

The rate of reversible adsorption process from Henry's sites to Langmuir's sites.

$$r = k_d C_D\left(C_H' - C_H\right) - k_d C_H \tag{5.A2.1}$$

$$\frac{k_{ad}}{k_d}=\frac{C_H}{C_D\left(C_H'-C_H\right)} \tag{5.A2.2}$$

Rearrange the equation

$$r = k_d\left(C_H' - C_H\right)\left[C_D - \frac{k_d}{k_{ad}}\frac{C_H}{\left(C_H'-C_H\right)}\right] \tag{5.A2.3}$$

Define $C^*\left[mol\cdot m^{-3}\right]$ as the equivalent gas concentration in Henry's site with Langmuir's sites concentration by solving Eqs. (5.A2.2) and Eq. (5.A2.3) for the same pressure p, then replace k_d/k_{ad} with S/b.

$$C^* = \frac{S}{b}\frac{C_H}{\left(C'_H - C_H\right)} = \frac{k_d}{k_{ad}}\frac{C_H}{\left(C'_H - C_H\right)} \tag{5.A2.4}$$

Consider a new irreversible adsorption process where the previous desorption process has been incorporated into C^*.

$$S + A^* \xrightarrow{k_{ad}} SA^* \tag{5.A2.5}$$

where A^* is the equivalent gas concentration in the irreversible adsorption process. The concentration of A^* is $\left[A^*\right] = C_D - C^*\left[mol \cdot m^{-3}\right]$.

The transfer rate can be re-written as Eq. (5.A2.6) and Eq. (5.A2.7).

$$r = k_1[S][A]^* \tag{5.A2.6}$$

$$r = k_1\left(C'_H - C_H\right)\left[C_D - C^*\right] \tag{5.A2.7}$$

Define an overall rate parameter $K\left[s^{-1}\right]$.

$$K = k_{ad}\left(C'_H - C_H\right) = \frac{\alpha}{SC'_H\sqrt{2\pi mkT}}\left(C'_H - C_H\right) \tag{5.A2.8}$$

$$r = K\left[C_D - C^*\right] \tag{5.A2.9}$$

5.9.3 Appendix III -Derivation of flux and concentration finite difference equations for the first and last half meshes

By performing mass balance for the first half mesh, one can obtain that the rate of mass entering the membrane surface equals to the rate of mass leaving the first half mesh by diffusion to the next mesh plus the rate of mass leaving the Henry's site by lateral transfer:

$$r = \cdot \qquad \cdot \qquad) \tag{5.A3.1}$$

Expand each term of the equation:

$$J_{(1,i)}\Delta y\Delta z = D_H\left(\frac{C_{H(1,i-1)}-C_{H(2,i-1)}}{\Delta x_1}\right)\Delta y\Delta z + k_{ad}\left[C_{H(1,i-1)}\times\left(C'_L-C_{L(1,i-1)}\right)-\frac{S}{b}C_{L(1,i-1)}\right]\times\left(\frac{\Delta x_1}{2}\right)\Delta y\Delta z \quad (5.A3.2)$$

Note the last term is multiplied by $\left(\frac{\Delta x_1}{2}\right)\Delta y\Delta z$ because the mass balance is conducted with the first half mesh where only the lateral transfer within that half mesh is counted. Divided by the mesh cross sectional area $\Delta y\Delta z$, the mass flux $J_{(1,i)}$ entering at node 1 at time i equals to the sum of the mass diffusion from node 1 to node 2 and the lateral mass flux from the Henry's sites to Langmuir's sites:

$$J_{(1,i)} = D_H\left(\frac{C_{H(1,i-1)}-C_{H(2,i-1)}}{\Delta x_1}\right) + k_{ad}\left[C_{H(1,i-1)}\times\left(C'_L-C_{L(1,i-1)}\right)-\frac{S}{b}C_{L(1,i-1)}\right]\times\left(\frac{\Delta x_1}{2}\right) \quad (5.A3.3)$$

where $C_{H(1,i\text{-}1)}$ is given by:

$$C_{H(1,i-1)} = S\times p_{u(i-1)} \quad (5.A3.4)$$

It is possible to have accumulation in the Langmuir's portion of the half of the 1st mesh adjacent to the surface; therefore, Eq. (5.A3.3) becomes:

$$\frac{C_{L(1,i)}-C_{L(1,i-1)}}{\Delta t} = k_{ad}\left[C_{L(1,i-1)}\times\left(C'_L-C_{L(1,i-1)}\right)-\frac{S}{b}C_{L(1,i-1)}\right] + FD_H\left[\frac{\left(C_{L(1,i-1)}-C_{L(2,i-1)}\right)}{\Delta x_1}-0\right]/\left(\Delta x_1/2\right) \quad (5.A3.5)$$

The concentration gradient is 0 at the entrance of the first Langmuir site mesh. The equation simplifies to:

$$\frac{C_{L(1,i)}-C_{L(1,i-1)}}{\Delta t}=k_{ad}\left[C_{L(1,i-1)}\times\left(C'_L-C_{L(1,i-1)}\right)-\frac{S}{b}C_{L(1,i-1)}\right]+FD_H\frac{\left(C_{L(1,i-1)}-C_{L(2,i-1)}\right)}{\Delta x_1^{\,2}/2} \tag{5.A3.6}$$

Similarly for downstream the last half mesh, the mass balance is:

$$r \quad . \quad . \quad) \tag{5.A3.7}$$

From the mass balance, one can obtain the flux at the last node by subtracting the diffusion term by the lateral transfer term.

$$J_{(N,i)}=D_H\left(\frac{C_{H(N-1,i-1)}-C_{H(N,i-1)}}{\Delta x_{N-1}}\right)-k_{ad}\left[C_{H(N,i-1)}\times\left(C'_L-C_{L(N,i-1)}\right)-\frac{S}{b}C_{L(N,i-1)}\right]\times\left(\frac{\Delta x_{N-1}}{2}\right) \tag{5.A3.8}$$

where $C_{H(N,i-1)}$ is given by:

$$C_{H(N,i-1)}=S\times p_{d(i-1)} \tag{5.A3.9}$$

The Langmuir site does not have molecules diffuse out at the surface. There for the concentration accumulation rate will be an addition of the lateral transfer rate and the diffusion rate from the 2nd cell from the bottom, where the Langmuir site concentration gradient at the permeate side surface is 0. Note that a negative net value of the lateral transfer term means that gas molecules are transferred from Langmuir's sites to the Henry's sites.

$$\frac{C_{L(N,i)}-C_{L(N,i-1)}}{\Delta t}=k_{ad}\left[C_{H(N,i-1)}\times\left(C'_L-C_{L(N,i-1)}\right)-\frac{S}{b}C_{L(N,i-1)}\right]+FD_H\frac{\left(C_{L(N-1,i-1)}-C_{L(N,i-1)}\right)}{\Delta x_{N-1}^2/2} \tag{5.A3.10}$$

5.9.4 Appendix IV - Details on the boundary conditions of the partial immobilization and non-instantaneous equilibrium models.

Downstream boundary $(x=x_{NX}=L)$

(1) Under ideal BCs and instantaneous equilibrium

$$C_D(x_{NX},t)=0 \quad \text{(a)}$$
$$C_H(x_{NX},t)=0 \quad \text{(b)} \tag{5.A4.1}$$

(2) Under real BCs and instantaneous equilibrium

$$C_D(x_{NX},t)=S\cdot p_D \quad \text{(a)}$$
$$C_H(x_{NX},t)=\frac{C'_H b p_D}{1+bp_D} \quad \text{(b)} \tag{5.A4.2}$$

(3) Under real BCs and non-instantaneous equilibrium

$$R_{AccumulationH(NX)}=R_{HH(NX)}+R_{transfer(NX)} \tag{5.A4.3}$$

$$R_{AccumulationH(NX)}=\frac{C_H\left(x_{NX},t\right)-C_H\left(x_{NX},t-\Delta t\right)}{\Delta t} \tag{5.A4.4}$$

$$R_{HH(NX)}=-D_H\frac{C_H\left(x_{NX},t-\Delta t\right)-C_H\left(x_{NX-1},t-\Delta t\right)}{\Delta x_{NX-1}{}^2/2} \tag{5.A4.5}$$

$$R_{transfer(NX)}=k_{ad}\left[\begin{array}{l} C_D(x_{NX},t-\Delta t)\times\left(C'_H-C_H(x_{NX},t-\Delta t)\right) \\ -\dfrac{S}{b}\times C_H(x_{NX},t-\Delta t)\end{array}\right] \tag{5.A4.6}$$

$$R_{DD(NX+1)}=R_{DD(NX)}-R_{transfer(NX)}-R_{AccumulationD(NX)} \tag{5.A4.7}$$

$$R_{DD(NX)}=-D_D\frac{C_D\left(x_{NX},t-\Delta t\right)-C_D\left(x_{NX-1},t-\Delta t\right)}{\Delta x_{NX-1}{}^2/2} \tag{5.A4.8}$$

$$R_{AccumulationD(NX)}=\frac{C_D\left(x_{NX},t\right)-C_D\left(x_{NX},t-\Delta t\right)}{\Delta t} \tag{5.A4.9}$$

$$\begin{aligned} C_H\left(x_{NX},t\right)=&\,C_H\left(x_{NX},t-\Delta t\right) \\ &+\Delta t\left\{\begin{array}{l} -D_H\dfrac{C_H\left(x_{NX},t-\Delta t\right)-C_H\left(x_{NX-1},t-\Delta t\right)}{\Delta x_1{}^2/2} \\ +k_{ad}\left[\begin{array}{l} C_D(x_{NX},t-\Delta t)\times\left(C'_H-C_H(x_{NX},t-\Delta t)\right) \\ -\dfrac{S}{b}\times C_H(x_{NX},t-\Delta t)\end{array}\right]\end{array}\right\}\end{aligned} \tag{5.A4.10}$$

$$J_{D(NX)} = R_{DD(NX)} \times \frac{\Delta x_{NX-1}}{2} = -D_D \frac{C_D\left(x_{NX}, t-\Delta t\right) - C_D\left(x_{NX-1}, t-\Delta t\right)}{\Delta x_{NX-1}}$$
$$- k_{ad} \times \left(C_D(x_{NX}, t-\Delta t) \times \left(C'_H - C_H(x_{NX}, t-\Delta t)\right) - \frac{SC_H(x_{NX}, t-\Delta t)}{b} \right) \qquad (5.A4.11)$$
$$\times \frac{\Delta x_{NX-1}}{2} - \frac{C_D\left(x_{NX}, t\right) - C_D\left(x_{NX}, t-\Delta t\right)}{\Delta t} \frac{\Delta x_{NX-1}}{2}$$

Chapter 6

Gas permeation model of mixed-matrix membranes with embedded impermeable cuboid nanoparticles

Haoyu Wu, Maryam Zamanian, Boguslaw Kruczek and Jules Thibault*

Abstract

In the packaging industry, the barrier property of packaging materials is of paramount importance. The enhancement of barrier properties of materials can be achieved by adding impermeable nanoparticles into thin polymeric films, know as mixed-matrix membranes (MMMs). Three-dimensional numerical simulations were performed to study the barrier property of these MMMs and to estimate the effective membrane gas permeability. Results show that horizontally-aligned thin cuboid nanoparticles offer far superior barrier properties compared to spherical nanoparticles for an identical solid volume fraction. Maxwell's model predicts very well the relative permeability of spherical and cubic nanoparticles over a wide range of the solid volume fraction. However, Maxwell's model shows an increasingly poor prediction of the relative permeability of MMM as the aspect ratio of cuboid nanoparticles tends to zero or infinity. An artificial neural network (ANN) model was developed successfully to predict the relative permeability of MMMs as a function of the relative thickness and the relative projected area of the embedded nanoparticles. However, since an ANN model does not provide an explicit form of the relation of the relative permeability with the physical characteristics of the MMM, a new model based on multivariable regression analysis is introduced to represent the relative permeability in a MMM with impermeable cuboid nanoparticles. The new model possesses a simple explicit form and can predict very well the relative permeability over an extensive range of the solid volume fraction and aspect ratio, compared with many existing models.

Keywords: Mixed-matrix membranes; Impermeable nanoparticles; Three-dimensional modelling; Relative permeability; Permeability predictive model

Publication status: Submitted to JMS.

***Corresponding author**

6.1 Introduction

6.1.1 Mixed-matrix membranes as barrier materials

Barrier thin films are widely used in food and beverage packaging, coating, drug release, fuel cells, and batteries [1-3]. Many of these films are made of polymer materials, of which the barrier properties are constrained due to the limitation in their thicknesses. By adding impermeable inorganic fillers into the polymeric matrix of the thin films, the permeation of water and gas molecules in barrier materials is further prevented or delayed. The embedding of a homogenously-dispersed inorganic filler into the continuous phase of a polymeric matrix is typically referred to as a mixed-matrix membrane (MMM). The shape, volume fraction, and dimensions of the nanoparticles within the polymer are important factors that determine the effective gas permeability of a mixed-matrix membrane. Wolf et al. [3] performed an exhaustive review of the effects of the shape of the fillers on the barrier properties of polymer/impermeable nanocomposite membranes. Their results, based on 1000 published data, showed a very wide variation of the relative permeability of MMMs. They nevertheless confirmed the superiority of layered nanoparticles to decrease the membrane relative permeability compared to isodimensional and elongated nanoparticles. Many researchers [4-6] also believe that fillers having high aspect ratios create a more tortuous path for diffusion and therefore improves the barrier properties by orders of magnitudes even for small volume fractions of the fillers [6]. For this reason, flake-like or plate-like fillers such as mica and clay minerals (hectorite, saponite and montomorillonite) are studied intensively due to their high aspect ratios [6-8]. The aspect ratio is defined as the ratio of the mean diameter of a circle of the same area of the filler to the mean thickness of the filler. There is a clear need to better understand the effect of the shape of

nanoparticles on the relative permeability of MMMs and have reliable theoretical predictions.

A number of researchers have studied and proposed models to characterize the permeation for both ideal and non-ideal morphology of MMMs [9]. Ideal membrane morphology refers to a two-phase membrane system: the continuous phase and the discontinuous phase. The majority of theoretical models to predict the effective permeability of MMMs were developed based on ideal membrane morphology, such as the models proposed by Maxwell [10], Bruggeman [11], Lewis-Nielsen [12,13], Pal [14], Cussler [15,16] and Bharadwajl [17]. Non-ideal morphology refers to MMMs for which a non-ideal polymer-particle interface exists due to poor polymer−particle adhesion, polymer-packing disruption near the dispersed particles, and repulsive forces between the two phases. MMMs are therefore sometimes characterized using a three-phase system, having the interface voids as the third phase, as proposed in a few modified models [18]. However, in reality, the interfacial defects are the result of many factors and vary from experiment to experiment, such that the accurate determination of the exact interface morphology is a challenge. In this study, we assume that the dispersed phase is nonporous (impermeable) and ideal MMM morphology exists with no defects and no distortion at the filler−polymer interface. It is also assumed that, for a given MMM, the fillers have identical shapes and sizes, and they are uniformly distributed within the polymeric membrane. The case where interfacial defects exist is briefly discussed at the end of this study.

6.1.2 Main prediction models of the relative permeability of MMMs

Many models, both analytical and numerical, for the prediction of the relative permeability of MMMs have been proposed over the years. Six of these analytical predictive models, considered most pertinent in this investigation, are presented in Table 6.1. These analytical models were proposed by Maxwell [10], Bruggeman [11], Lewis-Nielsen [12,13], Pal [14], Cussler [15,16] and Bharadwajl [17]. These models have been developed to describe the permeation of a species through MMMs and to estimate their relative permeability (P_r):

$$P_r = \frac{P_{eff}}{P_c} \tag{1}$$

where P_{eff} is the effective permeability of the MMM and P_c is the permeability of the continuous phase, i.e. that of a neat polymeric membrane. In all these models, P_r depends on the filler volume fraction ϕ, the permeability of the continuous phase P_c, and the permeability of the dispersed phase P_d. For a MMM with impermeable particles, $P_d = 0$, the mathematical expressions of Table 6.1 are significantly reduced. The first model used to predict the permeation properties of MMM was the Maxwell's model, a model initially proposed to estimate the dielectric properties of polymer composites. Among all models listed, the Maxwell's model is the most commonly used. Besides the permeability coefficients of the continuous phase (the polymer) and the dispersed phase (the fillers), the Maxwell's model uses only the volume fraction ϕ as a model parameter, regardless of the particle shape, size distribution and particle dispersion. The model is only applicable to a dilute two-phase MMM system containing spherical particles with $\phi < 0.2$. Bruggeman [11], also attempting to predict the dielectric properties of composite materials with randomly dispersed particles, modified the Maxwell's model in order to predict the relative permeability over a larger range of the volume fraction. Lewis and Nielsen [12.13] studied the mechanical properties of composite materials by experimentally exploring the relationship between the relative elastic modulus of composite materials and the volume fraction of its spherical fillers. The equation introduced an additional function ψ taking into account the maximum packing fraction ϕ_m. The model was often applied to predicting the *Pr* of MMMs. Pal's model was originally developed to determine the effective thermal conductivity of composite materials using the differential effective medium approach. This model also introduced an additional parameter, the maximum packing fraction ϕ_m. The Bruggeman's model is a special case of Pal's model when $\phi_m = 1.0$. Most models in Table 6.1, idealize the filler geometry and investigated only the effect of the filler volume fraction ϕ. To understand the impact of the filler's geometry, models such as the one proposed by Cussler's group relate the relative permeability to an aspect ratio as well as the volume fraction ϕ [15,16]. They extended the Maxwell's model by studying regular and random arrays of high aspect ratio impermeable particles, such as flakes and lamellae. They finally verified their model by performing experiments with the measurement of electrical resistance of salt solutions. Another well-known model is the two-dimensional model proposed by Bharadwajl [14]. Bharadwaj modified Nielsen's model and performed a

theoretical study on the effects of filler sheet length, concentration, orientation and degree of delamination on the relative permeability of MMMs. He concluded that dispersing long sheet of inorganic filler in a polymer matrix was particular beneficial for barrier properties.

Table 6.1 Predictive models for the relative permeability (P_r) of a migrating species in a MMM with nanoparticles [21].

Model	Equation	Eq. #
Maxwell (MXW) [10]	$P_r = \dfrac{P_d + 2P_c - 2\phi(P_c - P_d)}{P_d + 2P_c + \phi(P_c - P_d)}$	(2a)
	$P_d = 0: \quad P_r = \dfrac{1-\phi}{1+\phi/2}$	(2b)
Bruggeman (BGM) [11]	$P_r^{1/3}\left(\dfrac{P_d - P_c}{P_d - P_r P_c}\right) = (1-\phi)^{-1}$	(3a)
	$P_d = 0: \quad P_r = (1-\phi)^{3/2}$	(3b)
Lewis-Nielsen (LN) [12,13]	$P_r = \dfrac{1+2\phi(P_d - P_c)/(P_d + 2P_c)}{1-\psi\phi(P_d - P_c)/(P_d + 2P_c)}, \quad \psi = 1+\left(\dfrac{1-\phi_m}{\phi_m^{\,2}}\right)\phi$	(4a)
	$P_d = 0: \quad P_r = \dfrac{1-4\phi}{1+2\psi\phi}$	(4b)
Pal (PAL) [14]	$P_r^{1/3}\left(\dfrac{P_d - P_c}{P_d - P_r P_c}\right) = \left(1-\dfrac{\phi}{\phi_m}\right)^{-\phi_m}$	(5a)
	$P_d = 0: \quad P_r = \left(1-\dfrac{\phi}{\phi_m}\right)^{3/2\phi_m}$	(5b)
Cussler (CSL) [15,16]	$P_r = \dfrac{1}{1+\alpha\phi}, \quad \alpha\phi < 1$	(6a)
	$P_r = \dfrac{1-\phi}{1-\phi+\mu\alpha^2\phi^2}, \quad \alpha\phi > 1$ μ = 1 for flakes as periodic ribbons, μ = 4/9 for flakes as periodic hexagons.	(6b)

Bharadwaj (BDW) [17]	$P_r = \frac{1-\phi}{1+\frac{x_p}{3y_p}\left(\mu+\frac{1}{2}\right)\phi}$, μ = 0 for randomly dispersed fillers, μ = 1 for fillers perfectly aligned perpendicular to the gas flux	(7)

As previously stated, based on Wolf et al. [3] review, layered nanoparticles are more effective in reducing the permeability of MMMs than their isodimensional and elongated counterparts. Yet most of the available analytical models, including the majority of those listed in Table 6.1, are based on spherical nanoparticles. Therefore, the objective of this paper is two-fold. First, to show that the models listed in Table 6.1 cannot be used to accurately predict P_r of MMMs with dispersed layered nanoparticles over a wide range of volume fraction. Secondly, to develop a simple, yet general, mathematical model to predict P_r of MMMs for different geometries and dimensions of the filler particles in a 3D setting. Considering that a general analytical model which covers all geometries of nanoparticles may or may not exist, as an intermediate step between the numerical solution and an analytical model to predict P_r, we also demonstrate the applicability of an artificial neural network model for the prediction of P_r.

6.2 Gas transport in a MMM

A schematic diagram of a MMM is shown in Fig. 6.1. It is assumed that the nanoparticles are uniformly distributed throughout the whole membrane, such that it is possible to define an elementary cubic unit comprised of a single nanoparticle located at the center of the polymer cube. The membrane, therefore, consists of multiple identical elementary units juxtaposed to form the complete membrane. It can be easily shown that the permeability of a permeating species is identical for both a single elementary unit and the whole membrane [19,20]. Consequently, to estimate the permeability of the entire MMM membrane, it is sufficient to solve the Fick's second law of diffusion numerically for a single elementary unit. In this investigation, the polymer phase is assumed isotropic, and the nanoparticle located at the center of an elementary unit is assumed impermeable to

the permeating gas. Two different types of impermeable nanoparticles, often suggested as fillers in barrier films were used in this investigation. These are spherical and cuboid nanoparticles. An example of the former is TiO_2 nanoparticles, and an example of the latter is Montmorillonite (MMT) clay nanoparticles. The dimensions of each cubic elementary unit are L_x, L_y, and L_z (Fig. 6.1), whereas the spherical nanoparticle is defined with its diameter d_p, and the cuboid nanoparticle dimensions are x_p, y_p, and z_p.

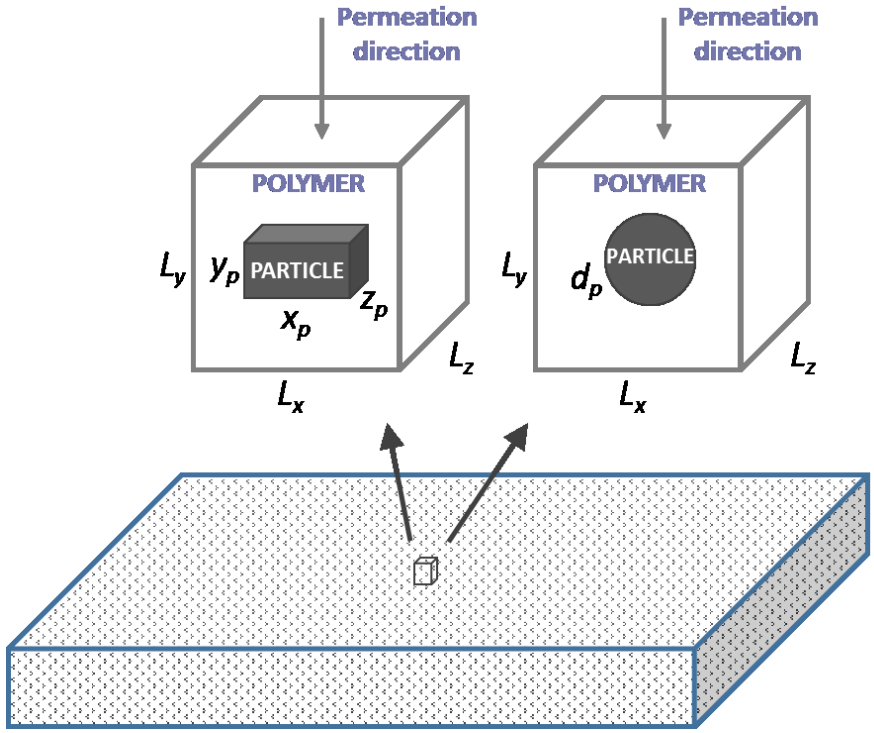

Figure 6.1 Schematic diagram of a MMM and one elementary unit with a nanoparticle located at its center; y is the direction of the gas permeation. The dimensions of the cuboid nanoparticle are x_p, y_p, and z_p, and the spherical particle is d_p. The dimensions of the polymer elementary unit are L_x, L_y, and L_z.

Gas permeation across a membrane follows three steps: sorption, diffusion, and desorption. The sorption and desorption processes follow Henry's law where, for a membrane of constant solubility S, the concentration of the migrating species at each surface of the membrane is proportional to the pressure as described in Eq. (1). It is assumed that the concentrations of gas molecules in the gas phase and within the membrane at the two gas-membrane interfaces are in instantaneous equilibrium. The diffusion process

follows the Fickian's first and second laws, as expressed in Eqs. (2) and (3). In a neat polymeric membrane, the diffusion occurs solely in the direction (y) perpendicular to the membrane. When permeable or impermeable particles are embedded within the polymeric matrix of the membrane, the diffusion occurs in the x, y and z directions in Cartesian coordinates.

$$C_s = S\,p \tag{1}$$

$$\vec{J} = \vec{J}_x + \vec{J}_y + \vec{J}_z = -D_c\left(\frac{\partial C}{\partial x}\vec{i} + \frac{\partial C}{\partial y}\vec{j} + \frac{\partial C}{\partial z}\vec{k}\right) \tag{2}$$

$$\frac{\partial C}{\partial t} = D_c\left[\frac{\partial^2 C}{\partial x^2} + \frac{\partial^2 C}{\partial y^2} + \frac{\partial^2 C}{\partial z^2}\right] \tag{3}$$

p is the gas pressure adjacent to a membrane surface and C is the concentration of the migrating species within the MMM, $\vec{J}$ is the time-varying local permeation flux (a vector), t is the time, x, y, z are the Cartesian coordinates to account for the three-dimensional diffusion within the membrane where y is the main direction of permeation. In this investigation, it is assumed that the membrane (continuous phase) has a constant and isotropic diffusivity D whereas the nanoparticles (dispersed phase) is impermeable and has a nil diffusivity. It is further assumed that the diffusivity is independent of concentration. In this investigation, we are therefore considering an ideal MMM with impermeable nanoparticles.

6.3 Methodology

The three-dimensional form of the Fick's second law of diffusion (Eq. (3)) can be discretized using finite differences. Eq. (11) represents the explicit discretization of Eq. (3) for an interior mesh point (i, j, k) that allows to calculate the concentration at the next time step knowing the current concentration at a given mesh point within the membrane. The change of concentration at mesh point (i, j, k) as a function of time depends on the current concentration at point (i, j, k) and the concentrations at the six neighbouring mesh points as illustrated in Fig.6.2.

$$C_{i,j,k}^{m+1} = C_{i,j,k}^{m} + \Delta t \left\{ \begin{array}{l} \dfrac{2D_c}{\Delta x_{i+1} + \Delta x_i} \left[\dfrac{C_{i+1,j,k}^{m} - C_{i,j,k}^{m}}{\Delta x_{i+1}} - \dfrac{C_{i,j,k}^{m} - C_{i-1,j,k}^{m}}{\Delta x_i} \right] \\ + \dfrac{2D_c}{\Delta y_{j+1} + \Delta y_j} \left[\dfrac{C_{i,j+1,k}^{m} - C_{i,j,k}^{m}}{\Delta y_{j+1}} - \dfrac{C_{i,j,k}^{m} - C_{i,j-1,k}^{m}}{\Delta y_j} \right] \\ + \dfrac{2D_c}{\Delta z_{k+1} + \Delta z_k} \left[\dfrac{C_{i,j,k+1}^{m} - C_{i,j,k}^{m}}{\Delta z_{k+1}} - \dfrac{C_{i,j,k}^{m} - C_{i,j,k-1}^{m}}{\Delta z_k} \right] \end{array} \right\} \tag{11}$$

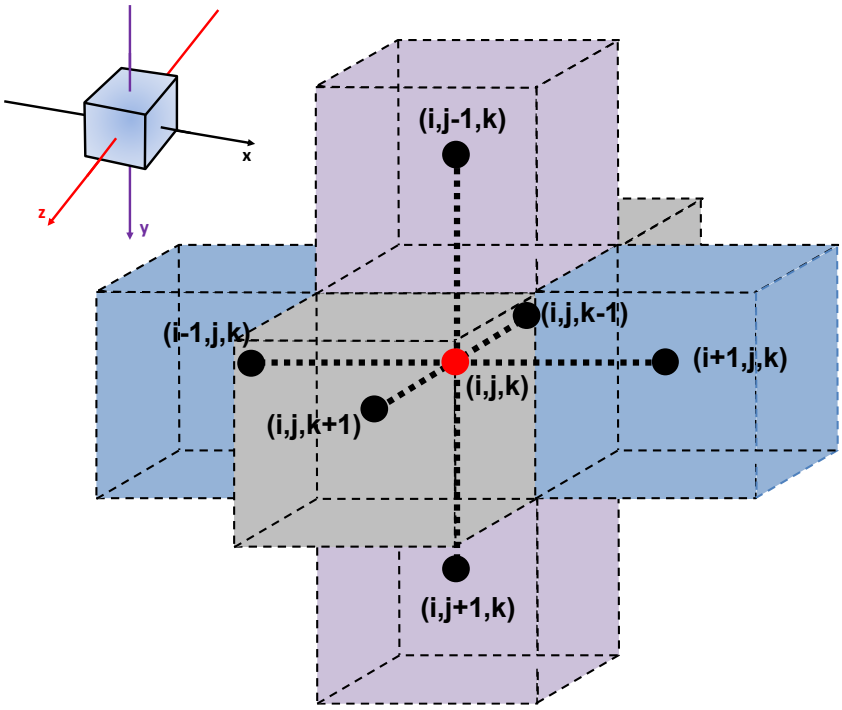

Figure 6.2 Nomenclature of an interior mesh point with its six neighbouring mesh points. x, y and z directions are represented by i, j and k, respectively.

It is important to reiterate that it is only necessary to solve for a single elementary unit to estimate the effective permeability of the mixed-matrix membrane. The elementary unit consists of a polymer cuboid ($L_x \times L_y \times L_z$) with a single nanoparticle at its center. To solve numerically for the temporal variation of the concentration at all points within the membrane, it is necessary to define the initial and boundary conditions. With respect to the initial condition, i.e. prior to the concentration step change on one side of the membrane at time $t = 0$, a nil concentration is assumed throughout the membrane (Eq. (12)). With respect

to the boundary conditions, twelve relations are required to completely define the problem: six boundary conditions at the periphery of the polymeric elementary unit and six boundary conditions at the polymer-solid interfaces. Eq. (13) provides the boundary conditions on both sides of the membrane (y-axis is the permeation direction). It is assumed that at the onset of permeation, a step change in the gas pressure is applied to the upstream side of the membrane ($y = 0$) whereas the gas pressure in the downstream side of the membrane ($y = L_y$) is kept under perfect vacuum. The resulting concentrations in the membrane at both surfaces are simply the product of the neighbouring pressure and the solubility S. Because all elementary units are identical, symmetry conditions prevail at the other four faces of the polymer parallelepiped as expressed in Eq. (14) for $BC_{3\text{-}6}$. Since the nanoparticle in the center of the elementary unit is impermeable, the mass flux at each of the six faces of the nanoparticle, assuming a cuboid nanoparticle, is zero (see $BC_{7\text{-}12}$ in Eq. (15)). The latter boundary conditions imply that the concentration of the migrating species inside the nanoparticle is zero.

$$\text{IC:}\quad C_{i,j,k}^{t<0} = 0 \qquad \forall i,j,k \tag{12}$$

$$\begin{aligned} &\text{BC}_1\text{: } C_{i,y=0,k} = p_0 S \qquad \forall i,k \\ &\text{BC}_2\text{: } C_{i,y=L_y,k} = 0 \qquad \forall i,k \end{aligned} \tag{13}$$

$$\text{BC}_{3\text{-}6}\text{:}\quad \left.\frac{\partial C}{\partial x}\right|_{x=0} = \left.\frac{\partial C}{\partial x}\right|_{x=L_x} = \left.\frac{\partial C}{\partial z}\right|_{z=0} = \left.\frac{\partial C}{\partial z}\right|_{z=L_z} = 0 \tag{14}$$

$$\begin{aligned} &\text{BC}_{7\text{-}8}\text{: } \left.\frac{\partial C}{\partial x}\right|_{x=\frac{(L_x-x_p)}{2}} = \left.\frac{\partial C}{\partial x}\right|_{x=\frac{(L_x+x_p)}{2}} = 0 \\ &\qquad \forall\left[\left(\frac{(L_y-y_p)}{2} \le \mathrm{y} \le \frac{(L_y+y_p)}{2}\right) \cap \left(\frac{(L_z-z_p)}{2} \le \mathrm{z} \le \frac{(L_z+z_p)}{2}\right)\right] \\ &\text{BC}_{9\text{-}10}\text{: } \left.\frac{\partial C}{\partial y}\right|_{y=\frac{(L_y-y_p)}{2}} = \left.\frac{\partial C}{\partial y}\right|_{y=\frac{(L_y+y_p)}{2}} = 0 \\ &\qquad \forall\left[\left(\frac{(L_x-x_p)}{2} \le \mathrm{x} \le \frac{(L_x+x_p)}{2}\right) \cap \left(\frac{(L_z-z_p)}{2} \le \mathrm{z} \le \frac{(L_z+z_p)}{2}\right)\right] \\ &\text{BC}_{11\text{-}12}\text{: } \left.\frac{\partial C}{\partial z}\right|_{z=\frac{(L_z-z_p)}{2}} = \left.\frac{\partial C}{\partial z}\right|_{z=\frac{(L_z+z_p)}{2}} = 0 \\ &\qquad \forall\left[\left(\frac{(L_x-x_p)}{2} \le \mathrm{x} \le \frac{(L_x+x_p)}{2}\right) \cap \left(\frac{(L_y-y_p)}{2} \le \mathrm{y} \le \frac{(L_y+y_p)}{2}\right)\right] \end{aligned} \tag{15}$$

The upstream and downstream fluxes are obtained from the concentration gradients at the upstream and downstream gas-membrane interfaces using Eq. (16). Convergence to the steady permeation rate is assumed to be reached when the fluxes at the upstream and downstream surfaces are the same within 0.001%. The effective permeability (P_{eff}) is calculated from the steady flux, the thickness L_y of the elementary unit and the feed pressure difference between the two sides of the elementary unit of the membrane (Δp) as expressed in Eq. (17).

$$J_{y=0} = -D_c \frac{\partial C_{y=0}}{\partial y} \tag{16a}$$

$$J_{y=L_y} = -D_c \frac{\partial C_{y=L_y}}{\partial y} \tag{16b}$$

$$P_{eff} = \frac{J_y L_y}{\frac{(p_0 - 0)}{RT}} \tag{17}$$

In Eq. (16), $J_{y=0}$ is the upstream permeation flux, and $J_{y=Ly}$ is the downstream permeation flux.

6.4 Results and discussion

6.4.1 Numerical simulation results

This section presents the results for the series of 3D simulated permeation experiments of gas molecules across a polymeric elementary unit with an impermeable nanoparticle in its center. The impermeable nanoparticle at the center of the elementary unit is either a sphere or a cuboid, representing the shape of the TiO_2 and the MMT nanoparticles, respectively. For a spherical nanoparticle, the diameter was varied whereas for a cuboid nanoparticle, the relative thickness, y_p/L_y, and the aspect ratio q were varied in order to assess the effect of the size and the shape of nanoparticles on the relative permeability (P_r) of mixed-matrix membranes. The aspect ratio (q) is defined by Eq. (18):

$$q = \frac{\sqrt{x_p z_p}}{y_p} \tag{18}$$

In the current investigation, we assumed that the *x*-*z* plane of a cuboid nanoparticle was parallel to the surface of the membrane, i.e. q is the square root of the projected area divided by the thickness of the nanoparticle.

Fig. 6.3 presents the relative permeability of MMMs obtained from the simulated permeation experiments with spherical nanoparticles for a filler volume fraction ϕ ranging from 0 to 0.52 and with cuboid nanoparticles for a ϕ ranging from 0 to 0.77. Since q has a significant impact on P_r, the results for the cuboid nanoparticles were grouped over a series of narrow ranges of the aspect ratio: from 0.51 - 0.56 to 7.00 - 7.29. Many more numerical results were obtained than those presented in Fig. 6.3, and they will all be used in developing a model to predict P_r. When q is large, the cuboid nanoparticle is a thin flat sheet with a large projected area, which the migrating species must circumvent to reach the permeate side of the membrane, thereby reducing the permeability of the membrane. On the other hand, when q is small, the cuboid has a small projected area with a large thickness (y_p).

As expected, the relative permeability decreases with an increase in the volume fraction occupied by the nanoparticles within each q range. It is evident that the aspect ratio has a major impact on the effective permeability of the membrane. Results of Fig. 6.3 show that P_r as a function of ϕ for MMMs with an impermeable sphere and an impermeable cube (having an aspect ratio of unity) is nearly identical. For impermeable cuboid nanoparticles with q smaller than unity, the relative permeability is greater than the relative permeability of MMMs with spherical and cubic nanoparticles. In contrast, when q is larger than unity, the situation is exactly the opposite. For a membrane with cuboid nanoparticles with the same ϕ, the greater the value of q, the smaller the value of P_r.

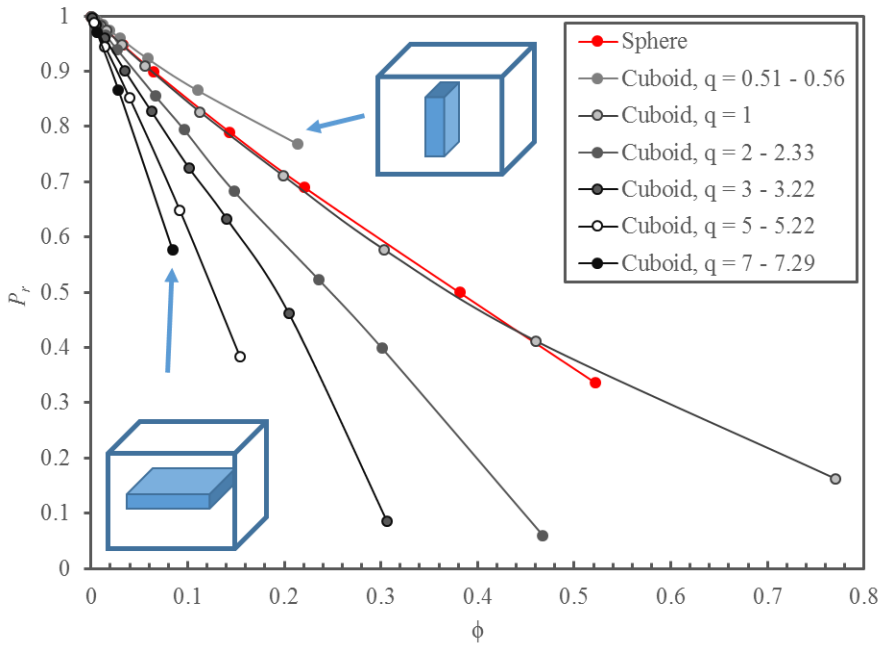

Figure 6.3 Plots of the relative permeability P_r of MMMs as a function of the solid volume fraction ϕ for spherical and cuboid impermeable nanoparticles, grouped by narrow ranges of the aspect ratio q. Data points were obtained numerically, and the solid lines are trend lines.

With the numerous estimations of P_r obtained numerically in this investigation, it was desired to verify if any correlation available in the literature could adequately predict the relative permeability of cuboids with large values of the aspect ratio. Fig. 6.4 compares the relative permeability obtained numerically with the one obtained using the six correlations of Table 6.1 for spherical nanoparticles for a volume fraction in the range [0.00, 0.52], and cuboid nanoparticles for four different narrow interval ranges of the aspect ratio: [2.0, 2.3], [3.0, 3.2], [5.0, 5.2], and [7.0, 7.3]. Results confirm that the relative permeability of spherical nanoparticles predicted by the model proposed by Maxwell is nearly identical to the one obtained numerically. The predicted P_r by the Maxwell model starts to deviate for a volume fraction in the vicinity of 0.25. On the other hand, three models (BGM, LN and PAL) accurately predict P_r over the whole range of ϕ. Only the models proposed by Cussler [15-16] and Bharadwajl [17], which were not developed for spheres, show more significant deviations. Based on the results of Fig. 6.3, it is not surprising that the same four models

were equally able to predict the relative permeability of the cuboid nanoparticle with an aspect ratio of unity (results not shown). For the prediction of P_r for cuboid nanoparticles with a q value other than unity, Cussler's model predicts better than the four models for the two larger q values [5.0, 5.2] and [7.0, 7.3]; however, the deviations are still significant. The model proposed by Bharadwajl [17], which includes some geometrical parameters, is able to reasonably represent the data for small ϕ. However, this model becomes less accurate in predicting P_r for higher ϕ. All the other models over-predicted P_r of MMMs with cuboid nanoparticles when q was greater than unity and under-predicted P_r when q was smaller than unity. It is evident that the available analytical models fail to predict accurately the relative permeability of MMMs with dispersed impermeable nano-cuboids with $q > 1$, in particular when ϕ becomes larger. The greater the value of q, the more significant is the deviation between the simulated and predicted relative permeability even at very small values of ϕ. For example, for $q = 5$, the deviation between the simulated P_r and the one predicted by the best existing model (BWD) becomes evident at $\phi \sim 0.02$.

These results show that it is imperative to develop a model that would predict the permeation behavior of MMMs embedding impermeable nano-cuboids with q different from unity.

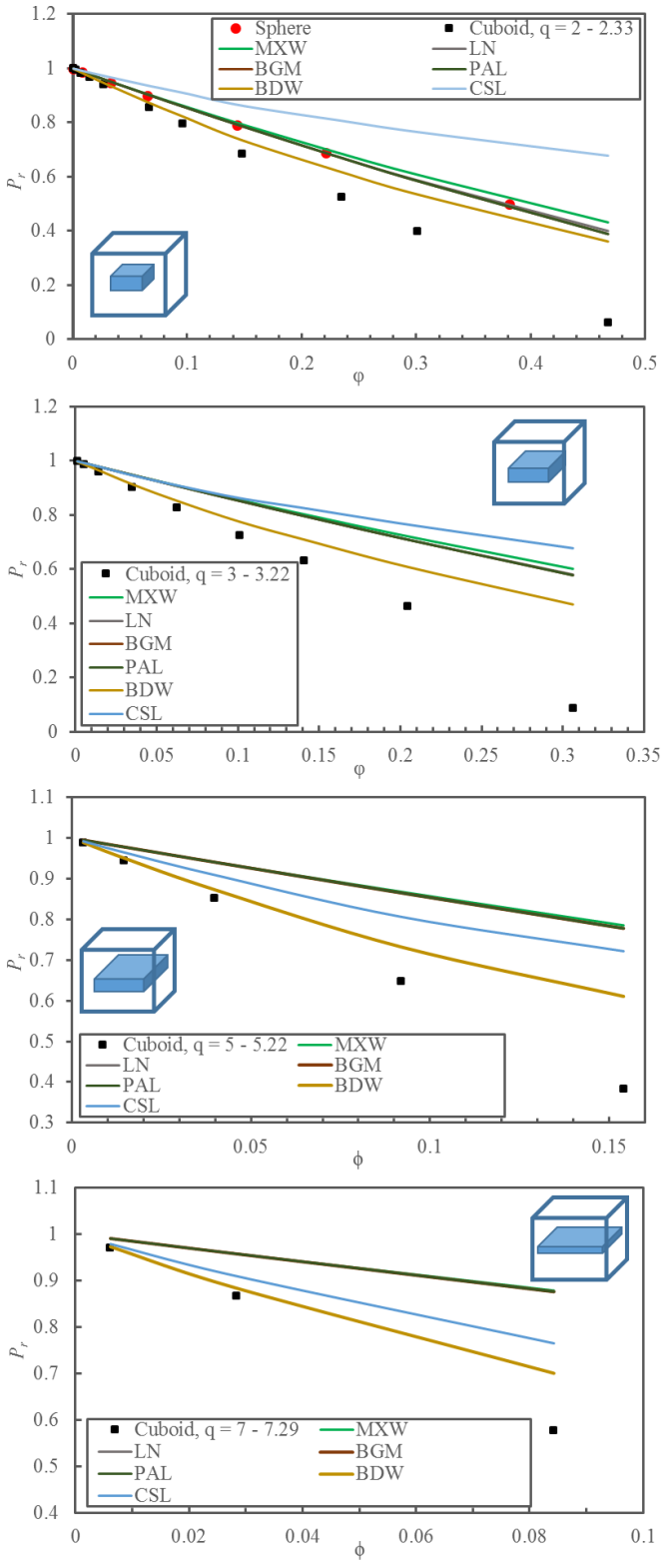

Figure 6.4 Comparison of the relative permeability of mixed-matrix membranes obtained numerically with the ones predicted by the six models presented in Table 6.1 as

a function of the filler volume fraction (ϕ). The comparison is made for a polymeric elementary unit containing an impermeable nanoparticle: a sphere and cuboids with four different ranges of the aspect ratio (q) ([2.0, 2.3], [3.0, 3.2], [5.0, 5.2], [7.0, 7.3]). Acronyms of each model are defined in Table 6.1.

6.4.2 Artificial neural network model for the prediction of the relative permeability

If the purpose is to find rapidly an accurate model that could be used for predicting the dependent variable, such as the relative permeability (P_r), an artificial neural network can be used. Artificial neural networks are now commonly used for a myriad of engineering applications. The high degree of plasticity of its structure is the main reason for their ability to efficiently represent the underlying causal relationship between input and output data. In this investigation, a three-layer feedforward neural network (FFNN) was used to predict P_r as a function of some input variables. Cybenko [19] showed that a three-layer FFNN was sufficient to encapsulate any input-output relationship if a sufficient number of neurons are used.

In this investigation, the FFNN consisted of an input layer, a hidden layer, and an output layer, as shown in Fig. 6.5. The input layer contains a number of neurons corresponding to the number of independent variables plus the bias neuron. The input layer simply transfers each set of independent variables to each functional neurons of the hidden layer. Each functional neuron of the hidden layer performs a weighted summation of all process inputs and a non-linear transformation of the weighted summation to generate the output of each neuron of the hidden layer. The outputs of the hidden layer, including the bias neuron of the hidden layer, are then sent to the output neuron. The output neuron performs the same task as the neurons of the second layer to generate the final output of the FFNN. A sigmoid function (Eq. (19)) was used as the transfer function for the hidden and output neurons. In this investigation, the inputs and outputs of the FFNN of Fig. 6.5 are by definition already scaled between 0 and 1 so that it was not necessary to scale them as it is usually done.

$$f(\Psi) = \frac{1}{1 + e^{-\Psi}} \qquad (19)$$

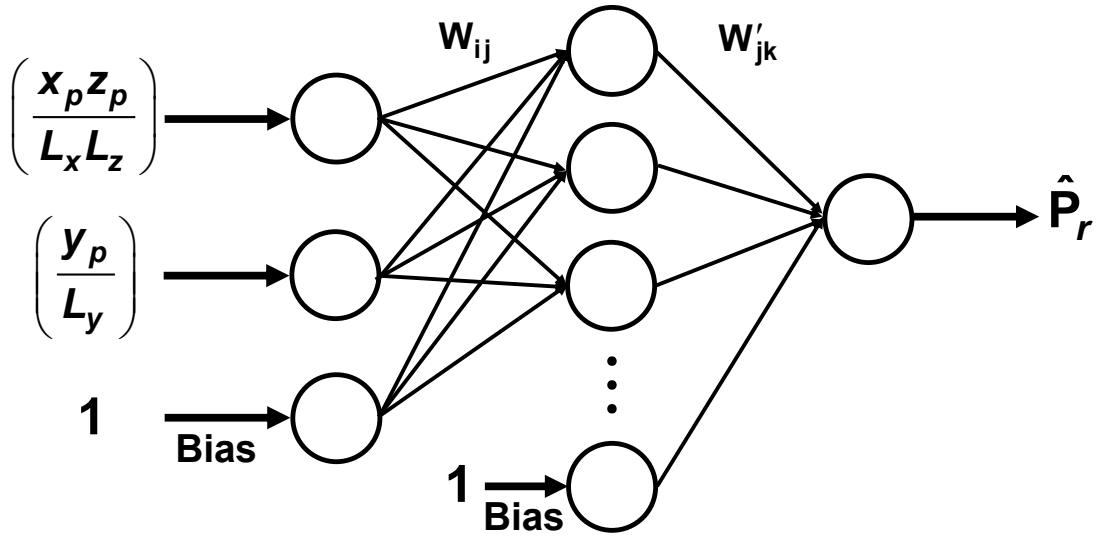

Figure 6.5 Feedforward neural network for the prediction of the relative permeability (P_r) for impermeable cuboid nanoparticles as a function of the normalized projected area ($x_p z_p / L_x L_z$) and the relative thickness (y_p / L_y).

Various input data vectors were explored in order to find the simplest neural network structure to accurately predict P_r. The two simplest structures of the FFNN were the ones that used only the relative dimensions of the nanoparticles within an elementary unit. In one case, the three relative lengths, x_p/L_x, y_p/L_y and z_p/L_z, were used. In the other case, the relative projected area ($x_p z_p / L_x L_z$) and the relative thickness (y_p / L_y) as shown in Fig. 6.5, were used. To determine the neural model for the prediction of P_r, 466 data points obtained by solving numerically the governing partial differential equation were divided equally into a training and a validation data set. The quasi-Newton nonlinear regression algorithm was used to adjust the weights of the FFNN that minimize the sum of squares of the training data set. At each iteration, the sum of squares of the validation data set was also evaluated and the set of weights that minimize the sum of squares of the validation data set was retained. The coefficient of regression for the FFNN with six hidden neurons (including the bias) was 0.9998 for both neural network structures mentioned above. The parity plot based on the FFNN of Fig. 6.5 is presented in Fig. 6.6.

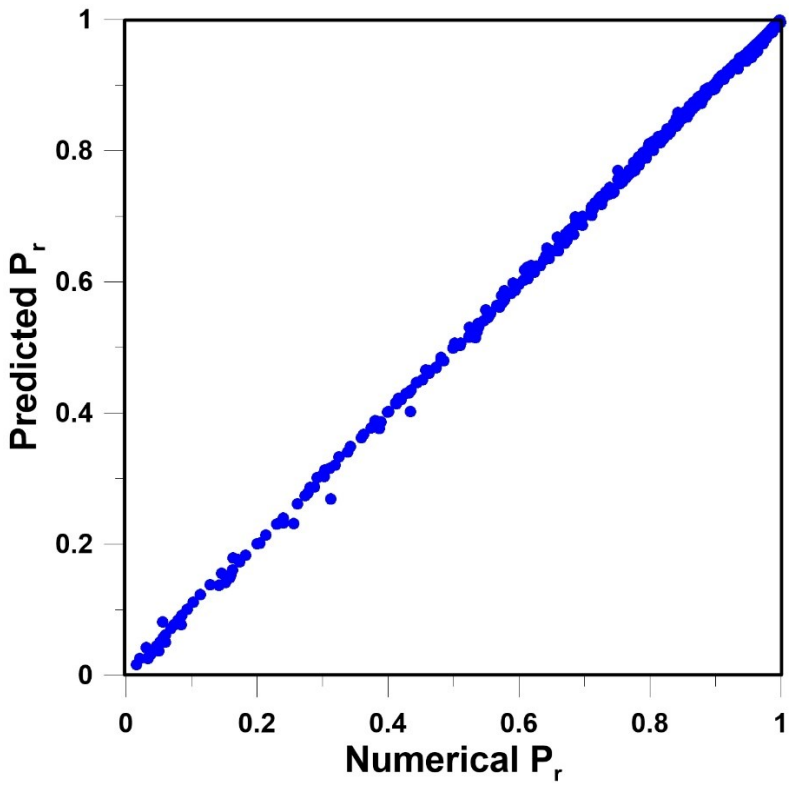

Figure 6.6 Parity plot of the predicted P_r and the numerically-determined P_r for the FFNN of Fig. 6.5 with six hidden neurons including the bias.

The FFNN is able to predict accurately P_r of mixed-matrix membranes containing impermeable cuboid nanoparticles. The accuracy of the neural model is excellent over the entire range of $x_p z_p / L_x L_z$ and y_p / L_y as the parity plot of Fig. 6.6 shows. The greatest deviation is observed for thin cuboids covering nearly the entire x-z area of the elementary unit. The latter condition is however extreme and will not be encountered in reality. The thinner the cuboid, the larger the deviation. The FFNN can be used with confidence to predict P_r. The mathematical model of the FFNN are given in Eqs. (20)-(22).

$$\begin{vmatrix} H_1 \\ H_2 \\ H_3 \\ H_4 \\ H_5 \end{vmatrix} = \mathrm{f}\left(\underset{\mathrm{W_{ij}}}{\begin{vmatrix} -12.13 & 0.7200 & -4.087 \\ -4.774 & -0.8497 & 0.9264 \\ 47.18 & 0.4026 & -50.00 \\ -3.616 & -0.1625 & 4.961 \\ 1.441 & -3.201 & -3.831 \end{vmatrix}} \bullet \begin{vmatrix} \frac{x_p z_p}{L_x L_z} \\ \frac{y_p}{L_y} \\ 1 \end{vmatrix} \right)$$

$$\hat{\mathrm{P}}_r = \mathrm{f}\left(\underset{\mathrm{W'_{jk}}}{\begin{vmatrix} 44.95 & 3.392 & -49.94 & 14.15 & 25.77 & -13.92 \end{vmatrix}} \bullet \begin{vmatrix} H_1 \\ H_2 \\ H_3 \\ H_4 \\ H_5 \\ 1 \end{vmatrix} \right) \tag{20}$$

$$\begin{aligned} H_j &= \frac{1}{1 + e^{-(W_{1j}\frac{x_p z_p}{L_x L_z} + W_{2j}\frac{y_p}{L_y} + W_{3j})}} \\ &= \frac{1}{1 + Exp\left(-\sum_{i=1}^{3} W_{ij}\, X_i\right)} \end{aligned} \tag{21}$$

$$\begin{aligned} \hat{P}_r &= \frac{1}{1 + e^{-(W'_{11}H_1 + W'_{21}H_2 + W'_{31}H_3 + W'_{41}H_4 + W'_{51}H_5 + W'_{61})}} \\ &= \frac{1}{1 + Exp\left(-\sum_{j=1}^{J} W'_{j1}\, H_j\right)} \end{aligned} \tag{22}$$

6.4.3 New analytical model for P_r of MMMs with impermeable cuboid nanoparticles

Although the neural network model presented in the previous section provides excellent predictions of the relative permeability of cuboid nanoparticles for a wide range of geometrical parameters, it does not provide a clear insight of the impact of the input variables on P_r as the analytical models listed in Table 6.1 do. On the other hand, the latter models, except for the Bharadwajl's correlation [17], fail to accurately predict P_r for cuboid nanoparticles with q different from unity. Therefore, it is desired to propose a new analytical model that will be valid for the widest possible ranges of ϕ and the geometrical parameters of the cuboid nanoparticles.

To clearly elucidate the relationship between the shape and the relative dimensions of nanoparticles and P_r, a multivariate covariance analysis was performed to assess the underlying correlation between all possible geometrical factors and P_r. For this analysis, the Pearson correlation coefficient (PCC), defined in Eqs. (23) to (25), was used.

$$\sigma = \sqrt{\frac{\sum_{i=1}^{n}\left(\mathrm{E}_i - \overline{\mathrm{E}}\right)^2}{n-1}} \tag{23}$$

$$\mathrm{Cov}\left(\mathrm{E}_A, \mathrm{E}_B\right) = \frac{\sum_{i=1}^{n}\left(\mathrm{E}_{Ai} - \overline{\mathrm{E}_A}\right)\left(\mathrm{E}_{Bi} - \overline{\mathrm{E}_B}\right)}{n-1} \tag{24}$$

$$\mathrm{PCC}\left(\mathrm{E}_A, \mathrm{E}_B\right) = \frac{\mathrm{cov}\left(\mathrm{E}_A, \mathrm{E}_B\right)}{\sigma_A \sigma_B} \tag{25}$$

where σ is the standard deviation of the variable E, Cov(E_A, E_B) is the covariance of E_A and E_B, $\bar{E}_A$ and $\bar{E}_B$ are the average values of E_A and E_B, and PCC(E_A, E_B) is the Pearson correlation coefficient between E_A and E_B. In this analysis, E_A corresponds to one geometrical variable to be tested, and E_B is P_r determined numerically. The results of this statistical analysis for five potential geometrical factors are presented in Table 6.2. The results show that $x_p z_p / L_x L_z$ has, in agreement with the results of the previous section, the highest negative PCC with P_r. The x_p/L_x ranks second because it is equivalent to the square root of the $x_p z_p / L_x L_z$. The ϕ also has a significant correlation factor with P_r. The aspect ratio and the relative thickness also have some impact on P_r but to a lesser degree. It is important to note that the five selected geometrical variables are not all mutually independent.

Table 6.2 Multivariate covariance analysis of geometrical factors and P_r.

Pearson correlation coefficient (PCC)					
Rank	Variable	Average	σ_{EA}	Cov(E_A, P_r)	PCC(E_A, P_r)
1	$x_p z_p / L_x L_z$	0.3381	0.3154	-0.0865	-0.9629
2	x_p/L_x	0.4961	0.2923	-0.0763	-0.9156
3	ϕ	0.1331	0.1821	-0.0436	-0.8401
4	q	2.5620	3.4326	-0.1937	-0.1981
5	y_p/L_y	0.4022	0.2753	-0.0144	-0.1831
-	P_r	0.7395	0.2850	-	-

To better comprehend the effect of these geometrical variables on P_r, one needs to examine the permeation process. Gas molecules entering a membrane will diffuse freely through the polymer matrix in the absence of impermeable nanoparticles. In that case, based on an elementary unit, the entire surface area of the polymer L_xL_z is available for diffusion. When a nanoparticle is introduced into an elementary unit, the gas molecules have to adopt a more tortuous path to diffuse around the impermeable nanoparticle. Fig. 6.7 present a plot of the isoconcentration lines within the polymer where the concentration within the cuboid particle is zero. Since the diffusion streamlines of gas molecules in the presence of an impermeable cuboid nanoparticle run perpendicular to the isoconcentration lines, one can easily imagine the diffusion path pf these gas molecules. Indeed, the diffusion streamlines are perpendicular to the *x-z* plane of the elementary unit at the gas-membrane interface and deviate progressively as they approach the impermeable nanoparticle. The density of the isoconcentration lines is indicative of the intensity of the local flux. The flux increases when the diffusion channel narrows down and decreases when it widens up.

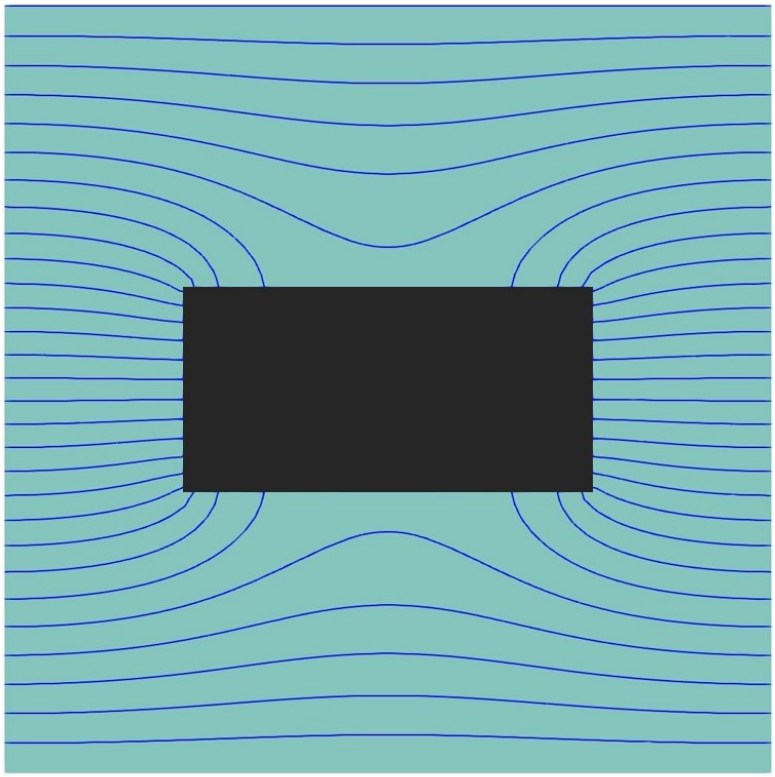

Figure 6.7. The steady-state iso-concentration lines of the migrating species on the half-cut plane of an elementary unit of a MMM with a cuboid nanoparticle with an aspect ratio $q = 2.07$ and a relative thickness $y_p/L_y = 0.25$.

Considering the local permeation flux's dependence on the size of the permeation channel for a given y-position, a dimensionless parameter A^*, defined in Eq. (26), is introduced. This dimensionless parameter is simply the ratio of the projected area that is available for diffusion (L_xL_z - x_pz_p) and the maximum surface area for diffusion (L_xL_z). It is logical to postulate that an increase in A^* will lead to an increase in P_r of the MMM, and vice versa. Fig. 6.8 clearly shows the strong relationship between P_r of a MMM with cuboid nanoparticles and the dimensionless parameter A^*.

$$A^* = \frac{(L_x L_z - x_p z_p)}{L_x L_z} \tag{26}$$

where x_pz_p is the projected area of the nanoparticle, while L_xL_z is the total permeation area of an elementary membrane unit.

In addition to the influence of A^* on P_r, Fig. 6.8 illustrates the impact of the relative thickness y_p/L_y over the range spanning from 0.0500 to 0.9833. For a nanoparticle with a fixed y_p/L_y, a decrease in x_pz_p leads to an increase of A^* and an increase in P_r. For a fixed A^*, P_r decreases when y_p/L_y increases. The plot of P_r versus A^* at the largest y_p/L_y is approaching the 45° line. In other words, P_r approaches A^* when y_p/L_y tends to 1.0. It is clear that the model to be developed must include the strong linear relationship of P_r with A^* as well as a nonlinear component to account for the effect of y_p/L_y.

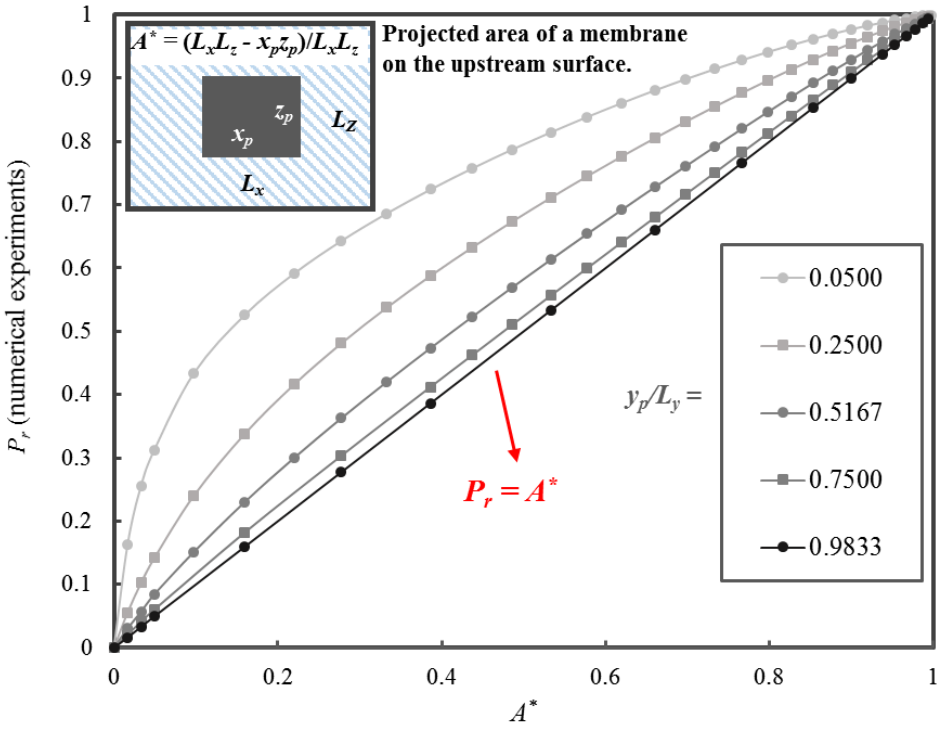

Figure 6.8 P_r of MMMs as a function of A^* for five values of y_p/L_y ranging from 0.0500 to 0.9833.

To characterize and better understand the contribution of the nonlinear portion (NLP) of the relative permeability curve, Fig. 6.9 is presented to highlight the breakdown of P_r in Fig. 6.8 into its linear ($P_r = A^*$) and NLP as a function of A^*. This data exploration is important in searching for the right form of the analytical equation in the development of an accurate predictive model. The contribution of the NLP that is related to y_p/L_y is clearly illustrated in Fig. 6.9. The nonlinear term first increases rapidly with A^* up to a maximum value before decreasing more gently to zero as A^* tends to unity. The location and the

magnitude of the maximum are a function of the relative thickness y_p/L_y. The maximum value is located in the interval of A^* between 0.16 to 0.38. The contribution of the nonlinear part can be as high as 0.37 of the value of P_r at $y_p/L_y = 0.05$ and $A^* = 0.18$.

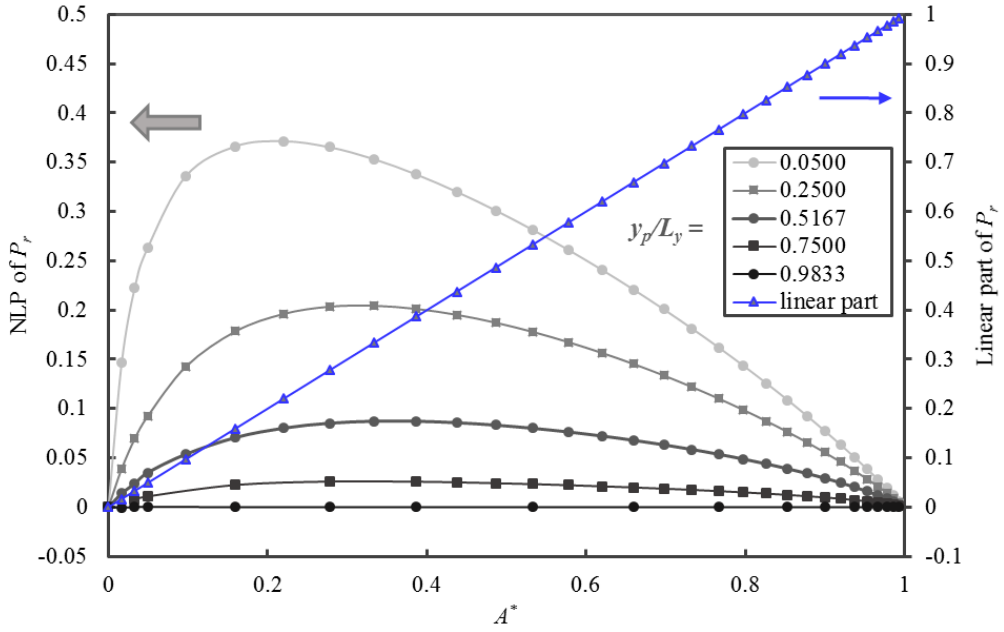

Figure 6.9 Plots of the linear and nonlinear portions of the P_r of a MMM as a function of A^* for five values of y_p/L_y ranging from 0.05 to 0.98.

Based on the insight of the above information, a new analytical model for the prediction of P_r is now presented in Eqs. (27) to (29). The model depends strictly on two simple geometrical parameters: A^* and y_p/L_y. Eq. (27) is the sum of the linear and nonlinear parts of the estimated P_r. The parameters a and b in Eq. (27), given by Eqs. (28) and (29), respectively, are a function of only the relative thickness. It is interesting to note that ϕ is not used explicitly in Eq. (27). On the other hand, both A^* and y_p/L_y indirectly determine the value of ϕ.

$$P_{rNew} = \frac{aA^*}{A^* + 2a - 1} - 0.5A^{*b} + A^* \tag{27}$$

$$a = 0.75 - 0.5\left|0.5 - \frac{y_p}{L_y}\right| \tag{28}$$

$$b = 1.5\left(1 - \frac{y_p}{L_y}\right) \tag{29}$$

Fig. 6.10 shows the comparison between the relative permeability obtained by solving numerically the Fick's second law of diffusion and the one predicted with the proposed model. To assess the accuracy of the model prediction, the average prediction error was calculated using Eq. (30).

$$\varepsilon_A = \sqrt{\frac{1}{n}\sum_{i=1}^{n}\left(P_{ri} - \hat{P}_{ri}\right)^2} \tag{30}$$

where ε_A is the average prediction error, n is the number of data for the average error calculation, P_r and $\hat{P}_r$ are the relative permeabilities obtained numerically and by the proposed model, respectively. Table 6.3 summarizes the average prediction error for the combination of the geometrical parameters presented in Fig. 6.10.

Given its simplicity, the proposed model predicts P_r accurately over a wide range of A^* and y_p/L_y. Table 6.3 shows that for each group, the relative particle thickness, ε_A is always below 0.03. The proposed model resorting to two simple geometrical parameters can be used with confidence to predict the permeability of MMMs with impermeable cuboid nanoparticles.

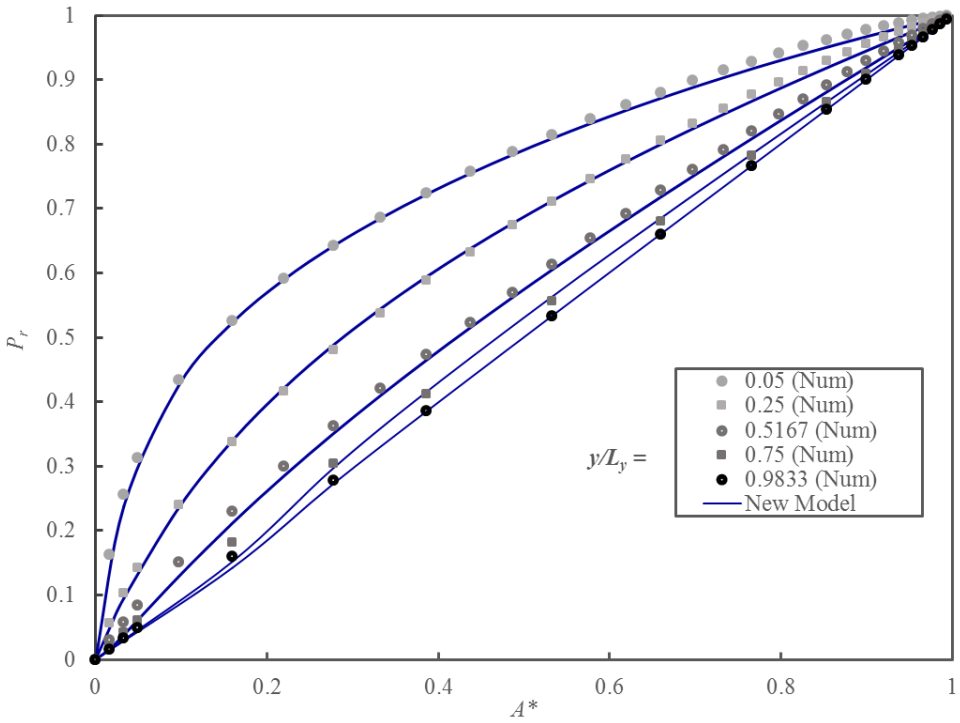

Figure 6.10. Plots of the P_r of MMMs embedding cuboid nanoparticles as a function of A^* for five different values of y_p/L_y.

Table 6.3. Average prediction errors of the P_r of Fig. 6.10 using the proposed model evaluated over five values of the y_p/L_y.

y_p/L_y	0.0500	0.2500	0.5167	0.7500	0.9833
A^*	0.03 – 0.99	0.03 – 0.99	0.03 – 0.99	0.16 – 0.99	0.16 – 0.99
ε_A	0.0098	0.0070	0.0110	0.0281	0.0048

6.4 Conclusion

In this paper, the permeation process of gas molecules through MMMs embedding impermeable spherical and cuboid nanoparticles of different aspect ratios was simulated using a three-dimensional finite-difference solution of the Fick's second law of diffusion. These numerical simulations allowed us to assess the effect of nanoparticles' shape and

size on the barrier properties of the resulting MMMs. Simultaneously, these simulations, which can be referred to as numerical experiments, allowed assessing the applicability of different analytical models to predict these membranes' relative permeability.

Simulation results showed that, for the same volume fraction, the relative permeability of MMMs with cuboid nanoparticles and the aspect ratio larger than unity was lower than the relative permeability of membranes with spherical nanoparticles. The relative permeability decreases with an increase in the aspect ratio of cuboid nanoparticles. The Maxwell's and similar models predict the relative permeability of MMMs with spherical nanoparticles very well, within a wide (small and medium) particle size range. However, Maxwell's model and other analytical models developed for spherical nanoparticles showed poor prediction of the relative permeability of MMMs with cuboid nanoparticles. Using an artificial neural network, we developed a feedforward neural network model, which accurately predicts the relative permeability of MMMs with both spherical and cuboid nanoparticles for a wide range of sizes and the aspect ratios. However, although very accurate, the developed feedforward neural network model lacks analytical models' simplicity and explicability. To overcome this limitation of neural network-based models, we used the Pearson correlation coefficient. We performed a very extensive multivariate covariance analysis to elucidate the relationship between the shape and the relative dimensions of nanoparticles, and the relative permeability of MMMs. This led to an analytical model, which involves only two geometrical parameters, the ratio of the projected area available for diffusion and the maximum surface area for diffusion, which depends on the nanoparticle's aspect ratio and the relative thickness of the nanoparticle. Despite its simplicity, the new model accurately predicts the relative permeability of the MMMs with cuboid nanoparticles for a wide range of sizes and aspect ratios. To our best knowledge, the model developed in this study is the first one in the literature which is applicable for MMMs with both spherical and layered nanoparticles.

The paper assumed an ideal case where the MMMs had ideal interfacial compatibility, no particle agglomeration, and particles were perfectly aligned. However, in reality, voids could exist due to poor adhesion between fillers and the polymer matrix; agglomeration of particles may create nanogaps between the particles and the polymer

chains. These non-ideal morphologies may increase or decrease the P_r. The effects of non-ideality need to be further investigated, even though it is very challenging to represent non-ideality.

6.5 Acknowledgement

The authors are grateful for the financial support of the Natural Science and Engineering Research Council of Canada.

6.6 Nomenclature

a	Parameter in Wu's model.
ANN	Artificial neural network
b	Parameter in Wu's model.
A^*	Relative projected area available for permeation A^*
C_s	Concentration at the membrane surface.
COV	Covariance.
d_p	Diameter of a rod or spherical nanoparticle.
d_{p1}	Outside diameter of a tube filler or long diameter of an elliptical rod filler.
d_{p2}	Inside diameter of a tube filler or a short diameter of an elliptical rod filler.
D_c	Diffusivity of dense membranes or the continuous phase of a mixed-matrix membrane.
D_d	Diffusivity for a nanoparticle.
E	A variable in multivariate covariance analysis.
FFNN	Feedforward neural network.
$f(\psi)$	Sigmoid transfer function.
H	Output of the hidden layer.
J	Permeation flux.
J_x	Permeation flux in x direction.
J_y	Permeation flux in y direction.

J_z	Permeation flux in z direction.
l_p	Length of a cylindrical rod, elliptical rod, or tube filler.
L_x	Dimension of an elementary unit at x direction.
L_y	Dimensions of an elementary unit at y direction.
L_z	Dimensions of an elementary unit at z direction.
MMM	Mixed-matrix membrane
NLP	Nonlinear portion.
p	Gas pressure.
P_c	Permeability of a dense membrane or the continuous phase of a mixed-matrixed membrane.
PCC	Pearson correlation coefficient.
P_d	Permeability for a nanoparticle.
P_{eff}	Effective permeability of a mixed-matrix membrane.
P_r	Relative permeability.
$\hat{P}_r$	Predicted relative permeability.
$P_{r\ (\mathrm{Num})}$	Relative permeability determined numerically.
$P_{r\ (\mathrm{New})}$	Relative permeability determined from Wu's model for cuboid nanofillers.
q	Aspect ratio in Wu's model.
R	Ideal gas constant.
S	Solubility.
W_{ij}	Weight connecting neuron i of the input layer to neuron j of the hidden layer
W'_{jk}	Weight connecting neuron j of the hidden layer to neuron k of the output layer
x_p	Dimension of a nanoparticle in the x direction.
y	Direction of permeation.
y_p	Dimension of a nanoparticle in the y direction.
y^*	Relative thickness of the nanoparticle.
z_p	Dimensions of a nanoparticle in the z direction.
α	Aspect ratio defined in Cussler's model.

ε	Average prediction error.
ϕ	The volume fraction of nanoparticles in MMMs.
ϕ_m	The maximum filler loading, i.e. the maximum volume fraction of nanoparticles in MMMs.
μ	A shape factor.
σ	Standard deviation.

6.7 References

[1] H.A. Silvério, W. Pires, F. Neto, D. Pasquini, Effect of Incorporating Cellulose Nanocrystals from Corncob on the Tensile, Thermal and Barrier Properties of Poly (Vinyl Alcohol) Nanocomposites, J. Nanomater. 2013 (2013) 1-9. https://doi.org/http://dx.doi.org/10.1155/2013/289641.

[2] S.E.M. Selke, J.D. Culter, Plastics Packaging: Properties, Processing, Applications, and Regulations, 3rd Ed. Carl Hanser Verlag, Munich, 2016. https://doi.org/10.1016/B978-3-446-40790-9.50001-9.

[3] C. Wolf, H. Angellier-Coussy, N. Gontard, F. Doghieri, V. Guillard, How the shape of fillers affects the barrier properties of polymer/non-porous particles nanocomposites: A review. J. Memb. Sci., 556 (2018) 393-418. https://doi.org/10.1016/j.memsci.2018.03.085.

[4] W. T. Brydges, S. T. Gulati, G. Baum, Permeability of glass ribbon-reinforced composites. J. Material. Sci., 10 (1975) 2044-2049. https://doi.org/10.1007/BF00557482

[5] S. Morimune-Moriya, T. Goto, T. Nishino, Effect of aspect ratio of graphene oxide on properties of poly (Vinyl alcohol) nanocomposites, Nanocomposites, 5 (2019) 84-93. https://doi.org/10.1080/20550324.2019.1647688

[6] X. Cheng, T.D. Papathanasiou, Barrier Properties of Flake-filled Membranes: Review and Numerical Evaluation, J. Plastic Film & Sheeting, 23(2007) 319-346. https://doi.org/10.1177/8756087907088437

[7] C.-C. Yang, Y.-C. Lee, Preparation and characterization of the PVA/MMT composite polymer membrane for DMFC, Electrochem. Soc. Trans. 13 (2008) 1–20. https://doi.org/10.1149/1.3055402

[8] V. Kaler, U. Pandel, R.K. Duchaniya, Development of TiO_2/PVA nanocomposites for application in solar cells, Mater. Today Proc. 5 (2018) 6279–6287. https://doi.org/10.1016/j.matpr.2017.12.237.

[9] H. Vinh-Thang and S. Kaliaguine, Predictive Models for Mixed-Matrix Membrane Performance: A Review, Chem. Rev., 113-7 (2013) 4980-5028. https://doi.org/10.1021/cr3003888.

[10] J.C. Maxwell, A Treatise on Electricity and Magnetism, 1st Ed., Oxford: Clarendon Press, London, 1873.

[11] D.A.G. Bruggeman, Berechnung verschiedener physikalischer Konstanten von heterogenen Substanzen. I. Dielektrizitätskonstanten und Leitfähigkeiten der Mischkörper aus isotropen Substanzen, Ann. Phys. 416 (1935) 636–664. https://doi.org/10.1002/andp.19374210205.

[12] T.B. Lewis, L.E. Nielsen, M. Company, Dynamic Mechanical Properties of Particulate- Filled Composites, J. Appl. Polym. Sci. 14 (1970) 1449–1471. https://doi.org/10.1002/app.1970.070140604.

[13] L.E. Nielsen, Thermal Conductivity of Particulate-Filled Polymers, J. Appl. Polym. Sci. 17 (1973) 3819–3820. https://doi.org/10.1002/app.1973.070171224.

[14] R. Pal, New Models for Thermal Conductivity of Particulate Composites, J. Reinf. Plast. Compos. 26 (2007) 643–651. https://doi.org/10.1177/0731684407075569.

[15] E.L. Cussler, S.T Hughes, W.J. Ward, III, and R. Aris, Barrier membranes, J. Memb. Sci. 38 (1988) 161-174. https://doi.org/10.1016/S0376-7388(00)80877-7.

[16] J.P. DeRocher, B.T. Gettelfinger, J. Wang, E.E. Nuxoll, and E.L. Cussler. “Barrier Membranes with Different Sizes of Aligned Flakes.” J. Memb. Sci. 254, 1 (2005) 21–30. https://doi.org/10.1016/j.memsci.2004.12.025.

[17] R.K. Bharadwaj, Modeling the barrier properties of polymer-layered silicate nanocomposites, Macromolecules. 34 (2001) 9189–9192. https://doi.org/10.1021/ma010780b.

[18] R. Mahajan, W. J. Koros, Mixed matrix membrane materials with glass polymers. Part 1, Polymer Eng. & Sci., 43 (2004) 1420-1431. https://doi.org/10.1002/pen.11042.

[19] A. Ebneyamini, H. Azimi, F.H. Tezel, J. Thibault, Modelling of mixed-matrix membranes: Validation of the resistance-based model, J. Memb. Sci. 543 (2017) 361–369. https://doi.org/10.1016/j.memsci.2017.08.064.

[20] A. Ebneyamini, H. Azimi, F.H. Tezel, J. Thibault, Mixed-matrix membranes applications: Development of a resistance-based model, J. Memb. Sci. 543 (2017) 351–360. https://doi.org/10.1016/j.memsci.2017.08.065.

[21] S. Zid, M. Zinet, E. Espuche, Modeling diffusion mass transport in multiphase polymer systems for gas barrier applications: A review, J. Polym. Sci. Part B Polym. Phys. 56 (2018) 621–639. https://doi.org/10.1002/polb.24574.

[22] G. Cybenko, Approximation by superpositions of a sigmoidal function, Math. Control, Signals, Syst. 2 (1989) 303–314. https://doi.org/10.1007/BF02551274.

Chapter 7

Generalized model for the prediction of the permeability of mixed-matrix membranes using impermeable fillers of diverse geometry

Haoyu Wu, Boguslaw Kruczek, and Jules Thibault*

Abstract

Using mixed-matrix membranes (MMMs) offers a myriad of opportunities to modify membrane transport properties for specific applications. This paper is concerned with evaluating and predicting the enhancement of barrier properties of packaging materials by embedding impermeable nanoparticles within the matrix of thin polymer films. Adding impermeable nanoparticles creates a more tortuous pathway for diffusion, thereby reducing the membrane's effective permeability. Various shapes of particles can be used, such as cuboids, rods, spheres, and tubes. Many models have been proposed in the literature to estimate the relative permeability coefficient of MMMs. These models' accuracy can be assessed by comparing their results with those obtained from physical or numerical experiments. The latter was performed by solving the three-dimensional Fick's second law of diffusion numerically. This paper proposes a novel model, which is a generalization of a model initially developed for impermeable cuboids dispersed in a continuous polymer phase. The proposed model is simple, yet it provides a more accurate prediction of the effective permeability coefficients of MMMs compared to the predictions of existing models. Although our model was developed initially for impermeable cuboids, it can also be easily adapted for impermeable fillers of different geometries such as spheres, rods, and tubes. Our model's application to other geometries simply requires a re-definition of some

geometrical parameters and an introduction of a correction factor when necessary. The model was verified to show excellent prediction results for all cases.

Keywords: Impermeable particles; Three-dimensional modelling; Relative permeability; Permeability predictive model; Particle geometry.

Publication status: To be submitted.

***Corresponding author**

7.1 Introduction

Mass transport of gas species in polymeric films is the focus of intense research for a myriad of applications. Some research effort aims to tune the properties of barrier materials, enhance the selectivity and permeation fluxes in membrane separation applications, reduce the membrane permeability in packaging and protective coating applications, and precisely control the permeation rate in drug delivery applications [1-3]. In addition to the synthesis of new polymers, significant efforts have been devoted to tuning polymer films' barrier properties by incorporating organic and inorganic particles in the polymer matrix. The resulting film is referred to as a mixed-matrix membrane (MMM) [4]. In packaging and coating applications, adding impermeable fillers creates physical obstacles to the migration of gas species within the MMM. As a result, the permeating species must adopt a more tortuous diffusion pathway to contour the embedded particles, which is referred to as the tortuosity effect [5-7]. The permeability of MMMs is expected to change significantly as corroborated by mass transfer experiments [5,7].

Multiple types of nanoparticles are currently used as fillers in MMMs [5]. These fillers come in various dimensions and shapes. They are used for different purposes, not only to modify membranes' permeability, but also to enhance their mechanical strength, optical properties, heat transfer properties, chemical stability, and electrical conductivity [4, 8-10]. Wolf et al. classified these fillers based on their geometries into (i) iso-dimensional particles: spherical silica, TiO_2, carbon black and fullerenes; (ii) elongated particles: carbon

nanotubes and cellulose nanofibers; (iii) layered particles: layered silicates and starch nanocrystals [5]. Among these fillers, the layered particles are found to have a more significant potential in reducing membrane permeability [5-7]. Some mathematical models have been proposed and will be discussed in a later section, to estimate the relative permeability coefficient of MMMs. However, the application of these models is limited as they resort mostly to the filler volume fraction. These models can only be used to predict the permeability of the specific particle geometry for which they were derived. The purpose of this paper is to develop a more general mathematical model for predicting the permeability coefficient of a MMM that would be valid not only for a specific particle geometry but for numerous other standard geometries of nanoparticles used as fillers. As mentioned in a review paper by Zid et al. [6], three-dimensional (3D) simulations are paramount in understanding and predicting the transport properties in the complex microstructure of a MMM. This paper continues to use the 3D simulation developed in a previous paper for estimating the relative permeability of fillers of various geometries in view of generating a universal predictive model for the relative permeability of a MMM. The model proposed by Wu et al. [11] for predicting the effective permeability of MMMs encapsulating impermeable cuboids was then used as a starting point and applied to the other standard geometries to assess and improve its predictive ability for other nanoparticle geometries. The final model is expected to serve as a tool to comprehend better the underlying relationship between the permeability of MMMs and the geometry, orientation, and relative size of the filler and provide guidance on an excellent membrane design.

7.2 Theoretical background

A schematic diagram of a mixed-matrix membrane with different filler geometries is shown in Fig 7.1. As described in the authors' previous work [11], the membrane is a two-phase system. It is assumed that the polymer phase is isotropic, and the nanoparticles are impermeable to the permeating species. It is also assumed that the nanoparticles are uniformly distributed throughout the whole membrane. To simplify the calculation, an elementary cubic unit comprised of a single nanoparticle located at the center of a polymer cube is defined. The effective permeability for a single elementary unit obtained by solving

the Fick's second law of diffusion is identical to solving for the effective permeability of the whole membrane [12,13]. Therefore, the results presented in this paper were obtained for a single elementary unit. In addition to the previously studied cuboid nanoparticles, this paper investigates many other types of impermeable fillers, namely solid rods, hollow cylinders, ellipses and spheres. The orientation of fillers significantly impacts the effective permeability of mixed-matrix membranes [14]. As a result, solid rods, hollow cylinders and elliptic rods were aligned both vertically and horizontally as depicted in Fig. 7.1. The dimensions of each elementary unit are L_x, L_y, and L_z (Fig. 7.1). In contrast, the cuboid particle dimensions are x_p, y_p,and z_p, the solid rod dimensions are defined with its diameter d_p and length l_p, the hollow cylinders and elliptic rods dimensions are defined with its diameters d_{p1} *and* d_{p2}, and length l_p, and the nanosphere is defined with its diameter d_p. For vertical elliptical rods, d_{p1} and d_{p2} are defined as the long and the short diameters. Different from the vertical elliptical rods, d_{p1} and d_{p2} is defined as the diameters in z-direction and y-direction for horizontal elliptical rods, respectively.

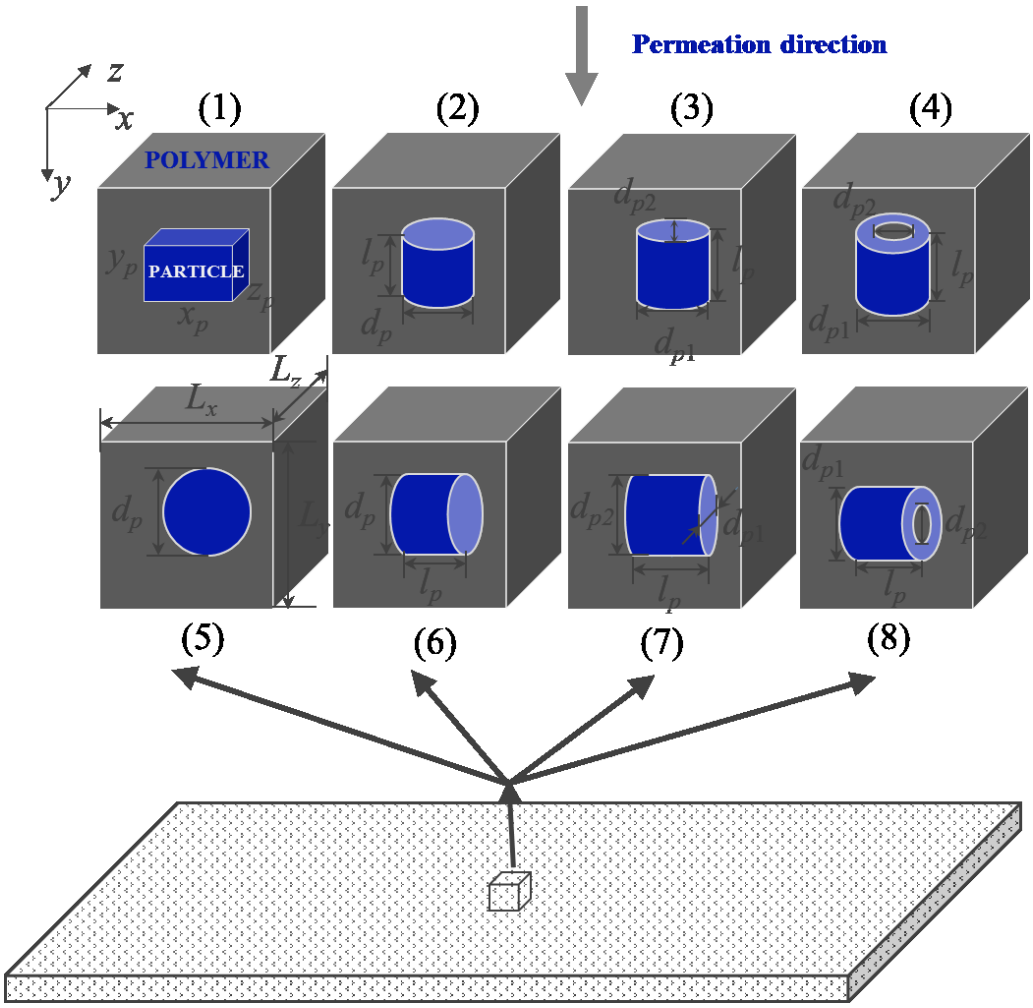

Figure 7.1 Schematic diagram of a mixed-matrix membrane and one elementary unit with a nanoparticle located at its center. y is the direction of the gas permeation. The dimensions of nanoparticles are x_p, y_p, and z_p for cuboids in (1), d_p and l_p for solid rods in (2) and (6), d_p for spheres in (5), d_{p1}, d_{p2} and l_p for hollow cylinders and elliptic rods in (3) (4) (7) and (8). The dimensions of the polymer elementary unit are L_x, L_y, and L_z.

The well-known solution-diffusion mechanism [15] explains the 3-step process of gas permeation across a dense membrane: (i) sorption, (ii) diffusion, and (iii) desorption. In a constant-temperature environment, the solubility S of permeating gases in a membrane is assumed constant. The sorption and desorption processes follow Henry's law, where the concentration of the migrating species at each surface of the membrane is proportional to its partial pressure, as described in Eq. (1). The time necessary for the concentration in the

gas phase and within the membrane at the two gas-membrane interfaces to reach equilibrium is usually several orders of magnitude shorter than the diffusion time. Therefore, it is assumed that equilibrium at the two gas-membrane interfaces is reached instantaneously. A diffusion process follows the sorption process as a result of a concentration gradient within the membrane. The diffusion process follows the Fickian's first and second laws, as expressed in Eqs. (2) and (3). In a neat polymeric membrane, the diffusion occurs solely in the direction (y) perpendicular to the membrane. When permeable or impermeable particles are embedded within the membrane's polymeric matrix, the diffusion occurs in the x, y and z directions in Cartesian coordinates. It is assumed that the membrane (continuous phase) and the nanoparticles (dispersed phase) have a different but constant and isotropic diffusivity: D_c for the membrane and D_d for the particles. It is further assumed that the diffusivity is independent of concentration. For an impermeable nanoparticle, D_d is equal to zero; this is the reason Eq. (3) is written only in terms of D_c, and the nil diffusivity will be taken into consideration with appropriate boundary conditions.

$$C_s = S\,p \tag{1}$$

$$\vec{J} = \vec{J}_x + \vec{J}_y + \vec{J}_z = -D_c\left(\frac{\partial C}{\partial x}\vec{i} + \frac{\partial C}{\partial y}\vec{j} + \frac{\partial C}{\partial z}\vec{k}\right) \tag{2}$$

$$\frac{\partial C}{\partial t} = D_c\left[\frac{\partial^2 C}{\partial x^2} + \frac{\partial^2 C}{\partial y^2} + \frac{\partial^2 C}{\partial z^2}\right] \tag{3}$$

C_s is the concentration of the migrating species within the membrane at the surfaces, p is the gas partial pressure of the migrating species adjacent to the membrane surfaces, C is the concentration of the migrating species within the mixed-matrix membrane, $\vec{J}$ is the time-varying local permeation flux (a vector), t is the time, x, y, z are the Cartesian coordinates to account for the three-dimensional diffusion within the membrane where y is the main direction of permeation.

The permeability coefficient P of the neat polymer is the product of its diffusivity and solubility, as shown in Eq. (4). In this paper, the permeability of a MMM is calculated via the relative permeability coefficient P_r, as defined in Eq. (5), which the ratio between the effective permeability coefficient P_{eff} of the MMM and the permeability coefficient of the

neat polymeric membrane, which is also the permeability coefficient of the continuous phase P_c of a MMM.

$$P = D \cdot S \tag{4}$$

$$P_r = \frac{P_{eff}}{P_c} \tag{5}$$

The most popular models for the prediction of the relative permeability for mixed-matrix membranes [11] are those proposed by Maxwell [16], Bruggeman [17], Lewis-Nielsen [18, 19], Pal [20], and Bharadwajl [21]. Among these models, Maxwell's model (Eqs. (6) and (7)) was the first model that was adapted from the thermal/electrical conductivity model, and commonly used as a prediction model for MMMs [22]. Maxwell's model uses only the filler's permeability and volume fraction ϕ as key parameters associated with the properties of the filler to calculate the effective permeability of the membrane. Maxwell's model has shown to be accurate for spheres and cubes for a wide range of the particle volume fraction [11]. The more recent models were developed by attempting to consider the shape and the aspect ratios of the filler particles, which expanded the range of validity of these predictive mathematical models. However, the volume fraction is not an elementary parameter of a filler. Based on a multivariate covariance analysis conducted on parameters of MMMs [11], apart from standard geometries, the correlation between the filler volume fraction and the relative permeability coefficient was found to be relatively weak. The ritual of using the volume fraction as a critical parameter in the expression of the relative permeability prediction might limit the applicability of a model to a narrow range of volume fraction. It may sometimes result in a cumbersome expression within the proposed models. On the other hand, the volume fraction may be a useful parameter for representing and comparing the relative permeability change when various geometries are used as no standard geometrical parameters yet exist.

$$P_r = \frac{P_d + 2P_c - 2\phi(P_c - P_d)}{P_d + 2P_c + \phi(P_c - P_d)} \tag{6}$$

$$P_d = 0: \quad P_r = \frac{1-\phi}{1+\phi/2} \tag{7}$$

In a previous paper [11], the authors solved the three-dimensional (3D) Fick's second law of diffusion numerically. The simulated results used to estimate the relative permeability coefficients of MMMs with fillers of basic geometry, namely impermeable cuboids, were analyzed better to comprehend the effect of each of its geometrical parameters. Unlike most predictive models that are based on the filler volume fraction as their fundamental parameter, the authors proposed a model (Eqs. (8)–(11)) that is using two geometrical parameters, namely the relative projected area available for permeation A^* and the relative thickness y_p/L_y of the filler for the prediction of the relative permeability of MMMs. The two parameters refer directly to elementary geometrical parameters. The model has a simple form and was found more accurate in predicting the relative permeability coefficients of cuboids over a wide range of volume fractions than all the other models mentioned above [11].

$$P_r = \frac{aA^*}{A^* + 2a - 1} - 0.5A^{*b} + A^* \tag{8}$$

$$A^* = \frac{(L_x L_z - x_p z_p)}{L_x L_z} \tag{9}$$ (24)

$$a = 0.75 - 0.5\left|0.5 - \frac{y_p}{L_y}\right| \tag{10}$$

$$b = 1.5\left(1 - \frac{y_p}{L_y}\right) \tag{11}$$

7.3 Methodology

The three-dimensional form of the Fick's second law of diffusion (Eq. (3)) was discretized using finite differences. Eq. (12) represents the explicit discretization of Eq. (3) for an interior mesh point (i, j, k) that allows calculating the concentration at the next time step, knowing the current concentration at a given mesh point within the membrane. The change of concentration at mesh point (i, j, k) as a function of time depends on the current concentration at point (i, j, k) and the concentrations at the six neighbouring mesh points, as illustrated in Fig. 7.2.

$$C_{i,j,k}^{m+1} = C_{i,j,k}^{m} + \Delta t \left\{ \begin{array}{l} \dfrac{2D_c}{\Delta x_{i+1} + \Delta x_i} \left[\dfrac{C_{i+1,j,k}^{m} - C_{i,j,k}^{m}}{\Delta x_{i+1}} - \dfrac{C_{i,j,k}^{m} - C_{i-1,j,k}^{m}}{\Delta x_i} \right] \\ + \dfrac{2D_c}{\Delta y_{j+1} + \Delta y_j} \left[\dfrac{C_{i,j+1,k}^{m} - C_{i,j,k}^{m}}{\Delta y_{j+1}} - \dfrac{C_{i,j,k}^{m} - C_{i,j-1,k}^{m}}{\Delta y_j} \right] \\ + \dfrac{2D_c}{\Delta z_{k+1} + \Delta z_k} \left[\dfrac{C_{i,j,k+1}^{m} - C_{i,j,k}^{m}}{\Delta z_{k+1}} - \dfrac{C_{i,j,k}^{m} - C_{i,j,k-1}^{m}}{\Delta z_k} \right] \end{array} \right\} \quad (12)$$

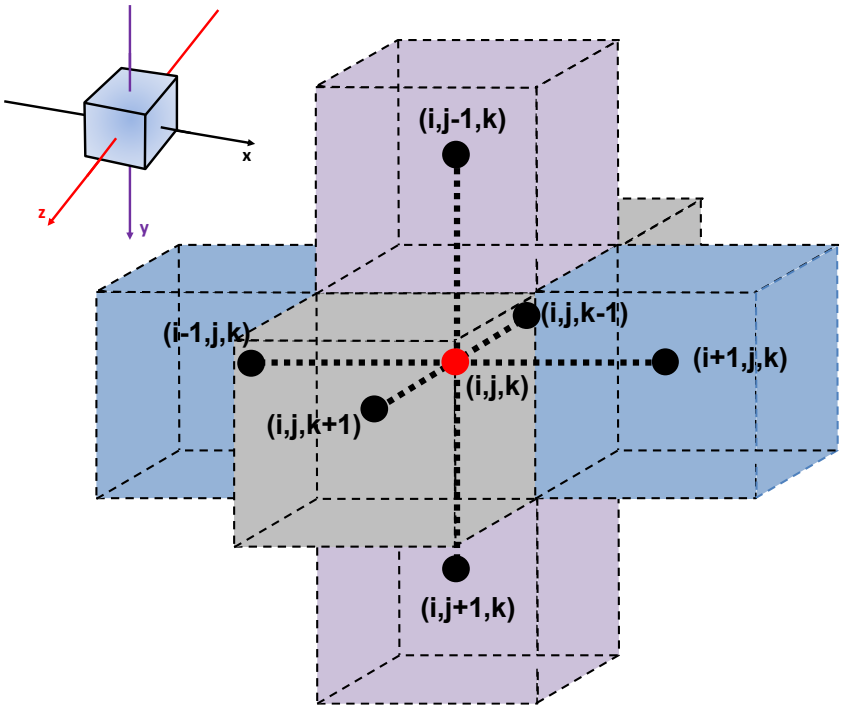

Figure 7.2 Nomenclature of an interior mesh point with its six neighbouring mesh points. x, y and z directions are represented by i, j and k, respectively.

It is important to reiterate that it is only necessary to solve for a single elementary unit to estimate a mixed-matrix membrane's effective permeability. The elementary unit consists of a polymer cuboid ($L_x \times L_y \times L_z$) with a single nanoparticle at its center. To solve numerically for the temporal variation of the concentration at all points within the membrane, it is necessary to define all initial and boundary conditions. Concerning the initial condition, i.e. before the concentration step-change on one side of the membrane at time $t = 0$, a nil concentration is assumed throughout the membrane (Eq. (13)). Concerning

the boundary conditions, twelve relations are required to define the problem: six boundary conditions at the periphery of the polymeric elementary unit and six boundary conditions at the polymer-solid filler interfaces. Eq. (14) provides the boundary conditions on both sides of the membrane (y-axis is the permeation direction). It is assumed that at the onset of permeation, a step-change in the gas pressure is applied to the upstream side of the membrane ($y = 0$), whereas the gas pressure in the downstream side of the membrane ($y = L_y$) is kept under perfect vacuum. The resulting concentrations in the membrane at both surfaces are simply the product of the neighbouring pressure and the solubility S. Because all elementary units are identical, symmetry conditions prevail at the other four faces of the polymer parallelepiped as expressed in Eq. (15) for $BC_{3\text{-}6}$. Since the nanoparticle in the center of the elementary unit is impermeable, the mass flux at each of the six faces of the nanoparticle, assuming a cuboid nanoparticle, is zero (see $BC_{7\text{-}12}$ in Eq. (16)). The latter boundary conditions imply that the concentration of the migrating species inside the nanoparticle is zero. Boundary conditions for other geometries are presented in the appendix.

$$\text{IC:}\quad C_{i,j,k}^{t<0} = 0 \qquad \forall i,j,k \tag{13}$$

$$\begin{aligned} &\text{BC}_1\text{: } C_{i,y=0,k} = p_0 S \qquad \forall i,k \\ &\text{BC}_2\text{: } C_{i,y=L_y,k} = 0 \qquad \forall i,k \end{aligned} \tag{14}$$

$$\text{BC}_{3\text{-}6}\text{:}\quad \left.\frac{\partial C}{\partial x}\right|_{x=0} = \left.\frac{\partial C}{\partial x}\right|_{x=L_x} = \left.\frac{\partial C}{\partial z}\right|_{z=0} = \left.\frac{\partial C}{\partial z}\right|_{z=L_z} = 0 \tag{15}$$

$$\begin{aligned} &\text{BC}_{7\text{-}8}\text{: } \left.\frac{\partial C}{\partial x}\right|_{x=\frac{(L_x-x_p)}{2}} = \left.\frac{\partial C}{\partial x}\right|_{x=\frac{(L_x+x_p)}{2}} = 0 \\ &\qquad \forall\left[\left(\frac{(L_y-y_p)}{2} \le y \le \frac{(L_y+y_p)}{2}\right)\cap\left(\quad p)}{2} \le z \le \frac{(L_z+z_p)}{2}\right)\right] \\ &\text{BC}_{9\text{-}10}\text{: } \left.\frac{\partial C}{\partial y}\right|_{y=\frac{(L_y-y_p)}{2}} = \left.\frac{\partial C}{\partial y}\right|_{y=\frac{(L_y+y_p)}{2}} = 0 \\ &\qquad \forall\left[\left(\frac{(L_x-x_p)}{2} \le x \le \frac{(L_x+x_p)}{2}\right)\cap\left(\frac{(L_z-z_p)}{2} \le z \le \frac{(L_z+z_p)}{2}\right)\right] \\ &\text{BC}_{11\text{-}12}\text{: } \left.\frac{\partial C}{\partial z}\right|_{z=\frac{(L_z-z_p)}{2}} = \left.\frac{\partial C}{\partial z}\right|_{z=\frac{(L_z+z_p)}{2}} = 0 \\ &\qquad \forall\left[\left(\frac{(L_x-x_p)}{2} \le x \le \frac{(L_x+x_p)}{2}\right)\cap\left(\quad p)}{2} \le y \le \frac{(L_y+y_p)}{2}\right)\right] \end{aligned} \tag{16}$$

The upstream and downstream fluxes are obtained from the concentration gradients at the upstream and downstream gas-membrane interfaces using Eq. (17). Convergence to the steady permeation rate is assumed to be reached when the fluxes at the upstream and downstream surfaces are the same within 0.001%. The effective permeability coefficient (P_{eff}) is calculated from the steady flux, the thickness L_y of the elementary unit and the feed pressure difference between the two sides of the elementary unit of the membrane (Δp) as expressed in Eq. (18).

$$J_{y=0} = -D_c \frac{\partial C_{y=0}}{\partial y} \tag{17a}$$

$$J_{y=L_y} = -D_c \frac{\partial C_{y=L_y}}{\partial y} \tag{17b}$$

$$P_{eff} = \frac{J_y L_y}{\frac{(p_0 - 0)}{RT}} \tag{18}$$

In Eq. (17), $J_{y=0}$ is the upstream permeation flux, and $J_{y=Ly}$ is the downstream permeation flux.

7.4 Results and discussion

In this section, the relative permeability (Pr) results for a large number of simulated permeation experiments across MMMs with impermeable nanofillers of various geometries are presented. The results are first compared with Maxwell's model, considered by many to be the benchmark model for estimating the P_r of MMMs. Then, a general correlation between P_r and two geometrical parameters is proposed, which is modified based on Wu's model [11] with the objective to predict accurately the P_r of MMMs embedding impermeable nanofillers of various geometries including vertically and horizontally oriented solids rods, cylindrical solid rods, elliptic solid rods, tubes (hollow rods), and spheres. Moreover, the proposed correlation is validated using all data available from the myriad of simulation results obtained in this investigation.

7.4.1 Comparison of the simulated results with Maxwell's Model

Figs. 7.3(a)-7.3(d) compare the simulated relative permeability (P_r) of MMMs with the relative permeability predicted by Maxwell's model for various geometries of the embedded nanoparticles. The relative permeability is presented as a function of the volume fraction ϕ, the only geometrical parameter used in the Maxwell's model. Fig. 7.3(a) shows the simulation results of P_r for spherical impermeable fillers as a function of the solid volume fraction ϕ up to a value of 0.45, which corresponds to a value of 0.975 for the relative diameter of d_p/L_y. Therefore, the range of the solid volume fraction is wide, and beyond the volume fraction, it would be physically achievable for MMM embedding spherical nanoparticles. As shown in Fig. 7.3(a), Maxwell's model predicts well the relative permeability of nanospheres over this wide range of volume fraction. Fig. 7.3(b) presents the results of the relative permeability of MMMs incorporating solid cylindrical rod fillers, oriented vertically and horizontally concerning the permeation direction, respectively. The solid cylindrical rod fillers are grouped based on their relative length (l_p/L_x for horizontally-oriented rods and l_p/L_y for vertically-oriented rods) for two values: 0.325 and 0.925. The relative length being fixed, the diameter d_p of the cylindrical rods was increased to increase their volume fraction. The figure first shows that Maxwell's model predicts relatively well the trend of how P_r varies with respect to the volume fraction of the filler particle but not the actual P_r values. Also, the larger the values of ϕ are, the less accurate are Maxwell's model predictions, especially for the shorter vertical rod. Also, Maxwell's model can both over-predict and under-predict the relative permeability, depending on the rod filler's orientation, volume fraction, and l_p/L_y or l_p/L_x ratio. Vertical cylindrical rod fillers with larger l_p/L_y ratios tend to be under-predicted by Maxwell's model, while the ones with smaller l_p/L_y ratios tend to be over-predicted. On the other hand, it is the reverse for horizontally-oriented rods.

Fig. 7.3(c) shows the results of the relative permeability for elliptical rod fillers. The results were grouped based on two l_p/L_x (horizontally-oriented fillers) or l_p/L_y (vertically-oriented fillers) ratios: 0.35 and 0.85. The short diameter d_{p2} of the elliptic rods is increased to increase their volume fraction while keeping the long diameter d_{p1} constant. In horizontally-oriented elliptical rods, the long axis is perpendicular to the permeation direction (y). The longer vertical elliptical rod's relative permeability is relatively well

predicted with the Maxwell model, whereas the longer horizontal elliptical rod shows a significant deviation. It is interesting to observe that P_r for the horizontal elliptical rods. However, it increases with a decrease in the volume fraction and does not tend to unity as in the vertical elliptical rods. Since the nanoparticle is impermeable and the longer diameter is constant and perpendicular to the direction of permeation, even a tiny short diameter will offer a barrier to permeation. As a result, the relative permeability tends to a fixed P_r value as the volume fraction decreases to zero, and there exists a discontinuity at zero volume fraction.

Fig. 7.3(d) shows the results for the annular tube fillers. The results were grouped based on two relative length l_p/L_x (horizontally-oriented fillers) or l_p/L_y (vertically-oriented fillers) ratios: 0.35 and 0.85. The inside diameter d_{p2} of the annular tubes is decreased to increase the filler volume fraction while keeping the outside diameter d_{p1} constant ($d_{p1}/L_x = d_{p1}/L_y = 0.85$). For horizontal annular tubes, similar behaviour of the relative permeability akin to the elliptical rods is observed. Indeed, if the outside diameter remains constant and the inside diameter is increased to increase the volume fraction, an infinitely thin impermeable tube will still offer a tortuous path for the gas permeation. For vertical tubes, the relative permeability is similar to the relative permeability of vertically-oriented cylindrical and elliptic rods.

All in all, a more considerable discrepancy in the prediction of the relative permeability is observed for all geometries studied in this project other than spherical fillers. The observed discrepancy is dependent on the fillers' shape, orientation and relative dimensions. The prediction of the relative permeability using Maxwell's model, which was derived for spherical fillers, is strictly based on the filler's volume fraction regardless of its orientation and partly on its dimensions. Therefore, a model that considers pertinent geometrical characteristics, and yet general, is needed to accurately predict the relative permeability of MMMs embedding impermeable fillers of various geometries with different shapes, orientations, and dimensions.

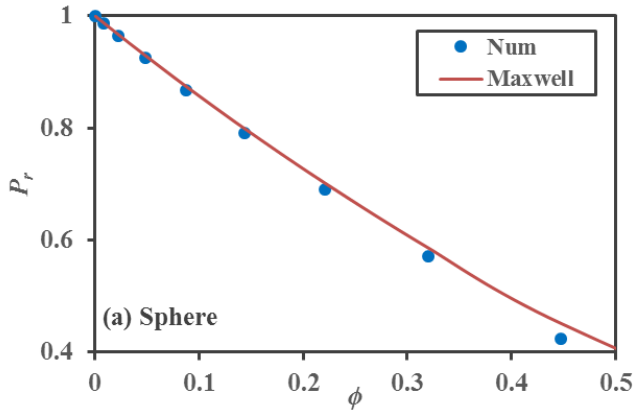
Num
Maxwell
(a) Sphere
P_r
ϕ

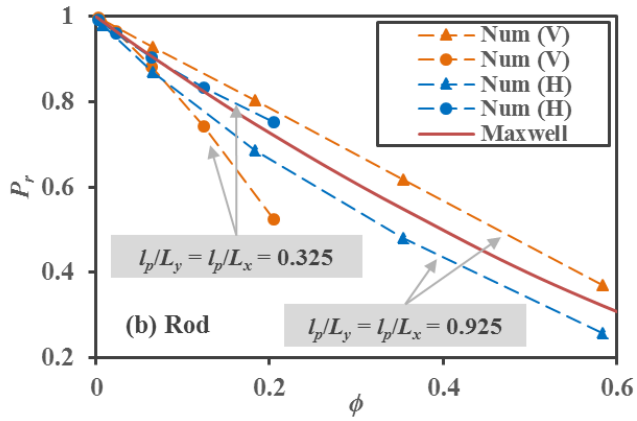
Num (V)
Num (V)
Num (H)
Num (H)
Maxwell
$l_p/L_y = l_p/L_x = 0.325$
(b) Rod
$l_p/L_y = l_p/L_x = 0.925$
P_r
ϕ

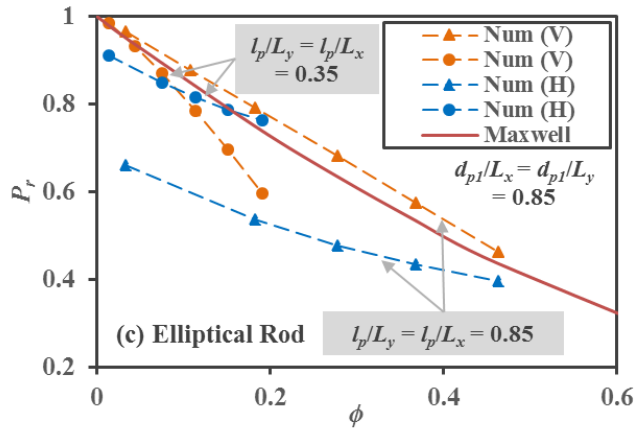
$l_p/L_y = l_p/L_x$ = 0.35
Num (V)
Num (V)
Num (H)
Num (H)
Maxwell
$d_{p1}/L_x = d_{p1}/L_y$ = 0.85
(c) Elliptical Rod
$l_p/L_y = l_p/L_x = 0.85$
P_r
ϕ

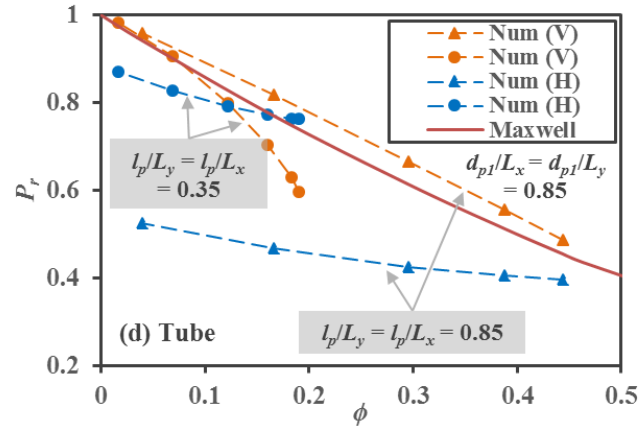
Num (V)
Num (V)
Num (H)
Num (H)
Maxwell
$l_p/L_y = l_p/L_x$ = 0.35
$d_{p1}/L_x = d_{p1}/L_y$ = 0.85
(d) Tube
$l_p/L_y = l_p/L_x = 0.85$
P_r
ϕ

Figure 7.3 Results of the P_r as a function of ϕ obtained from simulated permeation experiments of MMMs. The impermeable fillers are (a) spheres, (b) vertically- and horizontally-oriented cylindrical rods, (c) vertically- and horizontally-oriented elliptic rods, and (d) vertically- and horizontally-oriented annular tubes. Results are compared with the predictions from Maxwell's model.

7.4.2 A generalized model for the prediction of the P_r of MMMs with vertically-oriented fillers

Based on some geometrical similarities between the shape of the various fillers and the cuboid filler, the model proposed by Wu et al. [11] was first adapted to vertically-oriented geometries, including vertical cylindrical rods, elliptical rods, and annular tubes. Some of these geometrical similarities are: (1) all these geometries have lateral surfaces parallel to the main permeation direction, and (2) the top and bottom surfaces of these geometries are flat and perpendicular to the permeation direction. The three filler geometries oriented vertically share the same relative thickness defined as the length of the filler over the polymer elementary unit's length in the y-direction (l_p/L_y), which is symbolically represented with variable y^*. The projected areas of each vertically-oriented filler geometry correspond to its top surface but calculated differently depending on the geometry shown in Table 7.1. Table 7.1 also presents the relative projected area available for permeation (A^*). Eqs. (19)–(21) represent mathematically the model proposed by Wu et al. This simple model relies strictly on two general geometrical parameters A^* and y^*. It was used in this section to predict the relative permeability of MMMs embedding vertically-oriented impermeable fillers

Table 7.1 The expressions of the relative thickness y^* and the relative projected area available for permeation A^* of vertically-oriented fillers studied in this investigation.

Parameters	y^*	A^*
Cuboid	$\frac{y_p}{L_y}$	$1-\frac{x_p z_p}{L_x L_z}$
Vertical cylindrical rod	$\frac{l_p}{L_y}$	$1-\frac{\pi {d_p}^2}{4 L_x L_z}$
Vertical ellipse	$\frac{l_p}{L_y}$	$1-\frac{\pi d_{p1} d_{p2}}{4 L_x L_z}$
Vertical annular tube	$\frac{l_p}{L_y}$	$1-\frac{\pi\left({d_{p1}}^2-{d_{p2}}^2\right)}{4 L_x L_z}$

$$P_{r(\mathrm{Wu,V})}=\frac{aA^*}{A^*+2a-1}-0.5A^{*b}+A^* \tag{19}$$

$$a=0.75-0.5\left|0.5-y^*\right| \tag{20}$$

$$b=1.5\left(1-y^*\right) \tag{21}$$

Fig. 7.4 compares the relative permeability of MMMs for vertically-oriented cylindrical and elliptical rods determined numerically and predicted by Wu's model. The parity plot of Fig. 7.4(a) clearly shows that the relative permeability for MMMs with vertically-oriented cylindrical and elliptic rods is well predicted by the Wu's model ($P_{r(\mathrm{Wu,V})}$) [11]. Figs. 7.4(b) and 4(c) show the validation plots of $P_{r(\mathrm{Num})}$ and $P_{r(\mathrm{Wu,V})}$ with cylindrical and elliptical vertical rods as a function of A^*. Fig. 7.4(b) compares the numerical and simulated values of the relative permeability of MMMs with vertically-oriented impermeable cylindrical rods predicted for three different values of the relative thickness y^*: 0.125, 0.325 and 0.925. Fig. 7.4(c) presents a similar comparison for MMMs with vertically-oriented impermeable elliptical rods predicted for two different values of the relative thickness y^*: 0.35 and 0.85. All three figures clearly show the model proposed by Wu et al. for MMMs with cuboid nanoparticles to accurately predict the relative permeability of MMMs with vertically-oriented cylindrical and elliptical rods.

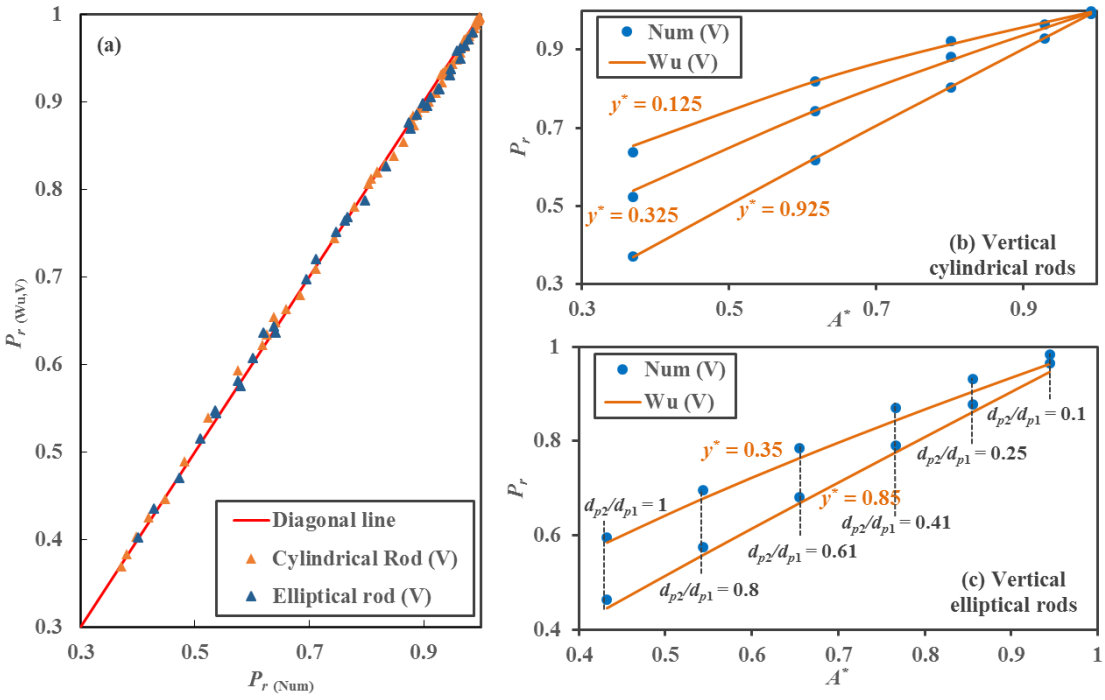

Figure 7.4 Comparison between $P_{r\ (Wu,V)}$ and $P_{r\ (Num)}$ of MMMs with vertical cylindrical and elliptical rods: (a) Parity plot of $P_{r\ (Wu,V)}$ and $P_{r\ (Num)}$, (b) Validation plot of $P_{r\ (Wu,V)}$ and $P_{r\ (Num)}$ as a function of A^* for cylindrical rods, and (c) for elliptical rods.

Fig. 7.5 compares the relative permeability of MMMs for vertically-oriented annular tubes determined numerically and predicted by the Wu's model via a parity plot (Fig. 7.5(a)) and a validation plot of $P_{r\ (Wu,V)}$ and $P_{r\ (Num)}$ (Fig. 7.5(b)) for three different values of the relative thickness y^*: 0.35, 0.52 and 0.85. Results of Fig. 7.5 show that the general trend in the data is relatively well captured by Wu's model. The predictions of the relative permeability are more accurate for more extensive and more extended annular tubes corresponding to smaller values of A^* and larger values of y^*. Larger values of A^* are associated with smaller ratios of diameters (d_{p2}/d_{p1}), that approaching a cylindrical rod. At higher values of A^* and smaller of y^*, the predictions are less accurate. In the worst case, the model of Wu under-predicts the P_r by approximately 0.03. It is not yet known why there is a discrepancy for vertically-oriented tubes, and it would therefore be possible to add a small correction factor.

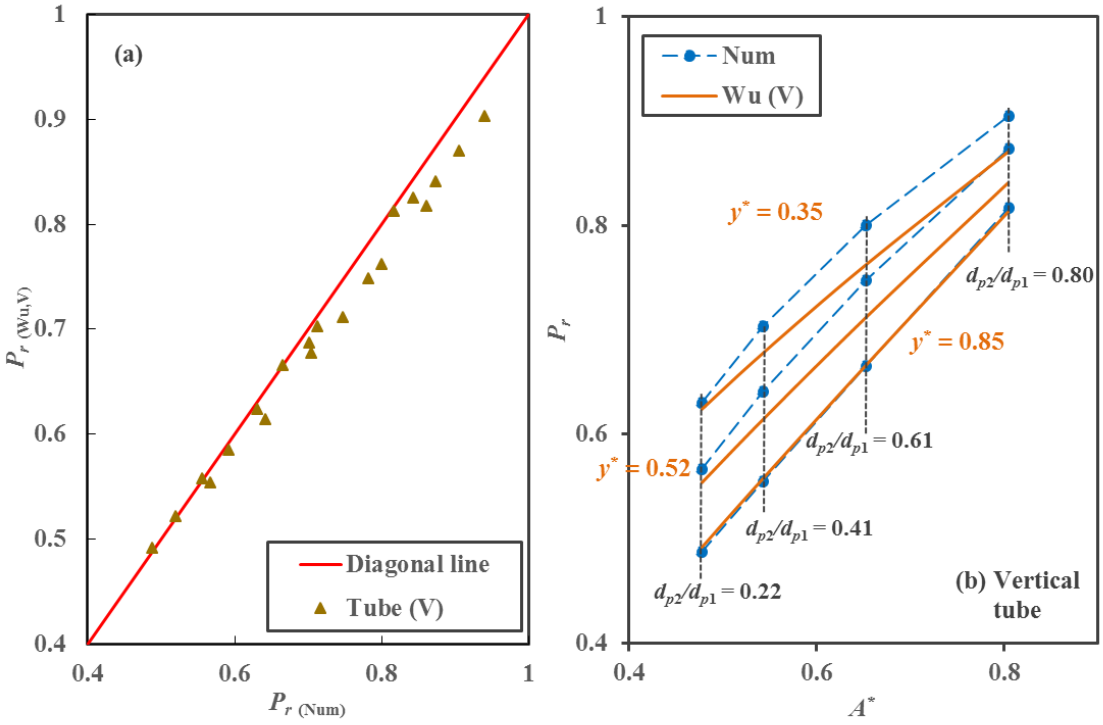

Figure 7.5 Comparison between $P_{r\,(Wu,V)}$ and $P_{r\,(Num)}$ of MMMs with vertical annular tubes: (a) Parity plot of $P_{r\,(Wu,V)}$ and $P_{r\,(Num)}$, and (b) Validation plot of $P_{r\,(Wu,V)}$ and $P_{r\,(Num)}$ as a function of A^*.

7.4.3 Generalized model for the prediction of the relative permeability of MMMs with spherical and horizontally-oriented fillers

Based on the positive results for the prediction of the relative permeability for MMMs with most vertically-oriented fillers, the analysis was pursued to determine if the same simple model proposed by Wu et al. [11] could be used to predict the relative permeability of MMMs with horizontally-oriented impermeable fillers. It was shown in Fig. 7.3 that the relative permeability of MMMs with vertically-oriented fillers was different than the one of MMMs with horizontally-oriented fillers. In horizontally-oriented fillers, the relative projected area available for permeation A^* can be easily defined as shown in Table 7.2 since it is associated with the filler projected area on the x-z plane. On the other hand, the thickness of the filler in the y-direction is not constant and varies in the permeation direction. To use the model proposed by Wu et al. [11], an average relative thickness y^*

has been defined, such that the product of the projected area of the filler and the relative thickness equals the volume of the filler. For horizontal annular tubes, two expressions are presented in Table 7.2, as will be explained later. The first expression is used for the results presented in Figs. 7.6, and 7.7.

Table 7.2 The expressions of y^* and A^* for MMMs with spherical fillers and three horizontally-oriented fillers, namely cylindrical rods, elliptical rods and annular tubes.

Parameters	y^*	A^*
Sphere	$\frac{2d_p}{3L_y}$	$1-\frac{\pi d_p^{\,2}}{4L_xL_z}$
Horizontal cylindrical rod	$\frac{\pi d_p}{4L_y}$	$1-\frac{d_p l_p}{4L_xL_z}$
Horizontal elliptical rod	$\frac{\pi d_{p2}}{4L_y}$	$1-\frac{d_{p1} l_p}{4L_xL_z}$
Horizontal annular tube	$\frac{\pi\left(d_{p1}^2-d_{p2}^2\right)}{4d_{p1}L_y}$ (a) (Figs. 7.6 and 7.7)	$1-\frac{d_{p1} l_p}{4L_xL_z}$
	$\frac{\pi d_{p1}}{4L_y}$ (b) (Figs. 7.8 and 7.9)	

Using the definitions of y^* and A^* in Table 7.2, the relative permeability of MMMs with spherical fillers and horizontally-oriented cylindrical rod, elliptical rod and annular tube fillers was predicted by the Wu's model and compared with the relative permeability obtained numerically. The parity plot of the relative permeability of MMMs with spherical, cylindrical rod and elliptical rod fillers is presented in Fig. 7.6(a), whereas the parity plot for MMMs with annular tube fillers is presented in Fig. 7.6(b). Fig. 7.6(a) indicates that the relative permeability of spheres, horizontally-oriented cylindrical and elliptical rods shows a strong correlation between the numerical and predicted permeability. All the data fall on a straight line that deviates slightly from the expected 45° line but coincides with unity's relative permeability. Fitting all the data points falling on this line, the following relationship was obtained: $P_{r(Wu)} = 1.11\ P_{r(NUM)} - 0.11$. It is therefore possible, using Eq.

(22), to add a correction factor to the model proposed by Wu et al. [11] for the prediction of MMMs with spheres, horizontally-oriented cylindrical and elliptical rods. Fig. 7.7 presents validation plots of $P_{r(\text{Num})}$ and $P_{r(\text{Wu,H})}$ (Eq. (22)) for MMMs with spheres and horizontally-oriented cylindrical and elliptic rods as a function of A^* for some conditions. Fig. 7.7(a) shows clearly that the model of Eq. (22) with a simple correction factor of the original Wu's model can accurately predict the relative permeability of mixed-matrix membranes with spherical fillers. Figs. 7.7(b) and 7.7(c) show similarly good predictions of the relative permeability of MMMs with horizontally-oriented cylindrical and elliptic rods, respectively, where different values of y^* prevailed.

$$P_{r(\text{Wu,H})} = \frac{P_{r(\text{Wu,V})} + 0.11}{1.11} \tag{22}$$

As shown in Fig. 7.6(b), the predictions of the relative permeability MMMs with horizontally-oriented annular tubes do not follow the same pattern as horizontal solid rods, but depend on the size of the annular tube and the ratio of the interior-to-exterior diameter. It was initially hypothesized that the relative permeability of MMMs with horizontally-oriented annular tubes could be the same as MMMs with horizontally-oriented cylindrical rods of the same outside diameter because they share the same projected area and the empty annular space is relatively stagnant when steady-state has been achieved. However, this is not the case, and the inner space assumed to be filled with the continuous polymeric phase impacts the relative permeability. MMMs with annular tubes, vertically- and horizontally-oriented, therefore need to be studied in greater detail.

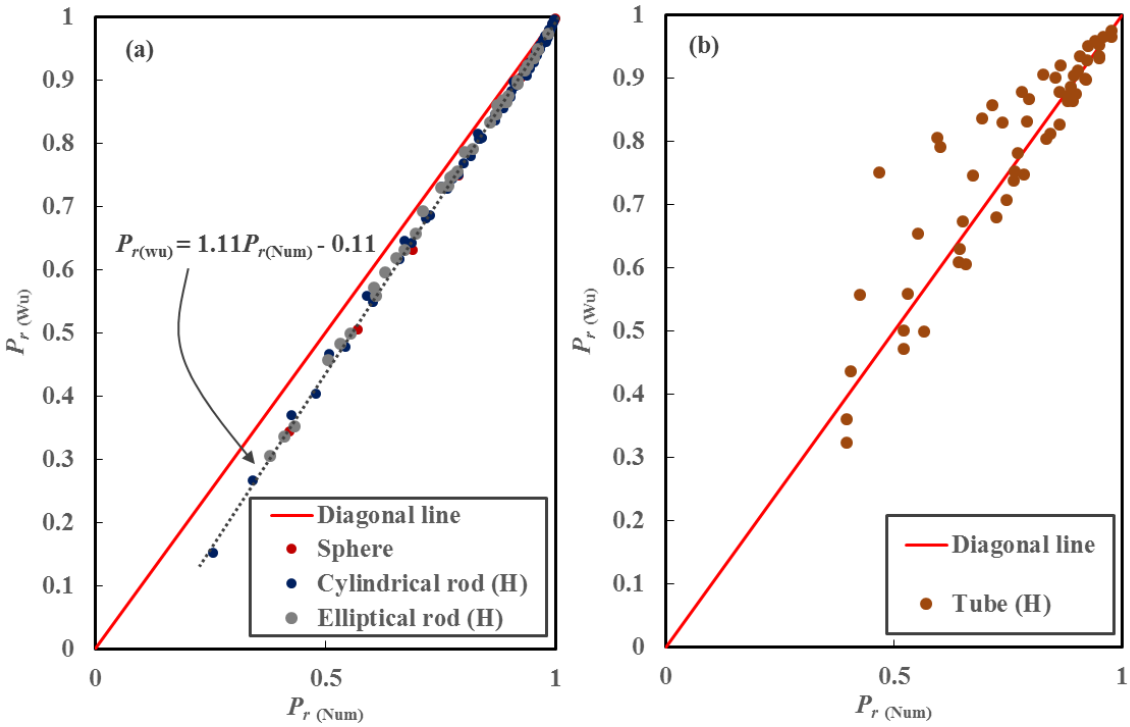

Figure 7.6 Parity plots of the P_r predicted by the Wu's model [11] as a function of the numerically simulated $P_{r(\text{Num})}$ of MMMs with four nanoparticle geometries: (a) spheres, horizontal cylindrical rods, and horizontally-oriented elliptical rods; and (b) horizontally-oriented annular tubes.

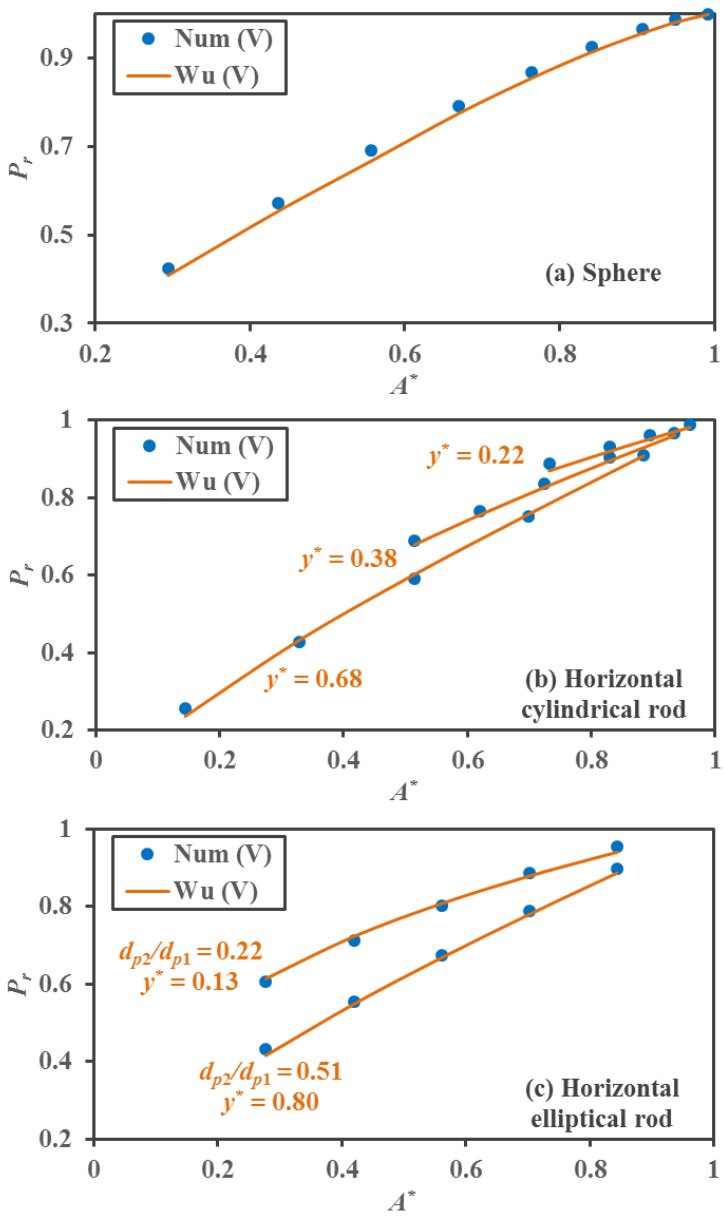

Figure 7.7 Comparison between $P_{r\ (\mathrm{Wu,H})}$ and $P_{r\ (\mathrm{Num})}$ of MMMs with spheres, and horizontally-oriented cylindrical and elliptic rods, plotted as a function of A^*.

The relative permeability of MMMs with horizontally-oriented annular tubes was further investigated. As d_{p2} is approaching zero, an annular tube becomes a cylindrical solid rod, and the relative permeability will therefore be well predicted with Eq. (22). Because a horizontally-oriented annular tube should behave approximately in the same manner as a horizontal cylindrical rod, an alternative form of y^*, as shown in Table 7.2, was then used in this investigation. Fig. 7.8 presents the ratio between $P_{r(\mathrm{Num})}$ of the cylindrical rods and

$P_{r(\text{Num})}$ of the annular tubes with the same d_{p1} for three groups of data with a constant y^* value of 0.67 for three values of l_p/L_x: 0.18, 0.52, and 0.85. For each data group, the ratio d_{p2}/d_{p1} of the annular tubes was changed while the d_{p1} remained constant. At the limit where the annular tube turns into a solid cylindrical rod, i.e. d_{p2}/d_{p1} approaches zero, the ratio becomes unity. As d_{p2}/d_{p1} increases, the tube's hollow volume increases the actual relative permeability ratio to the predicted relative permeability decreases, meaning the MMM becomes more permeable. The three lines of Fig. 7.8 were analyzed to find an additional correction factor for the model of Eq. (22) specific to annular tubes that would take into account the impact of the relative diameter d_{p2}/d_{p1}. Eq. (23) presents a relationship of the ratio mentioned above as a function of two geometrical parameters d_{p2}/d_{p1} and l_p/L_x obtained by data fitting and analysis.

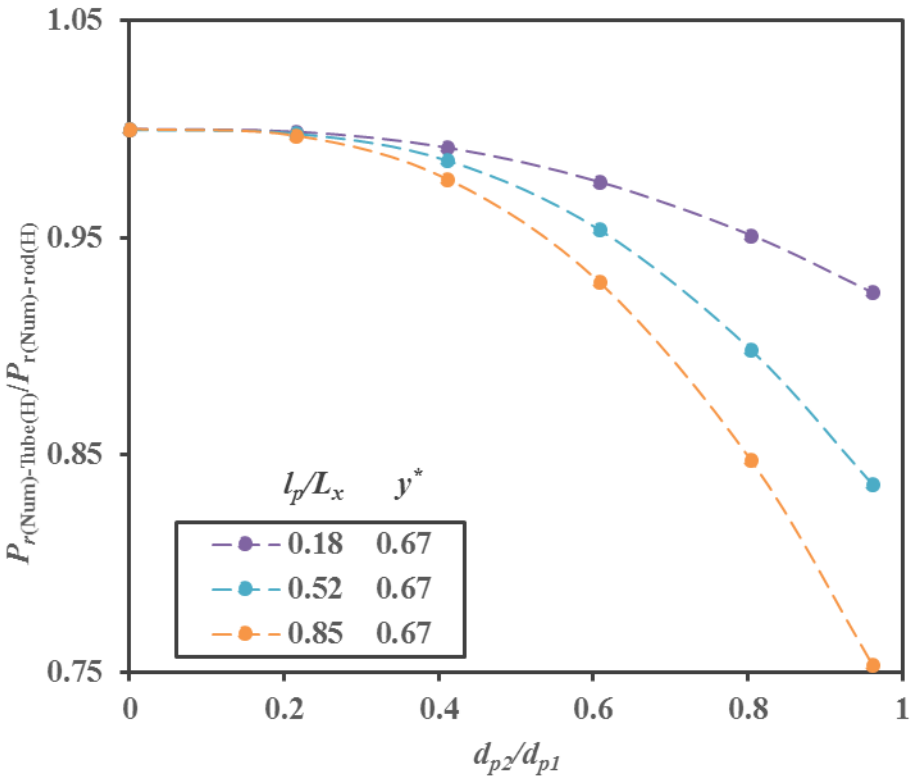

Figure 7.8 Plots of the ratio between $P_{r\ (\text{Num})}$ of the cylindrical rods and $P_{r\ (\text{Num})}$ of annular tubes with the same external diameter d_{p1} for a constant y^* value of 0.67 for values of l_p/L_x: 0.18, 0.52, and 0.85.

$$\frac{P_{r(Wu.H)-rod}}{P_{r(Wu,H,T)-tube}} = \left[1 + 0.1\left(\frac{l_p}{L_x}\right)\left(\frac{d_{p2}}{d_{p1}}\right) - 0.45\left(\frac{l_p}{L_x}\right)\left(\frac{d_{p2}}{d_{p1}}\right)^2\right] \quad (23)$$

Fig. 7.9 shows the predictions obtained by converting the $P_{r\ (Wu,H)}$ to $P_{r\ (Wu,H,T)}$ by Eq. (23). To verify the effectiveness of the correction of $P_{r\ (Wu,H)}$, a parity plot of $P_{r\ (Wu,H,T)}$ as a function of $P_{r\ (NUM)}$ and validation plots with more data are presented in Figs. 7.9(a) and 7.9(b), respectively. In Fig. 7.9(b), the validation was performed with three original sets and two new data sets. The new sets of data are with l_p/L_x = 0.35 and 0.68 and y^* = 0.67. The results show that the extended Wu's model provides an excellent estimation of MMMs with horizontally-oriented annular tubes.

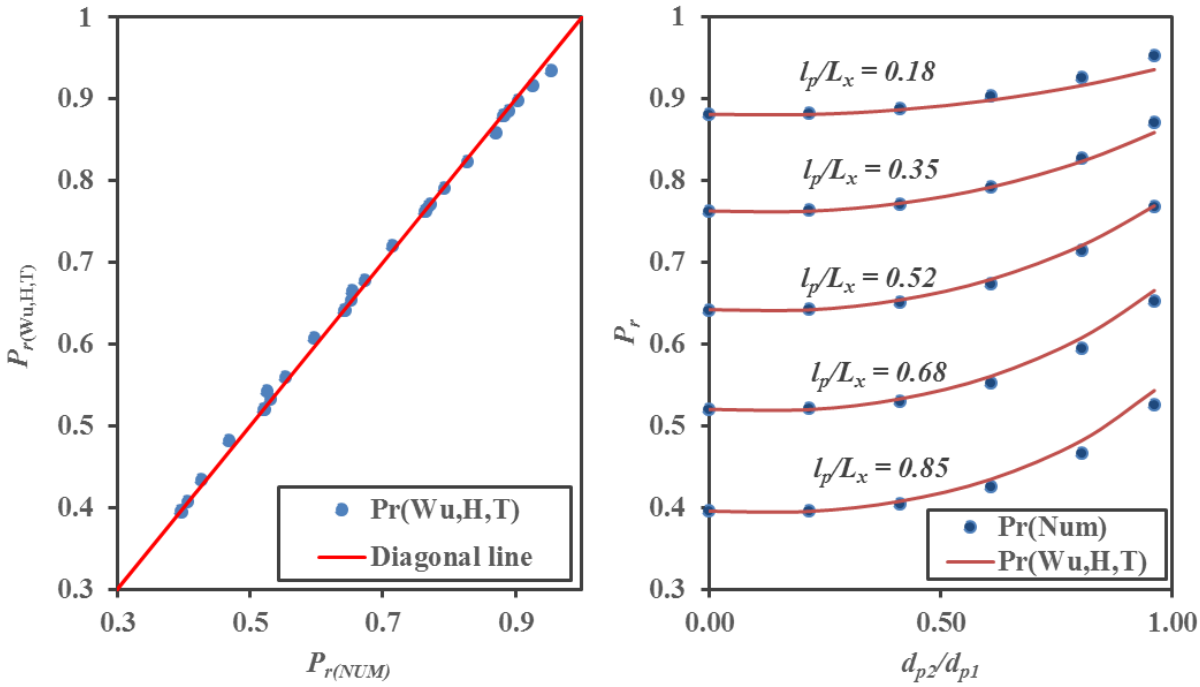

Figure 7.9 Model validation for the prediction of the relative permeability of MMMs with horizontally-oriented annular tubes: (a) Parity plot of $P_{r(Wu,H,T)}$ as a function of $P_{r(Num)}$; (b) Plots of $P_{r\ (Wu,H,T)}$ and $P_{r(Num)}$ as a function of d_{p2}/d_{p1} for four different tube geometries.

To gain a better quantitative understanding of the new model's prediction effectiveness for predicting the relative permeability for MMMs, the average prediction errors of all

results used in this investigation were calculated using Eq. (24) to assess the accuracy of the predictions for each type of geometry. Results are presented in Fig. 7.10, where they are compared to Maxwell's model, which serves here as a benchmark model. Results show that Maxwell's average prediction error is low for MMMs with spherical fillers, which is the solid geometry for which Maxwell's model was originally derived. However, Maxwell's model does not do as well in predicting the relative permeability of MMMs with the other filler geometries. The average prediction error of the generalized Wu's model is far inferior for the other geometries tested, and yet similar prediction of the relative permeability of MMMs with spherical fillers is obtained.

$$\varepsilon_A = \sqrt{\frac{1}{n}\sum_{i=1}^{n}\left(P_{ri} - \hat{P}_{ri}\right)^2} \tag{24}$$

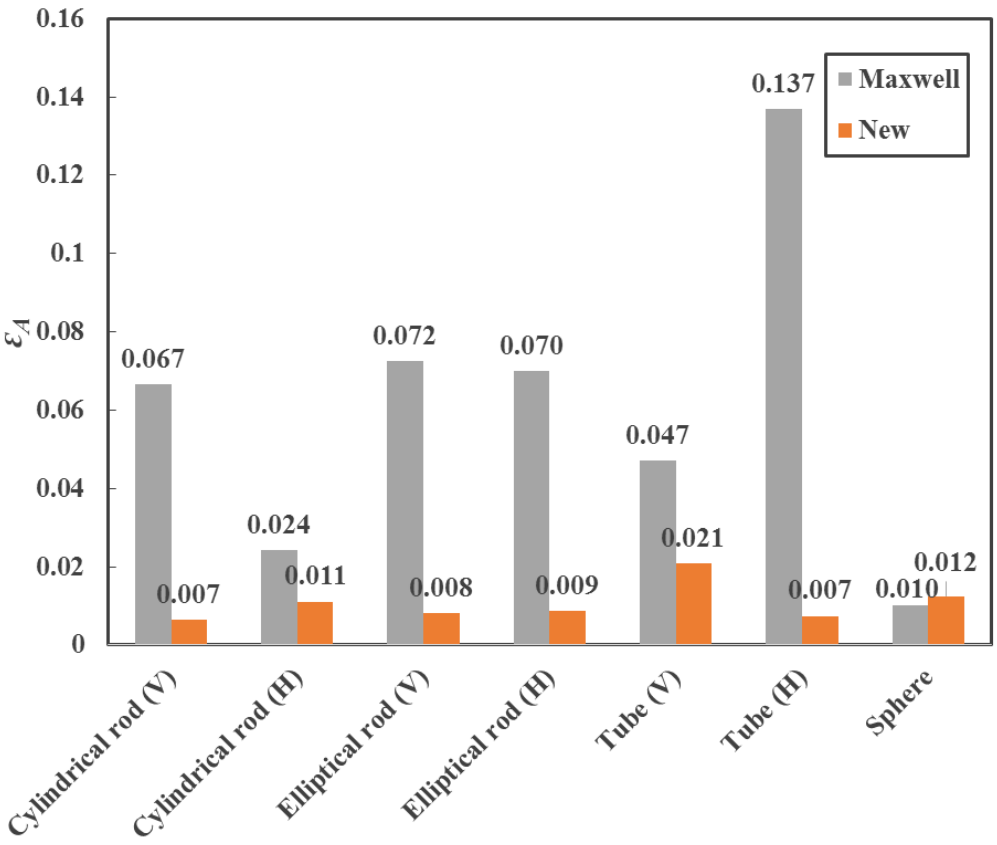

Figure 7.10 Comparison of the average prediction errors of the P_r for various filler geometries using the generalized Wu's model and Maxwell's model.

7.5 Conclusion

In this paper, we proposed a generalized model to predict the relative permeability of mixed-matrix membranes with various impermeable fillers. The model was developed based on a model previously derived for impermeable cuboid fillers dispersed in a continuous polymer phase. The proposed model relies on two simple geometrical parameters: the relative projected area available for permeation A^* and the relative thickness y^*. The model initially proposed by Wu et al. [11] for MMMs with cuboid nanofillers can be used directly for vertically-oriented cylindrical and elliptical rods. They share similar geometric attributes of cuboids. The model can be used to estimate the relative permeability of MMMs with vertically-oriented annular tubes but with less precision. The proposed model was also used to predict the relative permeability of MMMs with spheres and horizontally-oriented cylindrical rods, elliptical rods, and annular tubes but required the addition of a small correction term. Results show that the simple model derived by Wu et al. is accurate for predicting the relative permeability of MMMs. An additional correction factor was required for horizontally-oriented annular tubes

7.6 Acknowledgement

The authors gratefully acknowledge the financial support for this project provided by the Natural Science and Engineering Research Council of Canada.

7.7 Nomenclature

a	Parameter in Wu's model.
b	Parameter in Wu's model.
A^*	Relative projected area available for permeation A^*
C_s	Concentration at the membrane surface.
d_p	Diameter of a rod or spherical nanoparticle.
d_{p1}	Outside diameter of a tube filler or long diameter of an elliptical rod filler.
d_{p2}	Inside diameter of a tube filler or a short diameter of an elliptical rod filler.

D_c	Diffusivity of dense membranes or the continuous phase of a mixed-matrix membrane.
D_d	Diffusivity for a nanoparticle.
J	Permeation flux.
J_x	Permeation flux in x direction.
J_y	Permeation flux in y direction.
J_z	Permeation flux in z direction.
l_p	Length of a cylindrical rod, elliptical rod, or tube filler.
L_x	Dimension of an elementary unit at x direction.
L_y	Dimensions of an elementary unit at y direction.
L_z	Dimensions of an elementary unit at z direction.
MMM	Mixed-matrix membrane
p	Gas pressure.
P_c	Permeability of a dense membrane or the continuous phase of a mixed-matrixed membrane.
P_d	Permeability for a nanoparticle.
P_{eff}	Effective permeability of a mixed-matrix membrane.
P_r	Relative permeability.
$P_{r\ (\mathrm{Num})}$	Relative permeability determined numerically.
$P_{r\ (\mathrm{Wu,H})}$	Relative permeability determined from Wu's model for horizontal filler geometries.
$P_{r\ (\mathrm{Wu,H,T})}$	Relative permeability determined from Wu's model for horizontal tubes.
$P_{r\ (\mathrm{Wu,V})}$	Relative permeability determined from Wu's model for vertical geometries.
q	Aspect ratio in Wu's model.
R	Ideal gas constant.
S	Solubility.
x_p	Dimension of a nanoparticle in the x direction.
y	Direction of permeation.
y_p	Dimension of a nanoparticle in the y direction.
y^*	Relative thickness of the nanoparticle.

z_p	Dimensions of a nanoparticle in the z direction.
α	Aspect ratio defined in Cussler's model.
ε	Average prediction error.
ϕ	The volume fraction of nanoparticles in MMMs.
μ	A shape factor.
σ	Standard deviation.

7.8 Appendix

Boundary conditions for other geometries studied in this chapter.

a. Boundary conditions of MMM with spherical fillers:

$$\mathrm{BC}_{7\text{-}12}: \frac{\partial C}{\partial x} = \frac{\partial C}{\partial y} = \frac{\partial C}{\partial z} = 0, \quad \forall x, y, z \in \left[\left(x - \frac{L_x}{2} \right)^2 + \left(y - \frac{L_y}{2} \right)^2 + \left(z - \frac{L_z}{2} \right)^2 = r^2 \right] \tag{A.1}$$

b. Boundary conditions of MMM with vertical cylindrical rod fillers:

$$\begin{aligned} &\mathrm{BC}_{7\text{-}8}: \left. \frac{\partial C}{\partial y} \right|_{y = \frac{L_y - y_p}{2}} = \left. \frac{\partial C}{\partial y} \right|_{y = \frac{L_y + y_p}{2}} = 0, \ \forall x, z \in \left[\left(x - \frac{L_x}{2} \right)^2 + \left(z - \frac{L_z}{2} \right)^2 \le r^2 \right] \\ &\mathrm{BC}_{9\text{–}12}: \frac{\partial C}{\partial x} = \frac{\partial C}{\partial z} = 0, \ \forall x, z \in \left[\left(\left(x - \frac{L_x}{2} \right)^2 + \left(z - \frac{L_z}{2} \right)^2 = r^2 \right) \cap \frac{y_p)}{2} \le \mathrm{y} \le \frac{(L_y + y_p)}{2} \right) \right] \end{aligned} \tag{A.2}$$

c. Boundary conditions of MMM with horizontal cylindrical rod fillers:

$$\begin{aligned} &\mathrm{BC}_{7\text{-}8}: \left. \frac{\partial C}{\partial x} \right|_{x = \frac{L_x - x_p}{2}} = \left. \frac{\partial C}{\partial x} \right|_{x = \frac{L_x + x_p}{2}} = 0, \ \forall y, z \in \left[\left(y - \frac{L_y}{2} \right)^2 + \left(z - \frac{L_z}{2} \right)^2 \le r^2 \right] \\ &\mathrm{BC}_{9\text{–}12}: \frac{\partial C}{\partial y} = \frac{\partial C}{\partial z} = 0, \ \forall y, z \in \left[\left(y - \frac{L_y}{2} \right)^2 + \left(z - \frac{L_z}{2} \right)^2 = r^2 \right] \cap \frac{x_p)}{2} \le \mathrm{y} \le \frac{(L_x + x_p)}{2} \end{aligned} \tag{A.3}$$

d. Boundary conditions of MMM with vertical elliptical rod fillers:

$$\begin{aligned} &\mathrm{BC}_{7\text{-}8}: \left. \frac{\partial C}{\partial y} \right|_{y = \frac{(L_y - y_p)}{2}} = \left. \frac{\partial C}{\partial y} \right|_{y = \frac{(L_y + y_p)}{2}} = 0, \ \forall x, z \in \left[\frac{1}{a^2} \left(x - \frac{L_x}{2} \right)^2 + \frac{1}{b^2} \left(z - \frac{L_z}{2} \right)^2 \le r^2 \right] \\ &\mathrm{BC}_{9\text{–}12}: \frac{\partial C}{\partial x} = \frac{\partial C}{\partial z} = 0, \ \forall x, z \in \left[\frac{1}{a^2} \left(x - \frac{L_x}{2} \right)^2 + \frac{1}{b^2} \left(z - \frac{L_z}{2} \right)^2 = r^2 \right] \cap \frac{y_p)}{2} \le \mathrm{y} \le \frac{(L_y + y_p)}{2} \end{aligned} \tag{A.4}$$

e. Boundary conditions of MMM with horizontal elliptical rod fillers:

$$\begin{aligned}
&\mathrm{BC}_{7\text{-}8}\text{: } \left.\frac{\partial C}{\partial x}\right|_{x=\frac{(L_x-x_p)}{2}} = \left.\frac{\partial C}{\partial x}\right|_{x=\frac{(L_x+x_p)}{2}} = 0,\ \forall y,z\ \in \left[\frac{1}{a^2}\left(y-\frac{L_y}{2}\right)^2+\frac{1}{b^2}\left(z-\frac{L_z}{2}\right)^2 \le r^2\right] \\
&\mathrm{BC}_{9\text{–}12}\text{: } \frac{\partial C}{\partial y}=\frac{\partial C}{\partial z}=0,\ \forall y,z\ \in \left[\frac{1}{a^2}\left(y-\frac{L_y}{2}\right)^2+\frac{1}{b^2}\left(z-\frac{L_z}{2}\right)^2 = r^2\right]\bigcap\ \ \le x \le \frac{(L_x+x_p)}{2}\right]
\end{aligned} \tag{A.5}$$

f. Boundary conditions of MMM with vertical cylindrical tube fillers:

$$\begin{aligned}
&\mathrm{BC}_{7\text{-}8}\text{: } \left.\frac{\partial C}{\partial y}\right|_{y=\frac{(L_y-y_p)}{2}} = \left.\frac{\partial C}{\partial y}\right|_{y=\frac{(L_y+y_p)}{2}} = 0,\ \forall x,z\ \in \left[r_1^2 \le \left(x-\frac{L_x}{2}\right)^2+\left(z-\frac{L_z}{2}\right)^2 \le r_2^2\right] \\
&\mathrm{BC}_{9\text{–}12}\text{: } \frac{\partial C}{\partial x}=\frac{\partial C}{\partial z}=0,\ \forall x,z\ \in \\
&\left[\left(\left(x-\frac{L_x}{2}\right)^2+\left(z-\frac{L_z}{2}\right)^2 = r_1^2\right)\vee\left(\left(x-\frac{L_x}{2}\right)^2+\left(z-\frac{L_z}{2}\right)^2 = r_2^2\right)\right]\bigcap\ \ \le \mathrm{y} \le \frac{(L_y+y_p)}{2}\right]
\end{aligned} \tag{A.6}$$

g. Boundary conditions of MMM with horizontal cylindrical tube fillers:

$$\begin{aligned}
&\mathrm{BC}_{7\text{-}8}\text{: } \left.\frac{\partial C}{\partial x}\right|_{x=\frac{(L_x-x_p)}{2}} = \left.\frac{\partial C}{\partial x}\right|_{x=\frac{(L_x+x_p)}{2}} = 0,\ \forall y,z\ \in \left[r_1^2 \le \left(y-\frac{L_y}{2}\right)^2+\left(z-\frac{L_z}{2}\right)^2 \le r_2^2\right] \\
&\mathrm{BC}_{9\text{–}12}\text{: } \frac{\partial C}{\partial y}=\frac{\partial C}{\partial z}=0,\ \forall y,z\ \in \\
&\left[\left(\left(y-\frac{L_y}{2}\right)^2+\left(z-\frac{L_z}{2}\right)^2 = r_1^2\right)\vee\left(\left(y-\frac{L_y}{2}\right)^2+\left(z-\frac{L_z}{2}\right)^2 = r_2^2\right)\right]\bigcap\ \ \le x \le \frac{(L_x+x_p)}{2}\right]
\end{aligned} \tag{A.7}$$

7.9 References

[1] S.E.M. Selke, J.D. Culter, Plastics Packaging: Properties, Processing, Applications, and Regulations, 3rd Ed., Carl Hanser Verlag, Munich, 2016. https://doi.org/10.1016/B978-3-446-40790-9.50001-9.

[2] Å. Nyflött, Ç. Meriçer, M. Minelli, E. Moons, L. Järnström, M. Lestelius, M.G. Baschetti, The influence of moisture content on the polymer structure of polyvinyl alcohol in dispersion barrier coatings and its effect on the mass transport of oxygen. J. Coat. Technol. Res., 14 (2017) 1345-1355. https://doi.org/10.1007/s11998-017-9937-2

[3] Z.W. Abdullah, Y. Dong, I.J. Davies, S. Barbhuiya, PVA, PVA Blends, and Their Nanocomposites for Biodegradable Packaging Application, Polymer-Plastics Tech. & Eng., 56 (2017) 1307-1344. http://dx.doi.org/10.1080/03602559.2016.1275684

[4] A.A, Sapalidis, F.K. Katsaros, N.K. Kanellopoulos, PVA/Montmorillonite Nanocomposites: Development and Properties, in: John Cuppoletti (Ed.), Nanocomposites and Polymers with Analytical Methods, IntechOpen, Rijeka, 2011. pp. 29-50 https://doi.org/10.5772/18217.

[5] C. Wolf, H. Angellier-Coussy, N. Gontard, F. Doghieri, V. Guillard, How the shape of fillers affects the barrier properties of polymer/non-porous particles nanocomposites: A review. J. Memb. Sci., 556 (2018) 393-418. https://doi.org/10.1016/j.memsci.2018.03.085

[6] S. Zid, M. Zinet, E. Espuche, Modeling diffusion mass transport in multiphase polymer systems for gas barrier applications: A review, J. Polym. Sci. Part B Polym. Phys. 56 (2018) 621–639. https://doi.org/10.1002/polb.24574.

[7] Y. Cui, S. Kumar, B.R. Kona, D.V. Houcke, Gas barrier properties of polymer/clay nanocomposites, RSC Adv., 5 (2015), 63669-63690. http://dx.doi.org/10.1039/c5ra10333a

[8] C.-C. Yang, Y.-C. Lee, Preparation and characterization of the PVA/MMT composite polymer membrane for DMFC, Electrochem. Soc. Trans. 13 (2008) 1–20.

[9] V. Kaler, U. Pandel, R.K. Duchaniya, Development of TiO2/PVA nanocomposites for application in solar cells, Mater. Today Proc. 5 (2018) 6279–6287. https://doi.org/10.1016/j.matpr.2017.12.237.

[10] H.A. Silvério, W. Pires, F. Neto, D. Pasquini, Effect of Incorporating Cellulose Nanocrystals from Corncob on the Tensile , Thermal and Barrier Properties of Poly (Vinyl

Alcohol) Nanocomposites, J. Nanomater. 2013 (2013). http://dx.doi.org/10.1155/2013/289641.

[11] H. Wu, M. Zamanian, B. Kruczek, J. Thibault, Gas permeation model of mixed-matrix membranes with embedded impermeable cuboid nanoparticles, J. Memb. Sci. (under review).

[12] A. Ebneyamini, H. Azimi, F.H. Tezel, J. Thibault, Modelling of mixed-matrix membranes : Validation of the resistance-based model, J. Memb. Sci. 543 (2017) 361–369. https://doi.org/10.1016/j.memsci.2017.08.064.

[13] A. Ebneyamini, H. Azimi, F.H. Tezel, J. Thibault, Mixed-matrix membranes applications : Development of a resistance-based model, J. Memb. Sci. 543 (2017) 351–360. https://doi.org/10.1016/j.memsci.2017.08.065.

[14] A. Greco, Simulation and modeling of diffusion in oriented lamellar nanocomposites, Computational Material Sci., 83 (2014), 164-170. http://dx.doi.org/10.1016/j.commatsci.2013.11.019

[15] H. Wu, N. Alqasas, B. Kruczek, J. Thibault, Simulation of Time-Lag Permeation Experiments Using Finite Differences, J. Fluid Flow, Heat & Mass Transfer. 2 (2015) 14-25. https://doi.org/10.11159/jffhmt.2015.003

[16] J.C. Maxwell, A Treatise on Electricity and Magnetism, First Ed., Oxford: Clarendon Press, London, 1873.

[17] D.A.G. Bruggeman, Berechnung verschiedener physikalischer Konstanten von heterogenen Substanzen. I. Dielektrizitätskonstanten und Leitfähigkeiten der Mischkörper aus isotropen Substanzen, Ann. Phys. 416 (1935) 636–664. https://doi.org/10.1002/andp.19374210205.

[18] T.B. Lewis, L.E. Nielsen, M. Company, Dynamic Mechanical Properties of Particulate- Filled Composites, J. Appl. Polym. Sci. 14 (1970) 1449–1471.

[19] L.E. Nielsen, Thermal Conductivity of Particulate-Filled Polymers, J. Appl. Polym. Sci. 17 (1973) 3819–3820.

[20] R. Pal, New Models for Thermal Conductivity of Particulate Composites, J. Reinf. Plast. Compos. 26 (2007) 643–651. https://doi.org/10.1177/0731684407075569.

[21] R.K. Bharadwaj, Modeling the barrier properties of polymer-layered silicate nanocomposites, Macromolecules. 34 (2001) 9189–9192. https://doi.org/10.1021/ma010780b.

[22] S.A. Hashemifard, A.F. Ismail, T. Matsuura, Prediction of gas permeability in mixed matrix membranes using theoretical models, J. Memb. Sci. 347 (2010) 53-61. https://doi.org/10.1016/j.memsci.2009.10.005.

Chapter 8

Validity of the time-lag method for the characterization of mixed-matrix membranes

Haoyu Wu, Jules Thibault and Boguslaw Kruczek*

Abstract

The time-lag method is commonly used for the characterization of gas separation membranes. It allows the determination of the diffusion, permeability, and solubility coefficients from a single dynamic gas permeation experiment. This method is widely used for any membrane material, including glassy polymers, polymers with intrinsic microporosity, and mixed-matrix membranes. However, it is understood that for such determined transport coefficients, it is effective rather than intrinsic parameters that are estimated. In this paper, we focus on the applicability of the time-lag method for the characterization of theoretical mixed-matrix membranes (MMMs), in which impermeable particles of different shapes are ideally dispersed in a continuous polymer phase. Dynamic gas permeation experiments were simulated by solving the three-dimensional Fick's second law of diffusion numerically. The generated data allowed the estimation of the effective diffusion coefficient from the time lag and the ratio of the effective permeability and solubility coefficients.

For the hypothetical MMMs with a single layer of uniformly distributed particles, the diffusivity determined by the time-lag method is always higher than the ratio of the effective permeability and solubility coefficients; the latter is constant. In many cases, the effective diffusion coefficient estimated by the time-lag method was higher than the host polymer's intrinsic diffusion coefficient. However, as the number of layers increases, the difference between the two methods' effective diffusion coefficients rapidly decreases.

Regardless of the shape and orientation of the particles, the two effective diffusivity coefficients are practically the same for MMMs with at least five layers.

Keywords: Time-lag method; Mixed-matrix membranes; Impermeable nanoparticles; Three-dimensional modelling; Effective diffusivity coefficient

Publication status: Journal of Membrane Science, 618 (2021) 118715.

***Corresponding author**

8.1 Introduction

Membrane gas separation technology has attracted significant attention in the industry for many years due to its multiple advantages: small space footprint and energy cost, smooth operation and clean process [1]. The current uses and applications of membrane gas separation, include natural gas purification, hydrogen purification, and many others [2,3]. To foster a wider use of membrane technology, it is paramount to continually enhance membranes' performance. In turn, this requires a proper understanding of pertinent transport mechanisms and accurate membrane characterization.

Regardless of the type of gas permeation membranes, the solution-diffusion model generally describes the theoretical framework of transport of the permeating species. In this model, the permeation process is comprised of three steps: (1) gas molecules dissolve into the upstream surface of the membrane; (2) dissolved gas molecules diffuse through the membrane; and (3) gas molecules emerge from the downstream surface of the membrane by desorption [4,5]. The solubility coefficient (S) and diffusivity coefficient (D) are two intrinsic transport properties of the membrane. Their product, the permeability coefficient (P), which is also an intrinsic membrane property, signifies the overall ability of gas molecules to permeate through the membrane.

$$P = SD \tag{1}$$

In reality, *S*, *D*, and *P* represent intrinsic properties only for rubbery polymer membranes and non-interactive gases, for which gas sorption obeys Henry's law:

$$C = Sp \tag{2}$$

where *C* is the concentration of the permeating gas species within the membrane, *p* is the gas pressure in contact with the membrane, and the Henry's law constant (*S*) corresponds to the solubility coefficient. When gas sorption is not a linear function of pressure and/or *D* is not constant, Eq. (1) is still applicable; however, for effective transport coefficients [6]:

$$P_e = S_e D_e \tag{3}$$

The subscript *e* indicates that the coefficients in Eq. (3) are no longer intrinsic, as they depend on experimental conditions, particularly on the pressure and or pressure gradient at which they are determined. For example, in the case of glassy polymer membranes, two different sorption mechanisms are coinciding. One follows Henry's law in normally densified regions, and the other follows Langmuir's model in intersegmental defects (holes). As a result, the effective solubility coefficient is given by [7]:

$$S_e = \frac{C}{p} = S + \frac{C'_H}{1 + bp} \tag{4}$$

where C'_H and *b* are the hole saturation and the hole affinity constants, respectively. Regardless of the sorption model, if the sorption isotherm (the relationship between *C* and *p*) for the membrane material is known or can be measured experimentally, the appropriate value of S_e can be determined from the ratio of *C* and *p*.

The permeability coefficient, *P* or more generally P_e, is evaluated from steady-state molar flux (*J*) across the membrane:

$$P_e = \frac{JL}{(p_0 - p_d)} \tag{5}$$

where *J* is the permeation flux, *L* is the membrane thickness, p_0 and p_d are the feed and permeate pressures, respectively. Knowing P_e and S_e, which are normally determined in two separate experiments, the effective diffusivity is the ratio of P_e and S_e.

Alternatively, D_e can be determined experimentally using the time-lag method [8,9], which relies on a dynamic gas permeation experiment [10,11]. More specifically, a homogeneous membrane, which is initially free from any dissolved gas species, is suddenly exposed to a step increase in pressure at one side of the membrane (feed side) and the feed pressure (p_0) remains constant, while the other side (permeate side) of the membrane remains under high vacuum. The progress of a typical dynamic experiment, which illustrates the time-lag method, is presented in Fig. 8.1. The time-axis intercept of the linear portion of the curve is referred to as the time lag (θ), which is inversely proportional to the effective diffusivity coefficient:

$$\theta = \frac{L^2}{6D_e} \tag{6}$$

Therefore, knowing the experimental time lag, D_e can be readily determined. Moreover, the slope of the linear portion of the curve is directly proportional to P_e, so that P_e can be calculated from the rate of increase of downstream pressure in the downstream compartment:

$$P_e = \frac{V_d L}{ARTp_0}\left(\frac{dp_d}{dt}\right)_{t\to\infty} \tag{7}$$

where V_d is the downstream volume, A is the membrane area, R is the universal gas constant, and T is the absolute temperature. Eq. (7) implies that despite gas accumulation downstream from the membrane, the permeate side remains under a high vacuum, i.e., $p_0 - p_d \cong p_0$.

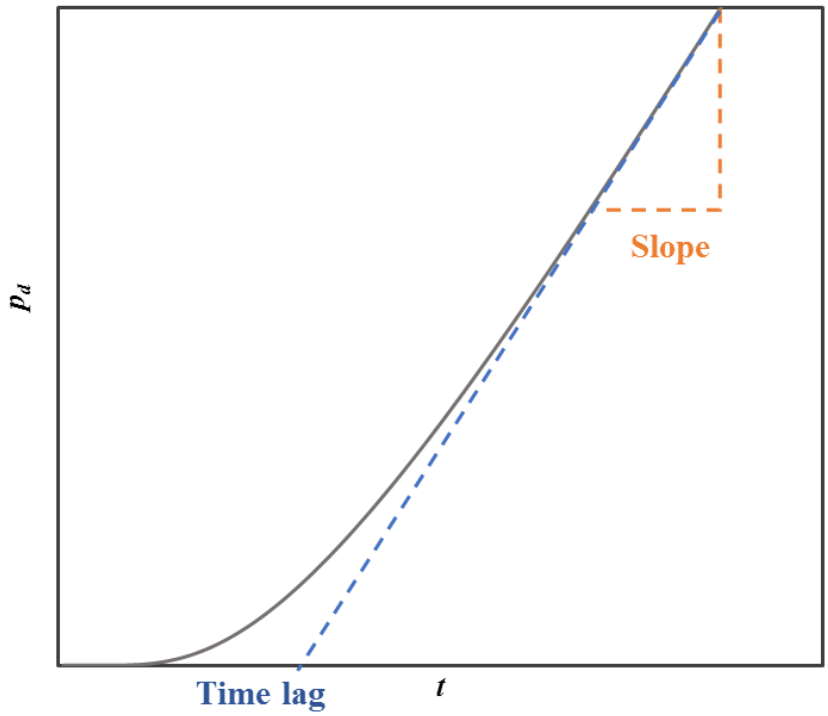

Figure 8.1 Schematic diagram illustrating the time-lag method.

For a given gas and membrane, D_e should be the same, regardless of how it is evaluated. On the other hand, there are examples for which D_e determined directly from the time-lag method is different from the value calculated from the ratio of P_e and S_e [12-15]. While the differences between the two values can be attributed to inherent experimental errors associated with the direct determination of P_e, S_e, and in particular D_e, the following question arises. Is there any fundamental reason making the two values of D_e different? In the underlying case of homogeneous rubbery membranes, in the absence of experimental errors, the two values should be identical because regardless of how they are determined, they represent the intrinsic properties of the rubbery polymer. On the other hand, for more complex membrane materials, such as glassy polymers, polymers with intrinsic microporosity (PIM), and mixed-matrix membranes (MMMs), the answer is not apparent.

This paper's objective is to investigate D_e determined by two different methods, focusing on MMMs comprised of impermeable nanoparticles uniformly dispersed in a continuous polymer phase. The MMMs are made of identical layers, each containing a

single layer of the particle across its thickness. The polymer phase is characterized by the constant S (Henry's law is applicable), and D. Impermeable particles can significantly reduce the effective membrane permeability ($P_e < P$) and diffusivity ($D_e < D$) coefficients. The primary reason is an increase in the diffusion path length for a given membrane thickness. In other words, membrane tortuosity increases, which decreases D_e and P_e. Furthermore, impermeable particles reduce the active membrane area, which decreases P_e. Finally, since impermeable particles have zero solubility, P_e, according to Eq. (3), must decrease. The effective solubility of MMMs with impermeable particles is given by [6]:

$$S_e = S(1 - \phi) \tag{8}$$

where ϕ is the volume fraction of impermeable particles in the MMM. The effective solubility is independent on the number of layers. The applications of MMMs with impermeable particles include packaging and a protective coating and control of the permeation rate in drug delivery applications [19-21].

Dynamic gas permeation experiments using MMMs consisting of a different number of layers, and different geometries and sizes of nanoparticles are simulated by solving the three-dimensional Fick's second law of diffusion numerically. The generated data is converted into the pressure response downstream from the membrane, from which D_e is calculated directly using the time-lag method, and from the ratio of P_e and S_e.

8.2 Theoretical background

Mixed matrix membranes (MMMs), which combine the features of inorganic (e.g., zeolites, metal-organic frameworks, graphene, and carbon-based materials) and polymeric (e.g., polyimides, polymers of intrinsic microporosity, polysulfone, and cellulose acetate) materials, have emerged as a concept to enhance separation performance of the existing membrane materials [22]. MMMs are considered for both gas separation and pervaporation application [23]. The main challenge in the formation of MMMs is a non-ideal polymer-particle interface. More specifically, in the case of poor polymer−particle adhesion, polymer-packing disruption near the dispersed particles, and repulsive forces between the two phases, nonselective interfacial voids might be formed. On the other hand, when the

adhesion between the two phases is excellent, the free volume in the polymer located near the filler surface might be reduced, leading to a rigidified polymer chain layer around the fillers with a lower permeability compared to the bulk phase of the host polymer. When dispersed particles are porous, another type of defect – pore blockage – might occur [24].

In this study, we assume that the dispersed phase is nonporous, and ideal MMM morphology exists with no defects and no distortion at the filler−polymer interface. Besides, we assume that for a given MMM, the fillers have identical shapes and sizes, and they are uniformly distributed. As a result, our MMMs can be split into n identical layers, and each layer has one particle across its thickness. In the limiting case, the membrane consists of a single layer of particles uniformly dispersed in the host polymer, as shown in Fig. 8.2. Moreover, the single-layer MMM can be divided into m identical elements, inside which a single particle is located in the center of the element. The particle in Fig. 8.2 is a cuboid with the dimensions x_p, y_p, z_p. The corresponding dimensions of the element are L_x, L_y, L_z, and $L_x = L_y = L_z$. Therefore, the thickness of the membrane depicted in Fig. 8.2 is $L = L_y$. In addition to being in the center of the element, the surfaces of the cuboid particle are parallel to the elementary unit's respective surfaces. The volume fraction (ϕ) occupied by the particles in this MMM is, therefore:

$$\phi = \frac{x_p y_p z_p}{L_x L_y L_z} \tag{9}$$

The other geometrical parameters, which characterize the MMM membrane are the number of particle layers (n), the dimensionless projected area of the particle (A_p) in the main direction of permeation (along the y-axis), and the dimensionless thickness of the particle (τ), which are defined as:

$$A_p = \frac{x_p z_p}{L_x L_z} \tag{10}$$

$$\tau = \frac{y_p}{L_y} \tag{11}$$

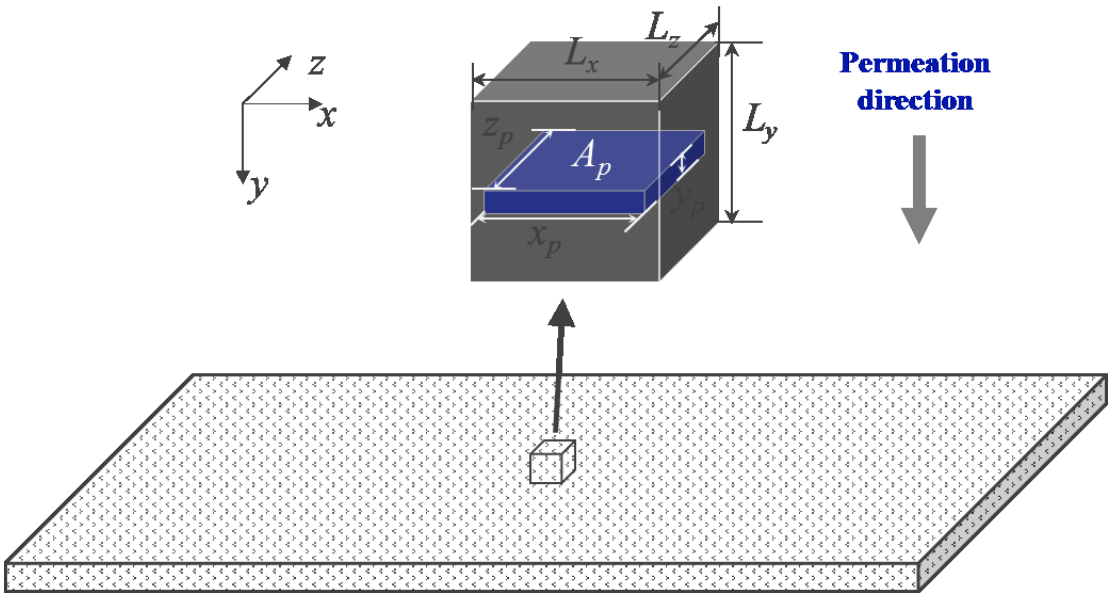

Figure 8.2 Schematic representation of a basic element (L_x, L_y, L_z) of a single-layer mixed-matrix membrane of thickness $L = L_z$. The membrane may consist of n of such layers parallel to each other. Each element contains one particle (in this case, a cuboid with dimensions x_p, y_p, and z_p) at its center. Gas permeation takes place along the y-axis.

Although the main direction of gas transport in the MMM shown in Fig. 8.2 occurs along the y-axis, impermeable particles make the permeation process inherently three-dimensional. Consequently, the dynamic gas permeation experiment required by the time-lag method is governed by the three-dimensional form of the Fick's second law of diffusion:

$$\frac{\partial C}{\partial t} = D\left[\frac{\partial^2 C}{\partial x^2} + \frac{\partial^2 C}{\partial y^2} + \frac{\partial^2 C}{\partial z^2}\right] \tag{12}$$

Due to the three-dimensional effects of an impermeable particle in an elementary unit, the governing partial differential equation cannot be solved analytically. In order to solve it, numerically, Eq. (12) is discretized using finite differences:

$$C_{i,j,k}^{m+1} = C_{i,j,k}^{m} + \Delta t \left\{ \begin{aligned} &\frac{2D}{\Delta x_{i+1} + \Delta x_i} \left[\frac{C_{i+1,j,k}^{m} - C_{i,j,k}^{m}}{\Delta x_{i+1}} - \frac{C_{i,j,k}^{m} - C_{i-1,j,k}^{m}}{\Delta x_i} \right] \\ &+ \frac{2D}{\Delta y_{j+1} + \Delta y_j} \left[\frac{C_{i,j+1,k}^{m} - C_{i,j,k}^{m}}{\Delta y_{j+1}} - \frac{C_{i,j,k}^{m} - C_{i,j-1,k}^{m}}{\Delta y_j} \right] \\ &+ \frac{2D}{\Delta z_{k+1} + \Delta z_k} \left[\frac{C_{i,j,k+1}^{m} - C_{i,j,k}^{m}}{\Delta z_{k+1}} - \frac{C_{i,j,k}^{m} - C_{i,j,k-1}^{m}}{\Delta z_k} \right] \end{aligned} \right\} \tag{13}$$

Eq. (13) represents the explicit discretization of Eq. (12) for an interior mesh point (*i, j, k*) that allows calculating the concentration at the next time step, knowing the current concentration at a given mesh point within the membrane. The change of concentration at mesh point (*i, j, k*) as a function of time depends on the current concentration at point (*i, j, k*) and the concentrations at the six neighbouring mesh points, as illustrated in Fig. 8.3.

To determine the effective transport coefficients of the MMM (P_e, S_e, and D_e), it is first necessary to solve numerically for the temporal variation of the concentration at all points within the membrane. The solution requires defining all initial and boundary conditions. It is important to emphasize that P_e and S_e of the elementary unit represent the entire MMM [25,26]. However, D_e of the elementary unit is representative of the single-layer, but not necessarily for the entire MMM. We will investigate the effect of the number of particle layers (n) on D_e of the MMM.

It is assumed that before the concentration step change on the upstream side of the membrane, i.e., at $t < 0$, there are no gas species dissolved in the membrane; thus the corresponding initial condition (IC) is given by:

$$\text{IC:} \quad C_{i,j,k}^{t<0} = 0 \qquad \forall i, j, k \tag{14}$$

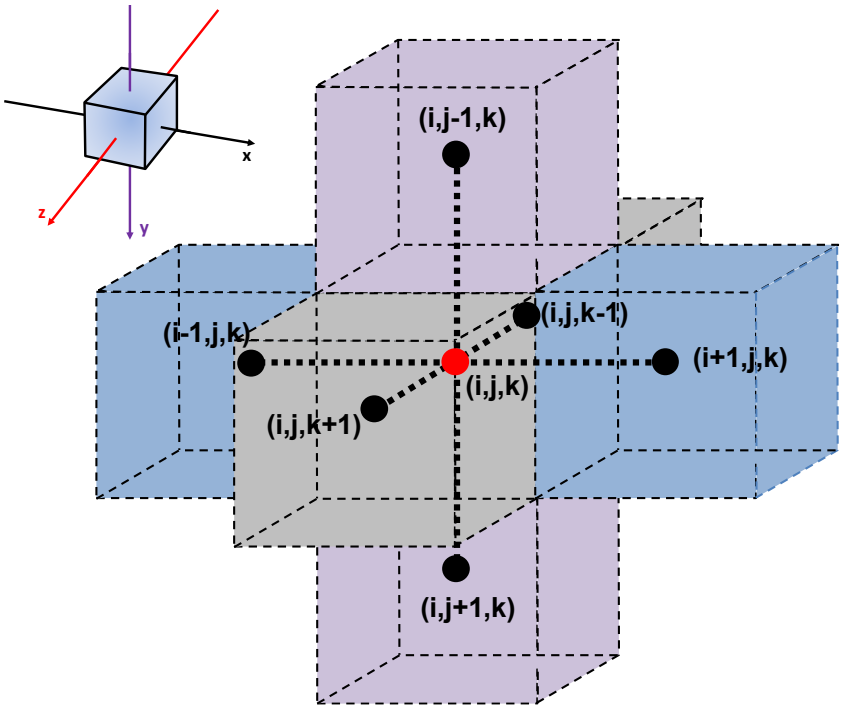

Figure 8.3 Nomenclature of an interior mesh point with its six neighbouring mesh points. x, y, and z directions are represented by i, j, and k, respectively [20].

With respect to the boundary conditions (BCs), twelve relations are required to completely define the problem: six boundary conditions at the periphery of the differential element and six boundary conditions at the polymer-solid filler interfaces. Eq. (15) provides the boundary conditions on both sides of the membrane, which is represented by the single unit (y-axis is the permeation direction). It is assumed that at the onset of permeation, a step change in the gas pressure is applied to the upstream side of the membrane ($y = 0$) whereas the pressure in contact with the downstream side of the membrane ($y = L = nL_y$) is zero. The resulting concentrations at both surfaces are simply the product of the neighbouring pressure and the solubility S coefficient:

$$\begin{aligned} &\text{BC}_1\text{: } C_{i,y=0,k} = p_0 S \qquad \forall i,k \\ &\text{BC}_2\text{: } C_{i,y=L,k} = 0 \qquad \forall i,k \end{aligned} \tag{15}$$

Since all elementary units are identical, symmetry conditions prevail at the four faces of the element that are parallel to the direction of permeation as expressed in Eq. (16) for $\text{BC}_{3\text{-}6}$. In addition, since the nanoparticle is impermeable, the mass flux at each of the six faces

of the cuboid nanoparticle is zero (see $BC_{7\text{-}12}$ in Eq. (17)). The latter boundary conditions imply that the concentration of the migrating species inside the nanoparticle is zero.

$$BC_{3\text{-}6}: \quad \left.\frac{\partial C}{\partial x}\right|_{x=0} = \left.\frac{\partial C}{\partial x}\right|_{x=L_x} = \left.\frac{\partial C}{\partial z}\right|_{z=0} = \left.\frac{\partial C}{\partial z}\right|_{z=L_z} = 0 \tag{16}$$

$$\begin{aligned}
&BC_{7\text{-}8}: \left.\frac{\partial C}{\partial x}\right|_{x=\frac{(L_x - x_p)}{2}} = \left.\frac{\partial C}{\partial x}\right|_{x=\frac{(L_x + x_p)}{2}} = 0 \\
&\qquad \forall y,z \in \left[\left(\frac{(L_y - y_p)}{2} \le y \le \frac{(L_y + y_p)}{2}\right) \cap \left(\frac{(L_z - z_p)}{2} \le z \le \frac{(L_z + z_p)}{2}\right)\right] \\
&BC_{9\text{-}10}: \left.\frac{\partial C}{\partial y}\right|_{y=\frac{(L_y - y_p)}{2}} = \left.\frac{\partial C}{\partial y}\right|_{y=\frac{(L_y + y_p)}{2}} = 0 \\
&\qquad \forall x,z \in \left[\left(\frac{(L_x - x_p)}{2} \le x \le \frac{(L_x + x_p)}{2}\right) \cap \left(\frac{(L_z - z_p)}{2} \le z \le \frac{(L_z + z_p)}{2}\right)\right] \\
&BC_{11\text{-}12}: \left.\frac{\partial C}{\partial z}\right|_{z=\frac{(L_z - z_p)}{2}} = \left.\frac{\partial C}{\partial z}\right|_{z=\frac{(L_z + z_p)}{2}} = 0 \\
&\qquad \forall x,y \in \left[\left(\frac{(L_x - x_p)}{2} \le x \le \frac{(L_x + x_p)}{2}\right) \cap \left(\frac{(L_y - y_p)}{2} \le y \le \frac{(L_y + y_p)}{2}\right)\right]
\end{aligned} \tag{17}$$

Although not explicitly stated, the above description of the problem implies an ideal polymer-particle interface such that there are no voids and rigidified polymer regions within the elementary unit and hence the entire membrane.

Knowing the concentration of the migrating species within the membrane, the application of the Fick's first law of diffusion allows the determination of the gas flux at any point, of which the gas fluxes in (J_0) and out (J_L) at the two membrane interfaces are of particular importance:

$$J_0 = -D\left.\frac{\partial C}{\partial y}\right|_{y=0} \tag{18a}$$

$$J_L = -D\left.\frac{\partial C}{\partial y}\right|_{y=L} \tag{18b}$$

When the dynamic gas permeation experiment reaches a steady-state, the gas fluxes in and out of the membrane are equal. The effective permeability coefficient can then be calculated using Eq. (5). In turn, the effective diffusivity based on the steady-state flux can be calculated from:

$$D_{e,F} = \frac{P_e}{S_e} \tag{19}$$

The subscript F signifies that D_e was determined from the steady-state flux in order to distinguish it from D_e determined from the time lag ($D_{e,T}$), where:

$$D_{e,T} = \frac{L^2}{6\theta_e} \tag{20}$$

The determination of the effective time lag (θ_e) of the MMM requires simulation of the pressure response downstream from the membrane, $p_d(t)$, i.e., generating the curve similar to that shown in Fig. 8.1. In turn, this requires the integration of the expression for the gas flux, leaving the membrane:

$$p_d(t) = \frac{ART}{V_d}\int_0^t J_L dt \tag{21}$$

Then, the linear portion of the p_d (t) curve is extrapolated to the time axis (Fig. 8.1), and the corresponding intersection represents the simulated effective time lag of the membrane required by Eq. (20).

8.3 Results

To facilitate the presentation of the results, dimensionless effective transport coefficients (P_r, S_r, D_r) of MMMs embedding impermeable particles are introduced, which are essentially the effective transport coefficients relative to the respective intrinsic coefficients of the polymer phase:

$$P_r = \frac{P_e}{P} \tag{22a}$$

$$S_r = \frac{S_e}{S} = 1 - \phi \tag{22b}$$

$$D_r = \frac{D_e}{D} \tag{22c}$$

It is important to emphasize that P_r from the steady-state flux and the time-lag methods will always be the same. However, the same cannot be said about D_r, which is why the respective dimensionless effective diffusivity coefficients will be referred to as $D_{r,F}$ and

$D_{r,T}$. Substituting Eqs. (22a) and (22b) into Eq. (22c) leads to the following expression for $D_{r,F}$:

$$D_{r,F} = \frac{P_e/S_e}{P/S} = \frac{P_r}{1-\phi} \tag{23}$$

Substituting Eq. (20) into Eq. (22c), $D_{r,T}$ becomes:

$$D_{r,T} = \frac{\theta}{\theta_e} \tag{24}$$

In the following sections, we will compare $D_{r,F}$ and $D_{r,T}$ values for mixed-matrix membranes with different geometries and sizes of nanoparticles.

8.3.1 *Single-layer MMMs*

We will first consider single-layer MMMs, which is the limiting case. Since P_r and S_r for the elementary unit are representative for the entire MMM, the corresponding $D_{r,F}$ will also be representative for the entire MMM. However, the same cannot be said about $D_{r,T}$, which may or may not depend on the number of particle layers. The effect of the number of particle layers on $D_{r,T}$ will be explored after investigating the limiting case for different geometries of dispersed particles.

8.3.1.1 Cuboid-based MMM

The geometry of cuboid particles is characterized by ϕ, A_p, and τ, which are defined by Eqs. (9-11), respectively. It is important to note that $\phi = A_p \cdot \tau$. In other words, the cuboid particles are fully defined by any two of ϕ, A_p, and τ parameters.

Fig. 8.4 presents the progress of the simulated dynamic time-lag experiments for two mixed matrix membranes differing by τ (0.05 for MMM1 versus 0.5 for MMM2) while having the same $A_p = 0.9$. As a reference, the corresponding dynamic experiment's progress with the neat polymer membrane is also included. The downstream pressure response in Fig. 8.4 is plotted as a function of the dimensionless time (t/θ), where θ is the simulated time lag of the neat polymer membrane. Consequently, the intercepts on the t/θ axis of the simulated pressure curve in Fig.8.4 represent the relative time lags (θ_e/θ). The latter strongly depends on the slope of the steady-state section of the pressure response curve. In

these simulations, as well as in all others that will be presented later, the steady-state is considered to be attained when the relative difference between the upstream flux defined by Eq. (18a) and the downstream flux defined by Eq. (18b) is 0.001% or less. For all membranes in Fig. 8.4, this condition is reached at $t/\theta > 3$, but for the sake of clarity, the time axis in Fig.8.4 ends at $t/\theta = 3$. The most crucial observation in Fig. 8.4 is that θ_e/θ of MMM2 is less than unity, which implies that $D_{r,T}$ is higher than D. Two factors determine the intersection of the extrapolated steady-state portion of the pressure response curve with the time axis (i.e., the time lag): the slope of the steady-state portion of the pressure response curve. More specifically, the higher the slope, the greater the time lag; also, the longer the time to reach steady-state, the greater than time lag. For a given membrane thickness, the presence of impermeable particles in MMMs always leads to a decrease in P_e (i.e. the slope) and an increase in the membrane tortuosity. The latter should increase the time required to reach steady-state permeation, which is the case for MMM1, but not for MMM2 in Fig. 8.4. Consequently, θ_e of MMM2 is smaller than θ, which is an unexpected result.

The graphical results shown in Fig. 8.4 are summarized in Table 8.1. It can be noticed that the relative permeability of both MMM1 and MMM2 is significantly less than unity. In addition, P_r of MMM2 with larger impermeable nanoparticles is smaller than P_r of MMM1, with smaller impermeable nanoparticles, which could be expected. However, the decrease in the permeability coefficient is not directly related to the size of the nanoparticle. There are numerous models for the prediction of P_r in MMMs not only for those with nonporous but also with porous particles; some models also allow for non-ideal polymer-particle interphase [24]. Considering the diffusivity coefficients by the two methods, since θ_e/θ of MMM1 was greater than unity, we already concluded that $D_{r,T}$ of MMM1 must be less than unity (it is 0.85). However, $D_{r,T}$ of MMM1 is two times greater than the corresponding value of $D_{r,F}$. Therefore, the results in Table 8.1 further emphasize the discrepancy between $D_{r,T}$ and $D_{r,F}$ for MMMs with impermeable particles.

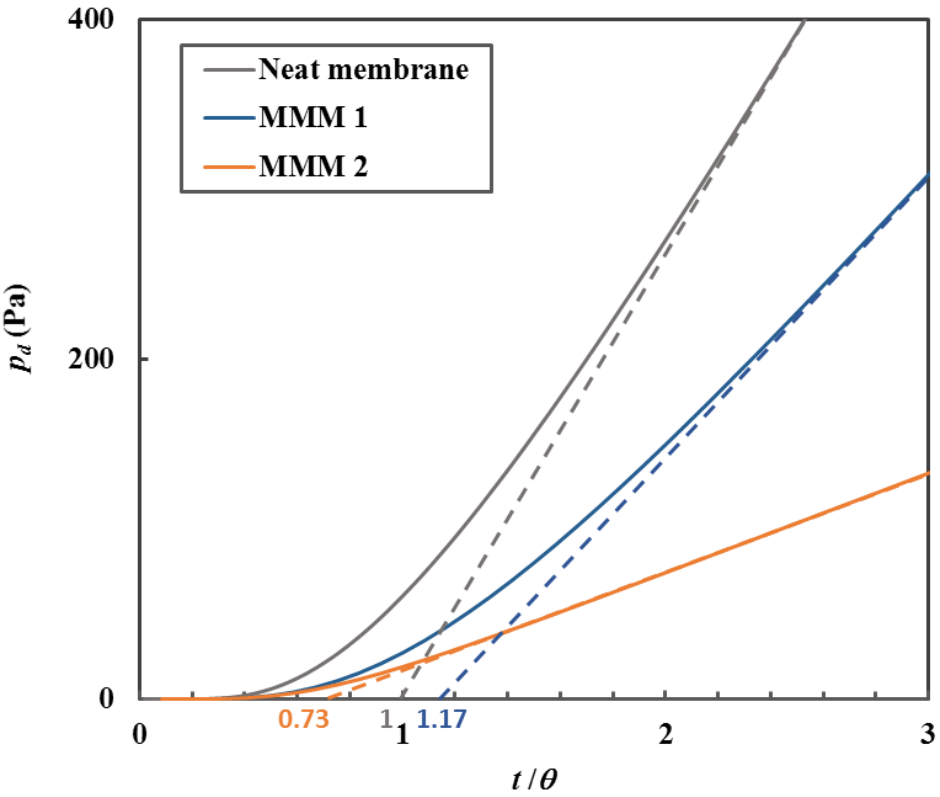

Figure 8.4 Simulated dynamic gas permeation experiments with two cuboid-based single-layer MMMs deferring by the relative thickness of particles (τ = 0.05 for MMM1; τ = 0.5 for MMM2); for both membranes A_p = 0.9. Results for the neat polymer membrane shown as a reference. The dotted lines represent an extrapolation of the steady-state portion of the pressure response curves.

Table 8.1 Summary of the relative transport properties of two cuboid-based single-layer MMMs differing by the relative thickness of the dispersed cuboid particles.

Membrane	A_p	τ	ϕ	P_r	S_r	$D_{r,F}$	$D_{r,T}$	t_{ss}/θ [(1)]
Reference	0	0	0	1	1	1	1	3.2
MMM1	0.90	0.05	0.045	0.43	0.95	0.45	0.85	3.4
MMM2	0.90	0.50	0.466	0.16	0.53	0.28	1.37	1.9

(1) t_{ss} is the time to reach 99% of the steady-state flux.

To better understand the effects of the relative thickness and the projected area of cuboid particles on the effective transport properties of the resulting single-layer MMMs and on the difference between $D_{r,T}$ and $D_{r,F}$ we performed additional simulations. Fig. 8.5 summarizes the results of these simulations. Fig. 8.5a provides the plots of $D_{r,T}$ and $D_{r,F}$ as a function of τ for three different values of A_p (0.06, 0.61, 0.97). To facilitate the visualization of these MMMs, Fig. 8.5b presents the basic elements of MMMs with A_p of 0.06, 0.61and 0.97, for three different τ values (0.1, 0.5, 0.90).

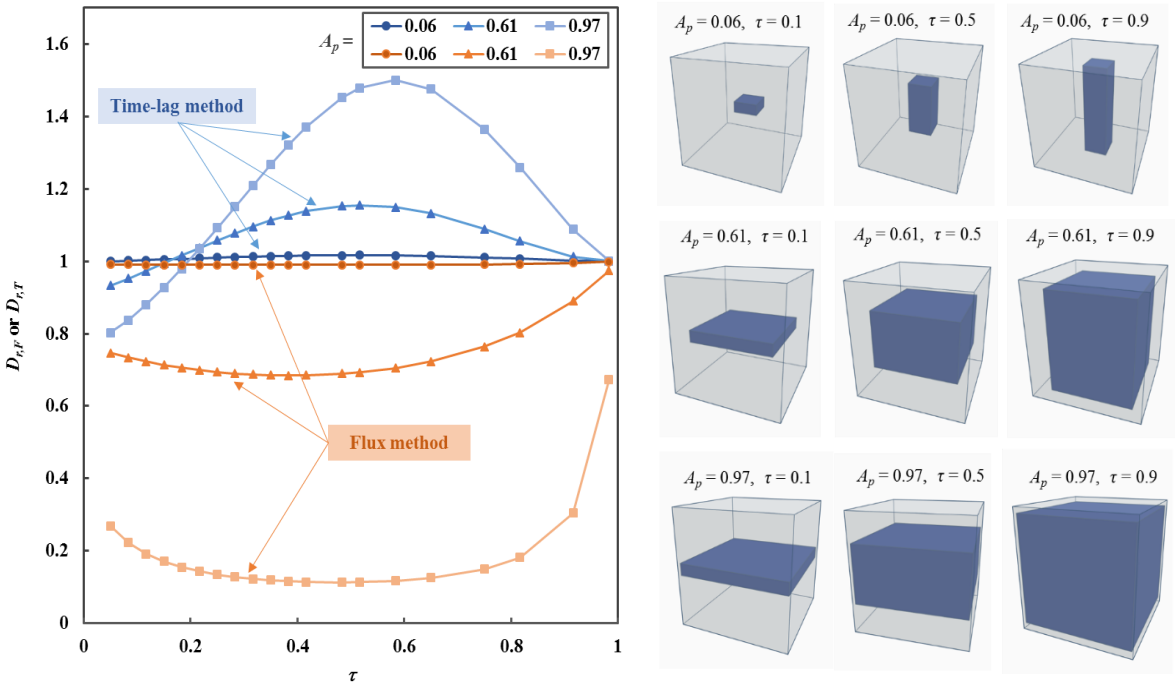

Figure 8.5 (a) The relative diffusivity of cuboid-based single-layer mixed matrix membranes determined by the steady-state flux and the time-lag methods as a function of the relative thickness of the particles for three different relative projected areas (0.06, 0.61, 0.97) of the particles. **(b)** Visual representation of the three series MMMs with the relative thickness of τ = 0.1, 0.5 and 0.9.

It is evident that for a given τ, the difference between $D_{r,T}$ and $D_{r,F}$ increases with A_p. This difference strongly depends on τ. As τ approaches unity, the difference disappears, and both $D_{r,T}$ and $D_{r,F}$ approach unity, i.e., the intrinsic diffusivity of the polymer phase. When the impermeable cuboid particle occupies the entire membrane's thickness, there will be no tortuous effect as the gas species will permeate straight along the y-axis. Even though

the relative diffusivity reaches unity when the relative thickness becomes unity, it is essential to note that the effective permeability and the effective solubility of the MMM decrease. At $\tau = 1$, both the effective permeability and effective solubility are equal to $(1 - \phi)$ times the permeability and solubility of the neat polymeric membrane, resulting in the relative diffusivity of unity.

In the other extreme, when $\tau = 0$, i.e., there are no particles present in the membrane, $D_{r,T} = D_{r,F} = 1$. However, while the difference between $D_{r,T}$ and $D_{r,F}$ decreases when τ approaches zero, there is a discontinuity at $\tau = 0$. As long as there is a cuboid particle present in the polymeric matrix, even of infinitesimal thickness, the permeating gas species will need to contour this impermeable particle to migrate through the membrane. The maximum difference between $D_{r,T}$ and $D_{r,F}$ occurs for τ between 0.5 and 0.6. In the extreme case for $A_p = 0.97$, this difference is as large as an order of magnitude compared to $D_{r,F}$. It is important to emphasize that regardless of A_p, $D_{r,T}$ is greater than unity for most τ values, except for τ less than 0.2. Interestingly, as A_p increases, the range of τ for which $D_{r,T} < 1$, increases. Simultaneously, even when $D_{r,T}$ is less than unity for $A_p = 0.97$, the corresponding difference between $D_{r,T}$ and $D_{r,F}$ is greater than for the particles with smaller A_p.

8.3.1.2 MMM with particles of different shapes

The difference between $D_{r,T}$ and $D_{r,F}$ is likely not unique to impermeable cuboid particles. To verify it, we extended the analysis to different geometries of impermeable particles. Fig. 8.6 presents the geometries for which dynamic gas permeations were simulated. In addition to cuboids (1), we considered cylindrical rods (2 and 6), elliptical rods (3 and 7), cylindrical tubes (4 and 8), and spheres (5). For cylindrical and elliptical rods, and for cylindrical tubes, we considered horizontal and vertical orientations.

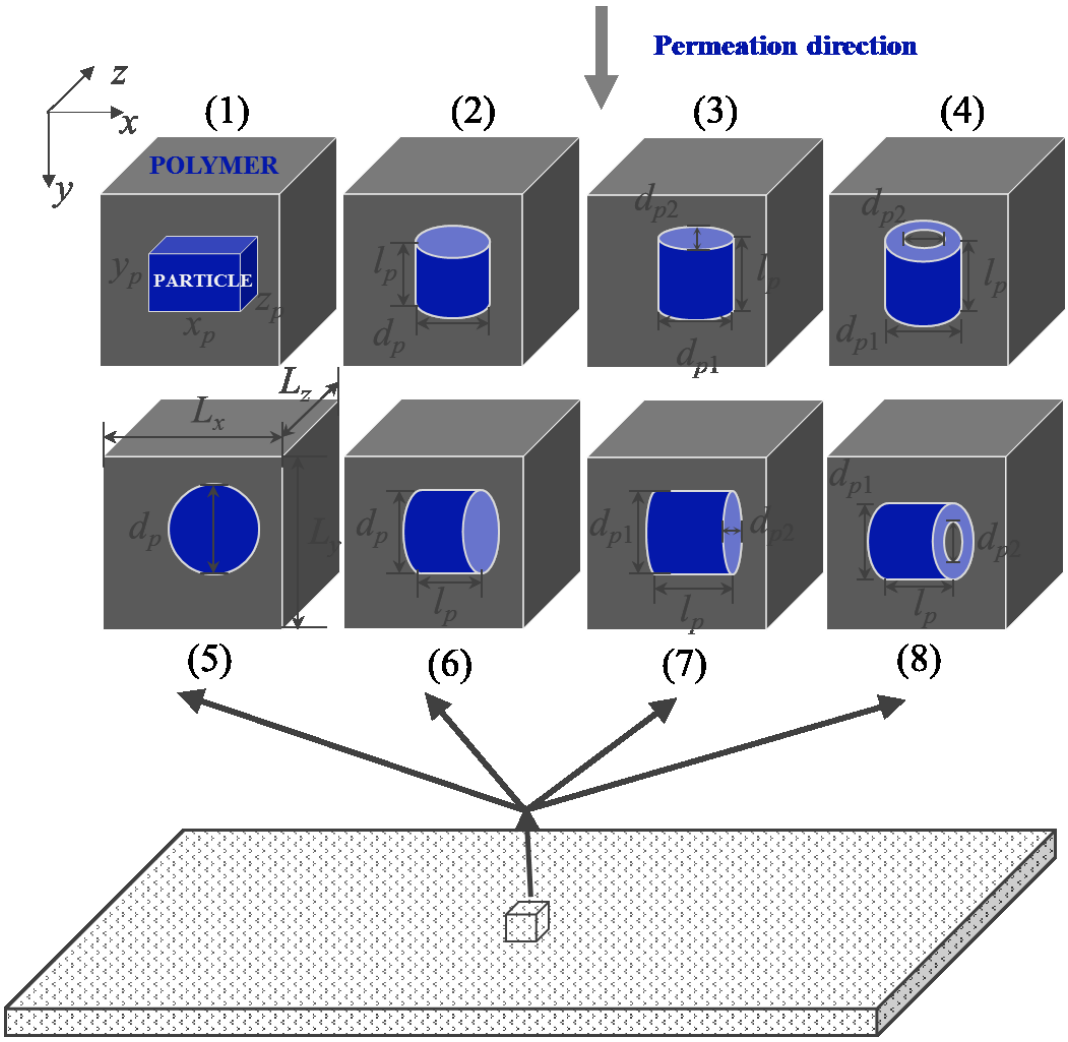

Figure 8.6 Schematic representation of a basic element of a single-layer mixed-matrix membrane with different geometries of particles. The particle is located at the center of the elementary unit with dimensions L_x, L_y, L_z. Gas permeation occurs in the y-direction. Characteristic dimensions for each geometry of particles are provided: (1) cuboid - x_p, y_p, z_p; (2) & (6) cylindrical rod - d_p, l_p; (3) & (7) elliptical rod - d_{p1}, d_{p2}, l_p; (4) & (8) cylindrical tube - d_{p1}, d_{p2}, l_p; (5) sphere – d_p.

As previously discussed, different cuboid particles can be compared based on of the relative thickness (τ) and the relative projected area (A_p), the product of which represents the volume fraction (ϕ) of particles in the resulting MMM. However, as shown in Fig. 8.6, different geometries are characterized by different sets of dimensions. The common ground to make representative comparisons between the geometries shown in Fig. 8.6 is their relative size, i.e. ϕ. Table 8.2 provides the characteristic dimensionless parameters of different geometries and how they correlate with ϕ. It is assumed that the

basic elementary unit of the MMM is a cube, i.e. $L_x = L_y = L_z$. It is important to emphasize that the parameters P1, P2 and P3 in Table 8.2 are independent of the number of layers of the elementary unit.

Table.8.2 Characteristic dimensionless parameters for different geometries of impermeable particles presented in Fig. 8.6 and their relationship with the volume fraction of particles.

Geometry	**P1**	**P2**	**P3**	**ϕ = f(P1,P2,P3)**
Sphere	$\frac{d_p}{L_y}$	-	-	$\phi = \frac{\pi}{6}\mathrm{P1}^3$
Cuboid	$\frac{y_p}{L_y}$	$\frac{x_p z_p}{L_x L_z}$	-	$\phi = \mathrm{P1P2}$
Cylindrical rod	$\frac{d_p}{L_y}$	$\frac{l_p}{d_p}$	-	$\phi = \frac{\pi}{4}\mathrm{P1}^3 \cdot \mathrm{P2}$
Elliptical rod	$\frac{d_{p1}}{L_y}$	$\frac{d_{p2}}{d_{p1}}$	$\frac{l_p}{d_{p1}}$	$\phi = \frac{\pi}{4}\mathrm{P1}^3 \cdot \mathrm{P2} \cdot \mathrm{P3}$
Cylindrical tube	$\frac{d_{p1}}{L_y}$	$\frac{d_{p2}}{d_{p1}}$	$\frac{l_p}{d_{p1}}$	$\phi = \frac{\pi}{4}\mathrm{P1}^3 \cdot \mathrm{P2} \cdot \mathrm{P3}(1 - \mathrm{P2})$

Fig. 8.7 presents the plots of D_r determined by the steady-state flux and the time-lag methods as a function of ϕ for the geometries of the particle shown in Fig. 8.6. These geometries are divided into four groups. The results for the first group (cuboid and sphere) are shown in Fig. 8.7a. There is an infinite number of different shapes of cuboids, but here we focused on the particular case of a cuboid – the cube. In this particular case, the volume fraction of cubic particles in the mixed matrix membrane is determined solely by the first dimensionless parameter (P1) in Table 8.2, facilitating the comparison between the cubes and spheres. Figs. 8.7b-d compare cylindrical rods, elliptical rods, and cylindrical tubes in their horizontal and vertical orientations. In this case, the volume fraction of particles is determined by either two dimensionless parameters (P1,P2) as in the case for cylindrical rods, or three dimensionless parameters (P1,P2,P3) as in the case of elliptical rods and cylindrical tubes. For the cylindrical rods (Fig. 8.7b), ϕ was primarily controlled by changing P1 (d_p/L_y) from 0 to 0.93 while keeping P2 (l_p/d_p) relatively constant (ranging

from 0.89 to 0.97). For elliptical rods and cylindrical tubes, ϕ was controlled by both P1 (d_{p1}/L_y) and P2 (d_{p2}/d_{p1}) while keeping P3 (l_p/d_{p1}) constant and equal to unity.

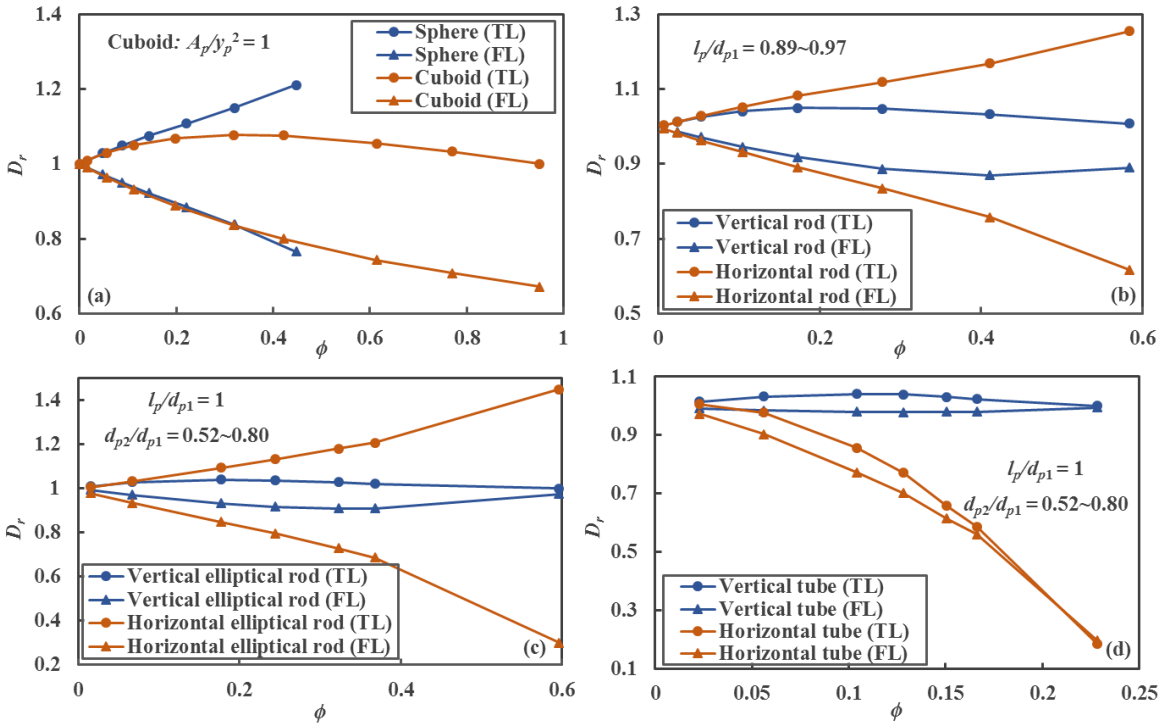

Figure 8.7 The relative diffusivity of single-layer mixed-matrix membranes with different geometries of particles estimated by the steady-state flux (FL) and the time-lag (TL) methods as a function of the volume fraction of the particles. Geometries of particles are divided into four groups, each group comparing two specific geometries: (a) spheres vs cubes, (b) horizontal vs vertical cylindrical rods, (c) horizontal vs vertical elliptical rods, (d) horizontal vs vertical cylindrical tubes.

Regardless of the shape of particles, the relative diffusivity coefficient estimated by the time-lag method is higher than the relative diffusivity obtained by the steady-state flux method. It proves that the difference between $D_{r,T}$ and $D_{r,F}$ is not unique to cuboid particles. Moreover, except for the horizontal tubes, $D_{r,T}$ is greater than unity for all particle shapes over practically the entire range of ϕ. Considering the spherical particles (Fig. 8.7a), the difference between $D_{r,T}$ and $D_{r,F}$ appears to be directly proportional to ϕ and the $D_{r,T}$ and $D_{r,F}$ plots appear to be mirror images of each other for $D_r = 1$. The cubic particles behave similarly as spherical particles up to $\phi \sim 0.15$; then, the shape of their respective $D_{r,T}$ and $D_{r,F}$ curves starts to resemble that seen in Fig. 8.5.

Figs. 8.7b-d allows assessing the effect of particle orientation. First of all, for the cylindrical and elliptical rods (Figs. 8.7b-c), the difference between $D_{r,T}$ and $D_{r,F}$ for their

horizontally-aligned orientation is significantly higher than for the respective vertical orientation. Moreover, similarly to the spherical particles, the difference between $D_{r,T}$ and $D_{r,F}$ appears to be directly proportional to ϕ, and $D_{r,T}$ and $D_{r,F}$ plots appear to be mirror images of each other for $D_r = 1$. For the cylindrical tubes, the difference between $D_{r,T}$ and $D_{r,F}$ for the respective horizontal and vertical orientations is similar for the entire range of ϕ. For the vertical orientations of different geometries shown in Figs. 7b-d, the difference between $D_{r,T}$ and $D_{r,F}$ decreases as ϕ increases (due to an increase in the longitudinal dimension), and they both approach $D_r = 1$. Similarly to cuboid particles shown in Fig. 8.5, these geometries have a constant projected area in the direction of permeation, which means that when their length approaches the membrane thickness, the tortuous effect should gradually disappear.

8.3.2 *Multilayer-layer MMMs*

Fig. 8.8 presents the effect of the number of layers (n) on the steady-state portions of the pressure response curves of a mixed-matrix membrane with a cuboid particle (A_p = 0.56, τ = 0.25, thus ϕ = 0.14). For the sake of clarity, the transient portions of the respective pressure curves are omitted. As the number of layers increases, the slope of the steady-state portion decreases. More specifically, since L is directly proportional to n, the slope in Fig. 8.8 is inversely proportional to n. An intercept in Fig. 8.8 corresponds to θ_e/θ, in which θ represents the time-lag of a single-layer neat polymer membrane. Since θ is directly proportional to L^2, θ_e/θ increases with n, this increase is not proportional to $[(n+1)/n]^2$, which would be the case if there were no impermeable particles. The results presented in Fig. 8.8 are quantified in Table 8.3.

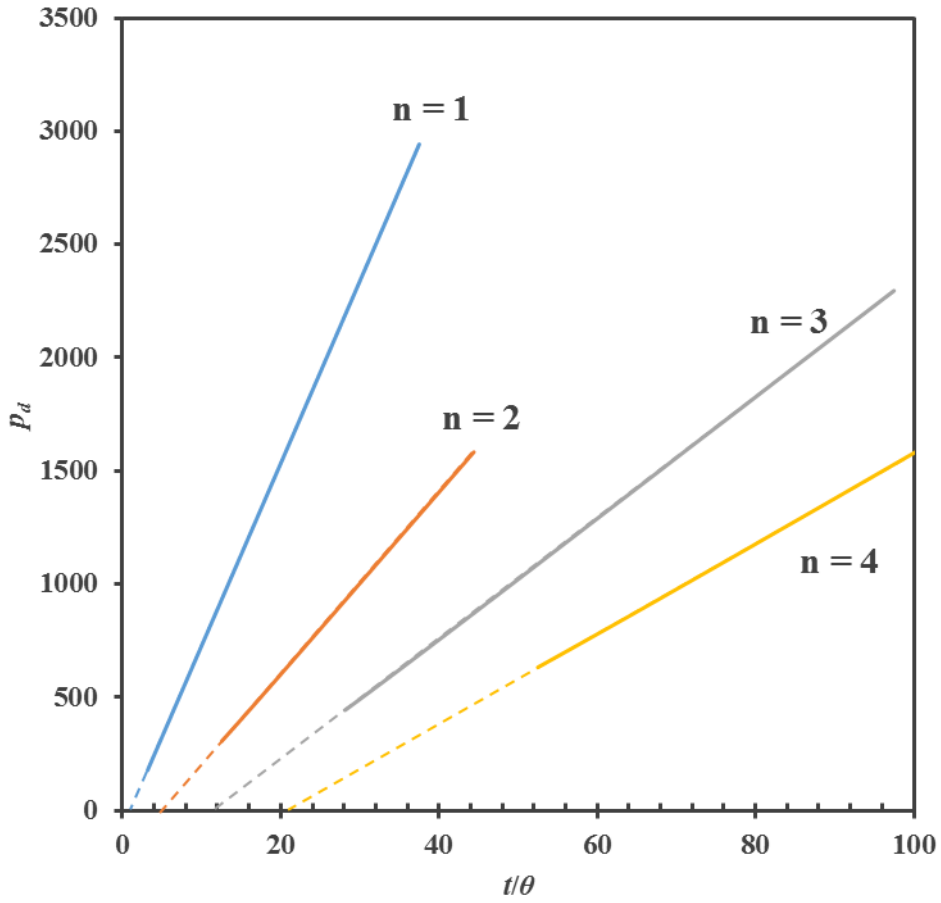

Figure 8.8 The effect of the number of layers on the steady-state portions of the pressure response curves of a mixed-matrix membrane with a cuboid particle ($A_p = 0.56$, $\tau = 0.25$, $\phi = 0.14$).

Table 8.3 Quantification of the results presented in Fig. 8.8 showiing the effect effect of the number layers on the relative time lag of a MMM containing impermeable cuboid particle ($A_p = 0.56$, $\tau = 0.25$).

n	θ_c/θ	$(\theta_c/\theta)_{n+1}/(\theta_c/\theta)_n$	$[(n+1)/n]^2$	$\{(\theta_c/\theta)_{n+1}/(\theta_c/\theta)_n\}/[(n+1)/n]^2$
1	0.9529	-	-	-
2	5.0839	5.335	4	1.334
3	11.969	2.254	2.25	1.046
4	21.608	1.805	1.77	1.016

An increase in the relative time lag with n (Column 3 in Table 8.3) does not match the increase that would occur if the membrane did not contain impermeable particles (Column 4). The latter represents the relative increase in the time lag of the neat polymer membrane with thickness. More specifically, for a given n, the value in Column 3 is greater

than the value in Column 4. However, the difference between the values in Columns 3 and 4 decreases with n. Column 5 presents the ratio of the respective values in Columns 3 and 4, and this ratio approaches unity as n increases.

Fig. 8.9 provides an alternative representation of the effect of n on the time lag of the same are MMM membrane. The steady-state pressure responses are plotted as a function of the relative time (t/θ), which is further normalized for the number of layers. Since the membrane thickness, $L = nL_y$ and θ_e are directly proportional to L^2 (Eq. 20), the relative time normalized by the number of layers in Fig. 8.8 is given by $t/(\theta \cdot n^2)$. It is important to note that as a result of plotting the pressure responses versus $t/(\theta \cdot n^2)$, the apparent slope in Fig. 8.9 should be divided by n^2 to obtain the actual slope of the pressure response curve, which would match the corresponding slopes in Fig. 8.8. Therefore, although the apparent slopes in Fig. 8.9 appear to be directly proportional to n, the actual slopes are inversely proportional to n. The intersection of the extrapolated linear portion of the pressure response with the relative-time axis normalized by the number of membrane layers represents the relative effective time lag, $\theta_e/(\theta \cdot n^2)$, from which $D_{r,T}$ can be readily calculated. The inset in Fig. 8.8 shows the effect of the number of layers on the relative effective time lag for this MMM.

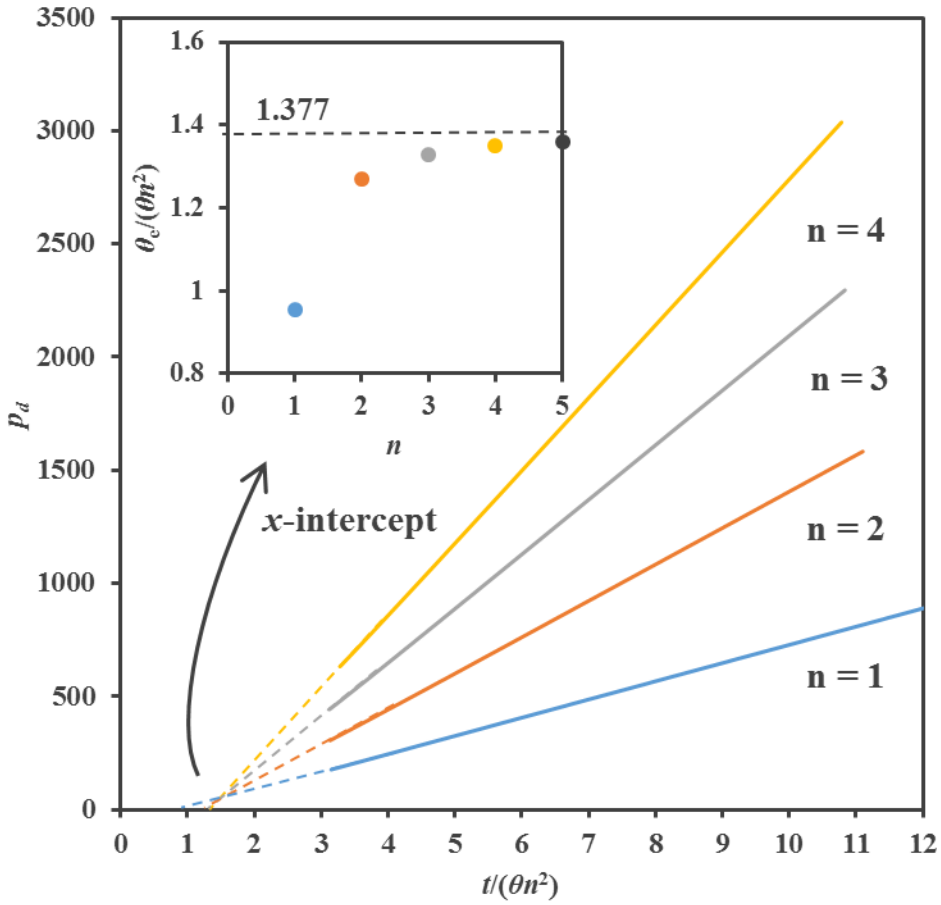

Figure 8.9 The effect of the number of layers on the steady-state portions of the pressure response curves of a mixed-matrix membrane with a cuboid particle ($A_p = 0.56$, $\tau = 0.25$, $\phi = 0.14$). The insert summarizes the effect of the number of layers on the relative effective time lag.

It can be noticed that as n increases, the relative effective time lag approaches a constant value. The value of 1.377, represented by the dashed line in the inset in Fig. 8.9, corresponds to the relative effective time lag calculated using P_e/S_e. Therefore, it appears that if n is sufficiently large, the relative effective time lag becomes independent of n, but also the corresponding $D_{r,T}$ approaches $D_{r,F}$. It is also important to note the ratios of the subsequent relative effective time lags in the inset in Fig. 8.9 correspond to the last column in Table 8.3.

To verify that the trend observed in Fig. 8.9 can be generalized to other geometries of dispersed particles, Fig. 8.10 presents the effect of n on D_r by the constant flux and time-

lag methods for all 8 cases considered in Fig. 8.6. For a given shape and orientation, the plots are generated for two different sizes of the dispersed particles. The size of the particles for which the simulations are presented in Fig. 8.10 is characterized in terms of geometrical parameters P1, P2 and P3 defined in Table 8.2. As previously noted, $D_{r,F}$ is independent of the number of layers because P_r and S_r of the elementary unit of the membrane are representative for the entire membrane. Consequently, $D_{r,F}$ values (horizontal lines in Fig. 8.10) are used as reference lines.

It is evident that regardless of the particle's geometry and size, and its orientation, $D_{r,T}$ rapidly decreases and approaches the value of $D_{r,F}$ as the number of layers increases. In other words, the trend in Fig. 8.8 is not unique to cuboid particles. The limiting case of the MMM consisting of a single layer discussed in the previous sections corresponds to the maximum difference between $D_{r,T}$ and $D_{r,F}$. Although the magnitude of this maximum difference strongly depends on the size, geometry and the orientation of the particle, the relative difference between $D_{r,T}$ and $D_{r,F}$ becomes less than 1% when the number of layers is five or higher, regardless of the geometry, size and orientation of the particle. Consequently, a discrepancy between $D_{r,T}$ and $D_{r,F}$ is more likely to occur in thin-film composite membranes, in which the dimensions of the filler particles are close to the membrane thickness, than in relatively thick MMMs.

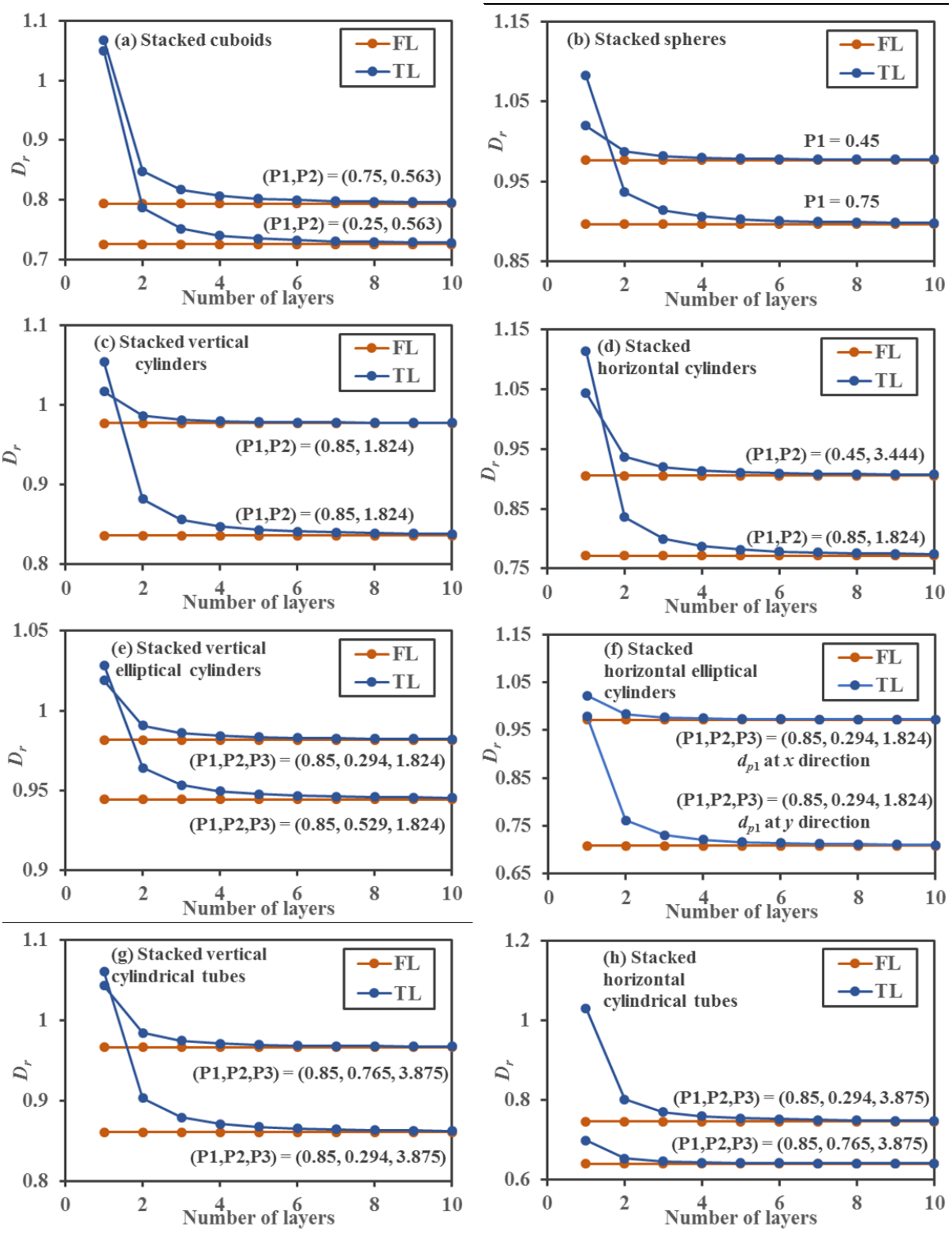

Figure 8.10 The effect of the number of layers in the mixed-matrix membranes, each layer containing an elementary unit with a nanoparticle in its center, on the relative diffusion coefficient determined by the time-lag method ($D_{r,T}$) for (a)

cuboids, (b) spheres, (c) vertical cylinders, (d) horizontal cylinders, (e) vertical elliptical cylinders, (f) horizontal elliptical cylinders, (g) vertical cylindrical tubes, and (h) horizontal cylindrical tubes. The respective diffusion coefficients by the constant-flux method ($D_{r,F}$), which represent the actual D_r are included as a reference. Geometrical parameters P1, P2, and P3, are defined in Table 8.2.

8.4 Discussion

As shown in the preceding section, it is possible that $D_{r,T}$ to be higher than $D_{r,F}$. If this is the case, then a question arises; which of the two diffusion coefficients better represents the diffusion process in the MMMs? Considering that $D_{r,T}$ might be higher than unity, which implies that the effective diffusivity of MMMs with impermeable particles is higher than that of the host polymer, it might be tempting to conclude that $D_{r,F}$ is more reliable than $D_{r,T}$. However, as counterintuitive $D_{r,T} > 1$ might appear, it is physically possible because of the time-lag method's nature. Consequently, a decrease in the time-lag resulting from the dispersion of impermeable particles in a host polymer membrane does not automatically imply the presence of voids at the polymer-particle interface.

Unlike $D_{r,F}$, which for a given shape, size, orientation and volume fraction of uniformly distributed particles is constant, $D_{r,T}$ decreases with the number of layers of particles (membrane thickness), eventually approaching the value of $D_{r,F}$. It is understood that when referring to effective transport property, for example, the effective diffusion coefficient, the property is unique for a given membrane material at specific conditions, such as temperature and pressure. However, this is not the case for the effective diffusion coefficient in MMMs determined by the time-lag method, which might also depend on the membrane thickness. The reason for this dependence arises from the fact that the tortuosity of MMMs depends on the membrane thickness. If a membrane consists of a single layer of impermeable particles, after contouring the particle, the permeating gas species will take the shortest path to exit the membrane. However, if there is another layer, they will need to contour another particle on their way out of the membrane. In other words, in the case of the MMMs considered in this study, the tortuosity increases with the number of particle layers, and the dependence of τ on n can be inferred from Fig. 8.9, keeping in mind that τ is inversely proportional to $D_{r,T}$. It means that for $n > 5$, τ is practically independent on n.

It can, therefore, be argued that since $D_{r,T}$ reflects a real the dependence of τ on the membrane thickness, while $D_{r,F}$ does not, the former provides a better representation of the diffusion process in MMMs with impermeable particles.

For the MMMs with uniformly dispersed nonporous particles, $D_{r,T}$ approaches $D_{r,F}$ when there are five or more layers of particles. Interestingly, as shown in Fig. 8.9, the number of required layers to match the two diffusion coefficients appears to be independent of the shape, size and orientation of the particle. However, what if particles were not uniformly distributed while their shape, size and orientation were kept unchanged? Would that push $D_{r,T}$ and $D_{r,F}$ further apart or closer together? Would it be ever possible to have $D_{r,T} = D_{r,F}$? Answering these questions requires a lot or of well-planned simulations, which are beyond the scope of this manuscript. However, studying the effect of non-uniform distribution of particles should be the next step in this research.

In this paper, we focused on MMMs with impermeable particles. At the other end, there is a myriad of MMMs employing permeable particles to increase their effective permeability and diffusion coefficients. The analysis of such membranes is also beyond the scope of this work. However, we speculate that if porous particles had the same shape, size and orientation, and were uniformly distributed, $D_{r,T}$ and $D_{r,F}$ would differ as in the case with impermeable particles. In other words, we speculate that the problem addressed in this paper is not unique to MMMs with impermeable particles.

Finally, although, as shown by our analysis, $D_{r,T}$ eventually approaches $D_{r,F}$, these two parameters should not be used interchangeably. Moreover, in the case MMMs, one should be cautious with a liberal application of the famous solution-diffusion equation:

$$P_e = S_e D_e \tag{3}$$

More specifically, knowing two of the three transport coefficient, for example, P_e and D_e from the time lag-method experiment, the ratio of P_e and D_e might not necessarily match S_e determined in a separate sorption experiment. In other words, when each of the three parameters in Eq. (3) are determined independently, the left-hand side might not always be equal to the right-hand side, and if they are not equal, it does not automatically imply that one or more of these transport coefficients are incorrect.

8.5 Conclusions

The paper was focused on investigating the validity of the time-lag method when applied to determine the effective diffusivity coefficient of MMMs with uniformly dispersed impermeable particles of different geometries in the continuous polymer phase. It was assumed that gas sorption in the host polymer membrane obeys Henry's law and that the corresponding diffusion coefficient is constant. In other words, it was assumed that the solubility, diffusion and permeability coefficients in the host polymer membrane represent the intrinsic properties. The three-dimensional Fick's second law of diffusion was solved numerically to simulate dynamic gas permeation experiments required by the time-lag method. The MMM's effective diffusion coefficient was determined by the time-lag method and the ratio of the effective permeability and solubility coefficients. The latter, for a given shape, size and orientation of particles, was constant regardless of the number of particle layers in the membrane.

In the limiting case of the MMMs containing a single layer of particles, except for the MMMs with uniformly distributed horizontal and vertical cylindrical tubes having negligible wall thickness, the relative effective diffusivity of mixed matrix membranes determined by the time-lag method was always higher than the ratio of the effective permeability and solubility coefficients. In some cases, the relative effective diffusivities of the mixed matrix membranes were greater than unity, indicating the actual effective diffusivity coefficients higher than those of the host polymer. This somewhat unexpected result arises from the nature of the time-lag method and has a perfect physical explanation. The difference between the relative diffusivity coefficients by the two methods rapidly decreases with increase the number of layers, and regardless of the geometry of the nanoparticle and its orientation, it becomes negligible for the MMMs containing five or more layers of nanoparticles. The dependence of the effective diffusivity determined by the time-lag method on the number of particle layers in MMMs reflects changes in the membrane tortuosity, which is inversely related to the effective diffusivity.

8.6 Nomenclature

A	Membrane area.
A_p	Dimensionless projected area of the particle.
b	Hole affinity constant in dual-mode sorption model.
C	Concentration of the permeating gas species within the membrane.
$C_{i,j,k}^{m}$	Concentration of the permeating gas species for an interior mesh point (i, j, k) at time step m.
C_H'	Hole saturation constant in dual-mode sorption model.
d_p	Particle diameter.
d_{p1}	Outside diameter of a cylindrical tube particle or diameter in the y-direction of the elliptical rod.
d_{p2}	Inside diameter of a cylindrical tube particle or diameter in the x-direction of the elliptical rod.
D	Intrinsic diffusivity.
D_e	Effective diffusivity of a mixed-matrix membrane.
$D_{e,F}$	Effective diffusivity of a mixed-matrix membrane determined from the time lag.
$D_{e,T}$	Effective diffusivity of a mixed-matrix membrane determined from the steady-state flux.
$D_{r,F}$	Relative diffusivity of a mixed-matrix membrane determined from the time lag.
$D_{r,T}$	Relative diffusivity of a mixed-matrix membrane determined from the steady-state flux.
J_L	Gas flux out of the membrane.
J_0	Gas flux into the membrane.
l_p	Particle length.
L	Membrane thickness.
L_x	Dimension of an elementary unit at x direction.
L_y	Dimensions of an elementary unit at y direction.
L_z	Dimensions of an elementary unit at z direction.
n	Number of particle layers in a mixed-matrix membrane.
p	Gas pressure.

p_0	Feed pressure.
p_d	Permeate pressure.
P	Intrinsic permeability.
P_e	Effective permeability of a mixed-matrix membrane.
P_r	Relative permeability of a mixed-matrix membrane.
P1, P2, P3	Characteristic dimensionless parameters of impermeable particles.
R	Universal gas constant.
S	Intrinsic solubility.
S_e	Effective solubility of a mixed-matrix membrane.
S_r	Relative solubility of a mixed-matrix membrane.
t	Permeation time.
T	Absolute temperature.
V_d	Downstream volume.
x_p	Dimension of a particle in the x direction.
y	Direction of permeation.
y_p	Dimension of a particle in the y direction.
z_p	Dimensions of a particle in the z direction.
Δx_i	Interior mesh size at i location at x direction.
Δy_j	Interior mesh size at j location at y direction.
Δz_k	Interior mesh size at k location at z direction.
ϕ	Volume fraction of particles in a mixed-matrix membrane.
τ	Dimensionless thickness of the particle.
θ	Time lag.
θ_e	Effective time lag of a mixed-matrix membranes.

8.7 Acknowledgement

The authors gratefully acknowledge the financial support provided by the Natural Science and Engineering Research Council (NSERC) Canada, Discovery Grant (DG), grant number: 04443.

8.8 References

[1] A. F. Ismail, T. D. Kusworo, A. Mustafa and H. Hasbullah, "Understanding the solution-diffusion mechanism in gas separation membrane for engineering students," *Regional Conf. Eng. Educ.*, Johor, Malaysia, pp. 155-159, 2005.

[2] R. Castro-Muñoz, K. V. Agrawal and J. Coronas, "Ultrathin permselective membranes: the latent way for efficient gas separation", *RSC Adv.*, vol. 10, 12653-12670, 2020.

[3] B. Seoane, J. Coronas, I. Gascon, M. E. Benavides, O. Karvan, J. Caro, F. Kapteijn, J. Gascon, "Metal–organic framework based mixed matrix membranes: a solution for highly efficient CO_2 capture?", *Chem. Soc. Rev.*, vol. 44, 2421-2454, 2015.

[4] J. Wijmans and R. Baker, "The solution-diffusion model: a review" *J. Memb. Sci*, vol. 107, no. 1-2, pp. 1–21, 1995.

[5] K. Ghosal and B. D. Freeman, "Gas separation using polymer membranes: an overview" *Polym. Adv. Tech.*, vol. 5, no. 11, pp. 673–697, 1994.

[6] S. Zid, M. Zinet, E. Espuche, Modeling diffusion mass transport in multiphase polymer systems for gas barrier applications: A review, *J. Polym. Sci. Part B Polym. Phys*. 56 (2018) 621–639. https://doi.org/10.1002/polb.24574.

[7] J.H. Petropoulos, Chapter 2: Mechanisms and Theories for Sorption and Diffusion of Gases in Polymers, in: D.R. Paul, Y.P. Yampol' skii (Eds.), Polymeric Gas Separation Membranes, CRC Press, an imprint of Taylor and Francis, Boca Raton, 2018, pp. 17-82.

[8] H. A. Daynes, "The Process of Diffusion through a Rubber Membrane," *Proc. Roy. Soc. A: Math., Phys. Eng. Sci.*, vol. 97, no. 685, pp. 286–307, Jan. 1920.

[9] R. M. Barrer and E. K. Rideal, "Permeation, diffusion and solution of gases in organic polymers," *Trans. Faraday Soc.*, vol. 35, p. 628, 1939.

[10] H. Wu, B. Kruczek, and J. Thibault, "Impact of Measuring Devices and Data Analysis on the Determination of Gas Membrane Properties" *J. Memb Sci Research*, vol. 4, pp. 4-14, 2018.

[11] S. Lashkari and B. Kruczek, "Effect of resistance to gas accumulation in multi-tank receivers on membrane characterization by the time lag method. Analytical

approach for optimization of the receiver" *J. Memb. Sci*, vol. 360, no. 1-2, pp. 442–453, 2010.

[12] A. Fuoco, M. Monteleone, E. Esposito, et.al, "Gas transport in mixed matrix membranes: two methods for time lag determination," *Computation*, vol. 8 (2), 2020 doi:10.3390/computation8020028

[13] M. M. Khan, S. Shishatskiy, & V. Filiz, "Mixed Matrix Membranes of Boron Icosahedron and Polymers of Intrinsic Microporosity (PIM-1) for Gas Separation." *Membranes*, vol. 8 (1), 1, 2018. https://doi.org/10.3390/membranes8010001

[14] L. N. Sridhar, R. K. Gupta, & M. Bhardwaj, "Barrier Properties of Polymer Nanocomposites" *Ind. Eng. Chem. Res.,* vol. 45,pp. 8282-8289.

[15] H. Boukehili, & P. Nguyen-Tri. "Helium Gas Barrier and Water Absorption Behavior of Bamboo Fiber Reinforced Recycled Polypropylene." *J. Reinforced Plastics and Composites*, vol. 31, no. 23, pp. 1638–1651, 2012. doi:10.1177/0731684412464090.

[16] L. M. Robeson, "Correlation of separation factor versus permeability for polymeric membranes" *J. Memb. Sci*, vol. 62, no. 2, pp. 165–185, 1991.

[17] L. M. Robeson, "The upper bound revisited" *J. Memb. Sci*, vol. 320, no. 1-2, pp. 390–400, 2008.

[18] B. D. Freeman, "Basis of Permeability/Selectivity Trade-off Relations in Polymeric Gas Separation Membranes" *Macromolecules*, vol. 32, no. 2, pp. 375–380, 1999.

[19] S.E.M. Selke, J.D. Culter, Plastics Packaging: Properties, Processing, Applications, and Regulations, 3rd Ed., Carl Hanser Verlag, Munich, 2016. https://doi.org/10.1016/B978-3-446-40790-9.50001-9.

[20] Å. Nyflött, Meriçer, Ç. Minelli, M. et al., The influence of moisture content on the polymer structure of polyvinyl alcohol in dispersion barrier coatings and its effect on the mass transport of oxygen. J. Coat. Technol. Res., 14 (2017) 1345-1355. https://doi.org/10.1007/s11998-017-9937-2.

[21] Z.W. Abdullah, Y. Dong, I.J. Davies, S. Barbhuiya, PVA, PVA Blends, and Their Nanocomposites for Biodegradable Packaging Application, Polymer-Plastics Tech. & Eng., 56 (2017) 1307-1344. http://dx.doi.org/10.1080/03602559.2016.1275684

[22] R. Castro-Muñoz, M. Z. Ahmad, V. Fíla, "Tuning of nano-based materials for embedding into low-permeability polyimides for a featured gas separation", *Front. Chem*., vol. 7, Article 897, January 2020. https://doi.org/10.3389/fchem.2019.00897

[23] R. Castro-Muñoza, J. Buera-González, Ó. de la Iglesia, F. Galiano, V. Fíla, M. Malankowska, C. Rubio, A. Figoli, C. Téllez, J. Coronas, "Towards the dehydration of ethanol using pervaporation cross-linked poly (vinyl alcohol)/graphene oxide membranes", *J. Memb. Sci.* 582 (2019) 423–434. https://doi.org/10.1021/acs.iecr.8b01564.

[24] H. Vinh-Thang, S. Kaliaguine, "Predictive models for mixed-matrix membrane performance: A review." Chem. Rev. 113 (2013) 4980−5028. https://doi.org/10.1021/cr3003888.

[25] A. Ebneyamini, H. Azimi, F.H. Tezel, J. Thibault, Mixed-matrix membranes applications: Development of a resistance-based model, J. Memb. Sci. 543 (2017) 351–360. https://doi.org/10.1016/j.memsci.2017.08.065.

[26] A. Ebneyamini, H. Azimi, F.H. Tezel, J. Thibault, Modelling of mixed matrix membranes: Validation of the resistance-based model, J. Memb. Sci. 543 (2017) 361–369. https://doi.org/10.1016/j.memsci.2017.08.064.

8.8 References

[27] A. F. Ismail, T. D. Kusworo, A. Mustafa and H. Hasbullah, "Understanding the solution-diffusion mechanism in gas separation membrane for engineering students," Regional Conf. Eng. Educ., Johor, Malaysia, pp. 155-159, 2005.

[28] J. Wijmans and R. Baker, "The solution-diffusion model: a review" J. Memb. Sci, vol. 107, no. 1-2, pp. 1–21, 1995.

[29] K. Ghosal and B. D. Freeman, "Gas separation using polymer membranes: an overview" Polym. Adv. Tech., vol. 5, no. 11, pp. 673–697, 1994.

[30] S. Zid, M. Zinet, E. Espuche, Modeling diffusion mass transport in multiphase polymer systems for gas barrier applications: A review, J. Polym. Sci. Part B Polym. Phys. 56 (2018) 621–639. https://doi.org/10.1002/polb.24574.

[31] J.H. Petropoulos, Chapter 2: Mechanisms and Theories for Sorption and Diffusion of Gases in Polymers, in: D.R. Paul, Y.P. Yampol'skii (Eds.), Polymeric Gas Separation Membranes, CRC Press, an imprint of Taylor and Francis, Boca Raton, 2018, pp. 17-82.

[32] H. A. Daynes, "The Process of Diffusion through a Rubber Membrane," Proc. Roy. Soc. A: Math., Phys. Eng. Sci., vol. 97, no. 685, pp. 286–307, Jan. 1920.

[33] R. M. Barrer and E. K. Rideal, "Permeation, diffusion and solution of gases in organic polymers," Trans. Faraday Soc., vol. 35, p. 628, 1939.

[34] H. Wu, B. Kruczek, and J. Thibault, "Impact of Measuring Devices and Data Analysis on the Determination of Gas Membrane Properties" J. Memb Sci Research, vol. 4, pp. 4-14, 2018.

[35] S. Lashkari and B. Kruczek, "Effect of resistance to gas accumulation in multi-tank receivers on membrane characterization by the time lag method. Analytical approach for optimization of the receiver" J. Memb. Sci, vol. 360, no. 1-2, pp. 442–453, 2010.

[36] A. Fuoco, M. Monteleone, E. Esposito, et.al, "Gas transport in mixed matrix membranes: two methods for time lag determination," Computation, vol. 8 (2), 2020 doi:10.3390/computation8020028

[37] M. M. Khan, S. Shishatskiy, & V. Filiz, "Mixed Matrix Membranes of Boron Icosahedron and Polymers of Intrinsic Microporosity (PIM-1) for Gas Separation." Membranes, vol. 8 (1), 1, 2018. https://doi.org/10.3390/membranes8010001

[38] L. N. Sridhar, R. K. Gupta, & M. Bhardwaj, "Barrier Properties of Polymer Nanocomposites" Ind. Eng. Chem. Res., vol. 45,pp. 8282-8289.

[39] H. Boukehili, & P. Nguyen-Tri. "Helium Gas Barrier and Water Absorption Behavior of Bamboo Fiber Reinforced Recycled Polypropylene." J. Reinforced Plastics and Composites, vol. 31, no. 23, pp. 1638–1651, 2012. doi:10.1177/0731684412464090.

[40] L. M. Robeson, "Correlation of separation factor versus permeability for polymeric membranes" J. Memb. Sci, vol. 62, no. 2, pp. 165–185, 1991.

[41] L. M. Robeson, "The upper bound revisited" J. Memb. Sci, vol. 320, no. 1-2, pp. 390–400, 2008.

[42] B. D. Freeman, "Basis of Permeability/Selectivity Trade-off Relations in Polymeric Gas Separation Membranes" Macromolecules, vol. 32, no. 2, pp. 375–380, 1999.

[43] S.E.M. Selke, J.D. Culter, Plastics Packaging: Properties, Processing, Applications, and Regulations, 3rd Ed., Carl Hanser Verlag, Munich, 2016. https://doi.org/10.1016/B978-3-446-40790-9.50001-9.

[44] Å. Nyflött, Meriçer, Ç. Minelli, M. et al., The influence of moisture content on the polymer structure of polyvinyl alcohol in dispersion barrier coatings and its effect on the mass transport of oxygen. J. Coat. Technol. Res., 14 (2017) 1345-1355. https://doi.org/10.1007/s11998-017-9937-2

[45] Z.W. Abdullah, Y. Dong, I.J. Davies, S. Barbhuiya, PVA, PVA Blends, and Their Nanocomposites for Biodegradable Packaging Application, Polymer-Plastics Tech. & Eng., 56 (2017) 1307-1344. http://dx.doi.org/10.1080/03602559.2016.1275684

[46] A. Ebneyamini, H. Azimi, F.H. Tezel, J. Thibault, Mixed-matrix membranes applications : Development of a resistance-based model, J. Memb. Sci. 543 (2017) 351–360. https://doi.org/10.1016/j.memsci.2017.08.065.

[47] A. Ebneyamini, H. Azimi, F.H. Tezel, J. Thibault, Modelling of mixed matrix membranes: Validation of the resistance-based model, J. Memb. Sci. 543 (2017) 361–369. https://doi.org/10.1016/j.memsci.2017.08.064.

8.9 Appendices

8.9.1 Appendix I

Considering all shapes in Fig. 8.7, cylindrical tubes, both horizontal and vertical, show the smallest difference between $D_{r,T}$ and $D_{r,F}$ for a given ϕ. However, since for the cylindrical tubes ϕ is determined by three dimensionless parameters, Fig. 8.7d does not provide the information on how each of these three dimensionless parameters affects the difference between $D_{r,T}$ and $D_{r,F}$. To elucidate this information, Fig. 8.A.1 presents the plots of $D_{r,T}$ as a function of $D_{r,F}$ for horizontal tubes, in which P2 (d_{p2}/d_{p1}) and P3 (l_p/d_{p1}) are varied, while P1 (d_{p1}/L_y) is kept constant. It can be noticed that for a given l_p/d_{p1}, $D_{r,T}$ increases linearly with $D_{r,F}$ when d_{p2}/d_{p1} decreases. This indicates that the error in $D_{r,T}$ is more pronounced as the wall thickness of horizontal tubes increases. The solid lines in Fig. 8.A.1 are practically parallel to each other; however, the lines become shorter as l_p/d_{p1} decreases. Eventually, as l_p/d_{p1} approaches to zero, the line should converge to a single point, $D_{r,T} = D_{r,F} = 1$. For a given d_{p2}/d_{p1}, there is also a practically linear relationship between $D_{r,T}$ and $D_{r,F}$ when l_p/d_{p1} decreases; however, the slope of the respective lines strongly depends on d_{p2}/d_{p1}. It is important to emphasize that for thin-wall tubes ($d_{p2}/d_{p1} = 0.80$), the slope is close to unity, which indicates a small error in D_r by the time-lag method. Although not shown here, the same holds for the vertical cylindrical tubes with negligible wall thickness. Moreover, for the vertical tubes with negligible wall thickness, $D_{r,T} \sim D_{r,F} \sim 1$. In other words, the time-lag method could be used with confidence to characterize MMM membranes with uniformly distributed horizontal and vertical tubes having a negligible wall thickness. At the other limit, i.e., when $d_{p2}/d_{p1} \rightarrow 0$ (cylindrical tubes become cylindrical rods), the error in $D_{r,T}$ is maximized and represented by Fig. 8.7b.

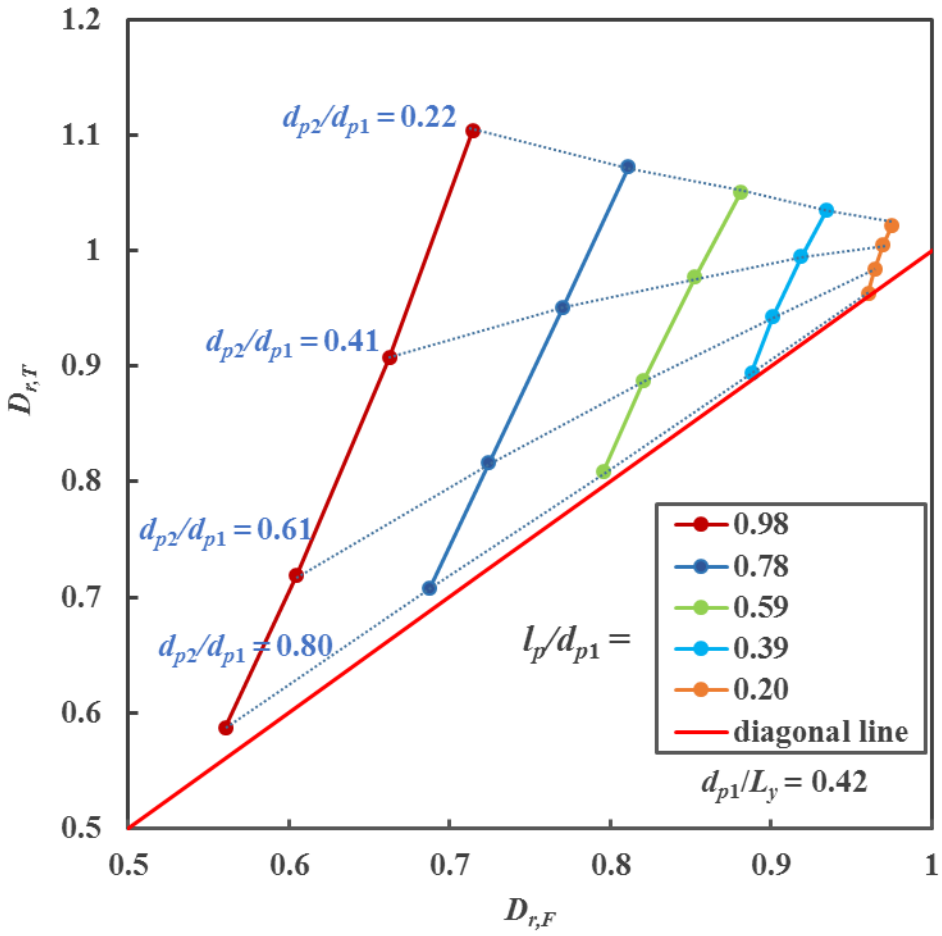

Figure 8.A.1 Plots of the relative diffusivity coefficient in mixed-matrix membranes with uniformly dispersed horizontal cylindrical tubes determined by the time-lag method ($D_{r,T}$) as a function of the actual relative diffusivity coefficient determined by the constant flux- method ($D_{r,F}$). The plots illustrate the effect of varying the wall thickness (d_{p2}/d_{p1}) while keeping the tube length (l_p/d_{p1}) and the outer tube diameter (d_{p1}/L_y) constant, and by varying the tube length (l_p/d_{p1}) while keeping the wall thickness (d_{p2}/d_{p1}) and the outer tube diameter (d_{p1}/L_y) constant. The references line, $D_{r,T} = D_{r,F}$ represent the limiting case of no error in in the relative diffusivity coefficient by the time-lag method.

8.8.2 Appendix II

This appendix provides additional plots of MMMs with multiple layers of nanoparticles for geometries that were not presented in Section 8.3.2. These plots are presented in Fig. 8.A.2. All these results corroborate that the conclusion that the time-lag method can accurately predict the effective diffusivity of MMMs granted that a given number of layers of elementary units are used.

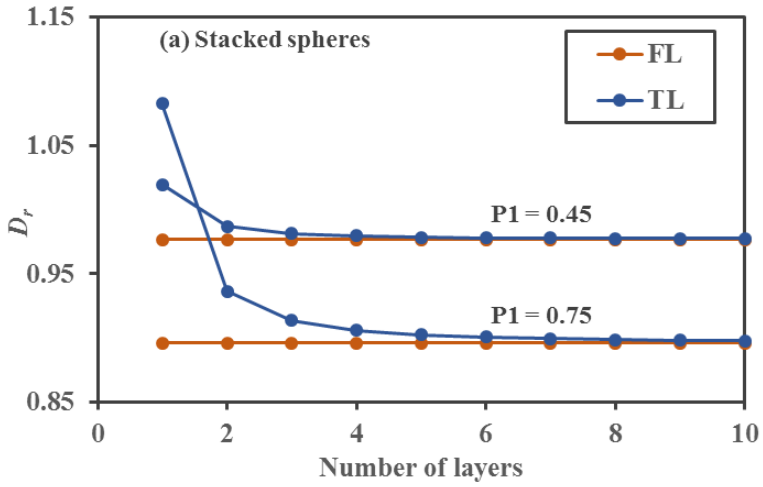
(a) Stacked spheres
FL
TL
P1 = 0.45
P1 = 0.75
D_r
1.15
1.05
0.95
0.85
0
2
4
6
8
10
Number of layers

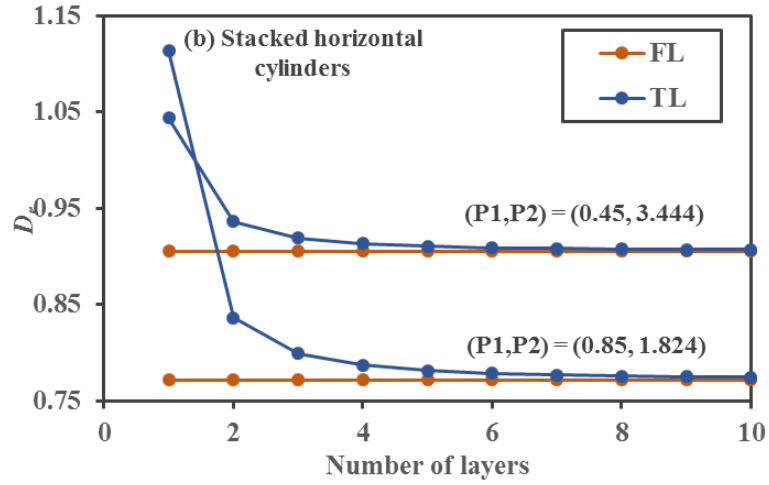
(b) Stacked horizontal cylinders
FL
TL
(P1,P2) = (0.45, 3.444)
(P1,P2) = (0.85, 1.824)
D_r
1.15
1.05
0.95
0.85
0.75
0
2
4
6
8
10
Number of layers

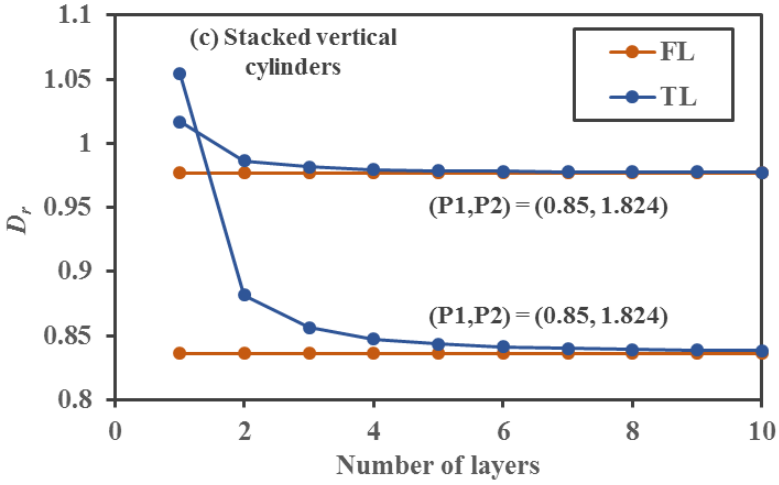
(c) Stacked vertical cylinders
FL
TL
(P1,P2) = (0.85, 1.824)
(P1,P2) = (0.85, 1.824)
D_r
1.1
1.05
1
0.95
0.9
0.85
0.8
0
2
4
6
8
10
Number of layers

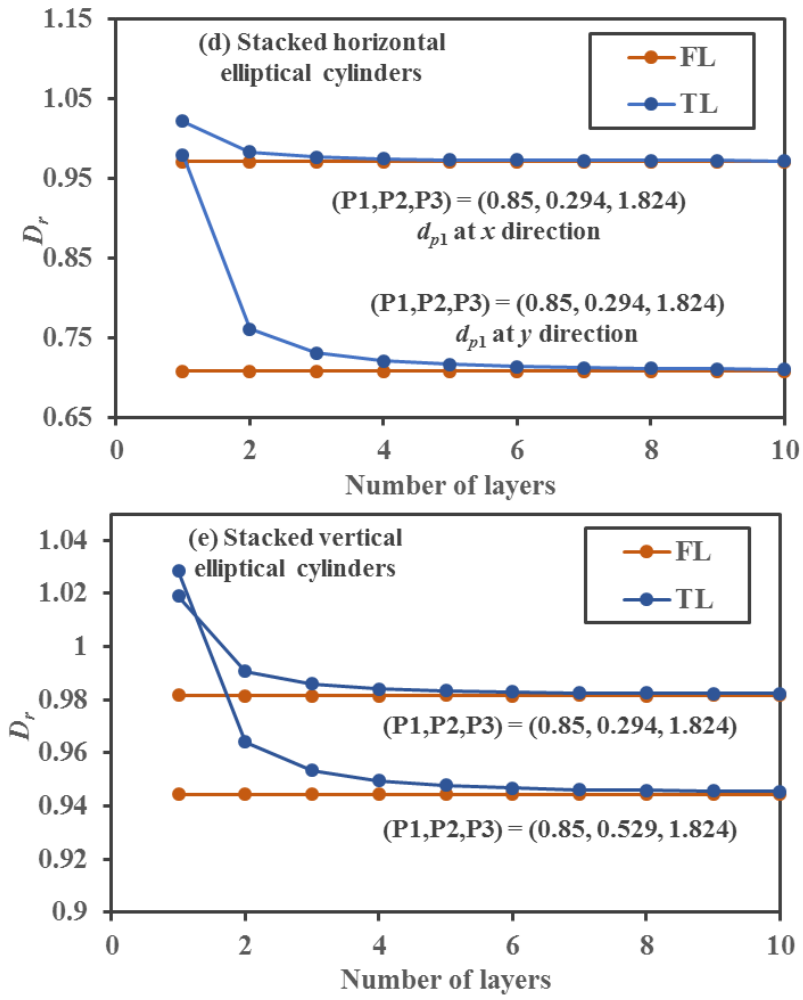

Figure 8.A.2 The effect of the number of layers in the mixed-matrix membranes, each layer containing an elementary unit with a nanoparticle in its center, on the relative diffusion coefficient determined by the time-lag method ($D_{r,T}$) for (a) spheres, (b) horizontal cylinders, (c) vertical cylinders, (d) horizontal elliptical cylinders, and (f) vertical elliptical cylinders. The respective diffusion coefficients by the constant-flux method ($D_{r,F}$), which represent the actual D_r are included as a reference. Geometrical parameters P1, P2, and P3 are defined in Table 8.2.

Chapter 9

Conclusions and Recommendations

9.1 Conclusions

This thesis's main motivation was the exiting results of the previous Ph.D. student, Dr. Neveen Al-Qasas, which showed tremendous potential for the membrane characterization by simultaneous monitoring of the upstream pressure decay and the downstream pressure rise in the commonly-used time-lag experiments, in a series of theoretical papers. While the accurate monitoring of the downstream pressure rise is well established, the pressure decay's accurate monitoring when the initial pressure at a typical level of feed pressures used in gas permeation experiments was a driving force for this project. Despite significant efforts and improvements in the state-of-the-art of the membrane testing system, the pressure decay's accurate monitoring at the feed-side remains challenging. Chapter 4, summarizes the current state in the development of the new testing system.

Recognizing that it is easy to be misguided by different experimental artifacts, we focused on the impact of measuring devices and data analysis on the determination of gas membrane properties in Chapter 3. In our analysis, we considered the classical time-lag method based on the downstream pressure rise. Based on its source, we classified noise into four categories: systematic errors from the experimental setup, random errors from the downstream pressure transducer, resolution errors from analogue-to-digital converter and extrapolation errors in the time-lag method. The systematic errors, resolution errors, and random errors could be minimized by careful calibration, accurate observation, and suitable upgrading of the measuring instrumentation to higher resolution options. A more economical and effective way is to manipulate the capacity parameter and the operational conditions to reduce uncertainties. In this case, a small capacity parameter is not always favoured. Rarely discussed in the literature, the extrapolation error associated with the time-lag method using the pressure data is significantly affected by the other types of errors

and noise. The size of the measuring window needs to be chosen carefully. The nonlinear regression method to determine the transport parameters has shown to be advantageous on decoupling *S* and *D*. With noise, the time-lag method is not able to obtain such accurate determination.

Chapter 5, which is a combination of experimental results and numerical simulations, shows that it is possible to extract more information for the membrane characterization from the classical time-lag method based on the downstream pressure rise by using the concept of an instantaneous time-lag. By analyzing the nitrogen permeation data obtained using high molecular weight PPO membranes, we observed a plateau in the instantaneous time-lag, which could be considered as an indication of reaching steady-state, or more precisely, pseudo-steady-state. However, following the plateau, as the experiment continued, we observed a clear, but unexpected upward deviation of the instantaneous time-lag curves. We explained experimental results in terms of the dual-mode sorption model with a non-instantaneous equilibrium between the Henry's and the Langmuir's. Our numerical experiments assuming the applicability of this model, could closely mimic the experimental data. However, recognizing the possibility of an experimental artifact, we would like to repeat experiments with other glassy polymers, displaying a similar behaviour as the high molecular weight PPO. These experiments are pending upon completing the new experimental system for the simultaneous monitoring of the downstream pressure rise and the upstream pressure decay.

Another foundation of this thesis was the recognition of the importance of numerical experiments. In gas transport in glassy polymers (Chapter 5) and mixed matrix membranes (Chapters 6-8), the governing partial differential equations cannot be solved analytically; the numerical solutions are the indispensable tool. In Chapter 2, we used a finite-difference numerical method as a tool to simulate the gas permeation process in a simple solution-diffusion membrane. By comparing with the benchmark analytical solution, the finite-difference numerical method, solving Fick's 2nd law of diffusion, was validated. Results have shown that predictions such as concentration profile, concentration gradient, pressure, and downstream time lag had good accuracy regardless of the uniform or the variable mesh scheme. However, a variable mesh scheme is recommended to capture the

steep gradient change at the membrane's upstream surface at early permeation time that could influence the upstream time lag determination. Results have shown that a variable mesh scheme where the first three uniform mesh sizes are transformed into 10 variable meshes (Factor 2) is a good compromise between accuracy and computation time. An explicit finite difference scheme is also recommended due to shorter computation time, but the two schemes gave similar prediction accuracy. The implicit method is recommended under nonlinear boundary conditions. The numerical tool was used to perform simulations throughout the thesis and could be used for future studies with confidence.

Because of the importance nowadays of mixed-matrix membranes, we wanted to investigate the applicability of the time-lag method to determine the properties (solubility, diffusivity and permeability) of these membranes. Our initial interest was to test mixed-matrix membranes embedding impermeable nanoparticles that could enhance the membrane barrier properties. It was envisaged to use in parallel experimental and numerical validations. Therefore, a series of simulations were performed to estimate the effective permeability of mixed-matrix membranes with a wide range of particle geometries and sizes and, most importantly, to determine if the time-lag method could be used for mixed-matrix membranes for estimating the effective diffusivity. In Chapters 6, we simulated the permeation process of gas molecules through mixed-matrix membranes embedding impermeable spherical and cuboid nanoparticles of different aspect ratios using a three-dimensional finite-difference solution of the Fick's second law of diffusion. These numerical simulations allowed us to assess the effect of nanoparticles' shape and size on the resulting mixed-matrix membranes' barrier properties. Simultaneously, these simulations, which can be referred to as numerical experiments, allowed assessing the applicability of different analytical models to predict these membranes' relative permeability.

Simulation results showed that, for the same volume fraction, the relative permeability of mixed-matrix membranes with cuboid nanoparticles and the aspect ratio larger than unity was lower than the relative permeability of membranes with spherical nanoparticles. However, Maxwell's model and other analytical models developed for spherical particles showed poor predictions of the relative permeability of MMMs with

cuboid particles. An analytical model, which involves only two geometrical parameters, the relative projected area available for permeation A^* and the relative thickness y^*, was obtained by applying multivariate covariance analysis. Despite its simplicity, the new model accurately predicts the relative permeability of the mixed-matrix membranes with cuboid nanoparticles for a wide range of sizes and aspect ratios. To our best knowledge, the model developed in this study is the first one in the literature with both spherical and layered nanoparticles. Additionally, accurate predictions on the MMM's relative permeability of both cuboid and spherical nanoparticles were also obtained with an artificial neural network.

The new model was then generalized in Chapter 7 to predict the relative permeability of mixed-matrix membranes with various geometries of impermeable fillers. The original model for cuboid nanofillers could be used directly for vertically-oriented cylindrical and elliptical rods as they share similar geometric attributes of cuboids. The model could be used to estimate the relative permeability of MMMs with vertically-oriented annular tubes but with less precision. The proposed model was also used to predict the relative permeability of MMMs with spheres and horizontally-oriented cylindrical rods, elliptical rods, and annular tubes but required an easy transformation.

When applied to determine the effective diffusivity coefficient of MMMs with uniformly dispersed impermeable particles of different geometries in the continuous polymer phase, the validity of the time-lag method was finally investigated in Chapter 8. It was proven that the time-lag method is layer sensitive. In the limiting case of the MMMs containing a single layer of nanoparticles, the relative effective diffusivities of the mixed matrix membranes were often greater than unity, indicating (counter-intuitively) the actual effective diffusivity coefficients greater than those of the host polymer. The error in the relative diffusivity coefficient by the time-lag method rapidly decreases with an increase in the number of layers. Regardless of the nanoparticle's geometry and orientation, it becomes negligible for the MMMs containing five or more nanoparticles layers. Therefore, in the case of MMMs with multilayer of uniformly dispersed nanoparticles, the accurate prediction of the effective diffusivity (assuming the solubility coefficient is known or can be determined experimentally) requires accurate prediction of the effective permeability,

which as we have shown in Chapter 7, is possible with the generalized model for the MMMs.

9.2 Recommendations

The current constant-volume system allows the measurement of upstream and downstream time-lag simultaneously. However, to obtain high accuracy results at the upstream side, the operation temperature control is necessary to reduce temperature variation as much as possible. Another MASc student is currently carrying out this work. High-quality results should be obtained with additional temperature control.

Studies in this investigation were conducted assuming a constant diffusivity coefficient. However, this is not always the case, especially for glassy polymers. Future studies may address the issue with a concentration-dependent diffusivity coefficient.

Simulations of MMMs were done, assuming the continuous polymer phase is strongly adhesive to the dispersed impermeable particle phase, resulting in zero gaps in between. It would be interesting to investigate numerically the effect of potential interfacial gaps between two phases on the relative permeability results as well as the time-lag results. The interfacial non-ideality of MMMs is essential and needs to be addressed.